Measuring the N-subjettiness jet shape in pp and Pb-Pb collisions with the ALICE experiment

Nima Zardoshti

Thesis submitted for the degree of
Doctor of Philosophy

Nuclear Physics Group,
School of Physics and Astronomy,
University of Birmingham.

September 2018

UNIVERSITY OF
BIRMINGHAM

University of Birmingham Research Archive

e-theses repository

This unpublished thesis/dissertation is copyright of the author and/or third parties. The intellectual property rights of the author or third parties in respect of this work are as defined by The Copyright Designs and Patents Act 1988 or as modified by any successor legislation.

Any use made of information contained in this thesis/dissertation must be in accordance with that legislation and must be properly acknowledged. Further distribution or reproduction in any format is prohibited without the permission of the copyright holder.

ABSTRACT

Fully corrected measurements of the τ_2/τ_1 jet shape are reported, in pp ($\sqrt{s} = 7$ TeV) and Pb-Pb ($\sqrt{s_{NN}} = 2.76$ TeV) collisions, using the ALICE detector. Fully corrected measurements of the ΔR jet shape are also presented in pp collisions. For each shape, measurements are made using four different reclustering algorithms, which probe the hard and soft scale splittings of the jet substructure. These are the exclusive k_T, exlcusive C/A (with and without minimisation) and soft drop groomer with C/A algorithms. In both collision systems, the shapes are presented at $40 \leq p_T^{jet,ch} < 60$ GeV/c, with a jet resolution of $R = 0.4$. The semi-inclusive hadron-jet coincidence technique is extended to two dimensions for the first time, in order to reject the combinatorial background in Pb-Pb collisions. A two-dimensional Bayesian unfolding procedure is used to correct the measured distributions, for detector (pp and Pb-Pb) and background (Pb-Pb) effects.

In pp collisions, the results are used to test QCD splitting functions and fragmentation patterns, with particular emphasis on measuring the two-prong nature of QCD jets. In Pb-Pb collisions, changes to this two-prong substructure, due to quenching effects in the quark-gluon plasma, are investigated. No modifications, relative to the vacuum, are observed .

Declaration of Author's Contribution

All research benefits from and builds upon preceding work. This is particularly true in large collaborations such as ALICE, where no output is possible without the work of countless people in every stage of the design, construction and operation of the experiment. The analysis detailed in this thesis is no different and would not have been possible without the work and effort of many collaborators. However, given this caveat, all the work produced and presented in this thesis, including figures and results, unless otherwise indicated, is my own work.

The majority of my analytical work consisted of developing a framework for the reclustering, processing and correction of jets and jet shapes, both in pp and Pb-Pb collisions. This framework was built upon the official ALICE analysis code. I also developed Monte-Carlo models, using the ALICE framework, in order to provide comparisons to the measured results. All this work can be found in chapters 4, 5 and 6.

In addition to the work mentioned above, I was also involved in the operation of the Central Trigger Processor at ALICE, through a service task and on-call duties. I have also served as an internal analysis reviewer, for both conference talks and publications.

ACKNOWLEDGEMENTS

Over the years, I have benefitted from the help, council and friendship of numerous people, which have all led me to where I am now. I would have to double the page count of this thesis in order to adequately thank everyone, so I will have to make do with thanking a select few who have been particularly influential during the four years of my PhD. For all those who are not mentioned below, it does not detract from your importance to me.

First of all, I would like to thank my supervisor Peter Jones, for all the help, supervision and advice during the course of both my undergraduate and PhD programs. I always come away from our chats, whether about physics, career paths or life in general, with the exact information I need and a much clearer mindset of how to approach the problems at hand. Your trust in my work has helped me develop the confidence for independent research, which I look forward to continuing. I am also grateful for your continued understanding in allowing me to have spent so much time at CERN, without ever objecting. I would also like to thank Lee Barnby, who supervised me during my undergraduate program as well as the first half of my PhD. I always appreciated that your door was forever open and approachable. I would also like to give a special mention to the members of the Birmingham ALICE group for their continued support throughout these years : David Evans, Roman Lietava, Orlando Villalobos Baillie, Anton Jusko and Marian Krivda.

No PhD can be completed without the help and expertise of countless academic colleagues. This is particularly important in large collaborations such as ALICE, where the ambitious targets are only attainable through the collective work of every individual. To this end, I thank every member of the ALICE collaboration, whether I have met you personally or not. However, for the purposes of this work, no one deserves more thanks and gratitude than Leticia Cunqueiro Mendez, without whom this analysis would not have been possible. I don't think that I can begin

to adequately thank you for all your help and advice, no matter what time of day or night, and your endless patience with my work. I feel indebted to you both for the work I have achieved and for your help with my future continuation in the field. However, to only call you an academic colleague is a huge disservice as you have more importantly become a friend. I am looking forward to continue working with you over the next few years.

No four years of life should be lived without filling them with good friendships and I feel lucky to have made many great friends during the course of this PhD. First and foremost are my fellow Birmingham Nuclear Physics PhD students of E318: Joe, Tanya, Sam, Robin, Chris, Jack, Kae, Harry, Emily, Anthony, Stuart (with full perspection), Pedro, Rebekah, Jakub, Marianna, Håkan, Yi Ming, Ollie, Ellie and Neil. I can honestly say that you have been one of the best parts of these last four years and I don't think I will ever be in an office as enjoyable as ours. I will miss all the long lunches, fascinating chats, board games and fantastic office atmosphere. Sorry that I was "never there", but from my perspective I really had the best afternoons with all of you. I would also like to thank my friends in Geneva who have shared so many adventures with me. In particular, I would like to thank everyone from the groups of "Kool Kids", "Frisbee time", "Geneva's Finest" and "Team Lucifer" who have made my time at CERN unforgettable. I would also like to thank Luis, for sharing an office with me at CERN and always being there to chat. To everyone mentioned here, I fully intend to keep our friendships going long after the pages of this thesis have worn out.

Last but by no means least, I would like to thank all the people who are closest to me in my life. This thesis is dedicated to you. Your love and support throughout all these years have made me the person I am today (so you can only blame yourselves) and you will always have the most important place in any acknowledgement or dedication I make in my life. To Sahil and Rania, for being the newest members of our family. To Richard, my best friend, for always (literally) being there. You have been family for a long time. To my mum and dad, words cannot describe what you mean to me. You are both in your own rights, the very best human beings I have ever had the pleasure of knowing and somehow you have managed to be even better parents. And finally to my brother and sister, no matter how far apart we live or what we are doing we never lose any love or closeness and I am forever appreciative of that. You have both become people who I am very proud of. I love you all.

You'll never walk alone

Contents

List of Tables

List of Figures

CHAPTER 1

Introduction

1.1 QCD

All natural interactions can be explained through the four fundamental forces. These forces act between particles via the exchange of mediating bosons, which determine the properties of their corresponding force. Gravity will be omitted from the discussions in this work, due to its insufficient strength on the subatomic scale. The electroweak theory [1, 2, 3] successfully combines the electromagnetic and weak forces and is considered one of the major successes of 20^{th} century physics. A large wealth of experimental results have since validated this theory. Due to a large coupling constant and the self interaction of its mediating bosons, gluons, the strong force is yet to reach the same level of theoretical and experimental validation. Quantum Chromodynamics (QCD) is the theoretical framework underpinning the current un-

derstanding of the nature of the strong force [4, 5, 6]. It states that colour charged particles (quarks and gluons, which will be referred to collectively as partons) interact via the strong force by exchanging gluons.

1.1.1 Strong Nuclear Force

The potential of the strong force can be written as [7, 8],

$$V_s(r) = -\frac{4}{3}\frac{\alpha_s}{r} + kr, \tag{1.1}$$

where α_s is the coupling strength of the interaction and r is the distance between colour charged centres. k is a constant, representing the field energy per unit length stored between colour charged centres, which is distributed in structures known as flux tubes [9]. At large distances, the kr term in equation 1.1 dominates. At a certain separation, it becomes more energetically favourable to create a new quark and anti-quark pair, rather than further increasing r. This leads to a phenomenon known as confinement [10], where colour charges are bound together. Confinement limits the size of nucleons and prohibits the observation of free colour charges in nature. This phenomenon contributes to the difficulties of studying strong interactions between colour charged particles.

It would be expected that in the limit of $r \to 0$, $V_s(r) \to \infty$. However, α_s is not constant, as given by [11],

$$\alpha_s(Q) = \frac{\alpha_s(\mu^2)}{1 + \frac{\beta_0}{4\pi}\alpha_s(\mu^2)\ln\frac{Q^2}{\mu 2}}. \tag{1.2}$$

$Q^2 = -q^2$, where q is the four-momentum exchange of the interaction. Since the

coupling increases without limit with increasing distance, it cannot be scaled with respect to coupling at infinity and instead a scale μ is chosen. $\beta_0 = \frac{1}{3}(11n_c - 2n_q)$, where n_q is the number of quark flavours and n_c is the number of colours. In QCD these values are six and three respectively, leading to $\beta_0 = 7$. By defining the QCD scale constant $\Lambda^2_{QCD} = \mu^2 exp[\frac{-4\pi}{\beta_0 \alpha_s(\mu^2)}]$, equation 1.2 can be rewritten as [11],

$$\alpha_s(Q) = \frac{4\pi}{\beta_0 \ln \frac{Q^2}{\Lambda^2_{QCD}}}. \tag{1.3}$$

At large Q^2 ($Q^2 >> \Lambda^2_{QCD}$), which corresponds to small r, α_s becomes vanishingly small. This occurs at a faster rate than the increase of the $\frac{1}{r}$ term in equation 1.1, resulting in $V_s(r) \to 0$. In this limit, perturbation theory applies and QCD processes are calculable. At small Q^2 (large distances), perturbation theory is not applicable since α_s becomes large. In this regime, techniques such as lattice QCD [12] and numerical methods must be used instead. Experimental data also plays a large part in quantifying processes at this level. This dependence of α_s on the energy, is known as the running coupling of the strong force and is shown through measurements in figure 1.1 [13].

1.1.2 Quark-Gluon Plasma

At sufficiently high energies, the running coupling of the strong force leads to deconfinement, where $\alpha_s \to 0$ and colour charges cease to interact with one another. This is known as asymptotic freedom [14]. However, long before these energies, there is a complementary phenomenon in bulk QCD matter known as Debye screening [15] (analogous to the Mott transition in QED [16]), where high temperatures and/or densities of nuclear matter induce a screening of colour charges. Thus, in dense QCD matter, long range interactions are screened. The Debye radius defines

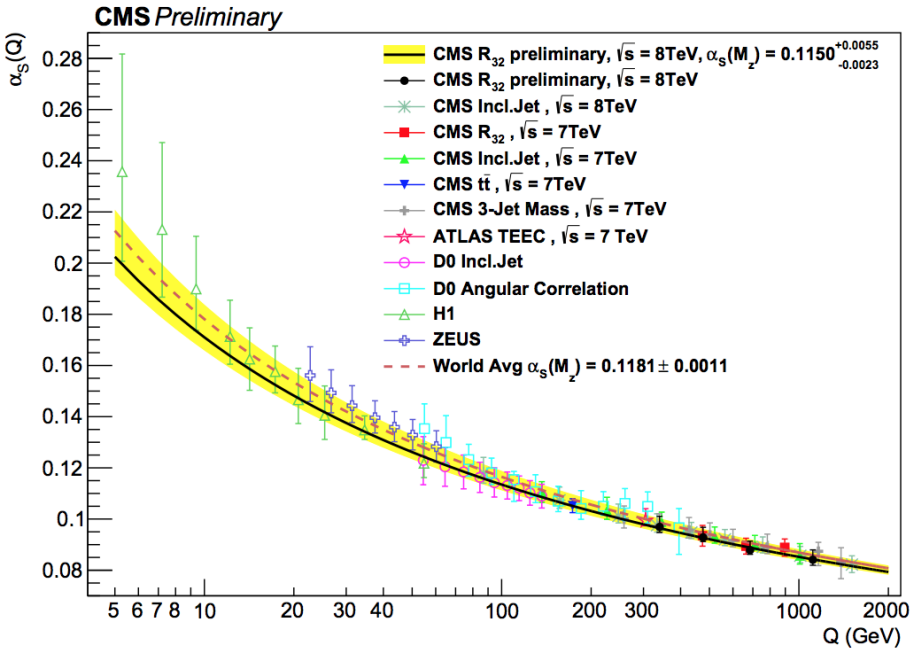

Figure 1.1: The coupling of the strong force is measured for different interaction energies, across a variety of experiments. The running coupling behaviour of the strong force means that the coupling becomes small at high Q^2 and large at large distances [13].

a distance from a colour charged centre, beyond which interactions are exponentially suppressed. This radius decreases with increasing temperature. At a certain temperature, this radius becomes smaller than the hadronic scale, such that quarks and gluons become unbound and are able to propagate freely over extended distances. This leads to a phase transition in QCD (figure 1.2) [17], at T $\sim$ 170 MeV, where quarks and gluons become deconfined. This results in a new state of matter, known as the Quark-Gluon Plasma (QGP), where quarks and gluons are the relevant degrees of freedom over hadrons. Since the phase transition occurs before the realisation of true asymptotic freedom ($\alpha_s \to 0$), the QGP medium is strongly interacting. This provides an ideal experimental opportunity with which to study the strong force, acting between unbound but strongly interacting colour charged particles.

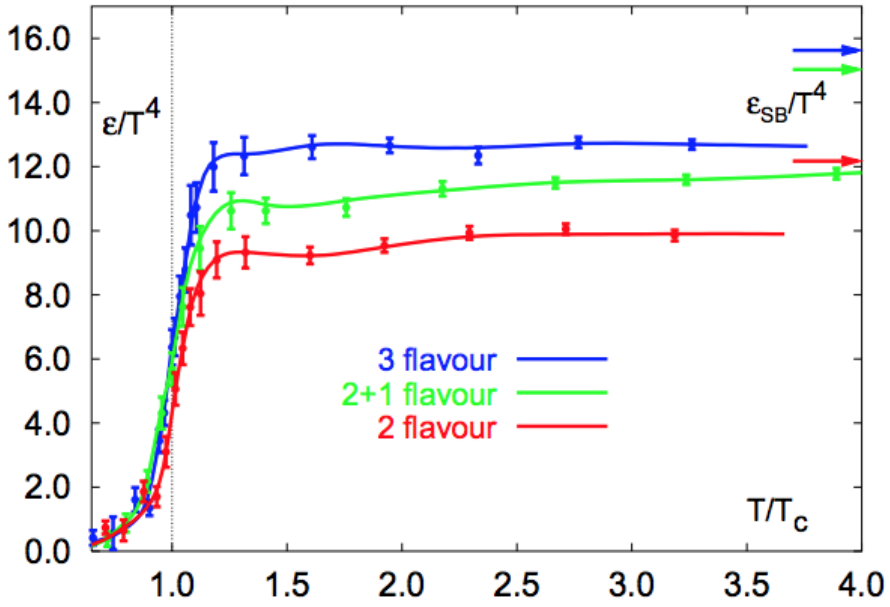

Figure 1.2: The QCD phase transition, predicted by lattice QCD calculations for models involving different numbers of (light) quark flavours. At a critical temperature of T $\sim$ 170 MeV, hadronic matter undergoes a phase transition to a state of free quarks and gluons [17].

1.1.3 Heavy Ion Collisions

Relativistic heavy ion collisions are the experimentally accessible method of creating the QGP medium. This experimental journey began in the 1980s and 1990s at the Super Proton Synchrotron (SPS) at CERN and the Alternating Gradient Synchrotron (AGS) at Brookhaven National Laboratory (BNL) respectively. At the SPS, centre of mass energies of $\sqrt{s_{NN}}$ = 17 GeV were achieved via fixed target collisions. In 2000, the same year that data taking at the Relativistic Heavy Ion Collider (RHIC) commenced, CERN announced the first indirect signatures of QGP creation [18]. This was inferred through measurements such as the suppression of J/ψ and strangeness enhancement. The next decade of experimental studies performed at RHIC, a dedicated heavy ion facility with a centre of mass energy of $\sqrt{s_{NN}}$ = 200 GeV, produced a wealth of new data; confirming the existence and creation of the QGP. Properties of the QGP such as its opacity to high momentum

hadrons (jet quenching) [19] and its "ideal liquid" nature [20], were also discovered.

The Large Hadron Collider (LHC), at CERN, is the culmination of experimental efforts in studying the QGP. Since becoming operational in 2008, the first phase of the LHC has seen the collision of Pb nuclei at a centre of mass energy of $\sqrt{s_{NN}} = 2.76$ TeV. The LHC's dedicated heavy ion experiment, ALICE, has already confirmed and extended the early measurements made at RHIC. The order of magnitude increase in centre of mass energy, compared to RHIC, creates larger and longer lived QGP systems, which are favoured experimentally [21]. This allows for a more detailed study of the properties of the QGP, which is the current goal of high energy heavy ion physics. In particular, this work will concern itself with probing the finer details of the energy loss of colour charged particles traversing the QGP. Despite the capabilities of the LHC, RHIC plays a vital role in the field. Amongst other things, beam energy scans at RHIC probe the energy dependence of observables, whilst systematic studies colliding different ion species form a control experiment for initial state effects.

Figure 1.3 shows the collision dynamics of a central heavy ion collision. Centrality defines the degree of overlap of the colliding nuclei, with central collisions having a larger amount of overlap than peripheral collisions [25]. The higher number of nucleons participating in central collisions, leads to a larger amount of energy being deposited. Therefore, central collisions produce the largest and longest lived QGP systems. Centrality is often quoted as a percentage, ranging from 0-100%, with the lower end of the scale attributed to the most head on collisions.

1.1.4 QGP Induced Energy Loss

One of the most compelling signatures of QGP creation, is the energy loss of high momentum partons traversing the medium. These partons are expected to interact

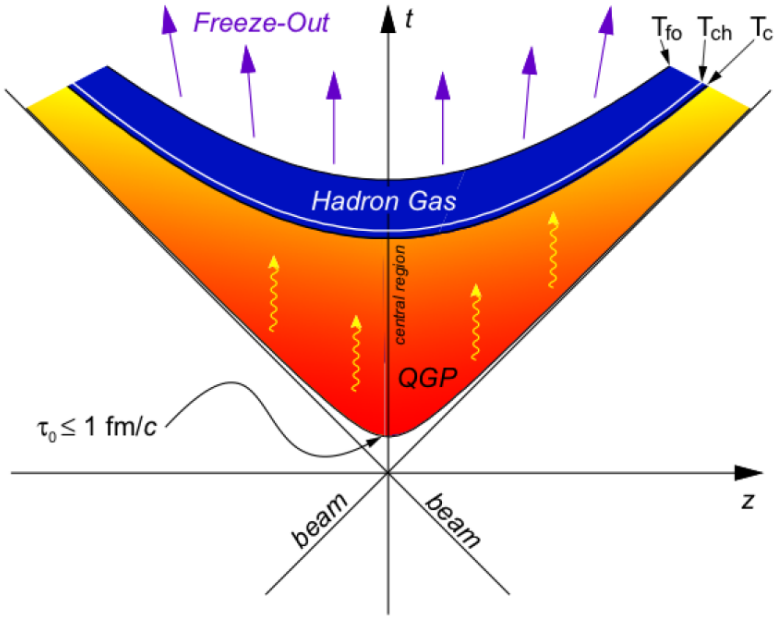

(a) Timeline of the creation, expansion and cooling of the QGP medium, following a heavy ion collision [22].

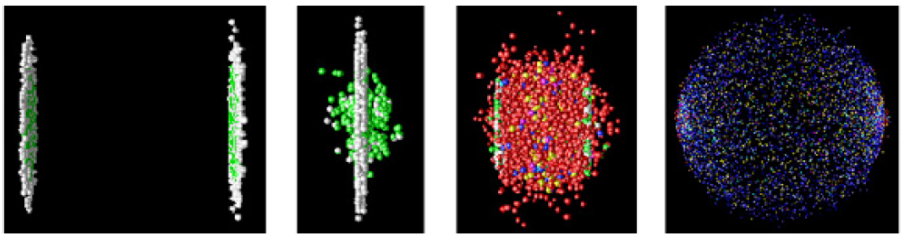

(b) A simulation of QGP creation, through relativistic heavy ion collisions. The two green disks are the lorentz contracted beams, the red system represents the thermalised QGP and the blue system is the cooled down hadronic gas [23].

Figure 1.3: The different stages of a central relativistic heavy ion collision are shown. The high temperatures and energy densities of the collision (a few GeV/fm^3 at the LHC [24]), deconfine the quarks and gluons which quickly thermalise into the QGP. The medium then expands rapidly and cools down. Once it reaches the critical temperature (T_c), the quarks and gluons are bound and a hadronic gas is formed. The system further cools to the chemical freeze-out temperature (T_{ch}), where inelastic collisions cease and the hadron species ratios become fixed. Finally, the system reaches the kinetic freeze-out temperature (T_{fo}), where elastic collisions also cease. This is the state of the particles as they pass through the detectors [22].

with scattering colour centres in the medium and lose energy via radiative and collisional processes. The two most prominent formalisms of radiative energy loss are the Baier-Dokshitzer-Mueller-Peigné-Schiff (BDMPS) [26] and Gyulassy-Levai-Vitev (GLV) [27] theories. Both formalisms attempt to describe this QCD energy loss in

an analogous manner to the QED energy loss of charged particles travelling through matter, known as the Landau-Pomeranchuk-Migdal (LPM) effect [28, 29, 30]. Analogous to the QED case, where the energy is carried away via photon emission, in QCD the energy loss is induced by the emission of gluons. The BDMPS formalism concludes that the energy is lost through the emission of many soft (low transverse momentum (p_T)) and semi-soft gluons. A transport coefficient, $\hat{q}$, determines the rate of p_T accumulation due to the scattering of partons travelling through the medium. In contrast, the GLV formalism expects that the energy is carried away by a few harder (high p_T) gluons. Both models include a medium length dependence for the energy loss.

The first experimental evidence to motivate energy loss models in the QGP, was the observation of the suppression of high p_T hadrons in heavy ion collisions, compared to pp collisions (vacuum) [31, 32, 33, 34]. These high p_T hadrons are taken as a proxy for the high p_T partons scattered in the initial stages of the collisions. The nuclear modification factor, R_{AA}, measures the ratio of the p_T yield of charged hadrons in heavy ion collisions compared to pp collisions. The pp yield is scaled by the number of binary nucleon-nucleon collisions occurring in the heavy ion events. Since this quantity is dependent on the centrality of the collision, R_{AA} is measured differentially in centrality. In the absence of medium effects, high p_T particle production in heavy ion collisions would be a superposition of multiple pp collisions, leading to an R_{AA} value of unity. However, as shown in figure 1.4, measurements of R_{AA} in $0-5\%$ most central Pb-Pb collisions, show a clear deviation from unity at high p_T. Measurements of R_{pA} (R_{AA} performed in p-Pb collisions) show no deviation from unity for high p_T hadrons. Since no QGP is expected to form in p-Pb collisions, this indicates that the deviation observed in central Pb-Pb collisions is a QGP effect. This deviation is due to the energy loss of the initial scattered partons as they traverse the QGP medium. Even though the magnitude of this energy loss can be ascertained through charged

hadrons, there is a much more powerful tool with which to study the behaviour of energy loss. This tool is known as jets.

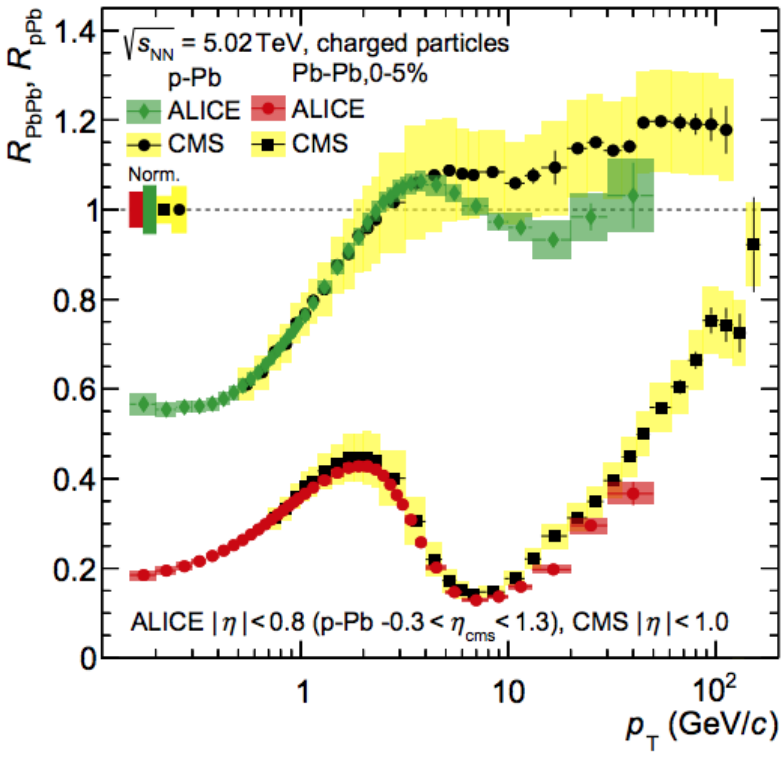

Figure 1.4: The nuclear modification factor is measured in central Pb-Pb and p-Pb collisions, at both the ALICE and CMS experiments. The production processes of charged hadrons with $p_T^{ch} <\sim 3$ GeV/c, are not linked to the hard scattered partons and therefore exhibit a different behaviour compared to their higher p_T^{ch} counterparts. The R_{AA} of charged hadrons above ~ 3 GeV/c shows strong quenching effects. The increase of R_{AA} towards unity, with increasing p_T^{ch}, is a consequence of the medium length dependence of the energy loss. Since the energy loss is not dependent on the energy of the parton, at higher p_T^{ch}, the lost energy represents a smaller fraction of the hadron's p_T^{ch}. The measurement of R_{pA} is used to disentangle medium effects from initial cold nuclear effects, since no QGP is expected to form in p-Pb collisions. The R_{pA} value of unity for hadrons arising from hard scatters, indicates that the deviations seen in Pb-Pb collisions are due to the QGP [35].

1.2 Jets

Jets are defined as collimated bunches of hadrons, originating from the fragmentation of high p_T partons which were scattered in the initial stages of the collisions. After a hard (high Q^2) interaction between constituents of the colliding nuclei, a pair of partons are scattered in a back to back configuration. These scattered partons lose virtuality, through fragmentation, resulting in a parton shower. At hadronisation scales (~ 1 GeV/c) the shower constituents hadronise into colourless hadrons. In central heavy-ion collisions, this hadronisation is expected to occur outside the medium due to the large timescales involved. Specially designed jet algorithms can identify the hadrons originating from a scattered parton and reconstruct its properties.

These algorithms begin by clustering the final state hadrons, based on a combination of their p_T and angular separation. At each step of the clustering, the clustered hadrons are replaced by a pseudo-particle. The four-momentum of this pseudo-particle is equal to the sum of the four-momenta of the clustered hadrons. This clustering, between hadrons and pseudo-particles, continues until a predefined criteria, often determined by a maximum angular size (jet radius), is met and a jet is defined (for more information on jet clustering algorithms, see section 2.1). In this way, jets provide a direct link to the initial scattered partons.

1.2.1 Parton Distribution Functions

The QCD factorisation theorem [36, 37, 38] postulates that jet production and evolution can be split into three independent stages. This has yet to be analytically proven, but is widely accepted in the theoretical communities and has been verified against experimental results. The power of factorisation lies in the fact that it

allows for the separate treatment of processes with different hardness scales, in the evolution of the jet.

The first of these are the parton distribution functions (PDFs) of the colliding nuclei. High energy collisions resolve the constituent quarks and gluons of the colliding nuclei. As such, the distribution of these constituents in the nucleons determine the incoming scatterers. PDFs describe the probability of finding any particular parton type, as a function of the momentum fraction of the nucleon which they carry. Since PDFs map a wide range of momentum scales, including the soft scales, they cannot be analytically calculated using pQCD. A data driven approach is used to obtain the PDFs from experimental data, using the Dokshitzer-Gribov-Lipatov-Altarelli-Parisi (DGLAP) [39, 40, 41] and Balitsky-Fadin-Kuraev-Lipatov (BFKL) [42, 43, 44, 45] evolution equations (these equations also appear in the fragmentation functions described later). In particular, deep inelastic scattering experiments and other hard processes contribute to the determination of PDFs. Figure 1.5 shows the PDFs of protons at the LHC, using data from previous collider experiments. The evolution equations also contain the QCD splitting functions [40], which describe the probability of partons radiating quarks and gluons. Modifications to the splitting functions, due to energy loss in the QGP, are an active area of theoretical and experimental interest and can provide information on the underlying QCD mechanisms. Studying these modifications forms a large part of the work carried out in this thesis.

1.2.2 Hard Scattering Cross Sections

Once the initial distribution of partons in the colliding nucleons has been ascertained, the next step is to calculate the cross section of partonic processes arising from the scattering of these constituents. These can be modelled as $i + j \rightarrow c + d$, where i and j are the initial state partons in the incoming nucleons and $c + d$ is the partonic

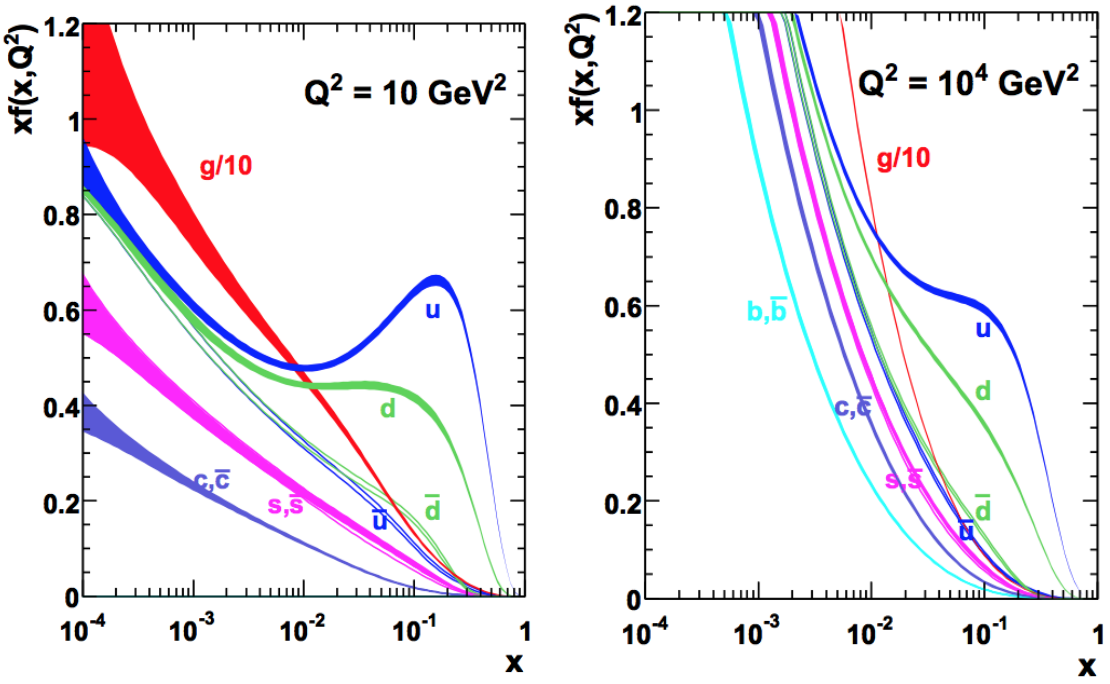

(a) $Q^2 = 10$ GeV^2 (b) $Q^2 = 1000$ GeV^2

Figure 1.5: The PDFs are determined by using global fits to available deep inelastic scattering data. The variable x represents the fraction of the nucleon's momentum carried by the parton. It can be seen that at LHC energies, gluon-gluon interactions are dominant. Quarks carry a large fraction of the proton's momentum [46].

state after scattering. Since this is a hard process, α_s is small enough so that it is calculable in pQCD [47]. The production cross section of the scattered partons (which give rise to jets) from the colliding nuclei can be modelled as,

$$\sigma(a+b \to c+d) = \sum_{i,j} \int dx_1 dx_2 dQ^2 f_i^a(x_1, Q^2) f_j^b(x_2, Q^2) \sigma(i+j \to c+d), \quad (1.4)$$

where a and b are the incoming nucleons and $f_i^a(x_1, Q^2)$ represents the PDF describing the probability of finding parton i, carrying a momentum fraction x_1 of hadron a, obtained at a given Q^2. Comparison of measurements of the clean leptonic production channels in hadron colliders [48], to theoretical calculations using PDFs and the Drell-Yan [49, 50] leptonic production cross sections, provide validation of QCD

and the factorisation theorem.

Non leptonic channels are not as clean and the final states observed in detectors include the fragmentation of the scattered partons into observable colour-less hadrons. Therefore, any full theoretical model must include a description of this fragmentation to facilitate comparison to experimental results. This forms the third and final part of the QCD factorisation theorem of jet production.

1.2.3 Fragmentation Functions

The mechanisms of the fragmentation and subsequent hadronisation of the scattered partons are not well understood. These processes are, by definition, soft and are not calculable in pQCD. Instead, they must be quantified experimentally by fitting fragmentation functions to measured data. The first definition of fragmentation functions described them as an inverse of PDFs, where they defined the probability of a hadron emerging from a given parton [51]. Developments in the field [52, 53, 54] have lead to expressions for fragmentation functions, of the form $D_i^h(z, Q)$, which describe the probability of a fragmenting hadron h, containing a fraction z of the longitudinal momentum of its parent parton i. The fragmentation functions also depends on the scale of the hard scattering process, Q, which gives rise to the parton i.

The parameters of these expressions are extracted from fits to measured data. The first measurements of fragmentation functions were made at the Positron-Electron Tandem Ring (PETRA) at DESY [55] and the Large Electron-Positron Collider (LEP) at CERN [56, 57]. Figure 1.6 shows a fragmentation quantity (related to the fragmentation functions), $F(z, p_{Tjet})$, measured by the ATLAS experiment in pp collisions [58]. This measurement includes the kinematic regime explored in this analysis. $F(z, p_{Tjet})$ is defined as the distribution of charged hadrons in bins of z,

normalised to the total number of jets. The number of charged hadrons in a jet falls with increasing z.

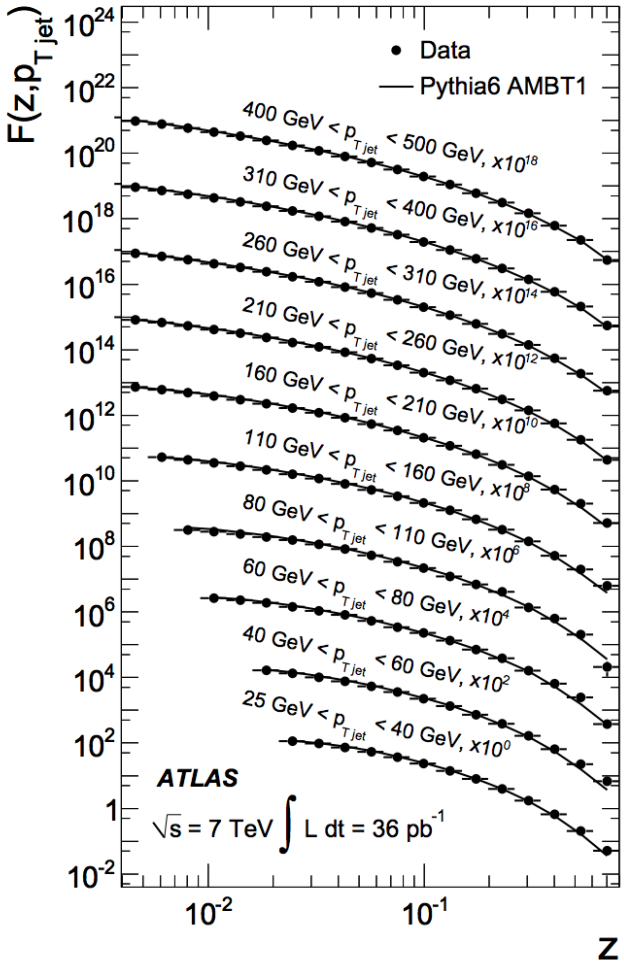

Figure 1.6: The fragmentation variable, $F(z, p_{Tjet})$, measured in differential bins of p_{Tjet} by the ATLAS experiment in pp collisions at $\sqrt{s} = 7$ TeV [58].

With the addition of these fragmentation functions, equation 1.4 describes the full cross section of the production of observed hadrons composing a jet, from the colliding nucleons. In this way, theoretical QCD models and calculations can be validated against experimental results in the vacuum (pp collisions) and modifications to the distributions due to energy losses in the QGP can be extracted from measurements in heavy ion collisions. Figure 1.7 shows measurements of the jet production cross section in pp collisions at CMS [59], compared to next to leading order (NLO) QCD calculations. The good agreement verifies the partonic theory of QCD, whilst

validating the factorisation theorem of jet production.

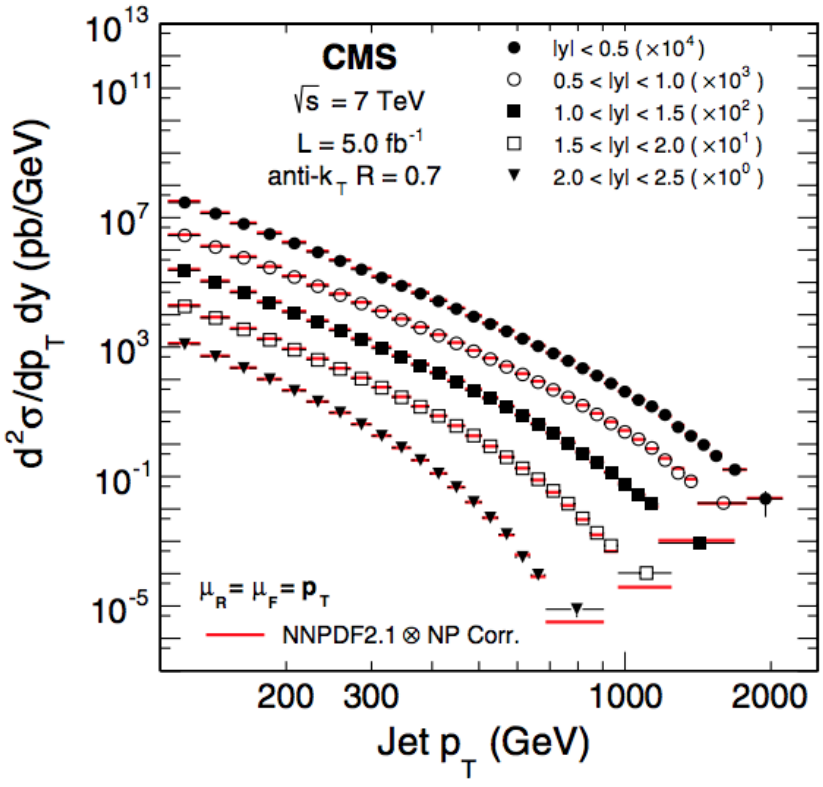

Figure 1.7: The jet production cross section measured for different angular geometries by the CMS collaboration in pp collisions at $\sqrt{s} = 7$ TeV [59]. A power law behaviour is observed at low p_T^{jet}.

1.2.4 Jet Quenching

Jet quenching is the observation that partons traversing the QGP medium undergo energy loss. Measurements of the charged hadron R_{AA} (figure 1.4) served as a proxy for this energy loss. However, jets provide a direct link to the scattered parton. Figure 1.8 shows measurements of jet R_{CP} at three LHC experiments [60]. R_{CP} is measured in the same way as R_{AA}, with the exception that the reference distribution is peripheral (non central) Pb-Pb collisions as opposed to pp collisions. In the case of jet R_{CP}, the distributions are composed of measured jet yields. A strong quenching effect is observed, similar to the case of charged hadrons. However, in contrast to

the charged hadron case, the jet quenching remains constant with increasing p_T^{jet}, which is currently not understood.

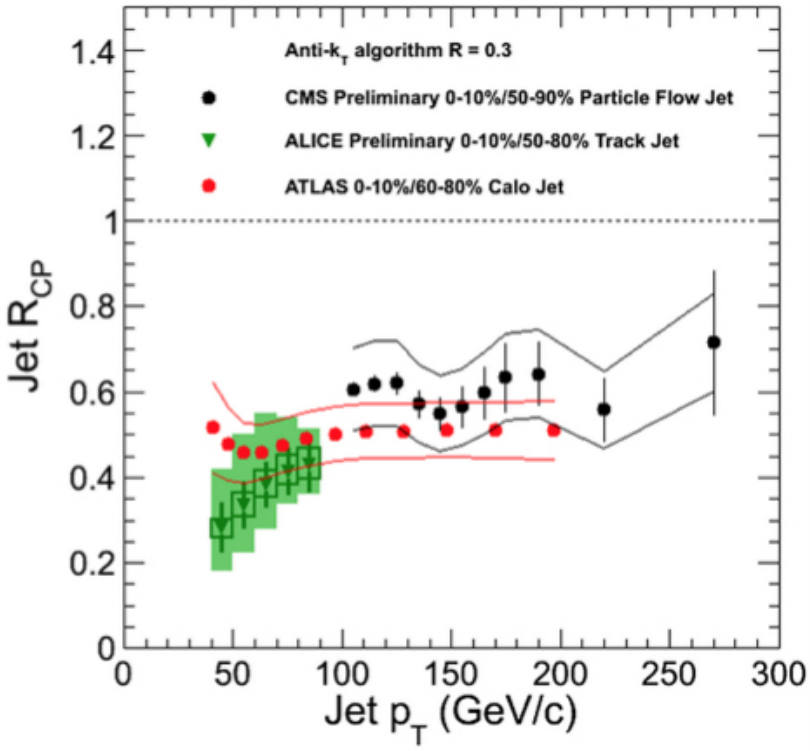

Figure 1.8: Measurements of Jet R_{CP} over a wide range of p_T^{jet} at the LHC. The reference distributions are jets measured in peripheral Pb-Pb events, where no or only small QGPs are expected to form [60].

R_{AA} measurements quantify jet quenching effects in a variety of systems. However, they give limited information about the mechanisms of the energy loss and the finer effects of quenching on jets. Modifications to the QCD splitting functions and the radiative and collisional energy loss processes can alter the fragmentation patterns of the constituents of the jet. To this end, a new field of jet studies, known as jet substructure, which can scrutinise these processes in finer detail, has undergone active development.

1.2.4.1 Colour Coherence

One such energy loss mechanism, is that of colour coherence [61, 62, 63]. This theory states that the medium can resolve and interact independently with constituents or structures within a jet, which have an angular separation above a critical angle. This is shown schematically in figure 1.9. A transverse resolution scale, Λ_{med}, which is linked to the critical coherence angle, dictates the role of coherence effects.

A small value of Λ_{med}, leads to a greater resolving power in the QGP, meaning that smaller substructures in the jet can interact independently with the medium. This is known as incoherent interaction and leads to a larger degree of energy loss and a change to the fragmentation pattern of the jet substructure, compared to vacuum. If Λ_{med} is larger than the transverse size of the jet, no substructure will be resolved and the jet will interact with the medium as a single emitter (coherent interaction). The emitted radiation will appear outside the jet cone, leading to a reduction of the jet energy scale. However, the jet substructure will remain vacuum like.

The colour coherence model has been the focus of a substantial amount of recent theoretical work. Not only are the mechanisms of the energy loss important in ascertaining the interactions between the jet and the medium, but the critical coherence angle is also directly related to the QCD transport coefficient ($\hat{q}$) [64] and can be used to extract its value. Investigating the presence and role of colour coherence effects on jet quenching, forms one of the motivations behind this analysis.

1.3 Jet Substructure

The study of jet substructure concerns itself with investigating the distribution of constituents clustered into a jet. Observables known as jet shapes can be constructed

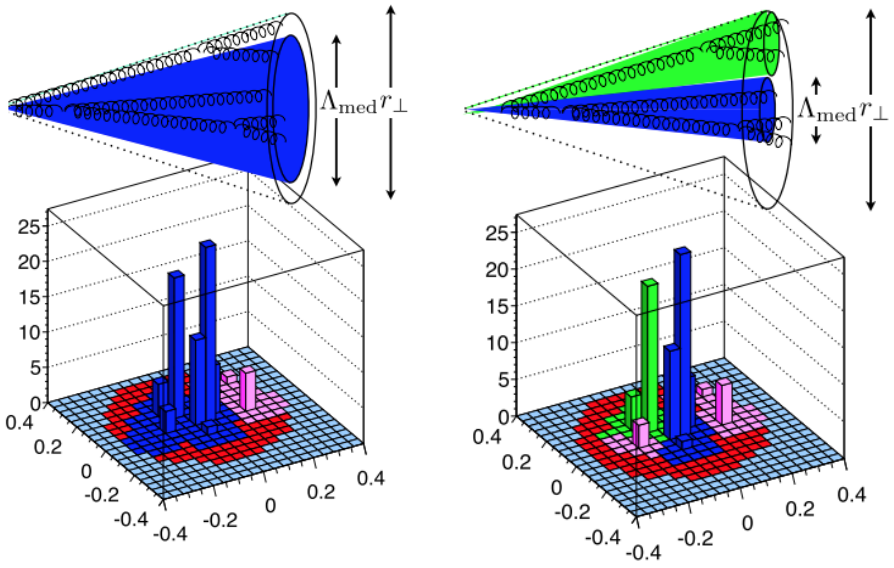

(a) Unresolved substructure (b) Resolved substructure

Figure 1.9: Unresolved (a) and resolved (b) jet substructures are shown, which lead to coherent and incoherent energy loss respectively. The resolving power of the QGP is controlled by the transverse resolution scale, Λ_{med}, whilst $r_\perp$ represents the diameter of the jet cone [62].

to measure different aspects of this fragmentation. By carefully defining jet shapes, they can have a clean link to theoretical calculations and be made sensitive to particular physical processes within the jet. Two jet shapes, measured for jets with a small radius at the ALICE experiment [65], will be discussed below. These are the angularity, g, and $p_T D$ jet shapes. Before defining these shapes, the angular coordinate system used in particle accelerators is shown in figure 1.10. The surface of the detector volume can be unraveled onto an angular plane. The axes of this plane are ϕ and η, with the variable R measuring distances on this surface. This distance R, between two points i and j, can be defined as,

$$R_{ij} = \sqrt{(\phi_i - \phi_j)^2 + (\eta_i - \eta_j)^2}. \tag{1.5}$$

Angularity is defined as,

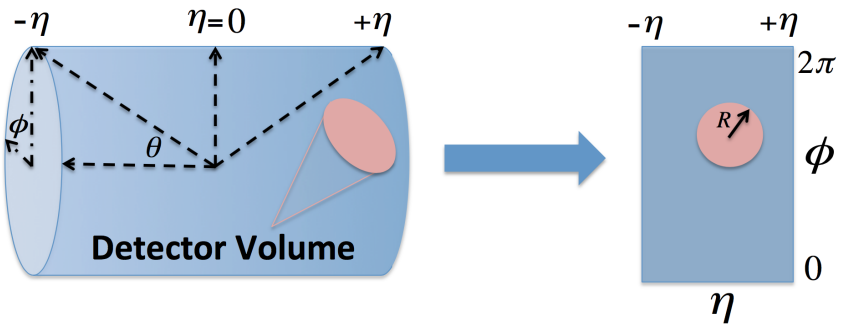

Figure 1.10: The surface of the detector volume is unraveled onto the two-dimensional plane of $\eta - \phi$. The pseudorapidity, η, is related to the polar angle, θ. This is given by $\eta = -\ln[\tan(\frac{\theta}{2})]$. ϕ represents the azimuthal angle. Distances on this plane are denoted by R.

$$g = \sum_i \frac{p_{T,i}}{p_T^{jet}} R_{jet,i}, \tag{1.6}$$

where the index i runs over all particles in the jet. $R_{jet,i}$ measures the angular distance between track i and the jet axis and is defined in equation 1.5. Small values of angularity represent jets where the bulk of the p_T is situated close to the core, whereas larger values indicate that the radiation is at large angles from the jet axis.

The p_TD jet shape is defined as,

$$p_T D = \frac{\sqrt{\sum_i p_{T,i}^2}}{\sum_i p_{T,i}}. \tag{1.7}$$

Values of p_TD close to unity indicate that a few of the jet constituents carry most of the p_T. Values near zero represent jets where the p_T is distributed between many softer particles. In figure 1.11, comparison of the measured jet shapes (black squares) to simulations (red circles and green open circles), which have been validated against pp collisions, show a significant deviation due to quenching effects. Jets traversing the medium are more collimated (smaller g) and exhibit a harder fragmentation

(larger $p_T D$), compared to the vacuum case.

These results support the colour coherence model of energy loss [65]. In the case of full coherence, where no substructure is resolved, the jet shapes in Pb-Pb collisions are expected to remain vacuum like and only the jet energy scale is reduced. Monte-Carlo (MC) simulations of the jet shapes in vacuum, using PYTHIA (see section 6.1), show that both shapes shift to lower values with increasing p_T^{jet}. PYTHIA is a full event generator which contains descriptions of the production and fragmentation of the scattered partons, along with hadronisation models used to produce a final state. The measurement of the $p_T D$ jet shape in Pb-Pb collisions, shows that the shape is shifted to larger values compared to simulations. This suggests that substructures in the jet are resolved by the medium. The measurements place an upper limit of 0.2 (the size of the jet radius) on the critical coherence angle. In this way, jet shapes can elude to the finer mechanisms of the energy loss and provide access to the fundamental properties of QCD.

1.3.1 Reclustering Jet Shapes

A new class of jet shapes, known as reclustering jet shapes, has recently emerged. These jet shapes access the partonic splittings of the jet, through the jet's reclustering history (see section 2.1.2). The jet constituents are reclustered with a given jet clustering algorithm and the reclustering history is unwound $N-1$ steps to obtain N axes (subjets) in the jet, which are branches of the splittings. By carefully choosing the reclustering algorithms, different scales of splittings can be accessed. Jet shapes are defined with respect to the returned axes and can be sensitive to modifications of the splittings induced by the QGP. Two reclustering jet shapes will form the focus of this analysis, which are considered in the $N = 2$ case. In this configuration, the reclustering history is unwound one step to obtain the last two axes that were

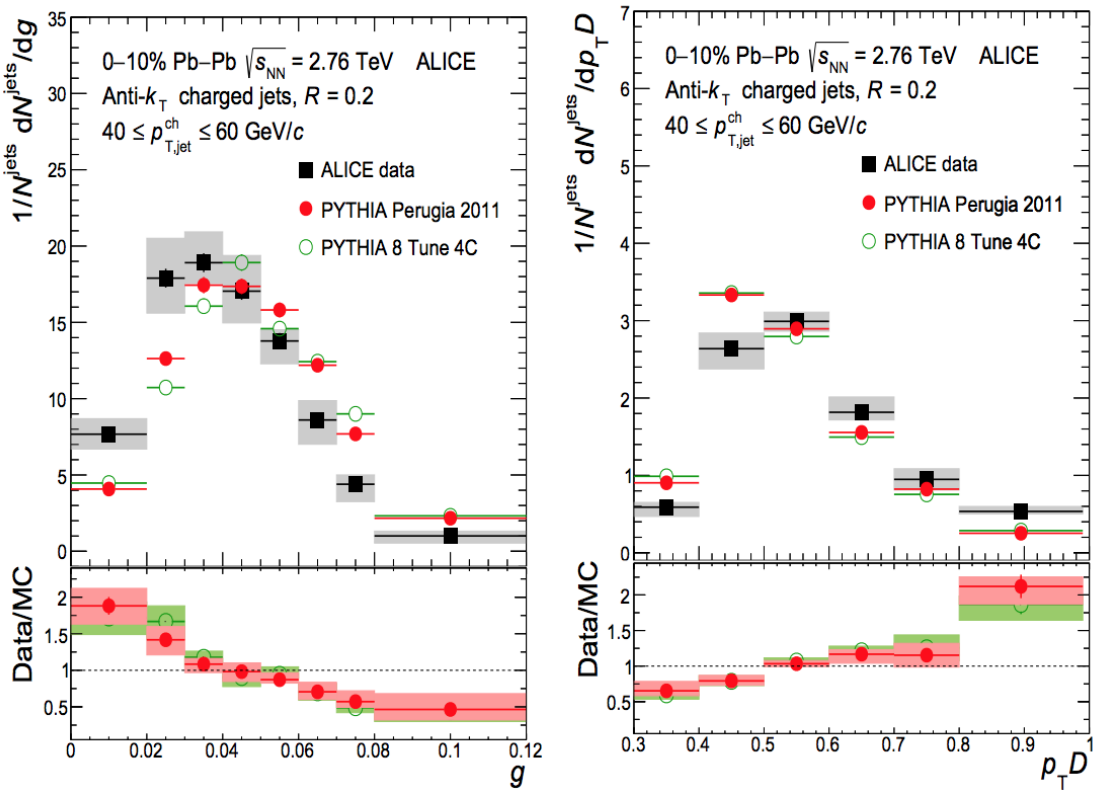

(a) Angularity, g (b) p_TD

Figure 1.11: The angularity (g) and p_TD jet shapes are measured in central Pb-Pb collisions by the ALICE experiment. Both shapes show strong deviations due to quenching effects, when compared to vacuum like simulations [65]

brought together.

1.3.1.1 ΔR

The ΔR jet shape measures the angular distance in the $\eta - \phi$ plane, between the two axes returned by the $N = 2$ reclustering case. This is equivalent to equation 1.5 and is given by,

$$\Delta R = \sqrt{(\phi_1 - \phi_2)^2 + (\eta_1 - \eta_2)^2}, \tag{1.8}$$

where the indices 1 and 2 represent the returned axes. Particular reclustering algo-

rithms can return the axes of the first and/or hardest splitting in the jet. A change in the rate of jets with a large angular separation between these prongs (ΔR), points to colour coherence effects in the medium. Colour coherence dictates that incoherently (independently resolved by the medium) interacting jet substructures would lose more energy in the QGP compared to coherently (unresolved) interacting ones. Upon successful measurement of this shape, jet R_{AA} measurements in differential bins of ΔR can be used to determine the critical coherence angle. This is considered to be beyond the statistical reach of the current data set. However, a successful measurement of ΔR would lay the foundations for such an analysis to be carried out in the upcoming high statistics LHC runs.

1.3.1.2 N-subjettiness

The N-subjettiness jet shape, τ_N, measures the N-prongness of a jet's substructure [66]. By unwinding the reclustering history $N-1$ times, N axes are obtained. The degree of alignment of jet constituents to these axes are then measured. This is obtained via,

$$\tau_N = \frac{\sum_i p_{T,i} min(\Delta R_{i,1}, \Delta R_{i,2}, \ldots, \Delta R_{i,N})}{p_T^{jet} R}, \tag{1.9}$$

where the index i runs over each constituent in the jet and $\Delta R_{i,1}$ is the $\eta-\phi$ distance between track i and the first returned axis. The denominator keeps τ_N between zero and one, with R being the jet radius. If all the high p_T radiation in the jet is well aligned to the reclustered axes, $\tau_N \to 0$, and the jet has N or fewer well defined cores. In the limit that the jet has exactly N constituents (which is the minimum number of constituents required for a τ_N measurement), $\tau_N = 0$. However, if the jet has at least $N+1$ cores, then some of the radiation will not be well aligned to

the returned axes and $\tau_N \to 1$. The ratio of τ_N/τ_{N-1} is sensitive to exactly N cores in the jet, as this configuration makes the numerator small and the denominator large. In this analysis, the value of τ_2/τ_1 is measured, which is sensitive to the two-prongness of jet substructure. Figure 1.12 shows the sensitivity of this variable in tagging two-prong W-jets compared to single-core QCD jets. This observable can successfully separate these jets based on their two-prong nature.

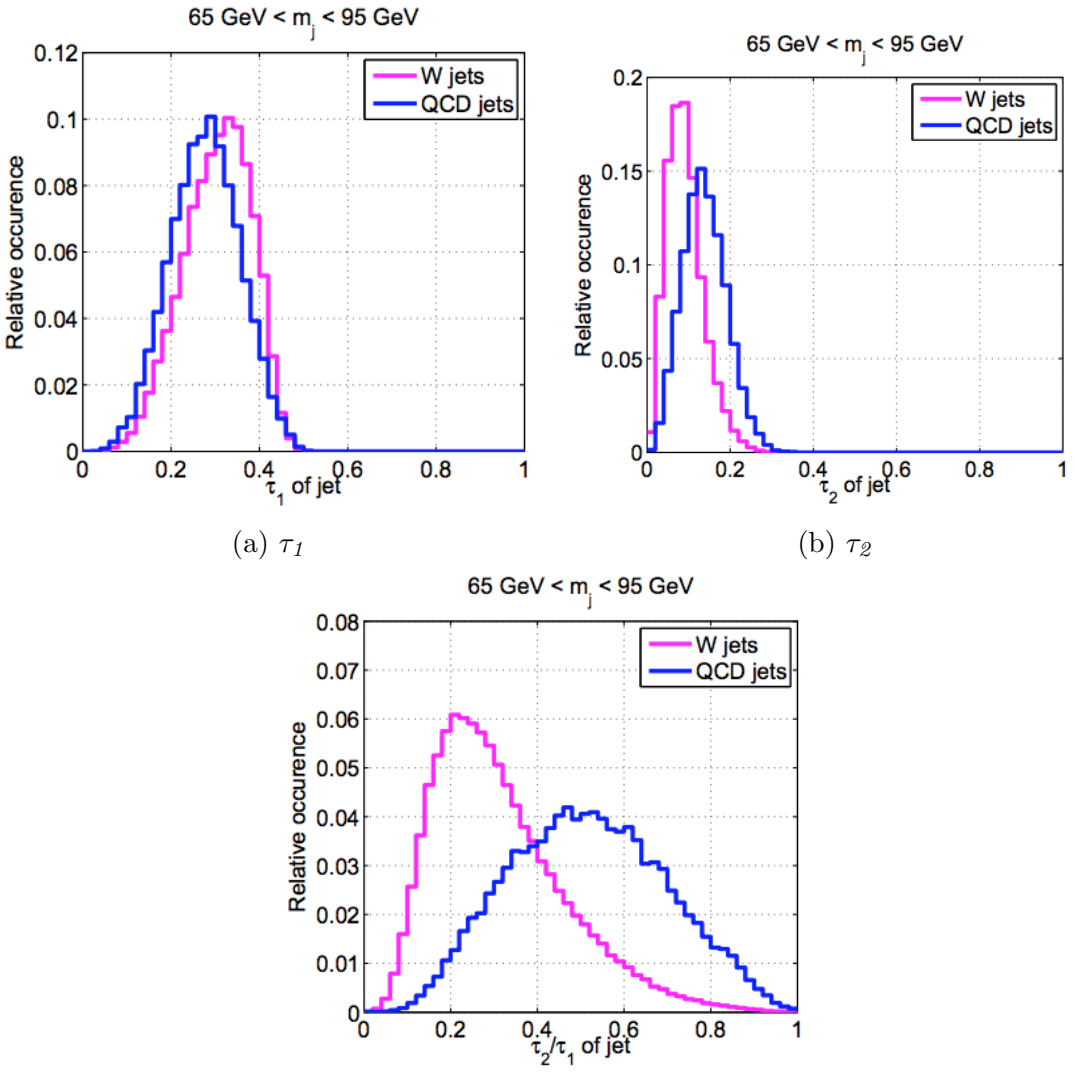

(a) τ_1 (b) τ_2

(c) τ_2/τ_1

Figure 1.12: Measurements of the τ_1, τ_2 and τ_2/τ_1 jet shapes in simulated W-jets (two-prong) and QCD jets (single-core). τ_1 and τ_2 do not show a large sensitivity to the differences in the two-prong nature of the jets. Their ratio however, exhibits good discrimination for two-prong jets [66].

Semi-hard BDMPS gluon emissions, induced by the medium, change the probability of two-prong jets in Pb-Pb collisions compared to pp [64]. In this way, quenching modifications to the splitting functions can be measured. Theoretical predictions of a change in the yield of two-prong jets, due to colour coherence effects in the QGP, have also been made [64]. The predictions for both effects are shown in figure 1.13. The τ_2/τ_1 jet shape, which is sensitive to the two-prongness of jet substructure, can be used to test and measure both effects in heavy ion collisions.

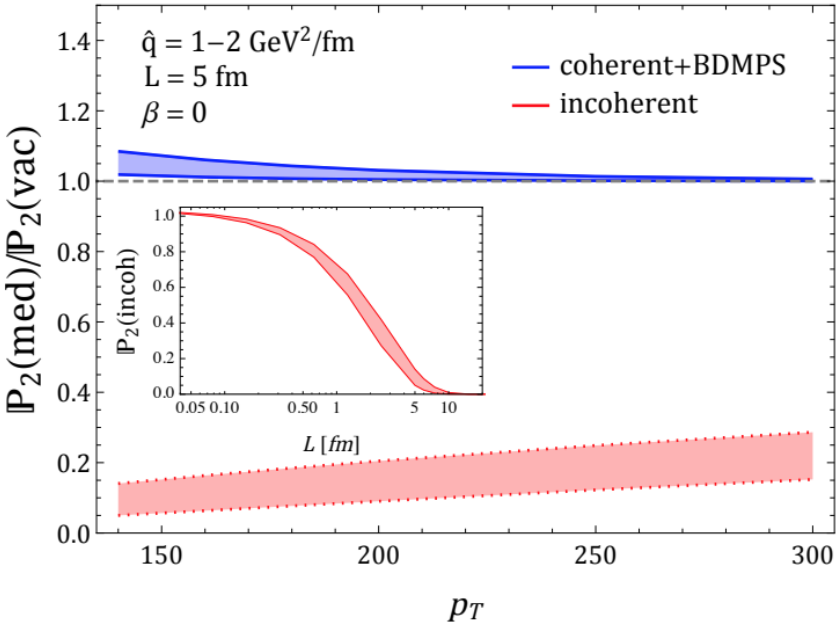

Figure 1.13: Theoretical predictions for the change in the probability of two-prong jets in the QGP medium, compared to the vacuum, are shown as a function of p_T^{jet}. Medium induced BDMPS gluon emissions are expected to add a semi-hard prong to the jets, which increase the probability of two-prong substructure. Incoherent radiation (extreme colour coherence where the critical coherence angle is very small), where the medium resolves every constituent in the jet independently, leads to larger energy loss and a significant reduction in the rate of two-prong jets [64].

1.4 Analysis Motivation

The analysis laid out in the rest of this work will concern itself with measuring the ΔR and τ_2/τ_1 jet shapes in pp (section 4) and Pb-Pb (section 5) collisions. A variety

of reclustering algorithms will be used (see section 2.1) which will probe both the hard and soft scales of the splittings. The hard scale will focus on the hardest (and sometimes first) splitting in the jet. The soft scale will be sensitive to emissions that happen late in the evolution and fragmentation of the parton.

The jets will be measured with a large radius (R=0.4), as this captures more information about the original scattered parton. However, this also incurs experimental difficulties, particularly in Pb-Pb collisions, due to capturing more of the large heavy ion background (see sections 2.2 and 2.3). These difficulties are further enhanced by the relatively low $p_T^{jet,ch}$ (the superscript ch indicates that the jet is reconstructed using only charged constituents) bin ($40 \leq p_T^{jet,ch} < 60$ GeV/c) in which the results are measured. Novel techniques, some of them applied for the very first time experimentally, will be used to overcome these problems. In this way, this analysis represents an exploratory effort which aims to identify and solve the difficulties encountered in such analyses and pave the way for a fully fledged jet substructure program at ALICE.

In pp collisions, the results will be used to test the fundamental understanding of QCD processes and jet substructure in the vacuum, whilst also validating MC simulations. This is crucial, as the pp and Pb-Pb data sets available for this work are at different centre of mass energies and cannot be directly compared. Therefore, MC models must be validated against vacuum measurements before being compared with the Pb-Pb data. This analysis will also be the first instance in the field of heavy ions where reclustering jet shapes are measured differentially for a range of reclustering algorithms, which show the sensitivity of the algorithms to different processes in the jet. This is of theoretical interest, particularly for the τ_2/τ_1 jet shape [67]. The measured jet shapes will be fully corrected for detector effects using an unfolding procedure (see section 2.4).

In Pb-Pb collisions, the jet shapes measured with the reclustering algorithms sensitive to the hard scales will be used to measure changes to the splitting functions induced by the medium. Hard (typically $p_T > 6$ GeV/c) or semi-hard (typically $2 < p_T < 6$ GeV/c) induced gluon radiation will transform single-core jets into two-prong objects, causing shifts in the ΔR and τ_2/τ_1 jet shapes. These jet shapes should also be sensitive to colour coherence effects, which would suppress the two-prong jet sample. However, QCD jets are predominantly single-core [68]. Therefore, the measured data sample might not have the statistical reach to observe coherence effects.

The large heavy ion background, induces experimental complications in measuring and unfolding observables for low $p_T^{jet,ch}$ jets with large radii, in Pb-Pb collisions. The semi-inclusive hadron-jet coincidence technique [69] (see section 2.3) will be extended for the first time to two dimensions, to obtain a measured sample which can be fully unfolded for detector effects and fluctuations in the background. Using this method, this analysis makes the first ever jet shape measurements for low $p_T^{jet,ch}$ jets with large radii in Pb-Pb collisions. Many of the techniques and difficulties that were encountered and overcome during the course of this work, have laid the foundation for further reclustering jet substructure measurements which are currently ongoing at ALICE.

CHAPTER 2

Analytical Tools

This chapter will detail the main analytical tools and methods used in this analysis. Many of these techniques were developed recently and analyses like this are exploring their capabilities and limitations in a variety of environments. In some cases, this analysis extends these techniques to new systems and conditions for the first time. Four methods will be described here, which include: The jet finding and reclustering algorithms (section 2.1), the background subtraction techniques used in heavy ion collisions to remove the event average background from the jets on an event-by-event basis (section 2.2), the semi-inclusive hadron-jet recoil method used to remove combinatorial jets in Pb-Pb collisions from the measured sample (section 2.3) and the two-dimensional Bayesian unfolding procedure used to simultaneously correct the $p_T^{jet,ch}$ and jet shapes for detector effects and background fluctuations(section 2.4). The jet finding techniques and background subtraction algorithms used in this anal-

ysis are implemented by the FastJet software package [70].

2.1 Jet Finding Algorithms

Jet finding algorithms are the tool which allows for the reconstruction of the properties of the partons scattered in the early stages of collisions, from the experimentally accessible final state hadrons. As such, they have been an integral part of all high energy accelerator experiments since the 1970s [71]. With advances in theoretical and experimental precision and the ever increasing complexity of the final state events with every new generation of accelerators, jet finding algorithms have also been continuously evolving. Some of the first jet finders needed to characterise the number of jets in an event first, before attempting to find the jet axes [71]. A more generalised approach was then sought, which gave rise to binary clustering algorithms [72]. These algorithms merged the closest pairs of particles together into clusters. This was repeated until pre-specified criteria were reached. More sophisticated classes of algorithms soon followed, such as cone algorithms [73]. These algorithms attempted to create regular shaped jets by placing a cone centered on a seed axis (for example the particle with the highest p_T), which would encompass other particles inside its radius. The axis was varied in iterative steps, until a stable axis was found. The particles encompassed within the final cone would form a jet.

Two of the most important qualities required of jet finding algorithms are collinear and infrared safety [74]. Collinear safety defines the jet finder's resilience to the splitting of a hard particle. Since the main purpose of jet finding is to reconstruct the initial parton's characteristics, a subsequent splitting of this parton should not change the final reconstructed jet. Infrared safety is a measure of the jet finding algorithm's resilience to soft radiation. Infrared safe algorithms are not influenced by soft emissions from the parton. Infrared safety is important for theorists when

making perturbative QCD calculations.

Many of the algorithm classes discussed have certain drawbacks which make them unsuitable for use at the LHC, such as poor computational performance in the higher multiplicity environments encountered at high energies. This lead to the adoption of the newest class of jet finding algorithms, known as sequential recombination algorithms.

2.1.1 Sequential Recombination Algorithms

Sequential recombination algorithms consider both the transverse momentum and angular separation of particles when combining them. All sequential recombination algorithms used at hadron colliders follow a similar methodology [74]. Two distance measures [75], d_{ij} and d_{iB} are calculated for every particle. d_{ij} is defined between every particle pair, i and j, as,

$$d_{ij} = min(p_{T,i}^{2a}, p_{T,j}^{2a}) \frac{R_{i,j}^2}{R^2}, \tag{2.1}$$

where R_{ij} is given by equation 1.5 and R is defined as the desired jet resolution (radius). The exponent a controls the relative power of the energy versus geometrical scales and is the separating factor for the different algorithms of this class. d_{iB} is the momentum space distance between the beam axes and particle i and is defined as

$$d_{iB} = p_{T,i}^{2a}. \tag{2.2}$$

Once the distance measures d_{ij} and d_{iB} have been calculated for all particles, they

are sorted in increasing order and the smallest value is picked. If d_{ij} is the minimum, then particles i and j are combined into one particle. There are multiple combination schemes that can be used. This analysis will employ the E-scheme which replaces particles i and j with a new particle with a four vector which is the sum of both original particles' four vectors. The new particle is added to the list of particles and particles i and j are removed. All affected d_{ij} and d_{iB} values are recalculated with the new particle. If d_{iB} is the minimum, particle i is labeled as a jet and is removed from the list of particles. A minimum p_T threshold is often defined for these jets to distinguish the jets of interest (originating form a hard scatter) from random beam debris or underlying events which are also clustered by the algorithms. This process is repeated until either all particles are part of a jet (inclusive clustering) or until a predetermined number of jets have been found (exclusive clustering). Since any collinearly split particles ($R_{i,j}$ is much smaller than R) will be recombined, this algorithm class guarantees collinear safety. The three different cases of the sequential reclustering algorithms will be discussed below. Figure 2.1 shows the clustering of the same event using each algorithm and the sensitivity of the clustering and jet areas to soft radiation. The discussion on this sensitivity for each algorithm will be presented in the sections below.

2.1.1.1 k_T Algorithm (a=1)

The k_T algorithm is the case of the sequential recombination algorithms where $a = 1$ [76]. As such, equation 2.1 can be written as

$$d_{ij} = min(p_{T,i}^2, p_{T,j}^2)\frac{R_{i,j}^2}{R^2}. \tag{2.3}$$

All d_{ij} pairs for particles that are separated by distances smaller than R, will be

sorted in increasing order of the pair's lowest p_T particle. This means that the k_T algorithm will begin by clustering soft particles first and only brings hard clusters together in the final steps of its recombination. This results in irregularly shaped jets, since soft particles were clustered together first. The k_T algorithm proves to be IRC safe since adding a soft particle, k, in the limit that $p_{T,k} \to 0$, does not affect the transverse energy or angle of a sufficiently high p_T jet [76].

2.1.1.2 Cambridge Aachen Algorithm (a=0)

The Cambridge-Aachen algorithm (C/A), is a special case of the sequential recombination scheme class where $a = 0$ [77]. This removes any energy dependence on the clustering and clusters based solely on the distance between particles, with d_{ij} reduced to

$$d_{ij} = \frac{R_{i,j}^2}{R^2}. \tag{2.4}$$

The closest particle pairs are combined first, until all clusters within a radius R have been combined into a jet. This method also returns irregularly shapes jets since there is no mechanism to govern smooth boundaries. The clustering of this algorithm maintains angular ordering (in the vacuum), which is theoretically desirable. The final steps of the algorithm bring together the largest splittings in a jet.

2.1.1.3 Anti-k_T Algorithm (a=-1)

The anti-k_T algorithm is an instance of the sequential recombination class where $a = -1$ [75]. This means that equation 2.1 can be written as,

$$d_{ij} = min(\frac{1}{p_{T,i}^2}, \frac{1}{p_{T,j}^2})\frac{R_{i,j}^2}{R^2}. \tag{2.5}$$

In this way, the negative exponent causes clustering to occur around a centered hard particle, as the the lowest d_{ij} values will be governed by the high p_T particles in an event. All particles in a radius smaller than R from the hard particle will be clustered in the same jet. The larger d_{ij} values between soft particles means that they will cluster to a hard particle (if available within the given radius), long before they cluster to each other. This results in regularly shaped jets, which are often cone shaped. To illustrate this we consider the three following scenarios:

- In the first case there is one hard particle with no other hard particles within a distance of $2R$ from it (this is the most probable scenario in vacuum). Clustering will therefore be centered around the hard particle and a cone shaped jet will form.

- In the second case there are two hard particles within a distance R of each other. The two particles will be combined into the same jet. If $p_{T,1} >> p_{T,2}$, then clustering will occur around the first particle and a cone shaped jet will form. If $p_{T,1} \sim p_{T,2}$, then the shape is more complicated as it is the union of two cones (with radius smaller than R) centered on each hard particle; plus a cone of radius R centered on the final jet.

- In the final case, the distance between the two hard particles, Δ_{12}, is $R < \Delta_{12} < 2R$. Two jets will form, but they will not both be perfectly canonical. If $p_{T,1} >> p_{T,2}$, then the first jet will be cone shaped whilst the second jet will miss the area that overlaps with the first jet. If $p_{T,1} \sim p_{T,2}$, then neither jet will be cone shaped and the overlapping part will be divided equally by a straight line between them.

The two important things to note in all the above cases are the predictability (and most likely regularity) of the jet's shape and the lack of influence of soft particles on the shape of the jet or the jet's clustering. This means that the anti-k_T algorithm is infrared safe and resilient to the presence of final state radiation and soft background.

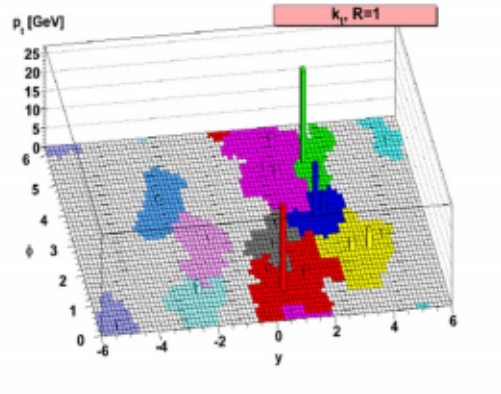

(a) k_T

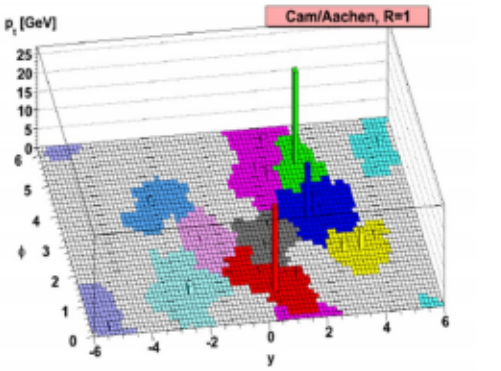

(b) C/A

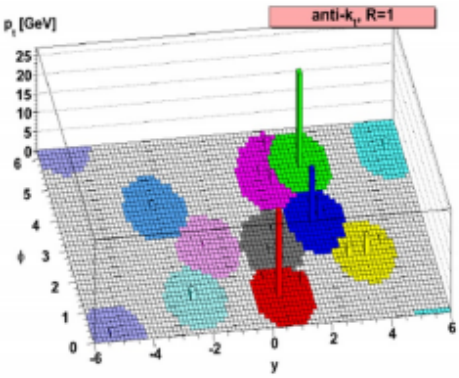

(c) Anti-k_T

Figure 2.1: Jets clustered in identical events, using the three sequential recombination algorithms, are shown. The different colours distinguish between different jets. The larger susceptibility of the k_T and C/A algorithms to soft radiation is apparent in the irregular shape of their jets. The canonical shape of the anti-k_T jets shows the algorithm's resilience to soft radiation. These figures also show that the algorithms will cluster all tracks into a jet, irrespective of their origin (soft or hard processes). Therefore, a p_T^{jet} threshold is needed to select jets that arise from hard scatters [74].

2.1.2 Clustering and Reclustering

Jet finding algorithms are used in two key ways in this analysis. The first instance is to use jet finders in their most traditional capacity, to cluster an event and identify the jets arising from hard scatters. At the LHC, the anti-k_T algorithm is the most favoured algorithm for this task as it clusters jets around hard cores and is less susceptible to soft radiation and pile-up (multiple soft interactions per bunch crossing that independently occur alongside a hard scatter [78]). The regular jet shapes are favourable to both experimentalists and theorists, since they have well defined areas which are used for calibration and calculations. The choice of jet area is important to an analysis. A jet area should be large enough to capture as much information about the fragmenting jet as possible, so as to build a complete reconstruction of the initial scattered parton. However, the jet area should also be small enough to minimise the effects of the underlying event and pile-up, which are clustered within the jet cone. In this analysis a jet resolution of $R = 0.4$ is chosen, in line with both of these requirements [79]. The kinematics of the final reconstructed parton returned by the anti-k_T algorithm, obtained by summing the four-momenta of all the constituents of the jet, defines the jet axis.

The second instance of using jet finding algorithms in this analysis, is to recluster the constituents in a jet. This is done to resolve its subjets and access the jet substructure. In this case the jet finder works in an identical manner to the former case, but is limited to the particles already clustered into the jet. Additionally, the clustering history of the algorithm is retained. Once completed, the clustering steps are reversed $N-1$ times to obtain N subjets (axes) in exclusive mode. The choice of reclustering algorithm is therefore dependent on the the physics aim of the analysis and the substructure observables in question. This analysis uses four different reclustering algorithms in $N = 1$ (one subjet is found) and $N = 2$ (two subjets are found) exclusive modes to measure the τ_2/τ_1 and ΔR jet shapes (section 1.3.1)

and test different physical scales in the jet. These algorithms are detailed below. The following discussions will pertain to jets found in a vacuum with no underlying event.

2.1.2.1 k_T

The first reclustering algorithm used is the k_T algorithm. For the case where $N = 1$, the axis returned by the algorithm is the same as the original jet axis, since both are just a linear sum of the four momenta of all constituents in the jet and therefore independent of the order of recombination. In the $N = 2$ case, the final step of the reclustering history brings together the two hardest structures in the jet, since the k_T algorithm clusters soft particles first. Therefore, the two axes returned in this case are the axes of hardest splitting in the jet. Hence, the k_T algorithm is ideal for probing the hard scale substructures in a jet. The ΔR and τ_2/τ_1 jet shapes constructed with this algorithm are sensitive to the axes of hardest splitting. This can be used to test for hard and semi-hard QCD radiation in the jet. In contrast, the anti-k_T algorithm, although ideal for finding jets in an event, would not be suitable to this substructure analysis since the final reclustering step involves combining a soft particle with the rest of the jet. The axes, obtained from unwinding the reclustering history, would not be relevant to the required physics.

2.1.2.2 C/A

The next reclustering algorithm chosen is the C/A algorithm. For the case where $N = 1$, C/A returns the jet axis for the same reasons as discussed for the k_T algorithm. For the $N = 2$ case, the final step of the reclustering is to bring together the furthest separated structures in the jet. Therefore, the axes obtained are the axes of largest splitting. In this way, the C/A algorithm gives access to the angular

ordered tree. However, this only holds for an idealised jet with no contribution from other processes in the jet cone. In reality, the insensitivity of the C/A algorithm to a constituent's p_T, means that the algorithm is highly susceptible to large angle radiation in the jet cone. This can hide the true widest angle emission from the scattered parton. Uncorrelated (not originating from the hard scattered parton) particles at large angles from the jet axis are indistinguishable, to the reclustering algorithm, from true large angle emissions from the scattered parton. As both sets of radiation tend to be soft, they will be referred to collectively as soft splittings. Therefore the C/A algorithm holds little physical value, other than a sensitivity to soft radiation (which can still be of theoretical interest outside the scope of this work). However, the next two algorithms considered in this analysis use and build upon the C/A algorithm. Therefore, to understand and isolate the effects of their added components, measurements of the jet shapes using the default C/A algorithm must be made.

2.1.2.3 C/A with Minimisation

The first of the algorithms to build upon the C/A algorithm, introduces an additional local minimisation step to the procedure [80]. In both the $N = 1$ and $N = 2$ cases, the axis(es) returned by the C/A algorithm is(are) taken as seeds for a local minimisation of N-subjettiness. The axis(es) are varied until a local minimum of N-subjettiness is found and the new axis(es) is(are) returned. This minimisation is of both experimental and theoretical interest as it could serve to reduce the effects of the underlying event, since this tends to increase N-subjettiness. It is expected that the minimisation will have a larger effect in Pb-Pb compared to pp collisions, since the higher multiplicities expected in the jet cone will lead to more possibilities for a local minimisation.

2.1.2.4 Soft Drop

The second algorithm to build upon the C/A algorithm is the soft drop jet groomer [81]. Jet groomers are tools used to remove constituents from a jet in order to highlight and uncover substructures of interest. The soft drop groomer was designed to remove soft large angle radiation from within a jet cone and uncover a hard splitting. It begins by reclustering the jet with a given reclustering algorithm, in this case C/A. It then unwinds the reclustering history one step backwards to find the two final clusters in the jet that were brought together. These clusters, a and b, are then tested against the soft drop condition given by,

$$\frac{min(p_{T,a}, p_{T,b})}{|p_{T,a}| + |p_{T,b}|} > z_{cut}(\frac{\Delta R_{ab}}{R})^{\beta}, \tag{2.6}$$

where z_{cut} is the soft drop threshold, β is an angular exponent, R is the jet resolution and ΔR_{ab} is equivalent to R_{ij} given by equation 1.5. If the soft drop condition is satisfied, the jet composed of the two subjets, a and b, is labelled as the final soft dropped jet and is returned by the groomer. However, if the condition is not satisfied, then the cluster with the lowest p_T is removed and the the reclustering history of the remaining subjet is unwound one step backwards and the two resulting clusters are tested against the soft drop condition. This process is iterated until the condition is satisfied or only one single track remains. If the soft drop condition is satisfied, the jet composed of the two clusters passing the soft drop condition is returned. This jet is then reclustered with the C/A algorithm. In the case of $N = 2$, this returns the same axes as those of the two subjets which passed the soft drop condition.

The z_{cut} and β parameters control the grooming procedure and determine the type and extent of the groomed radiation. Given that the z_{cut} value is not large, for values of $\beta > 0$ soft large angle emissions are removed whilst collinear emissions

are maintained. The amount of soft-collinear emissions groomed away from the jet increases as $\beta \to 0$. At the limit of $\beta = 0$, all large angle and collinear soft radiation is removed from the jet. For values of $\beta < 0$, soft drop effectively places cuts on the relative p_T of hard structures in the jet. Figure 2.2 illustrates these effects in each emission region for varying values of β. Since soft drop grooms away soft radiation from the jet, this reclustering algorithm will be used to uncover hard splittings in the jet and test for changes to the N-pronged substructure of jets. It is ideal to remove both large angle and collinear soft radiation from the jet, in order to obtain a cleaner picture of the hard splittings. In addition to this, since the background from the heavy ion environment in Pb-Pb collisions is expected to be uncorrelated to the jet (and soft), removing both the large angle and collinear soft radiation from the jet can minimise the effects of this background. This points to values of $\beta \leq 0$ as being appropriate for this analysis. However, care must be taken in the measured sample so as not to bias the hard splittings themselves. Therefore, negative values of β are also ruled out. For these reasons, the value of $\beta = 0$ is selected for the soft drop procedure used in this work. This reduces equation 2.6 to

$$\frac{min(p_{T,a}, p_{T,b})}{|p_{T,a}| + |p_{T,b}|} > z_{cut}. \tag{2.7}$$

When soft drop is used with $\beta = 0$, the value of z_{cut} determines the minimum momentum fraction required of the softer cluster in order for it to pass the soft drop condition. Low values of z_{cut} will allow soft clusters to satisfy the grooming conditions and remain in the jet, whilst high z_{cut} values will only keep the hardest splittings. Therefore a balance must be reached to remove soft background without biasing and removing any true hard or semi-hard splittings. To this end, the value of $z_{cut} = 0.1$ is chosen for this analysis. This has the advantage of satisfying the above requirements, whilst also being one of the favoured values used by theorists

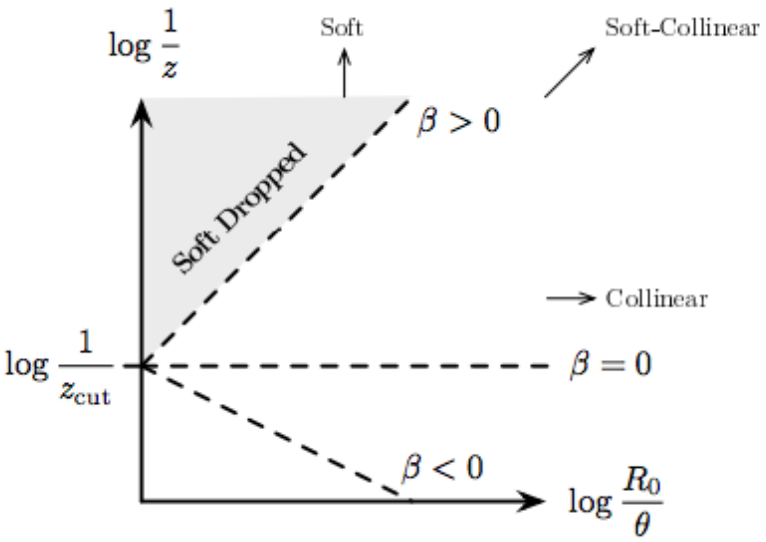

Figure 2.2: The effect of the soft drop grooming procedure is shown for different emission regions in the $(\log \frac{1}{z}, \log \frac{R_0}{\theta})$ plane. This plane is obtained in the soft limit, where the soft drop criteria in equation 2.6 is reduced to $z > z_{cut}(\frac{\theta}{R_0})^{\beta} \Rightarrow \log \frac{1}{z} < \log \frac{1}{z_{cut}} + \beta \log \frac{R_0}{\theta}$. Here z is equivalent to $\frac{min(p_{T,a},p_{T,b})}{p_{T,a}+p_{T,b}}$, θ is equivalent to ΔR_{ab} and R_0 is the jet radius. This formalisation in terms of logarithms allows for the β limits to be drawn as straight lines. For each limit, everything above the dashed line is groomed away by soft drop, as illustrated for the case of $\beta > 0$. It can be seen that values of $\beta > 0$ groom away soft radiation. Soft collinear radiation is removed in increasing amounts as $\beta \to 0$ and completely at $\beta = 0$. For $\beta < 0$, soft drop begins regulating the p_T of hard substructures [81].

in their calculations [81].

Once the soft large angle and collinear radiation has been removed from the jet, a hard splitting is uncovered. Due to the nature of the C/A reclustering, this is also the splitting with the largest angle in the jet. Therefore, the soft drop algorithm using C/A reclustering with parameters $z_{cut} = 0.1$ and $\beta = 0$, maintains angular ordering whilst uncovering a hard splitting in the jet's substructure. This algorithm is ideal in testing for changes to the N-pronged nature of jets due to hard and semi-hard emissions. Not only is soft drop an experimentally valuable tool, but it also has desirable properties for theorists. The soft drop groomer removes non-global logarithms that are a significant obstruction to the resummation of jet

observables [82]. Groomed jets are also less sensitive to hadronisation effects. For these reasons, the soft drop grooming tool is becoming one of the most widely used algorithms in all aspects of the jet substructure field and this analysis will be one of the first experimental analyses to employ and test it in Pb-Pb collisions.

2.1.3 Reclustering Algorithms with Different Jet Topologies

A conceptual expectation of the behaviour of the ΔR and τ_2/τ_1 jet shapes will be discussed here for two jet topologies. The first are single-core jets, where most of the p_T^{jet} is concentrated within a central cluster. The second are two-core jets, where the p_T^{jet} is divided (not necessarily equally) between two distinct hard substructures in the jet cone. In both cases, there will be some soft radiation at large angles from the jet axis within the cone. This radiation will tend to be near the boundaries of the jet radius, since the concentric area is larger at larger radii and therefore has a higher probability of containing an uncorrelated particle.

Each topology will be considered in two different environments. First is the vacuum encountered in pp collisions, where soft radiation uncorrelated to the hard scatter is largely absent. Next is the heavy ion environment encountered in Pb-Pb collisions, where there is a considerable amount of uncorrelated background within the jet cone. The latter case will be considered assuming that a background subtraction procedure (see section 2.2) has been applied to remove the average background from the jet. However, fluctuations in the background and inefficiencies in the subtraction techniques can cause a significant amount of background to remain within the jet cone. The desired result (for the k_T and soft drop with C/A algorithms) would be to demonstrate that the τ_2/τ_1 value is high for single-core jets and low for two-prong jets, regardless of the environment considered. This would show that the jet shape is sensitive to hard substructures within the jet but resilient to soft contamination.

Ideally, the axes returned by these two algorithms (ΔR) would pick out the hard substructures in the jet.

2.1.3.1 Single-core Jets - Vacuum

For this case we will consider jets with a strong single-core structure, with very few soft tracks at large angles. A schematic example is shown in figure 2.3. For the case of $N = 1$, the axes returned by all four algorithms should be situated in the jet core. A low τ_1 value is expected, since the high p_T constituents of the jet will also be in the core and therefore close to this axis. This is shown in figure 2.4 for the different algorithms. The soft drop algorithm removes large angle soft radiation from the jet. Note that the k_T and C/A algorithms return identical axes (the jet axis) for $N = 1$.

For the $N = 2$ case, the axes returned will be highly dependent on the reclustering algorithm used. The k_T algorithm will cluster soft particles first and will bring together the two hardest structures in the jet in the last step. Therefore, the axes obtained by unwinding the reclustering algorithm one step backwards (ΔR) will be the axes of hardest splitting. These will be close to each other inside the jet core. The τ_2 value will be small, since the hard constituents are close to the two axes in the core. Therefore the τ_2/τ_1 value will be large (since both τ_2 and τ_1 are small), which is expected for single-core jets when using this algorithm. A schematic representation is shown in figure 2.5.

For the $N = 2$ case with the C/A algorithm, the reclustering will be sensitive to the (mostly soft) large angle radiation in the jet cone, since the algorithm has no p_T dependence in its clustering and clusters solely based on the distance between constituents. The last step in the reclustering will bring together the furthest separated clusters in the jet. These will be the jet core and the furthest large angle radiation or cluster from the core. The ΔR shape will therefore tend towards the jet radius,

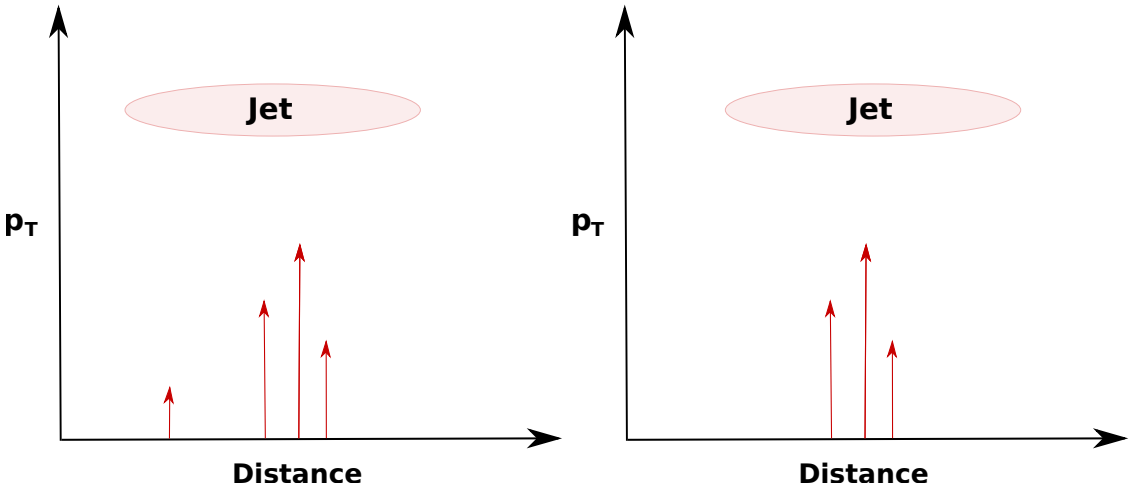

(a) Ungroomed jet (b) Jet groomed with soft drop

Figure 2.3: Example of a single-core jet in vacuum. The red arrows represent the jet constituents. Most of the p_T^{jet} is concentrated in the core of the jet with a soft track appearing at a large angle away from the core. For the case of the groomed jet, soft drop removes the large angle soft radiation.

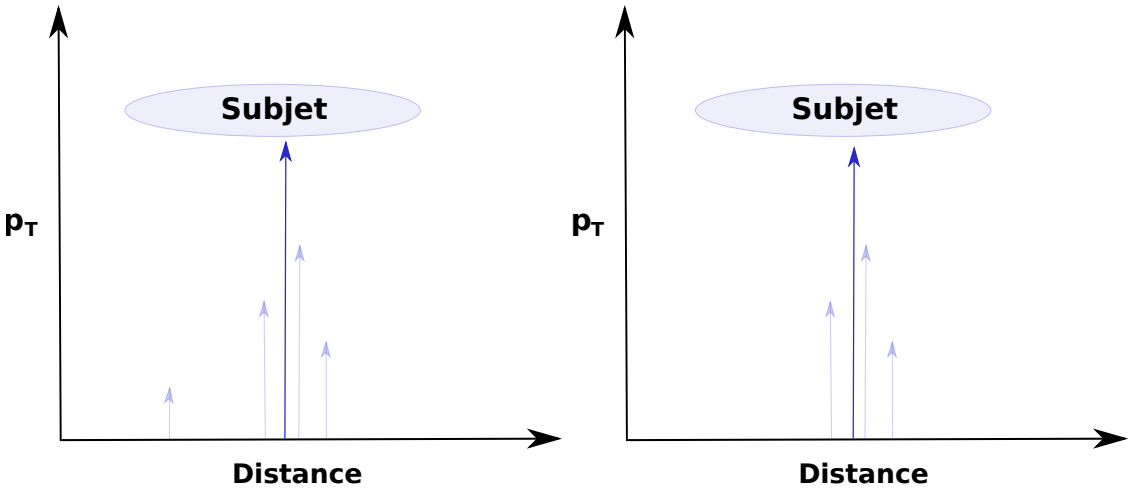

(a) k_T and C/A algorithms (b) Soft drop with C/A

Figure 2.4: The axis (solid blue) returned in the $N = 1$ case for the different reclustering algorithms is shown. The reclustering has been performed on the jets in figure 2.3. The axis is within the jet core for all agorithms. Constituents clustered in the same subjet appear in the corresponding transparent colour.

depending on how far from the core the furthest cluster happens to be. A schematic is shown in figure 2.6. However the τ_2 value will be small, since all the high p_T tracks will be close to the axis remaining in the core. In fact, the change between τ_2 and τ_1 is expected to be smaller here than in the k_T algorithm, since in the latter

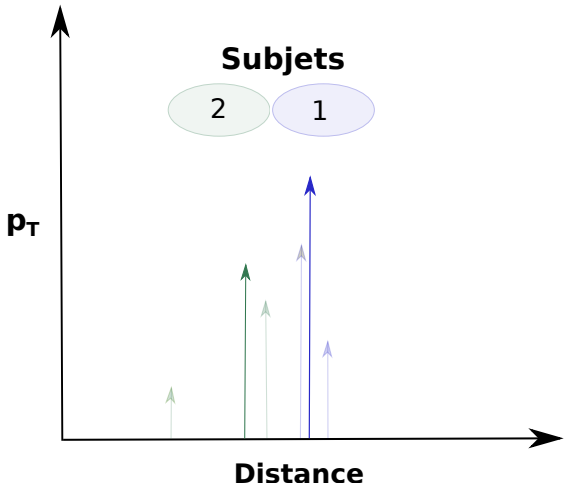

Figure 2.5: The axes (blue and green) returned in the $N = 2$ case for the k_T reclustering algorithm are shown. The reclustering has been performed on the jet in figure 2.3a. Both axes remain inside the jet core. Constituents clustered in the same subjet appear in the corresponding transparent colour.

case the extra axis in the core would slightly reduce the τ_2 variable compared to τ_1. Hence, an even larger τ_2/τ_1 value is expected for the C/A algorithm compared to k_T.

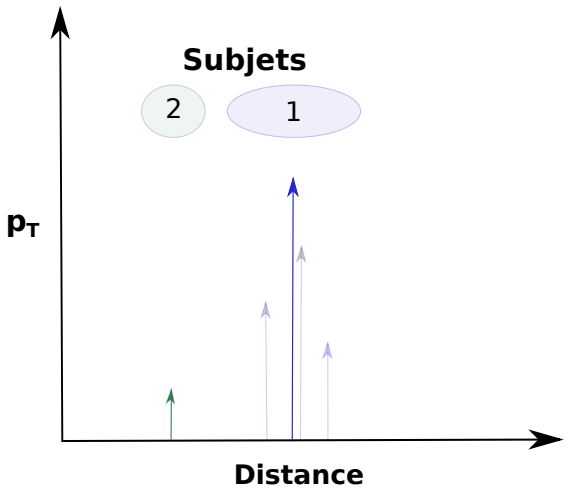

Figure 2.6: The axes (blue and green) returned in the $N = 2$ case for the C/A reclustering algorithm are shown. The reclustering has been performed on the jet in figure 2.3a. One axis remains in the core whilst the other axis is pulled to the large angle radiation. Constituents clustered in the same subjet appear in the corresponding transparent colour.

In the vacuum case where the constituents are few, the minimisation procedure is not expected to have a large effect on the axes obtained. Therefore, the ΔR and

τ_2/τ_1 jet shape are not expected to change significantly with respect to the C/A case. Only very small shifts to lower values are anticipated due to the minimisation. For this reason, this algorithm is not included in the schematic representations shown in this section.

The soft drop procedure is expected to have a significant effect on the results of the C/A reclustering. With a $z_{cut} = 0.1$, any large angle structure not exceeding 10% of the p_T^{jet} will be removed. For the suitably high p_T^{jet} used in this analysis, this means that in most cases the large angle soft tracks are removed by the grooming procedure. This can be seen in figure 2.3. Therefore for the $N = 2$ case, both of the reclustered axes returned by C/A will be in the jet core as shown in figure 2.7. This results in small ΔR and τ_2 values. Therefore, the τ_2/τ_1 value will be similar to that of the k_T algorithm.

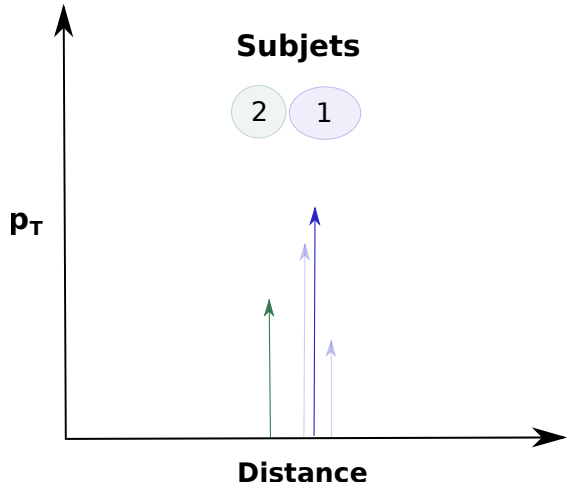

Figure 2.7: The axes (blue and green) returned in the $N = 2$ case for the soft drop with C/A reclustering algorithm are shown. The reclustering has been performed on the jet in figure 2.3b. Removal of large angle radiation causes both axes to remain in the core. Tracks clustered in the same subjet appear in the corresponding transparent colour.

In vacuum conditions, the ΔR (the reclusterd axes) variable can change significantly depending on the reclustering algorithm used. Despite this, the τ_2/τ_1 value should remain large for all single-core jets. This holds true for all the algorithms considered here. This is expected for single-core jets, as a large τ_2/τ_1 value represents a jet

that is not two-prong. The ΔR variable should pick out the hard structures in the jet when the k_T and soft drop with C/A algorithms are used.

2.1.3.2 Single-core Jets - Heavy Ion Environment

Heavy ion collisions produce large levels of uncorrelated background which are clustered into the jet cone. Background subtraction algorithms are used to remove the event average background contribution from both the p_T^{jet} and the jet shape. The main background subtraction technique used in this analysis, constituent subtraction (section 2.2.2), corrects the jet at the constituent level by removing and modifying particles within the jet. However, local fluctuations in the background and inefficiencies in the subtraction techniques means that there is often a significant amount of background still present in the jet after subtraction. Therefore for the purpose of this discussion, we will assume the presence of a non-negligible amount of soft background in the jet cone, smearing the "true" jet signal.

For the case of $N = 1$, the axis returned by the jet finder is not expected to change much compared to the vacuum case since the background is, to a good approximation, homogenous around the jet core. However, since there is a non negligible amount of p_T uncorrelated to the core, the τ_1 values should be larger for each algorithm. This can be understood as the background smearing the strong single-core nature of the jet's substructure. For the case of the soft drop algorithm, the grooming procedure will remove some of this soft large angle background. The extent of the grooming will determine by how much the τ_1 value is lowered. The axis is not expected to be modified due to the grooming, since the grooming will remove radiation in a homogeneous manner around the core.

As in the vacuum, the behaviour of the $N = 2$ case varies with the reclustering algorithm used. For the k_T algorithm, the results are highly dependent on the

performance of the background subtraction technique and the presence of local fluctuations in the background, which can vary on a jet-by-jet basis. If the subtraction manages to remove most of the uncorrelated background from the jet, then a similar picture to the vacuum case as shown in figure 2.5 occurs. In this case, the soft structures are clustered first and the final step of the algorithm is to bring together the hard structures in the jet. The axes will remain in the core (small ΔR). The value of τ_2 will still be higher than the vacuum case, due to the residual background which is uncorrelated to these axes. However, it will be similar in value to τ_1 since in both cases the axes remain in the core. Therefore the τ_2/τ_1 value will be large, as expected for single-core jets.

In some cases, the remaining background in the jet can be large enough and far enough away from the core, that even though the soft particles will be clustered together first, the soft cluster that is formed is not immediately combined with a hard cluster in the core. In this scenario, the soft cluster can remain independent whilst the jet core is clustered and these two substructures are only brought together in the final step of the reclustering. When the clustering history is unwound one step, the second axis is placed in the soft substructure, resulting in a large value of ΔR. The value of τ_2 will still be larger than in the vacuum case, due the background uncorrelated to either the core or soft axis. Since one axis is placed in a soft cluster, the contribution of these particular soft constituents to τ_2 will be small. However, since these particles are soft, their individual contributions to the τ_1 variable were small as well. Therefore, their lower contribution to τ_2 does not cause a large change between τ_1 and τ_2. In this way, the value of τ_2/τ_1 is not modified much, even though the axes (ΔR) have been. In effect, the τ_2/τ_1 obtained with the k_T algorithm shows resilience to soft substructures in the jet. This is ideal for this analysis, since the purpose of the τ_2/τ_1 jet shape measured with the k_T algorithm is to be sensitive to hard and semi-hard radiation only.

For the C/A reclustering algorithm in the $N = 2$ case, the last step of the reclustering will bring together the furthest separated structures in the jet. These will include the core and the furthest soft structure from the core. The much greater presence of uncorrelated background in the jet cone, compared to the vacuum case, means that the probability of finding radiation at larger angles (approaching the jet radius) increases. The ΔR value should therefore have a higher peak at the jet radius. Similar to the case for the k_T algorithm, where one of the axes was moved to a soft cluster, despite the large change in ΔR the τ_2 jet shape shouldn't change much relative to τ_1. The value of τ_2/τ_1 should be high and similar to the vacuum case.

The minimisation procedure using the C/A axis is expected to have a larger impact than in vacuum, due to the higher number of constituents present in the jet. The extent of this impact will become apparent through measurement of the variables and will depend on the distribution of background within the jet.

The soft drop groomer will act to remove the soft large angle radiation which remains post subtraction. The axes returned by the algorithm in the $N = 2$ case are highly dependent on the success of the background subtraction and grooming components in removing the soft radiation. If enough soft radiation is removed to uncover the jet core as the furthest separated structure, then the axes returned will be in the core with a small ΔR value. The τ_2 jet shape will have a low value, similar to the vacuum case. Since the τ_1 value for this well groomed jet would also be low, the τ_2/τ_1 shape will be large. However, for the cases where an uncorrelated substructure makes up at least 10% of the final p_T^{jet} (i.e the p_T of the substructure is higher than the z_{cut}), the grooming procedure is halted and one of the axes returned will be placed in this substructure, whilst the other remains in the core. This has a similar effect to the k_T case where one axes was placed in the soft radiation. The ΔR value will increase, but there will be little relative change between the τ_1 and τ_2 values since the contribution from the soft constituents to τ_1 is small. Both values will be

slightly larger compared to the vacuum case and the τ_2/τ_1 value will remain large too.

In the presence of the heavy ion background, the value of the ΔR variable is highly dependent on both the reclustering algorithm and the amount of background removed by the subtraction techniques. Even in the cases of the k_T and soft drop with C/A algorithms, one of the axes could be drawn to a soft substructure in the jet if a significant portion of background remains in the jet post subtraction. However, the τ_2/τ_1 jet shape obtained for all algorithms, shows a resilience to the soft substructures present in the jet. It remains large for single-core jets, regardless of the soft background contribution.

2.1.3.3 Two-core Jets - Vacuum

For this case, the considered jets will have two distinct substructures. These are sufficiently separated from each other and each carry a significant fraction of the overall p_T^{jet}. There will also be a few soft particles at large angles, from the jet axis, within the jet cone. This topology is shown schematically in figure 2.8, both with and without the soft drop groomer having been applied to the jet.

For the $N = 1$ case, the axis returned by all four algorithms will be similar and will be close to the jet axis. In the case of the k_T and C/A algorithms, the axis will be identical. The minimisation procedure is expected to induce a slight shift towards the substructure with higher p_T. The soft drop algorithm will remove soft tracks or clusters at large angles from the two cores. However, this should have minimal effect on the returned axis due to the soft nature of the particles removed. Figure 2.9 shows the axis returned for the k_T, C/A and soft drop with C/A algorithms. The amount of radiation removed by the soft drop algorithm with C/A reclustering, is inversely proportional to the angular separation of the two hard prongs of the jet. The larger

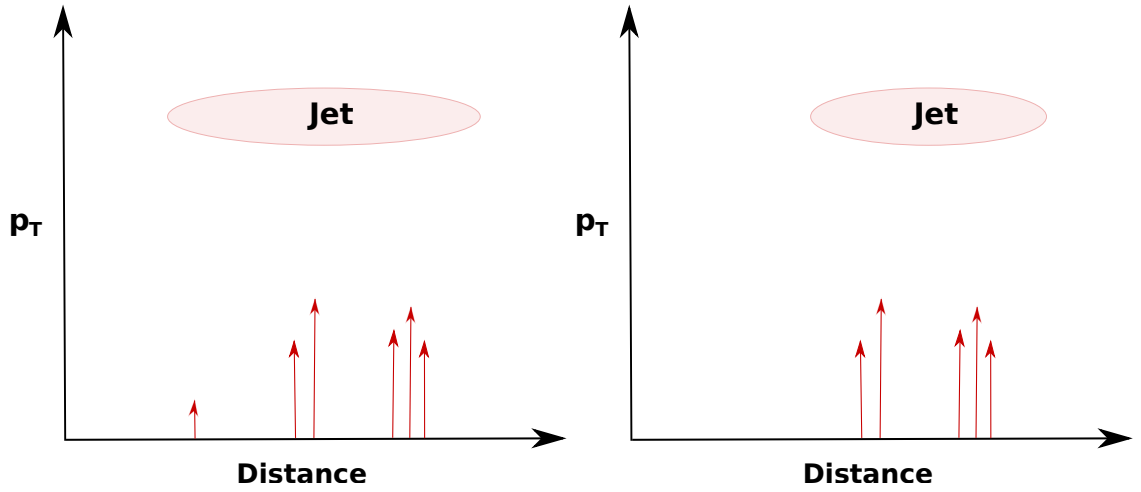

(a) Ungroomed jet (b) Jet groomed with soft drop

Figure 2.8: Example of a two-prong jet in vacuum. The red arrows represent the jet constituents. Most of the p_T^{jet} is concentrated in two distinct substructures in the jet with a soft track appearing at a large angle away from the jet axis. For the case of the groomed jet, soft drop removes the large angle soft radiation.

this separation, the more likely it is that the soft track will cluster together with one of the hard prongs first, before the prongs cluster together. In this case, the final step of the reclustering would bring the hard cores of the jet together, both of which will pass the soft drop criteria. In this scenario, the soft track will not be groomed away from the jet. However, the separation between the two prongs of the jet can be small enough that the prongs are clustered together before being clustered to the soft track. In this case, the soft track is groomed away from the jet. Given the axis (close to the jet axis) returned by the $N = 1$ case, each hard core in the jet will be at a large distance to this axis. The τ_1 value will therefore be large across all algorithms.

The axes returned for the $N = 2$ case are strongly dependent on the reclustering algorithm used. For the k_T algorithm, the soft structures in the jet would be clustered together first and the final step would bring together the two hard prongs. The axes returned would lie in each of the two prongs, meaning that the ΔR jet shape would be sensitive to the hard substructures in the jet. Since the hard clusters are both

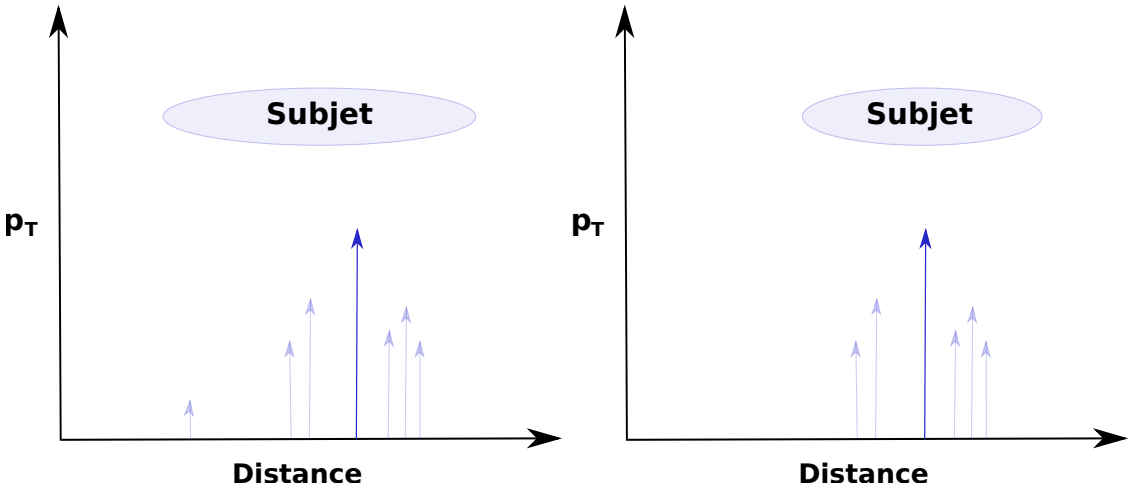

(a) k_T and C/A algorithms (b) Soft drop with C/A

Figure 2.9: The axis (solid blue) returned in the $N = 1$ case for the different reclustering algorithms is shown. The reclustering has been performed on the jets in figure 2.8. The axis lies close to or on the jet axis for all algorithms. Constituents clustered in the same subjet appear in the corresponding transparent colour.

very close to one of the returned axes, the τ_2 variable will be small. Therefore the τ_2/τ_1 jet shape will be small (high τ_1 and low τ_2), which is expected for two-prong jets. A schematic of this situation is shown in figure 2.10.

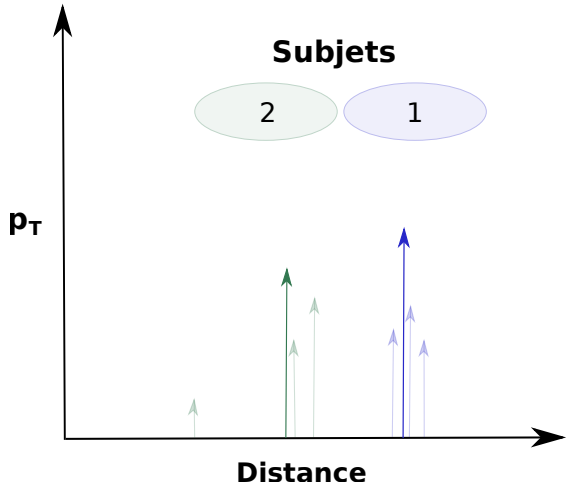

Figure 2.10: The axes (blue and green) returned in the $N = 2$ case for the k_T reclustering algorithm are shown. The reclustering has been performed on the jet in figure 2.8a. Each axis is placed within one of the hard prongs of the jet. Constituents clustered in the same subjet appear in the corresponding transparent colour.

For the C/A algorithm, the axes returned by the $N = 2$ case can be sensitive to both soft and hard structures in the jet. Similar to the soft drop grooming procedure, the

sensitivity of the C/A algorithm depends on the angular distance between the soft substructures and the prongs in the jet (which decreases with increasing distance between the prongs). Figure 2.11a shows the case where the hard prongs of the jet are closer to each other, than to the soft track in the jet. The final step of the reclustering will combine the soft track with the cluster comprised of the two prongs. Hence the axes returned (ΔR) will be sensitive to the soft substructure and τ_2 will be large. This leads to a τ_2/τ_1 value which is also large, showing that the algorithm is not sensitive to the hard substructures in the jet. However, figure 2.11b shows the case where the angular separation of the hard prongs is larger than the separation of the soft track to its nearest prong. In this case, the C/A algorithm will combine the soft tack with the nearest prong first (since they are closer), before bringing together the two hard prongs in the final step of the reclustering. In this case, the returned axes (ΔR) are strongly correlated to the two hard prongs and τ_2 will be small. This leads to a low τ_2/τ_1 value, showing that the algorithm can also be sensitive to the hard prongs in the jet. Therefore, the required separation between the two prongs, in the determination of single or two-core jets, determines the sensitivity of this algorithm to hard or soft substructures for this configuration of jets.

The minimisation procedure for $N = 2$, is not expected to significantly modify the axes returned by the C/A algorithm in vacuum. Therefore, the ΔR and τ_2/τ_1 jet shapes follow the same arguments as the C/A case.

For the soft drop case using C/A relustering, the axes returned by the $N = 2$ mode should be sensitive to the two hard prongs of the jet. Any soft tracks appearing at large enough angles, where they would have remained independent and would only have been combined with the two prongs in the last reclustering step, will be removed by the soft drop groomer. Therefore, the final reclustering step will bring together the hard prongs of the jet and the axes (ΔR) will each fall in one of these

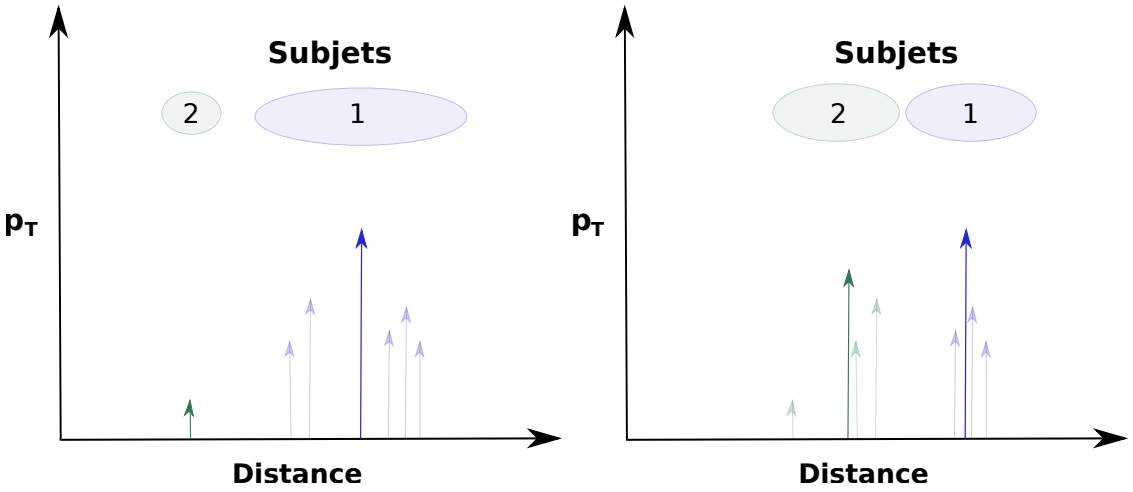

(a) Larger angular separation between the soft track and its nearest prong, than between the two hard prongs.

(b) Larger angular separation between the two hard prongs, than between the soft track and its nearest prong.

Figure 2.11: The axes (blue and green) returned in the $N = 2$ case for the C/A reclustering algorithm are shown. In (a) the reclustering has been performed on the jet in figure 2.8a, whilst in (b) the soft track appears closer to the two prongs. Constituents clustered in the same subjet appear in the corresponding transparent colour.

hard cores. Since each of the hard substructures of the jet are strongly correlated to one of the axes, the value of τ_2 and hence τ_2/τ_1 will be low. Therefore, the soft drop with C/A algorithm is sensitive to two-prong jets. A schematic depicting this situation is shown in figure 2.12.

In vacuum conditions, the k_T and soft drop with C/A algorithms are sensitive to the hard cores in two-prong jets. The sensitivity of the C/A algorithm (with and without minimisation) to the hard substructures in two-prong jets, is dependent on the angular separation of the hard and soft substructures in the jet.

2.1.3.4 Two-core Jets - Heavy Ion Environment

The presence of the heavy ion environment adds a non negligible amount of background to the jet, which can still partially remain in the cone after subtraction. For the case of $N = 1$, the axis returned by all reclustering algorithms is not expected to

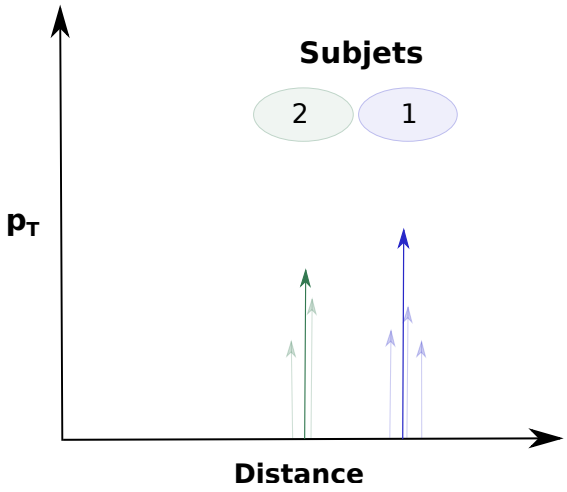

Figure 2.12: The axes (blue and green) returned in the $N = 2$ case for the soft drop with C/A reclustering algorithm are shown. The reclustering has been performed on the jet in figure 2.8b. Each axis is placed within one of the hard prongs of the jet. Tracks clustered in the same subjet appear in the corresponding transparent colour.

change much compared to the vacuum case, since the background is homogeneous in nature. The axis will be close to the jet axis. However, the value of τ_1 will increase due to the large amount of p_T uncorrelated to the returned axis. As with the case of single-core jets, the minimisation and soft drop algorithms can slightly reduce this τ_1 value.

For the $N = 2$ case, the axes returned are dependent on the reclustering algorithm and the interplay between the angular separation and/or p_T of the soft clusters and hard prongs of the jet. For the k_T algorithm, the soft background constituents will be clustered together first and are expected to then cluster with one of the hard prongs of the jet before the hard prongs are clustered together in the final step. Both axes (ΔR) would appear correlated to the hard substructures of the jet. In this case, τ_2 would be small, since the bulk of the p_T^{jet} is correlated to the axes. This leads to a low τ_2/τ_1 value, as expected for two-prong jets. This is expected to be the most common outcome for two-prong jets in the presence of background. However, one can also imagine a case where the soft tracks form clusters with sufficiently high p_T and separation from the hard cores, that they are not clustered to one of the

prongs before the prongs are clustered to each other. In this case, one axis will be placed in the soft structure and one axis will be situated near the jet axis (since this cluster contains the two prongs). Therefore, ΔR would not be sensitive to the hard substructures of the jet and τ_2 will be large, leading to a large τ_2/τ_1 value. However, this scenario is expected to be rare and to not contribute much to the measured distributions.

The C/A algorithm with $N = 2$, follows the same arguments as in the vacuum case for two-core jets. The outcome is highly dependent on the angular distance between soft background tracks and their nearest hard prong, compared to the angular distance between the two prongs themselves. If the former is larger than the latter, then the last step would cluster the soft track with a cluster comprised of the two prongs. ΔR would sensitive to the soft substructure of the jet and the τ_2 and τ_2/τ_1 values would both be large. If the opposite occurs and the latter is larger than the former, then the soft tracks are clustered to their nearest prong first and the last clustering step would bring together the two hard prongs. ΔR would follow the hard substructures and τ_2 and τ_2/τ_1 would both be low. In the presence of the heavy ion background, the increased multiplicity of soft tracks increases the frequency of the first scenario (one axis placed in the soft cluster) relative to the vacuum case. The extent of this increase will be determined experimentally.

The minimisation procedure is expected to have a larger effect in the high multiplicity environment of heavy ion collisions (compared to vacuum) and could serve to reduce the N-subjettiness jet shapes. This will in turn move ΔR towards the hard substructures of the jet. However, the extent of this change is dependent on the distribution of the background and will be determined experimentally through this analysis.

The soft drop grooming algorithm will remove soft large angle tracks from the jet

cone, greatly reducing the effect of the soft background on the C/A reclustering. If no soft clusters appear at angular distances (relative to their nearest hard prong) larger than the separation between the two hard prongs, then the axes returned (ΔR) will be correlated to the hard prongs. τ_2 and τ_2/τ_1 will both be small. If any soft clusters appear with an angular distance to their nearest prong which is greater than the angular distance between the prongs themselves, they will be clustered to the hard prongs in the last step of the reclustering. In most cases, the soft drop algorithm will remove such a soft cluster. This would lead to the hard prongs being the furthest separated clusters in the jet. They would then be picked out by the C/A reclustering. However, in some cases the soft cluster might carry at least 10% of the p_T^{jet}. In this case, the soft cluster is not removed by the groomer and one of the axes is pulled towards the soft cluster. This results in a large ΔR. Since the other axis is placed in the cluster containing the two hard prongs, it will be in a similar position to the jet axis. This will result in large values of τ_2 and τ_2/τ_1. However, the soft drop algorithm ensures that this eventuality is greatly suppressed compared to the case where C/A is used without any soft drop grooming applied a priori.

In the presence of the heavy ion background, the value of the ΔR variable is expected to be highly dependent on the reclustering algorithm used. The degree of background remaining after the subtraction procedures, together with its angular distribution, also play a large role in the determination of ΔR. For the majority of two-prong jets, the k_T and soft drop with C/A algorithms are both expected to still be sensitive to the hard substructures in the jet. The C/A reclustering algorithm is sensitive to the angular distribution of soft constituents in the jet, which will determine the sensitivity of the axes returned to the hard prongs. A data driven approach will be employed to evaluate the effect of the minimisation procedure as it is dependent on the exact nature of the remaining soft radiation in the jet cone.

2.2 Background Subtraction Techniques

Due to the large number of binary nucleon-nucleon collisions occurring in central Pb-Pb collisions [83], there is a large multiplicity of particles, originating from soft processes, in the event [84]. These particles are collectively known as the heavy ion background and are uncorrelated to the hard production processes that give rise to jets. However, they are clustered in the jet cone by the jet finding algorithms which leads to a smearing of the jet signal. Figures 2.13a and 2.13b show the measured charged particle multiplicities per unit of pseudorapidity, in pp and Pb-Pb collisions respectively. The $0-10\%$ most central Pb-Pb events have approximately 300 times more charged particles per unit of pseudorapidity than pp events. In this analysis, all particles above 150 MeV/c are accepted, in order to maximise the information from the hard scatter clustered into the jet cone. However, as shown in figure 2.14, such a low constituent cut-off captures a vast amount of the heavy ion background as well. The average p_T contribution per unit area (for a more detailed description of this variable, see section 2.2.1), in the $0-10\%$ most central Pb-Pb collisions, is 138.32 ± 0.02 GeV/c [87]. This distribution has a standard deviation of 18.51 ± 0.01 GeV/c, showing that fluctuations in this value can be large. For the low $p_T^{jet,ch}$ values used in this analysis ($40 \leq p_T^{jet,ch} < 60$ GeV/c), the amount of background p_T present in the jet is often larger than the signal arising from the hard process. This background must be removed from the jet in order to uncover this underlying signal.

This analysis uses three main background subtraction techniques in Pb-Pb collisions. These are the area-based subtraction [88], constituent subtraction [89] and derivatives subtraction [90] techniques. These techniques were initially developed to remove pile-up from pp collisions. They have since been extended to remove the heavy ion background in Pb-Pb collisions as well. These algorithms can be applied to

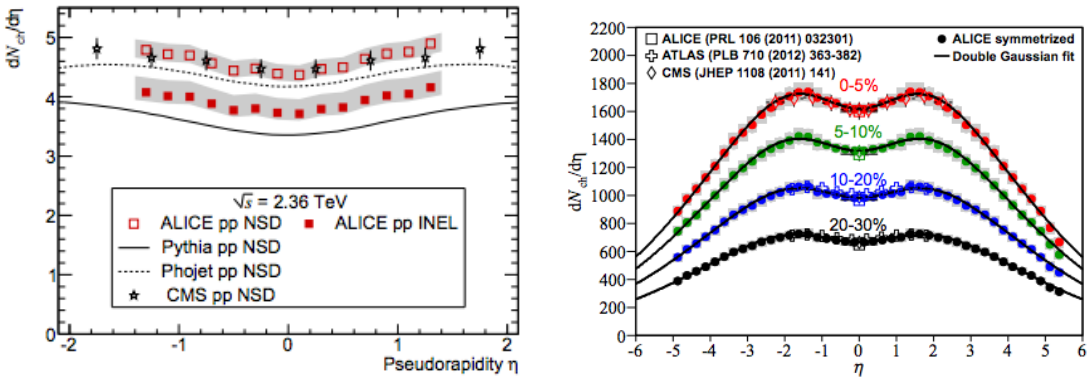

(a) pp [85] (b) Pb-Pb [86]

Figure 2.13: The charged particle multiplicity per unit of pseudorapidity distributions, measured at the ALICE experiment, are shown for pp and Pb-Pb collisions (for different centralities).

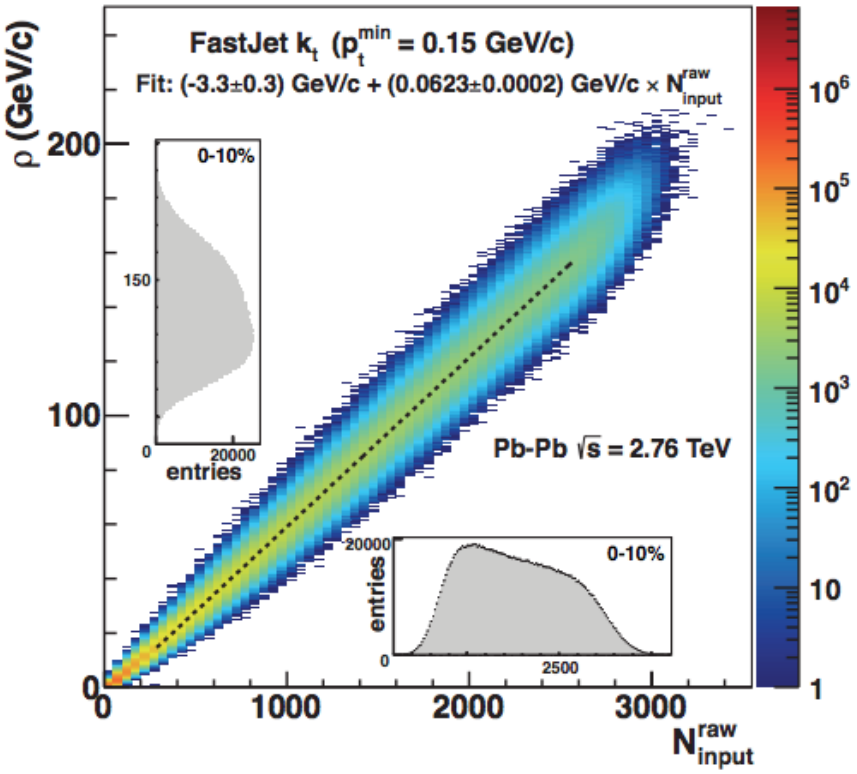

Figure 2.14: The charged particle background p_T density per unit area, ρ, as a function of the (uncorrected) event multiplicity is shown for Pb-Pb collisions ($|\eta| < 0.9$). On each axis, the section pertaining to the $0-10\%$ most central events is highlighted [87].

clustered jets and are not dependent on the jet finding algorithms used. Constituent subtraction is the default subtraction mechanism in this work, with derivative subtraction (at second order) used to provide a systematic cross-check. The area-based subtraction does not correct the measured jet shapes. It only corrects the energy scale of the jet. Therefore, it will be used to highlight the effects of the unsubtracted heavy ion background on jet shapes, whilst providing the opportunity to compare these shapes at the correct energy scale. To this end, the jet sample measured using this subtraction technique will often be labeled as "no subtraction". These techniques all remove the event average background from the jet. Local fluctuations in the background are corrected for via the unfolding procedure (see section 2.4).

2.2.1 Area-Based Subtraction

The area-based subtraction technique is used to remove the event average background contribution from the p_T^{jet}. The calculation relies on two ingredients. The jet area, A^{jet}, and the p_T density per unit area of the background, ρ. For most jet algorithms, due to the irregularity of the shape of the jets, the area of a jet cannot be trivially calculated. The approach taken to determine A^{jet}, is to populate the event uniformly with ghost particles. Ghosts are particles with zero (or extremely low) p_T, which are artificially added to an event. The number of ghosts added within a given area (density of ghosts) determines the area of each ghost ($\frac{Area}{N_{ghosts}}$). The event is then clustered with the desired jet algorithm. Since the ghost particles have no (or very little) p_T, their presence does not alter the jets returned by the jet finder. Once clustered into a jet, the number of ghost particles present in a jet is used to determine the area of that jet (since the area of each ghost is known). In this way, the calculation of the jet area requires no prior knowledge of the shape of the jet.

To determine ρ, the event is clustered using the k_T algorithm. A smaller jet radius

($R = 0.2$ in this work) than the radius used for the actual jet finding is selected. The k_T algorithm has the tendency to cluster the soft background of the event, without the need for hard structures. Therefore, by using the k_T algorithm with a small radius, the event will be clustered into mostly soft jets with areas $\sim \pi R^2$. ρ can then be calculated via,

$$\rho = median[\{\frac{pT,j}{A_j}\}], \tag{2.8}$$

where the index j runs over the jets clustered with the k_T algorithm. Using the median value minimises the contribution of jets originating from a hard scatter to the calculation of the average background density.

Once A^{jet} and ρ have been determined, the corrected p_T^{jet}, $p_{T,Sub}^{jet}$, can be obtained by using

$$p_{T,Sub}^{jet} = p_T^{jet} - (\rho A^{jet}). \tag{2.9}$$

In this way, the event average background contribution to the energy scale of the jet is removed. However, no correction has been applied to the jet's substructure. Figure 2.15 shows the effect of this background subtraction technique on the p_T^{jet} spectrum in Pb-Pb collisions (black). Comparisons to pp (green) and unsubtracted Pb-Pb (blue) are also shown. The uncorrected p_T^{jet} distribution in Pb-Pb experiences a very large shift towards higher values, compared to pp collisions. This is due to the presence of the heavy ion background. Subtracted jets appearing at negative p_T^{jet} values were clustered with a p_T^{jet} lower than ρA^{jet} (these are explained in more detail in section 2.3.1). The area-based subtraction mechanism corrects the p_T^{jet} reasonably accurately for $p_T^{jet} \geq 20$ GeV/c. The discrepancies at lower values are due to the

larger effect of background fluctuations at these p_T^{jet}, since the subtraction technique only removes the event average background contribution and does not correct for local fluctuations.

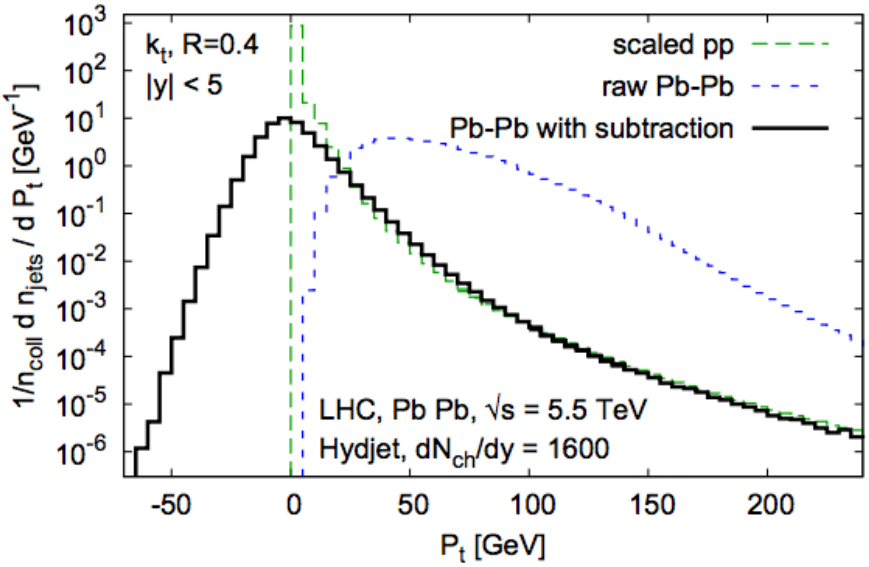

Figure 2.15: The effect of the area-based subtraction procedure on the p_T^{jet} distributions is shown for Pb-Pb collisions. Uncorrected p_T^{jet} distributions for pp and Pb-Pb collisions are shown for comparison [88].

2.2.2 Constituent Subtraction

The constituent subtraction technique can be considered an extension to the area-based method. However, in this technique jets are corrected at the constituent level by removing and modifying the particles clustered in the jet. The first step of the algorithm is to determine ρ using equation 2.8. An additional variable, ρ_m, is also calculated by substituting mass, m, for p_T in equation 2.8. This allows for the simultaneous correction of both the p_T and mass of the jet constituents. For the remainder of this discussion, corrections to the mass will not be discussed. However, the steps for the mass correction are identical to the p_T correction with only the variables interchanged.

The next step adds ghosts to the event. The jets are reclustered, incorporating the ghosts in to themselves. The ghosts are then assigned a transverse momentum, $p_{T,g}$, given by,

$$p_{Tg} = A_g \rho, \tag{2.10}$$

where A_g is the area of each ghost particle. ρ is independently calculated for each event. A distance measure between each particle-ghost (i,g) pair inside the jet, ΔR_{ig}, is then defined such that,

$$\Delta R_{ig} = p_{T,i}^{\alpha} \sqrt{(\phi_i - \phi_g)^2 + (\eta_i - \eta_g)^2}. \tag{2.11}$$

These distance measures are then sorted in increasing order for each jet. The algorithm then begins an iterative process, starting with the particle-ghost pair with the lowest ΔR_{ig}. If $p_{T,i} \geq p_{T,g}$, the value of $p_{T,g}$ is subtracted from $p_{T,i}$. The $p_{T,g}$ for that particular ghost is then set to zero. If however, $p_{T,i} < p_{T,g}$, then $p_{T,i}$ is subtracted from $p_{T,g}$ and $p_{T,i}$ is set to zero. The process is then repeated with the particle-ghost pair with the next lowest distance measure (with the p_T of the previous pair now updated).

The procedure iteratively continues, until all particle-ghost pairs have been processed. All ghosts and particles with zero p_{Ti} are then discarded and the jet is reclustered with the remaining particles. In this way, the subtraction procedure has corrected the jets at a constituent level. The α parameter in equation 2.11 can be used to preferentially start the subtraction with softer ($\alpha > 0$) or harder ($\alpha < 0$) particles in the jet [89]. However, in this analysis we wish to introduce no additional bias in the subtraction process and will therefore use $\alpha = 0$ as our parameter.

A drawback to this procedure is that, in addition to removing jet constituents that end up with a p_T of zero (mostly the soft background particles), the algorithm can modify the p_T of the remaining particles in the jet. This is an important feature of the procedure in removing the average background contribution. In reality though, each jet constituent is either a particle arising from a hard process or is a background particle. An ideal subtraction algorithm should therefore only remove constituents arising from the background without modifying the particles originating from the hard scattered parton, as this invariably changes the underlying substructure.

These subtraction algorithms are still very much in their infancy and will need continuous improvement. However despite the above feature, constituent subtraction performs very well when correcting jet substructure. This is because the ghost particles are distributed homogeneously in the jet cone and therefore the background is removed uniformly (with $\alpha = 0$). In addition to being a good approximation of the distribution of the average uncorrelated background, the uniformity of the subtraction procedure also mitigates (to an extent) against substantial changes to the "true" jet's underlying structure. Therefore, constituent subtraction provides the best current approach to removing the background and correcting the underlying substructure of jets at constituent level in heavy ion collisions.

Figure 2.16 shows the performance of constituent subtraction (black) in removing pile-up from the jet mass observable, validating it with respect to the area-base method. The presence of pile-up (blue), which acts in a similar manner to the heavy ion background, shifts the jet mass to significantly larger values. Constituent subtraction then removes this pile-up from the jets. Jets simulated without pile-up (red), show the distribution which the subtraction mechanism is aiming to correct back to. Constituent subtraction does a very good job of correcting the observable. The area-based technique (open circles), correcting for mass instead of p_T, is also provided for comparison. Both algorithms perform well in removing the pile-up,

with constituent subtraction producing a distribution which is slightly closer to the no pile-up case.

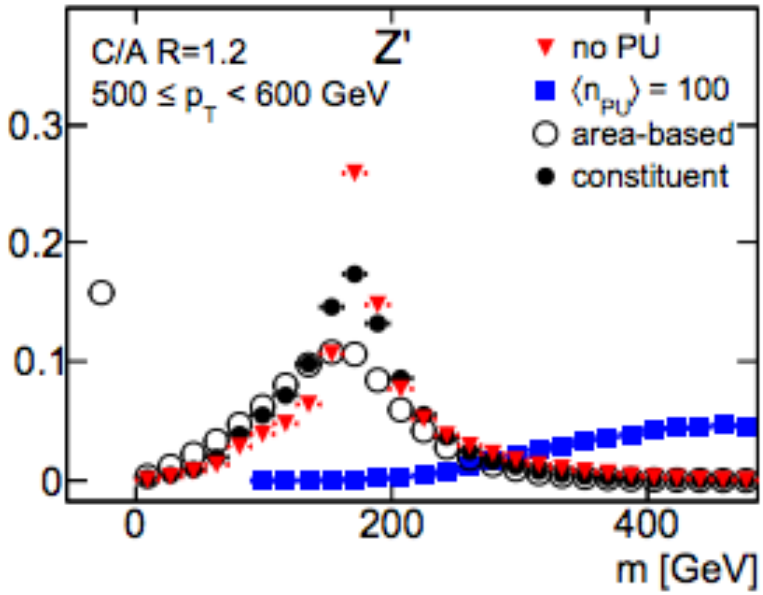

Figure 2.16: The performance of constituent subtraction and area-based subtraction in removing pile-up from the jet mass observable is shown. The simulated jets are clustered with the anti-k_T algorithm with $R = 1.0$ [89].

2.2.3 Derivative Subtraction

Derivative subtraction is a numerical approach that builds on the area-based subtraction method to remove background from the jet and correct jet shapes. As with the other algorithms mentioned here, ρ is determined using equation 2.8. Ghosts with very low $p_{T,g}$ are added to each jet. The value of the jet shape after subtracting the background, $V_{jet,sub}$, is re-written in terms of its derivatives with respect to $p_{T,g}$, such that,

$$V_{jet,sub} = V_{jet} - \rho V_{jet}^{[1]} + \frac{1}{2}\rho^2 V_{jet}^{[2]} + \ldots, \tag{2.12}$$

where V_{jet} is the value of the jet shape measured in the presence of background. The

derivatives, indicated by the [n] superscripts, are calculated numerically for each jet by rescaling $p_{T,g}$ and re-evaluating the jet shape for multiple rescaled values. Once the derivatives have been numerically evaluated, the subtracted jet shape value can be obtained. The value of $V_{jet,sub}$ grows more accurate when including higher order derivatives. This comes at the cost of computational intensity. Therefore in this work, the jet shapes are evaluated up to their second order derivative. When using derivative subtraction, p_T^{jet} is corrected using the area-based subtraction method.

The performance of the derivative (open circles) and constituent subtraction (black) methods are shown for the $\sqrt{d_{12}}$ jet shape in the presence of pile-up (blue), in figure 2.17. $\sqrt{d_{12}}$ is the k_T splitting scale and is given by,

$$\sqrt{d_{12}} = min(p_{T,1}p_{T,2})\Delta R_{12}, \tag{2.13}$$

where the indices 1 and 2 refer to the two subjets returned with k_T reclustering at $N = 2$. ΔR_{12} is given by equation 1.5. Pile-up shifts the true jet shape (red) to much larger values. The jet shape is corrected well using either subtraction algorithm. Even though both methods show similar performances when correcting jet shapes, there are some features that make constituent subtraction the preferred algorithm for this analysis. One of the main drawbacks of the derivative subtraction algorithm is its inferior computational speed compared to constituent subtraction. Another problem is that the numerical approach can sometimes fail for a small number of jets, producing unrealistic values for the shape. Sometimes the algorithm even fails to evaluate derivatives for an entire jet shape. As will be shown in chapter 5, the soft drop algorithm seems to be incompatible with derivative subtraction.

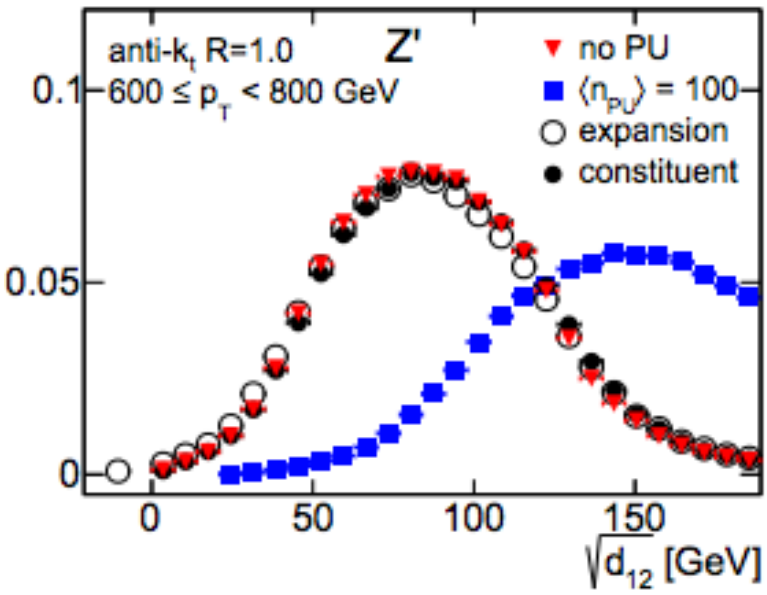

Figure 2.17: The performance of derivative and constituent subtraction in removing pile-up from the $\sqrt{d_{12}}$ observable is shown. Simulated jets are clustered with the anti-k_T algorithm with $R = 1.0$ [89].

2.3 Semi-Inclusive Hadron-Jet Coincidence Technique

2.3.1 Combinatorial Jets

Jet finding algorithms are designed to cluster all tracks in an event, regardless of their origin. The distribution of jets returned per event will include jets not arising from hard scatters. These are known as "fake" or "combinatorial" jets and will contain mostly soft, uncorrelated particles. They must be removed from the measured sample for analyses interested in reconstructing the hard scattered partons. In pp collisions, where the event multiplicity is low, a suitable minimum p_T^{jet} cut can be used to remove these unwanted jets. In these collisions, there are not enough particles arising from soft processes to create jets above this threshold. In this analysis, a $p_T^{jet,ch} \geq 10$ GeV/c cut is used in pp collisions.

The high multiplicity environment of heavy ion collisions enhances this effect. Even after performing background subtraction, which removes the event average back-

ground contribution from each jet, local fluctuations in the background can cause a significant number of combinatorial jets to remain in the measured sample. The contribution of combinatorial jets will reduce with increasing p_T^{jet}, since a larger upward fluctuation of the background is required. This contribution is also related to the jet radius, as a larger radius will cluster a larger amount of the background into the jet. For analyses interested in measuring jets with a low p_T^{jet} and large radius, combinatorial jets can significantly smear the sample and must be removed.

The approximate frequency of combinatorial jets can be measured as a function of p_T^{jet}. The assumption made to measure this contribution is that the majority of jets arising from a hard scatter will contain a high p_T track, resulting from the fragmentation of the initial scattered parton. This assumption is based on measurements of the fragmentation functions of jets at LHC energies in pp (figure 1.6) [58] and Pb-Pb [92] collisions. On average, a jet will contain at least one track carrying approximately $20\% - 30\%$ of the p_T^{jet} for jets of $40 \leq p_T^{jet} < 60$ GeV/c . Conversely, since combinatorial jets arise from soft processes, the presence of high p_T particles are expected to be greatly suppressed.

Figure 2.18 shows the approximate contribution of combinatorial jets as a function of p_T^{jet}, for jets with $R = 0.2$ and $R = 0.3$ which have had the event average background removed from their p_T^{jet} [91]. The jet populations are measured in three ways. First is the unbiased population (black), where all jets returned by the jet finder are accepted. The next two distributions require that the jets contains at least one track with either $p_T > 5$ GeV/c (green) or $p_T > 10$ GeV/c (red). In this way, combinatorial jets are suppressed in the two latter distributions. The difference between these distributions and the unbiased sample gives an indication of the contribution of combinatorial jets for any given p_T^{jet} bin. The contribution of combinatorial jets decreases with increasing p_T^{jet}. The jet samples are combinatorial free at $p_T^{jet} > 40$ GeV/c and $p_T^{jet} > 50$ GeV/c for jet radii of $R = 0.2$ and $R = 0.3$

respectively. This indicates that this analysis' desired $40 \leq p_T^{jet,ch} < 60$ GeV/c bin for jets with a resolution of $R = 0.4$, will have a significant contribution from combinatorial jets, which must be corrected for. This is particularly apparent when considering that a jet with $R = 0.4$ is four times larger than a jet with $R = 0.2$.

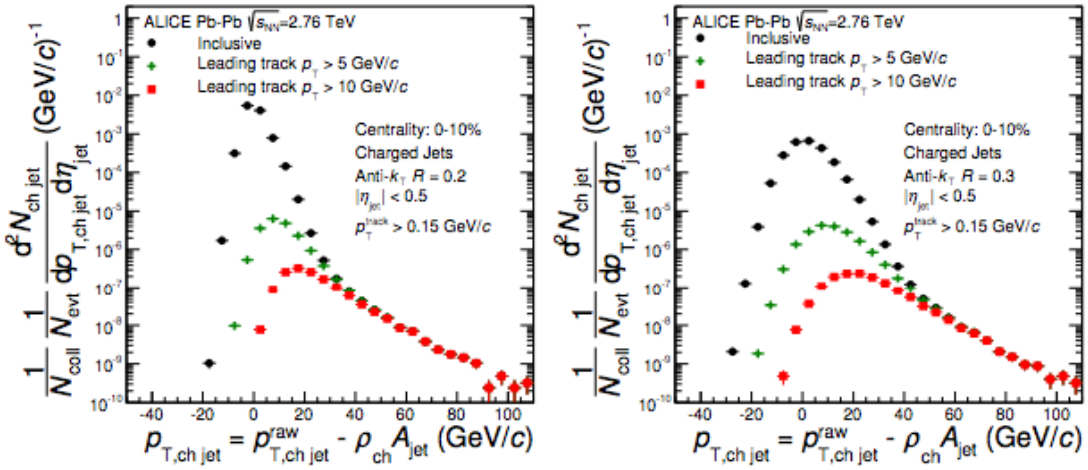

Figure 2.18: The presence of combinatorial jets in the measured jet sample is estimated by placing minimum p_T^{ch} thresholds on the leading (highest p_T) constituent of the jet. The figure on the left shows jets measured with $R = 0.2$ and the figure on the right shows jets measured with $R = 0.3$ [91].

One method to reject combinatorial jets, is to require the jet to have at least one track above a certain p_T threshold, as mentioned above. This guarantees a hard production process. However, this biases the measured sample towards jets with a harder fragmentation pattern. This is not desirable for analyses such as this which are measuring some aspect of the fragmentation pattern of jets. The semi-inclusive hadron-jet coincidence technique [69], also referred to as the recoil jet method, provides an alternative method to reject combinatorial jets without incurring fragmentation biases.

2.3.2 Recoil Jet Method

The recoil jet method does not reject combinatorial jets on a jet-by-jet basis, but rather corrects distributions at the ensemble-average level. Two jet yields are measured recoiling from two high p_T trigger hadron classes. To begin with, two high p_T trigger track (TT) windows are selected. The higher window is called the signal class, with the lower window referred to as the reference class. The data are split between these two classes so that each event is exclusive to a single class. In each event, if available, one hadron in the given trigger track window is randomly selected. A $\Delta\phi$ window, relative to the trigger hadron, is defined such that $|\pi - \Delta\phi| < 0.6$ (back to back to the trigger hadron). Jet finding is then performed in this phase-space window, with no minimum p_T^{jet} threshold imposed. It is expected that the contribution of combinatorial jets is uncorrelated to the trigger track p_T and will be equal in the yield of jets recoiling from the two classes. Therefore, by subtracting the reference yield from the signal yield (each yield is first normalised to the number of trigger hadrons in its class), this contribution is removed and a combinatorial free yield of jets is obtained. Any effects on the background induced by the recoiling jet traversing through it, are not considered. The magnitude of these effects can be different for the two trigger hadron classes.

The high p_T trigger hadron classes ensure that the events selected (and in particular the recoil regions where the jet finding is performed in) contain a hard process, since particles with p_T larger than $5 - 7$ GeV/c are expected to mostly originate from high energy jets [93]. Since the trigger is a single high p_T hadron, it is unaffected by the background making it an experimentally clean trigger. Tracking efficiency (see section 3.4) can cause losses in the number of trigger hadrons detected. However, care is taken to ensure that the tracking efficiency is uniform across the p_T ranges chosen for the reference and signal classes. Therefore, no correction needs to be applied for the tracking efficiency. By choosing appropriate ranges for the trigger

hadron p_T classes, biases in centrality, flow and multiple partonic interactions can also be eliminated in the measured jet sample through the subtraction procedure [69] (since they contribute equally to both classes) . To this effect, the p_T ranges chosen in [69] for the reference and signal classes were $8-9$ GeV/c and $20-50$ GeV/c respectively. In the analysis performed in chapter 5, the same reference trigger track p_T was chosen but the signal p_T window was reduced to $15-45$ GeV/c to maximise statistics. However, the separation between the two classes is still large enough to ensure a healthy difference yield.

Figure 2.19 shows the $p_T^{jet,ch}$ yields measured in pp and Pb-Pb collisions using the recoil jet method [69], for jets with a radius of $R = 0.4$. In both samples, the average background in each event has been removed from its corresponding jets using the area-based method. In the regions where combinatorial jets dominate, the difference between the signal (red) and reference (blue) yields is expected to be small. The negative $p_T^{jet,ch}$ regions represent jets that were clustered with a $p_T^{jet,ch}$ below the average background of the event and are much more heavily populated in Pb-Pb than pp. These jets are expected to be almost entirely combinatorial and correspondingly have similar signal and reference yields in both pp and Pb-Pb collisions. As the $p_T^{jet,ch}$ is increased, the contribution of combinatorial jets is expected to fall, which is represented by the increasing difference between the signal and reference yields. In pp collisions, the absence of significant background means that this separation starts at a much lower $p_T^{jet,ch}$ than in Pb-Pb collisions, where background fluctuations are expected to be large. Combinatorial jets are not significantly present in pp collisions and setting a minimum $p_T^{jet,ch}$ threshold should be enough to remove them from the sample. In Pb-Pb collisions, the small separation between the two yields at 40 GeV/c shows that rejecting combinatorial jets at this $p_T^{jet,ch}$ is necessary for samples measured with this jet radius ($R = 0.4$).

In both pp and Pb-Pb collisions, the selection of the high p_T trigger hadron biases

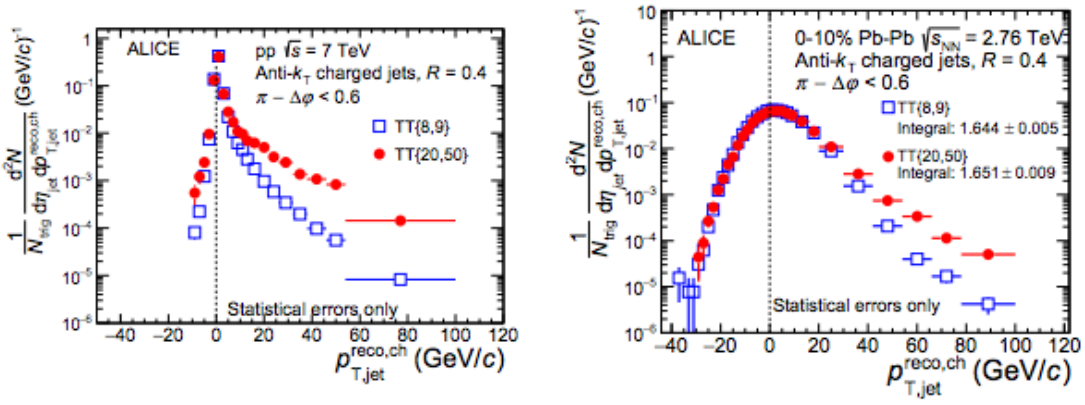

(a) pp (b) Pb-Pb

Figure 2.19: The signal (TT$\{20-50\}$) and reference (TT$\{8-9\}$) $p_T^{jet,ch}$ yields, measured in pp and Pb-Pb collisions for jets with resolution $R = 0.4$, are shown [69]. The separation between the signal and reference yields increases with increasing $p_T^{jet,ch}$, as the contribution of combinatorial jets is suppressed.

towards jets with a hard (high z) fragmentation on the trigger hadron side. However, the fragmentation of the recoiling jets is uncorrelated to that of the jet containing the trigger hadron and no fragmentation bias is imposed on the measured recoil jet yield. Even though many of the common experimental biases, incurred when rejecting combinatorial jets, are not present in the recoil jet method; there are some remaining biases that must be noted. Since the scattered partons forming the jets had an equal p_T when scattered, the measured yield is biased against jets with $p_T^{jet,ch} < p_{T,Trigger}$. No kinematic constraint is placed for $p_T^{jet,ch} > p_{T,Trigger}$. However this bias is calculable in pQCD [94] and can be accounted for. Another bias arising from the selection of the high p_T trigger track in Pb-Pb collisions is due to quenching effects. Since partons lose energy whilst traversing the QGP, the trigger track selection biases towards jets that were produced near the surface of the medium and underwent little energy loss. This means that the measured jet sample in the recoil window is biased towards jets that traversed a larger length of the medium and have undergone stronger quenching effects. However, this bias can be desirable for analyses that are measuring these effects. The recoil jet method provides a suitable, data driven approach for obtaining a combinatorial free sample

of jets, which in turn allows for measurements of jets with a large radius at low $p_T^{jet,ch}$ in Pb-Pb collisions.

2.3.3 Extension to 2D

In this analysis, the recoil jet method will be extended to two dimensions for the first time (see section 5.3.2), in order to make a combinatorial free measurement of jet shapes in Pb-Pb collisions for a given low $p_T^{jet,ch}$ bin. The underlying method in two dimensions is the same as the one-dimensional case described above. However, the signal and reference yields are measured in two dimensions (jet shape vs $p_T^{jet,ch}$) and the difference yield obtained is also in 2D. A projection of the shape distribution in the difference yield is then performed for given $p_T^{jet,ch}$ bins to produce a final jet shape difference yield. It should be noted that the recoil method does not correct individual jets for their $p_T^{jet,ch}$ or jet shape. Instead, it corrects the yield in each $p_T^{jet,ch}$ and jet shape bin.

2.4 Bayesian Unfolding

The aim of most experimental analyses is to measure the "true" distribution of a physical process, as it occurs in nature. However, measured distributions are often smeared by detector inefficiencies and other experimental effects, which can distort the "true" distribution. These distortions will be different between experiments, due to different detector configurations and experimental conditions. This results in a variety of different measured distributions, attempting to describe the same "true" distribution. A correction procedure, known as unfolding, must be applied to the measured distributions to disentangle these distortions and uncover the "true" distribution. This allows for comparison of results, both across different experiments

and with theoretical calculations at particle level. This analysis employs a two-dimensional Bayesian unfolding procedure [95], to simultaneously correct the $p_T^{jet,ch}$ and jet shape. In addition to detector effects, in Pb-Pb collisions at the LHC, large local fluctuations in the heavy ion background (which remain post subtraction) can significantly smear the true signal and must also be corrected for through unfolding.

2.4.1 Bayes' Theorem

The unfolding procedure used in this analysis is based on Bayes' theorem. This states that the probability of a measured effect, E_j (measured value), being due to a cause, C_i (truth value), can be expressed as,

$$P(C_i|E_j) = \frac{P(E_j|C_i)P_0(C_i)}{\sum_{l=1}^{n_c} P(E_j|C_l)P_0(C_l)}. \tag{2.14}$$

$P(E_j|\mathrm{C}_i)$ is the probability of the i^{th} cause to produce the j^{th} effect. $P_0(C_i)$ is the initial probability of the i^{th} cause occurring, with n_c being the total number of possible causes. After making a number of measurements, N_{obs}, a frequency distribution of effects, n_E, is obtained. The best estimate of the true number of events, for the i^{th} cause, can then be calculated as,

$$\hat{n}(C_i) = \frac{1}{\epsilon_i}\sum_{j=1}^{n_E} n(E_j)P(C_i|E_j), \tag{2.15}$$

where ϵ_i is the efficiency. Summing $\hat{n}(C_i)$, over all possible causes (i values), gives the fully unfolded "true" distribution, $\hat{N}$.

2.4.2 Experimental Evaluation

The ingredients needed to calculate equations 2.14 and 2.15 can be obtained experimentally. $n(E_j)$ is j^{th} bin of the measured data sample. $P(E_j|\mathrm{C}_i)$ is obtained using MC simulations. The MC is generated at particle (truth) and detector levels for pp collisions (see section 4.3.3) and at particle and embedded levels for Pb-Pb collisions (see section 5.4.1). These provide a mapping between causes and effects and give access to the $P(E_j|\mathrm{C}_i)$ values. The efficiency, ϵ_i, is calculated by dividing the counts in a detector level bin by the counts in the appropriate truth level bin.

The only remaining component needed to calculate $\hat{n}(C_i)$, is $P_0(C_i)$. This is obtained through an iterative process. To begin with, a P_0 distribution is constructed, for all i values, from a best guess estimate of the distribution of the physical process. The truth level distribution from MC is often used for this. The first iteration of the unfolded distribution, $\hat{N}$, is then calculated. An updated P_0 value is obtained from $\frac{\hat{n}(C_i)}{\hat{N}}$. The updated value is then put into equation 2.15 and $\hat{N}$ is recalculated. This process is iteratively repeated, until the $\hat{N}$ distribution converges onto a stable solution. This indicates that the true P_0 distribution has been obtained. In this way, the unfolding procedure allows for the calculation of the "true" distribution, $\hat{N}$, without any prior knowledge of P_0. In fact, the knowledge of P_0 is increased through the iterative steps. One of the properties of this unfolding method, is that the final $\hat{N}$ solution is independent of the choice of the initial P_0 guess. The closer the initial P_0 distribution to the true P_0 value, the faster the solution will converge.

2.4.3 Unfolding Matrix

The software package used to perform this Bayesian unfolding procedure, RooUnfold [96], takes advantage of the unfolding matrix, M. Equation 2.15 can be rewritten

as,

$$\hat{n}(C_i) = \sum_{j=1}^{n_E} M_{ij} n(E_j), \tag{2.16}$$

where M_{ij} is an index of the unfolding matrix and is given by,

$$M_{ij} = \frac{P(E_j|C_i)P_0(C_i)}{[\sum_{l=1}^{n_E} P(E_l|C_i)][\sum_{l=1}^{n_c} P(E_j|C_l)P_0(C_l)]}. \tag{2.17}$$

In this analysis, the data distribution is measured in two dimensions of $p_T^{jet,ch}$ and jet shape. Therefore, the unfolding matrix must be in four dimensions. These are $p_{T,Truth}^{jet,ch}$, jet shape$_{Truth}$, $p_{T,Det}^{jet,ch}$ and jet shape$_{Det}$. In this configuration, the unfolded distribution, $\hat{N}$, is also obtained in two dimensions of $p_T^{jet,ch}$ and jet shape. Under the rules of matrix multiplication, the $p_T^{jet,ch}$ and jet shape binnings of the measured distribution must be equivalent to the binnings of the $p_{T,Det}^{jet,ch}$ and jet shape$_{Det}$ dimensions of the unfolding matrix respectively. This also holds for the $p_T^{jet,ch}$ and jet shape binnings of the unfolded distribution, which must be equivalent to the binnings of the $p_{T,Truth}^{jet,ch}$ and jet shape$_{Truth}$ dimensions of the unfolding matrix respectively.

RooUnfold is provided with the two-dimensional measured distribution and a four-dimensional response matrix, which contains the mapping of the $P(E_j|\mathrm{C}_i)$ values (but in four dimensions). The response matrix is constructed from MC as mentioned in section 2.4.2. The program uses this response matrix to construct the unfolding matrix, according to equation 2.17. It then begins the iterative process of calculating the unfolded distribution, for a requested number of iterations. The validity of the unfolded solution is then tested for a set of criteria, which are described in section 4.4.3.

The statistical errors are calculated using the method described in [96]. Systematic

errors are evaluated by repeating the unfolding process with a modified response matrix and comparing the final solutions. Sources of systematic error modify the mapping between causes and effects, changing the $P(E_j|\mathrm{C}_i)$ values. This results in a new response matrix and hence unfolding matrix, which must be evaluated independently.

CHAPTER 3

The ALICE Detector

This chapter will describe the ALICE detector, which is part of the LHC particle accelerator complex at CERN (section 3.1). Particular emphasis will be placed on the detector subsystems used in the analyses described in chapters 4 and 5. These are the Inner Tracking System (ITS) (section 3.2.3), Time Projection Chamber (TPC) (section 3.2.4) and V0 scintillators (section 3.2.5). The centrality estimators and triggers used in the measured data sets will also be described (section 3.3). Lastly, the track reconstruction procedure will be detailed (section 3.4), in preparation for the use of the datasets (section 3.5) in subsequent chapters.

3.1 The Large Hadron Collider

3.1.1 Overview

The Large Hadron Collider (LHC) is a particle accelerator located at the Swiss-French border, measuring 26.7 km [97] in circumference. It is composed of two rings which accelerate hadrons in opposite directions. The primary beams are proton and Lead (^{208}Pb) nuclei, leading to three main collision systems of pp, p-Pb and Pb-Pb at differing centre of mass energies ($\sqrt{s}$). Recently, a short Xe-Xe run was also performed at $\sqrt{s_{NN}}$ = 5.44 TeV, to obtain results with lighter nuclei. The LHC design energies, which were realised in Run 2, are $\sqrt{s}$ = 14 TeV, $\sqrt{s_{NN}}$ = 8.16 TeV and $\sqrt{s_{NN}}$ = 5.26 TeV for the pp, p-Pb and Pb-Pb collision systems respectively. However, the pp and Pb-Pb datasets used in this analysis were obtained in Run 1 and are at $\sqrt{s}$ = 7 TeV and $\sqrt{s_{NN}}$ = 2.76 TeV respectively.

The LHC hosts four main experiments. These are the ALICE, ATLAS, CMS and LHCb experiments. ALICE is optimised for the study of heavy ion collisions, which it uses to study the QGP. ATLAS and CMS are general purpose detectors, focusing on pp collisions to test and study the standard model. However, they also run a significant heavy ion program. LHCb is optimised for the study of b-physics (bottom quark physics) and is searching for evidence of new physics beyond the standard model. Figure 3.1 shows the schematic representation of the LHC ring and its four main experiments.

3.1.2 Accelerator Complex

Prior to injection into the LHC, the nuclei are passed through a series of smaller accelerators [99]. Protons are obtained from a proton source, stripping hydrogen

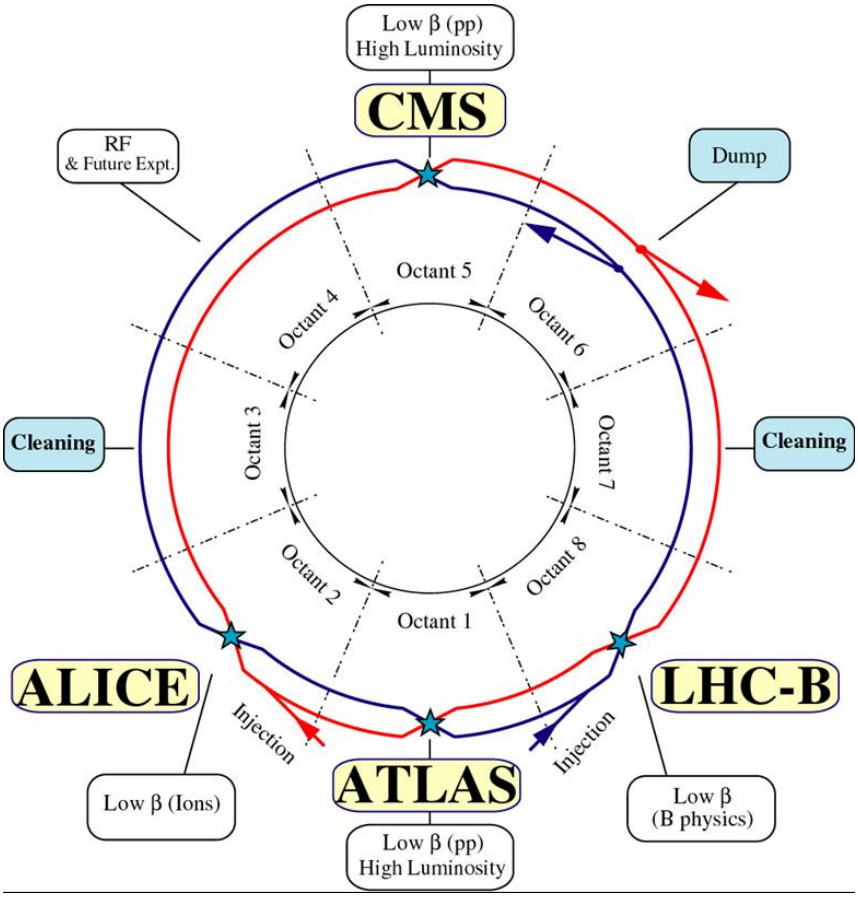

Figure 3.1: A schematic representation of the LHC accelerator complex is shown [98].

atoms of their electrons and injecting them into a linear accelerator (LINAC 2), which accelerates the protons to 50 MeV. From here, the protons are passed into the Proton Synchrotron Booster (PSB), which accelerates them to 1.4 GeV. The protons are then further accelerated by passing into the Proton Synchrotron (PS) and subsequently the Super Proton Synchrotron (SPS) which boost them to 25 GeV and then 450 GeV respectively. They are then injected into the LHC ring, which accelerates them to the required experimental energies. A similar procedure occurs for the Pb ions. The Pb nuclei are stripped of their electrons by passing through a series of foils, before continuing through a linear accelerator (LINAC 3) and the Low Energy Ion Ring (LEIR), which accelerate them. These ions are then injected into the PS and follow the same path as the protons. The energy of the Pb ions at each stage is lower than that of the protons. A schematic of the accelerator chain is

shown in figure 3.2.

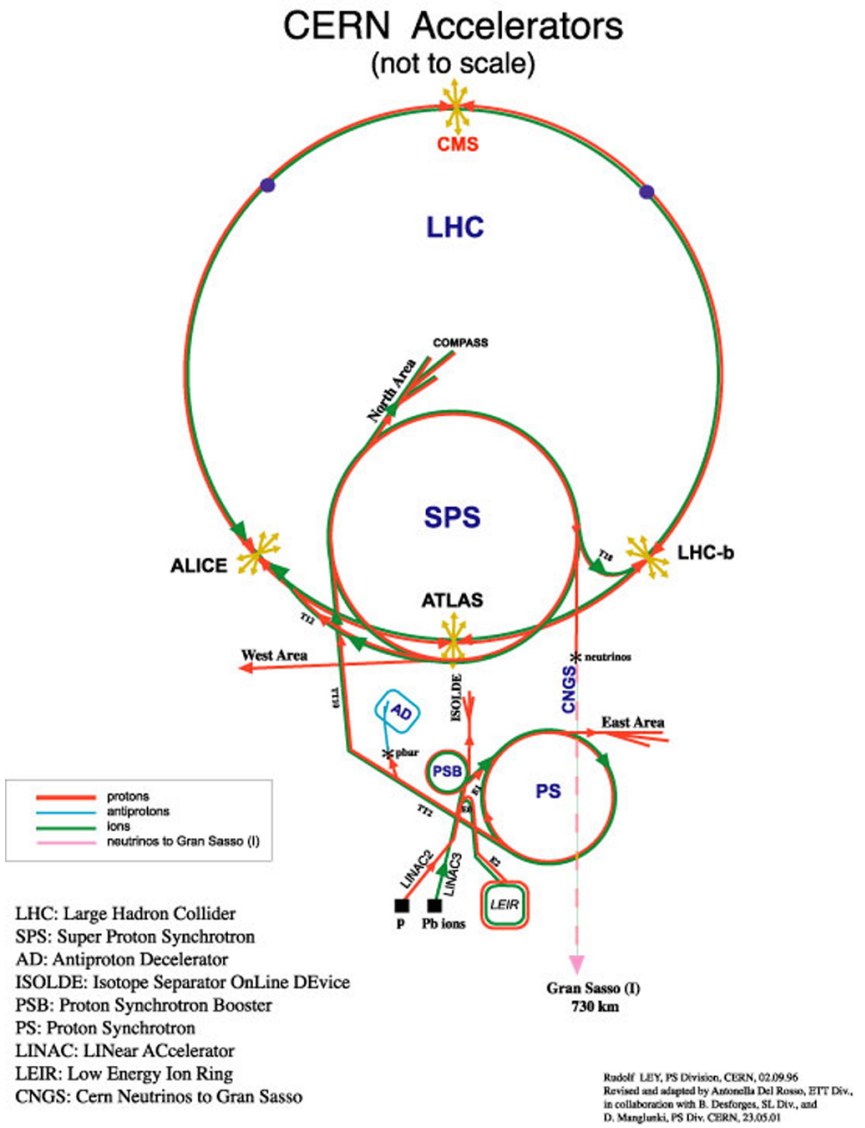

Figure 3.2: A schematic representation of the LHC accelerator chain is shown [100].

The LHC ring uses dipole magnets, with peak fields of 8.33 T, to steer the beams. The beams are focused using quadrupole magnets, particularly at the interaction points. The acceleration of the beams occurs within a straight segment of the ring, using 400 MHz radio frequency (RF) cavities [101]. These RF cavities are also responsible for constraining the nucleons in bunches as they rotate around the ring. At maximum capacity, each beam can contain up to 2808 proton bunches which have a separation of 25 ns.

3.1.3 Luminosity and Event Rate

Due to the design choice of the ALICE detector, particularly with regards to including a large TPC with a long event processing time, a reduction in the interaction rate is required at the ALICE interaction point. This is important in mitigating against the effects of pile-up. Pile-up occurs when multiple proton-proton collisions occur within the same bunch crossing. Experience has shown that the maximum safe interaction rate for the ALICE detector is 700 kHz [102].

At its Run 1 design luminosity in pp collisions, the LHC can deliver a luminosity of $L = 10^{34}$ cm^{-2}s^{-1}. When combined with the total inelastic cross section of pp collisions at $\sqrt{s} = 7$ TeV ($\sigma_{inel} = 73.2 \pm 2.6$ mb [103]), this gives an interaction rate on the order of 700 MHz. Therefore, a significant reduction in this interaction rate is needed at the ALICE interaction point. This can be achieved by reducing the focusing of the beams before collisions. The LHC's design luminosity for Pb-Pb collisions is $L = 10^{27}$ cm^{-2}s^{-1}, which when combined with the total hadronic cross section of Pb-Pb collisions at $\sqrt{s_{NN}} = 2.76$ TeV ($\sigma_{had} \sim 7.65$ b [104]), results in an interaction rate of 3-4 kHz.

The pp and Pb-Pb datasets analysed in this work were collected during the 2010 and 2011 run periods respectively. For the pp collisions, run with the minimum bias trigger (see section 3.3.1), the event rate was $\mathcal{O}(10)$ kHz and reached 95% of the detector read out rate. This corresponds to a delivered luminosity of $L = 10^{30}$ cm^{-2}s^{-1}. The Pb-Pb collisions, run with minimum bias and central triggers (see section 3.3.2), were delivered with an interaction rate of 4 kHz which is comfortably within the tolerance of the ALICE detector. This rate will be increased in the Pb-Pb interactions of later runs.

3.2 ALICE Detector

3.2.1 Overview

A Large Ion Collider Experiment (ALICE) is the LHC's dedicated heavy ion experiment, with the primary aim of studying the QGP. The design of the ALICE detector was based on tracking and identifying low p_T particles in high multiplicity environments. At the time of design, the expected multiplicities for central Pb-Pb collisions at LHC energies at mid-rapidity, ranged from $\frac{dN}{d\eta} = 2000 - 8000$ [105]. As such, the ALICE detector was optimised to study environments with $\frac{dN}{d\eta} \sim 4000$, with the ability to function up to values of twice this amount. However, the first actual measurements at ALICE showed this to be a significant over-estimate, with actual $\frac{dN}{d\eta}$ values in the $0 - 5\%$ most central collisions being 1601 ± 60 [106].

Figure 3.3 shows the layout of the ALICE detector and its detector subsystems. There are fifteen overall sub-detector systems which can be broadly split into three categories: the central barrel, the forward detectors and the muon spectrometer. The central barrel detectors are encased within a solenoid magnet (B = 0.5 T). They are primarily tasked with tracking and/or identifying particles. Tracking can be performed for particles with p_T as low as 100 MeV/c. The upper particle p_T limit for robust tracking is $\sim$ 100 GeV/c. Particle identification can be done reliably for particles with $p_T \leq 20$ GeV/c, using several methods. The ITS, TPC, Transition Radiation Detector (TRD) and Time of Flight (TOF) detectors cover the full range in azimuth and have an 18 segment azimuthal layout. In particular, this work uses the charged tracking capabilities of the ITS and TPC subsystems. The forward detectors are primarily used for characterising the event, with the V0 scintillators playing a large part in the triggering, centrality determination and event plane determination used in this analysis. The muon spectrometer is used to measure

quarkonium and light vector meson production at large rapidities.

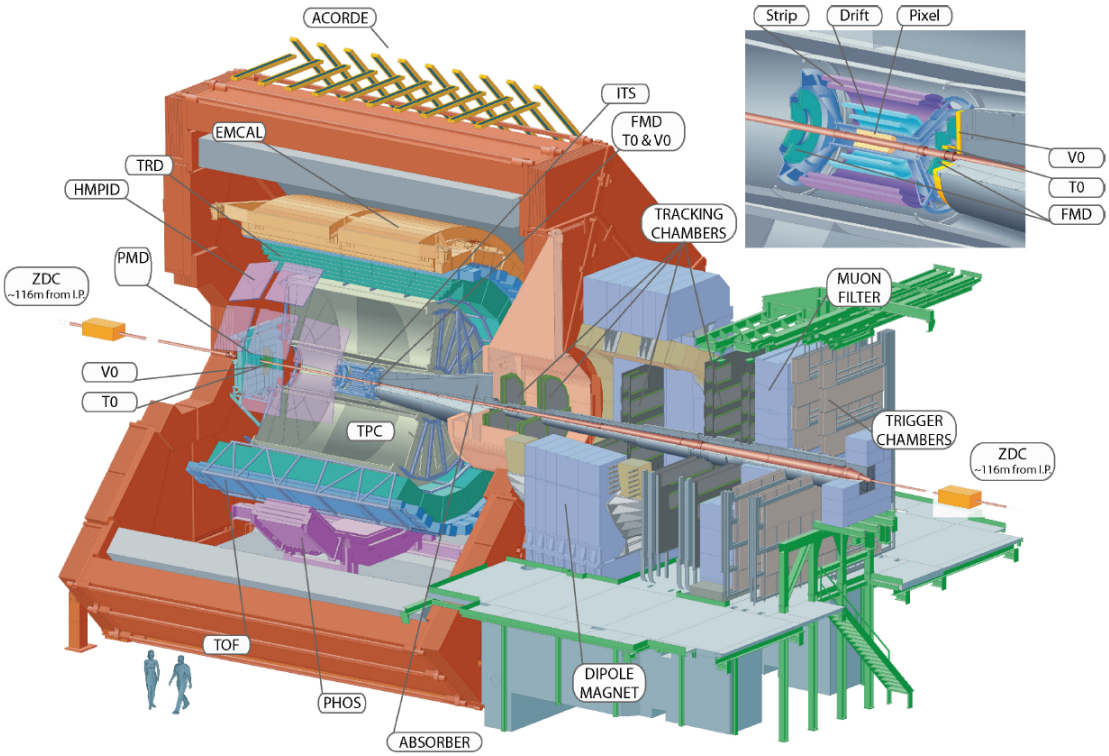

Figure 3.3: A schematic representation of the ALICE Detector is shown. The central barrel is housed within the solenoid magnet which is shown in orange. The muon arm of the detector is situated on the right hand side of the figure. On the top right of the image, a more detailed view of the different layers of the ITS is presented [105].

3.2.2 ALICE Co-ordinate Systems

There are two main co-ordinate systems (plus one directional system) used in this analysis, which are outlined below. For each system, the origin lies at the centre of the central barrel: the nominal intersection point of the two beams.

3.2.2.1 Cartesian Co-ordinates

This system is described using orthogonal axes labeled x, y and z. The x-axis points towards the centre of the LHC, with the y-axis pointing vertically upwards. The z-axis is parallel to the beam line and points towards the muon arm of the detector.

3.2.2.2 Cylindrical Polar Co-ordinates

This system is described using one radial co-ordinate, r, and two angular co-ordinates θ and ϕ. r is defined as the radial distance from the beam line with θ and ϕ being the polar and azimuthal angles with respect to the beam line. A quantity known as rapidity, y, can be defined such that

$$y = \frac{1}{2}\ln(\frac{E + p_z c}{E - p_z c}), \tag{3.1}$$

where E is the energy of the particle and p_z is its momentum in the z direction. The difference between the rapidities of two particles is lorentz invariant. Experimentally it is convenient to use an approximation to rapidity known as pseudorapidity, η, which can be related to the polar angle. This is given by,

$$\eta = -\ln[\tan(\frac{\theta}{2})]. \tag{3.2}$$

3.2.2.3 Sides A and C

The C side of the detector is the side with the muon arm located on it, with the opposite side labelled as the A side.

3.2.3 Inner Tracking System

The ITS is the first detector system surrounding the interaction point and is designed to deal with the high multiplicity densities expected in heavy ion collisions. At its innermost layer, which is constrained in radius by the beam pipe, the track density can reach values of 90 cm^{-2} [107]. To achieve the required granularity, six layers

of silicon detectors, covering the pseudorapidity range $|\eta| \leq 0.9$, are used. These are split into three sub detectors, each comprising of two sequential layers. From the inner to outermost layer, these are the Silicon Pixel Detectors (SPD), Silicon Drift Detectors (SDD) and Silicon Strip Detectors (SSD). Table 3.1 shows both the distance of each sub detector from the interaction point, along with their spatial resolutions in the $r\phi$ and z directions. A schematic is shown in figure 3.4.

ITS Subsytems				
Detectors	Radial Distance From the Interaction Point		Spacial Resolution	
	First Layer / cm	Second Layer / cm	$r\phi/\mu m$	$z/\mu m$
SPD	3.9	7.6	12	100
SDD	15.0	23.9	35	25
SSD	38.0	43.0	20	830

Table 3.1: The radial distance of each of the ITS' detector subsystems from the interaction point along with their spacial resolutions in the $r\phi$ and z directions are shown [105].

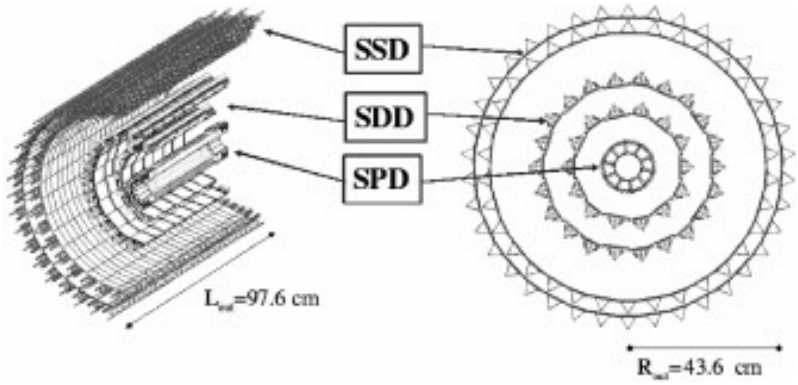

Figure 3.4: A schematic representation of the ALICE ITS system is shown. The innermost layer is the SPD, with the SDD and SSD forming the middle and outer layers respectively [108].

The main tasks of the ITS include vertex determination and the tracking of low momentum particles [105]. This is particularly important for particles which have $p_T^{ch} < 200$ MeV, as these do not reach the next detector system (TPC). The ITS also complements and improves the tracking performed by the TPC.

3.2.3.1 Silicon Pixel Detector

The SPD constitutes the two innermost layers of the ITS. It plays a fundamental role in the determination of both the position of the primary vertex and of the impact parameter of secondary tracks originating from weak decays. To achieve the required granularity at distances so close to the beam pipe, the SPD is comprised of 9×10^6 cells (pixels) which are finely segmented in two dimensions. The size of each pixel is 50×425 μm^2 [109]. Particles passing through a cell are localised by inducing a binary signal in the cell. The small distances to the beam pipe also necessitate a radiation hard design for the SPD, with a total dose of 275 krad [110] estimated at the innermost layer, over a ten year running period.

3.2.3.2 Silicon Drift Detector

The SDD is finely segmented in one direction but coarsely in the other. Along the coarsely segmented direction, the track position is determined by measuring the drift time of the charge induced by the travelling track. This allows for an increased spatial resolution, at the expense of a limited event rate under which the SDD can operate (maximum drift time of the ALICE SDD is 6 μs [105]). This design was chosen to complement the high multiplicity, low frequency events of heavy ion collisions.

3.2.3.3 Silicon Strip Detector

The SSD has a strip like configuration, where it is finely segmented in one direction but coarsely in the perpendicular one. It is double sided, with a 35 mrad angle [105] between the two sides. This allows for a two-dimensional reconstruction of track positions. Such a strip like configuration is only possible at these large distances

from the interaction point, where track densities are much lower (< 1 cm^{-2}) than their values at the SPD. One of the primary functions of the SSD is to match tracks between the ITS and TPC.

3.2.4 Time Projection Chamber

The next detector immediately surrounding the ITS is the TPC, which is the primary tracking system of the central barrel. It is particularly important in the measurement of the momentum of charged particles, vertex determination and particle identification (PID). The TPC has a cylindrical shape with its inner and outer radii measuring ~ 85 cm and ~ 250 cm respectively [105]. In the longitudinal direction, the TPC has a length of ~ 5 m which is split in half by a central cathode. A diagram of the TPC is shown in figure 3.5.

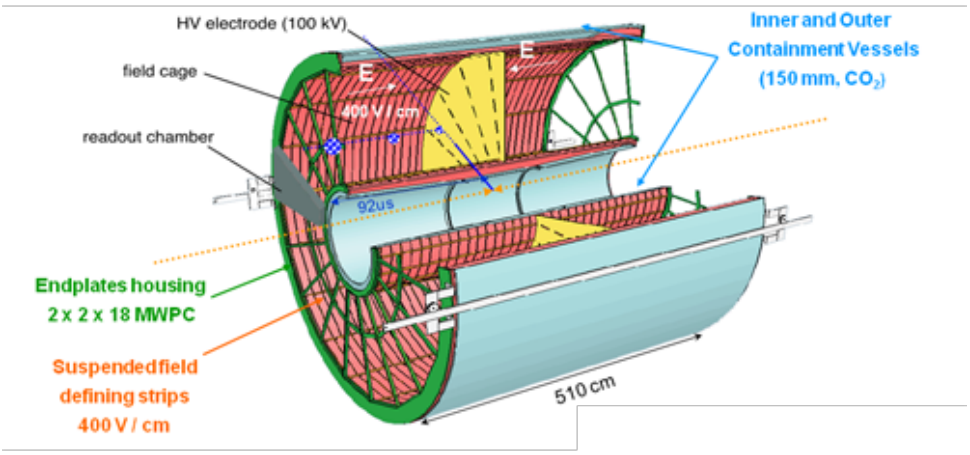

Figure 3.5: A schematic representation of the ALICE TPC system [111].

The TPC covers the full range in azimuth. It also has a coverage of $|\eta| \leq 0.9$ for

tracks with a full radial track length (this defines the η limit used in this analysis), which can be increased to $|\eta| \leq 1.5$ for tracks with shorter track lengths (down to a minimum of one third of the total radial length). The momentum resolution is better than 1% for tracks with $0.2 < p_T < 1$ GeV/c, $\sim 5\%$ for tracks with $p_T \sim 10$ GeV/c and up to 30% for tracks with $p_T \sim 100$ GeV/c. The position resolution is 800-1100 μm in $r\phi$ and 1100-1250 μm in the z direction and is dependent on the position of the particle within the detector [105].

The TPC is a gaseous chamber. Charged particles traversing the TPC ionise the atoms of the gas, liberating electrons. These electrons are then drifted, under a uniform electric field of 400 Vcm^{-1}, to one end of the TPC which is instrumented with multi-wire proportional chambers (MWPCs). As the electrons approach the MWPCs, they are accelerated by the larger electric field, which causes them to avalanche. This avalanche is detected on cathode pads. There are a total of 5504 pads, situated in 63 pad rows, in the inner readout chamber and 9984 pads, situated in 96 pad rows, in the outer readout chamber [105]. The cathode pad readouts are segmented into 18 trapezoidal sections on each end plate. The position of the charge induced on the pads gives the x and y position of the traversing particle, whilst the z position is determined by the drift time of the liberated electrons. The long drift time of the TPC (~ 92 μs) is the limiting factor in the maximum collision rate that can be processed at ALICE.

The gas mixture selected for the ALICE TPC is a Ne/CO_2/N_2 mix at a 90 : 10 : 5 ratio (at atmospheric pressure). This composition was selected due to its low diffusion, low radiation length (low multiple scattering), drift speed and stable properties [105]. One of the drawbacks of this gas mixture is the steep temperature dependence of its drift velocity. Therefore, the TPC temperature is kept under strict control with $|\Delta T| \leq 0.1$ k. This is done using heat screens and cooling circuits [105]. Due to the dependence of the positional resolution on the stability of the drift velocity, the

electric field is also kept extremely uniform [105].

3.2.5 V0

The V0A and V0C detectors are two plastic scintillators, placed at the A and C side of the ALICE detector respectively. They are comprised of four concentric rings, which in turn house eight scintillator counters each. Schematic representations of the V0A and V0C detectors are shown in figure 3.6. The V0A covers a range of $2.8 < \eta < 5.1$, whilst the V0C covers the range $-3.7 < \eta < -1.7$ [112]. They are located at 340 cm and 90 cm from the interaction point respectively.

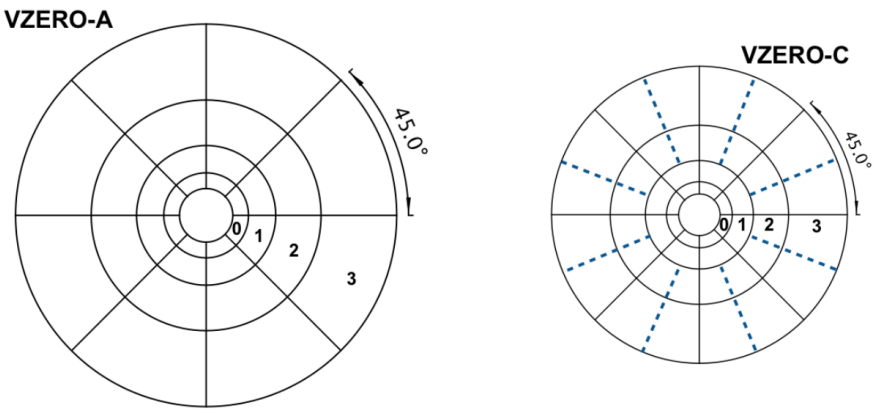

Figure 3.6: A schematic representation of the ALICE V0A and V0C systems is shown [112].

There is a correlation between the signal amplitude on the V0 scintillators and the number of primary emitted particles in an event. As such, these detectors are primarily used for determining event centrality and triggering [105]. Both the minimum bias and central trigger used in this analysis use the V0 scintillators, as described in the next section.

3.3 Triggering

The high event rate at the LHC, coupled with the finite capacity to store recorded events, necessitates the need for triggering. Only events of interest are sampled and recorded. Additionally, the time between collisions is much shorter than the time taken for most detectors to read out and process an event, which means that certain events need to be prioritised. The Central Trigger Processor (CTP) is responsible for co-ordinating this triggering process, based on inputs received from an array of detectors. It can then signal readout detectors to initiate the processing and recording of an event.

The CTP has three trigger levels, which must be sequentially satisfied for an event to be fully recorded. The first level is the L0 level, which relies on fast detectors (such as the V0) to detect the initial signals coming from an event. If particular event criteria (depending on the defined trigger conditions) have been satisfied, an L0 signal is generated to initiate event processing by the chosen readout detectors. At this stage, the CTP also checks if any of the readout detectors are already busy recording an event. The busy statuses of the Data Acquisition (DAQ) system and the CTP itself are also checked. Either of these criteria can result in the CTP vetoing the event and not generating the L0 signal. Once a L0 signal has been generated, further criteria are checked based on inputs to the CTP. If successful, this can result in the generation of an L1 signal. A final stage of checks are then performed, which can result in either an L2a (accept) or L2r (reject) signal being sent out by the CTP. If the readout detectors receive an L2a signal, the event is read out to the DAQ where it is recorded. A L0 signal can be sent to detectors in as little as 1.2 μs after an interaction. A L2 signal takes about 88 μs to be generated, which is approximately the same as the drift time of the TPC.

A more detailed description of the trigger criteria used for the data sets in this

analysis will be presented in the following subsections.

3.3.1 Minimum Bias

The pp data sample used in this analysis (Chapter 4) was collected using the minimum bias trigger. This trigger is designed to select inelastic events with minimum physics bias, whilst rejecting beam backgrounds. In pp collisions, the trigger conditions require at least one recorded hit in the V0A, V0C or SPD [113]. This forms the input to the L0 trigger, which is then generated upon the fulfilment of this criterium. If the trigger is not vetoed, then the event is read out. In Pb-Pb collisions, the minimum bias trigger requires at least two hits in either of the V0A, V0C or SPD. This then forms the basis for the central trigger, which is described below.

3.3.2 Central Trigger

The Pb-Pb data sample used in this analysis (Chapter 5) was collected using the central trigger. The central trigger is built upon the minimum bias trigger, with the added requirement that the sum of amplitudes in the V0 detectors, in a given collision, should be above a given threshold. The value of this sum is sent to the CTP as an L0 input [114]. The correlation of the V0 amplitudes to the event centrality is shown in figure 3.7. By placing minimum limits on the sum of the V0 amplitudes, the centrality of the triggered events can be varied. After the data taking period, offline tests showed that the placement of the V0 amplitude threshold for the central trigger resulted in a 100% efficiency for the $0 - 8\%$ most central events and 80% efficiency for the $8 - 10\%$ most central events [114].

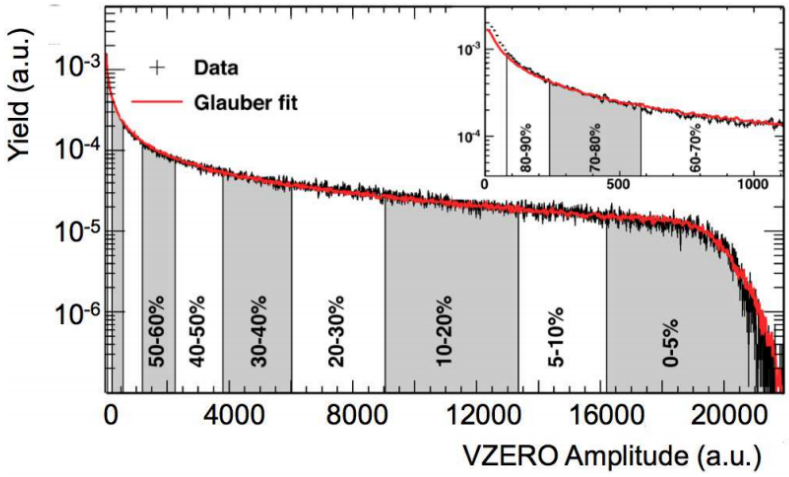

Figure 3.7: The sum of the amplitudes induced in the V0 detectors, in Pb-Pb collisions at $\sqrt{s_{NN}} = 2.76$ TeV, are shown [112]. The centrality percentiles are shown in shaded bands. A Glauber model [115] has also been fitted to the data

3.4 Tracking

Once the signals induced by traversing particles are measured by each detector (the detector data are converted into clusters, independently for each detector, in a process known as clusterisation), a tracking process is employed to combine the information from the detectors and reconstruct tracks attributing to the traversing particles. This process aims to determine the trajectory, momentum and species of the particles passing through the detector material.

The tracking process detailed below begins by determining the interaction vertex, with subsequent track finding and matching performed in the TPC and ITS. The track finding is done in three stages, employed via an inward-outward-inward scheme [102]. The schemes refer to the tracking direction, with the outward scheme starting from the centre of the detector and continuing to the outermost tracking layers. Conversely, the inward scheme begins tracking in the outermost tracking layers and continues inwards towards the interaction point.

3.4.1 Interaction Vertex

The interaction vertex, defined experimentally as the space point to which a maximum number of tracklets converge, is determined using the SPD. Tracklets are lines passing through pairs of clusters (one in each layer) in the SPD [102]. By construction, the first interaction vertex found has the highest number of contributing tracklets and is taken to be the primary vertex. In pp collisions where pile-up is expected, the algorithm is repeated several times to find multiple vertices. Clusters that have already been used to determine a previous interaction vertex are discarded in subsequent iterations.

3.4.2 Track Reconstruction

3.4.2.1 TPC Tracking

Track reconstruction begins from the outer layers of the TPC and moves inwards. The TPC readout chambers are composed of 159 pad rows, which can each produce a cluster when a particle passes through them. The first step is to define track seeds. These are determined using two TPC clusters and the primary vertex, or three TPC clusters without the vertex point. These seeds are then propagated inwards and the tracks are slowly built up at each layer by updating them with the nearest TPC cluster (within a proximity cut). Care is taken not to reconstruct the same physical track multiple times, given that clusters can be reused by different seeds. Pairs of tracks containing over a certain fraction of common clusters are compared and the lower quality track is rejected. This process is carried inwards through the TPC and a preliminary particle identification in performed. This is done in order to assign a mass to the particle and correct for ionisation energy losses in the tracking process. Figure 3.8 shows the tracking efficiency of the TPC. This is the ratio of

the reconstructed tracks to primary particles generated in a simulation, which is approximately 80% for particles with $p_T^{ch} > 1.0$ GeV/c and largely independent of the event multiplicity. The 20% loss of tracks is attributed to the dead zones between readout sectors, where incident particles are not detected. The drop in efficiency at $p_T^{ch} < 0.5$ GeV/c, is due to energy loss in the detector material [102].

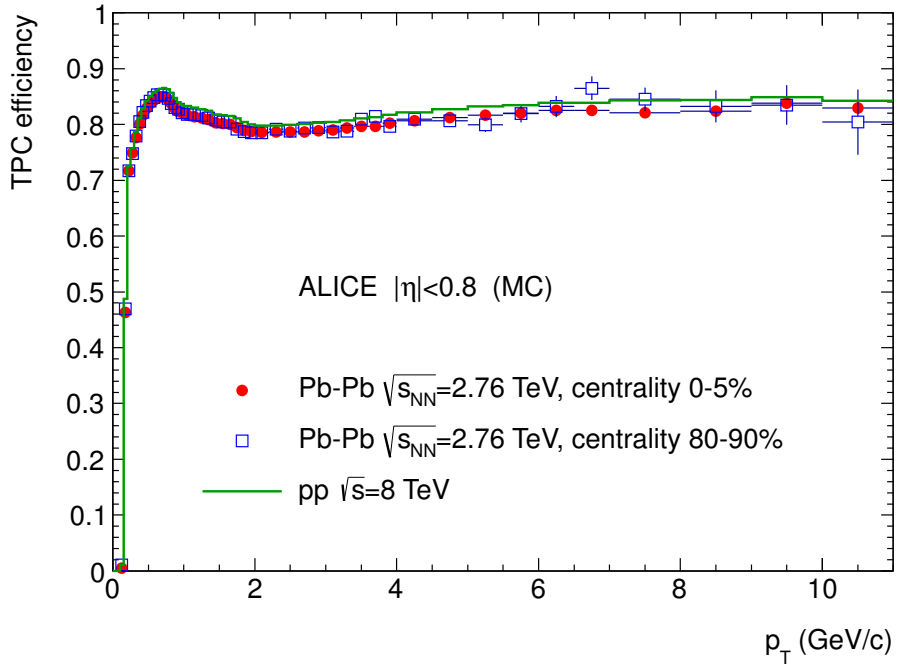

Figure 3.8: The tracking efficiency of the ALICE TPC as a function of p_T^{ch}, for primary particles in pp and Pb-Pb collisions [102].

3.4.2.2 ITS Tracking

The next step of the tracking procedure is to extend the tracking into the ITS. The tracks reconstructed in the TPC are propagated to the outermost layer of the ITS and become the new seeds. The tracking is performed inwards through the ITS and the tracks are updated at each subsequent layer with clusters that satisfy a maximum proximity cut. Each track is also assigned a χ^2 value based on a fitting performed using the Kalman filter technique [116]. At each updated layer, the tracks form new seeds for the next layer. Due to detector inefficiencies, seeds that aren't

updated with a cluster in a given layer are still used as seeds for subsequent layers, with a penalty applied to their χ^2 value. In this way, each TPC track has a series of possible tracks extending from it in the ITS. These possible ITS tracks are sorted by their χ^2 values and the highest quality ITS track emanating from each TPC track is selected. Checks are performed to ascertain that no cluster sharing exists between the selected candidate tracks in the ITS; and in case of clashes, alternative tracks are picked and tested.

Since the tracking efficiency for particles with $p_T^{ch} < 0.5$ GeV/c falls steeply in the TPC, a standalone tracking is also performed with the ITS, using clusters that weren't used in the TPC-ITS tracks. Seeds are created using two clusters from the three innermost layers of the ITS, in addition to the primary vertex point. The seeds are then propagated outwards and updated with clusters in each layer of the ITS (with a given proximity cut). This creates multiple possible tracks from the original starting seed, which are then sorted and selected based on their χ^2 values. Once a track is selected, its clusters are removed and the process is repeated. This method enables tracking down to 80 MeV/c [102].

3.4.2.3 Refitting

Once the reconstruction of tracks in the ITS has been completed, an outward refitting to the clusters associated to each track is performed. At this stage, detectors beyond the TPC can also be used in the tracking process, although this was not the case for the data used in this analysis. Finally, one last inward refitting is performed; starting from the outer layers of the TPC to the innermost layer of the ITS. At this stage, the final properties of the tracks such as their position and momentum, are determined. These tracks are then used to find the interaction vertex with a higher precision than with just the SPD tracklets.

3.4.2.4 Hybrid Tracks

Due to problems with the ITS cooling system during LHC Run 1, up to 20% and 30% of the SPD was switched off during the 2010 and 2011 data taking periods respectively [102]. This resulted in large gaps in the $\eta - \phi$ plane for the reconstructed track distribution. Therefore, in addition to the track reconstruction method detailed above, which still accounts for the vast majority of the reconstructed tracks, two sets of complimentary tracks were introduced in the affected regions to create a uniform distribution in the $\eta - \phi$ plane. These are tracks that successfully passed the ITS refit but had no hits in the SPD and tracks that did not pass the ITS refit altogether. Despite constraining both of these sets of tracks to the primary vertex, they still have a lower p_T resolution than the standard tracks. This lower resolution is preferred over an inhomogeneous $\eta - \phi$ distribution. Figure 3.9 shows the contribution of each track type in the ϕ plane. The sum of these hybrid tracks results in a homogenous distribution, despite the inactive sectors of the SPD.

3.5 Data Sets

The remainder of this thesis will focus on analysing the events measured and reconstructed using the ALICE detector. In pp collisions, 1.48×10^8 events were recorded in the LHC10d and LHC10e data sets. Jet finding will be performed on these events, leading to calculations of the ΔR and τ_2/τ_1 jet shapes. In Pb-Pb collisions, 1.62×10^7 events at $0 - 10\%$ centrality are obtained using the LHC11h data set. Jet finding, accompanied by background subtraction techniques, will be performed on these events, resulting in measurements of the ΔR and τ_2/τ_1 shapes. In both collision systems, the measured jet shapes will be compared to MC models, in order to test for specific physical processes and interpret the results.

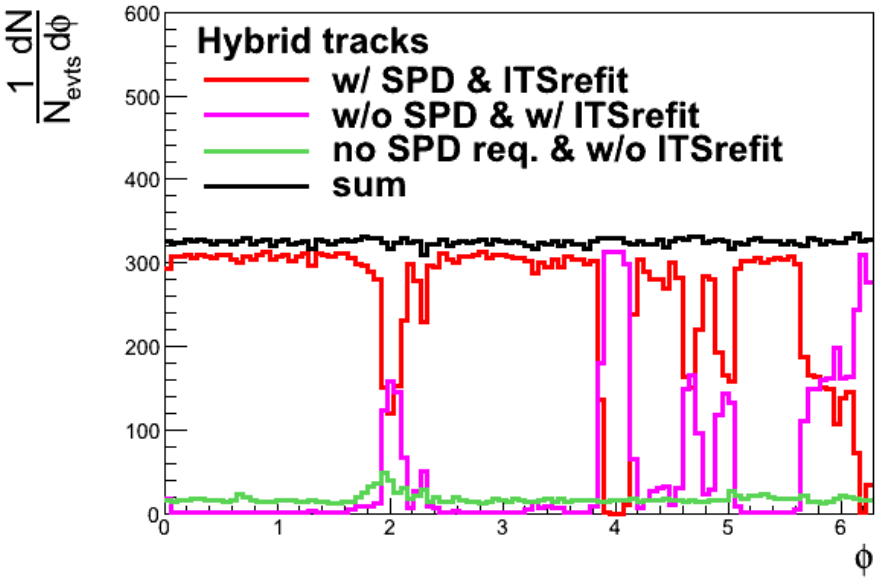

Figure 3.9: The ϕ distribution of the track sets used to construct the hybrid track class, in the 2010 $0-10\%$ centrality Pb-Pb dataset. The depletion in the distribution of standard tracks (with SPD hits and a successful ITS refit) (red), represents the affected sectors of the SPD [117]. For the 2011 Pb-Pb datasets, the tracks without an ITS refit were discarded.

CHAPTER 4

pp Analysis

This section will detail the analytical procedures used to obtain the final fully corrected measurements of the ΔR and τ_2/τ_1 jets shapes in pp collisions, starting from raw reconstructed tracks (as discussed in section 3.4.) Results from each intermediate stage will be presented to showcase the methodology. This will comprise of clustering the tracks into jets and calculating the raw jet shapes. A response matrix is then constructed, by matching truth and detector level MC generated jets. A two-dimensional Bayesian unfolding procedure is applied to correct the raw jet shapes in both shape and $p_T^{jet,ch}$, resulting in the final fully corrected results. Four different reclustering algorithms are employed to calculate the jet shapes, as discussed in section 2.1.2.

4.1 Clustering Jets

In order to reconstruct the kinematics of the initial scattered partons, the tracks measured by the detector are clustered into jets using the anti-k_T algorithm. The minimum bias pp data sets used in this analysis yield 337,984 jets at $R = 0.4$, with a $p_T^{jet,ch} \geq 10$ GeV/c cut imposed. Single track jets have been removed from the sample, since at least two tracks are required to compute the ΔR and τ_2 jet shapes. The $p_T^{jet,ch}$ distribution of this ensemble is shown in Fig 4.1 and follows the expected QCD jet production power law.

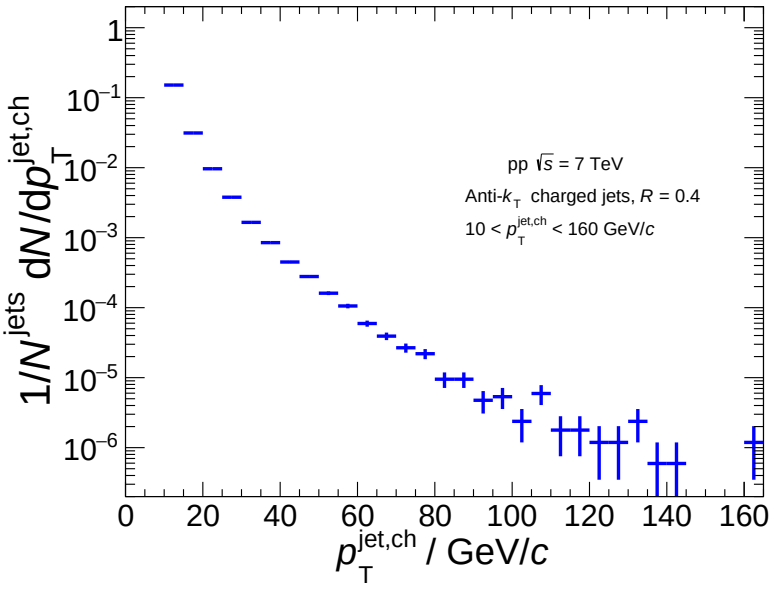

Figure 4.1: The $p_T^{jet,ch}$ distribution, obtained for the measured pp data sets, is shown.

The $\phi^{jet,ch}$ and $\eta^{jet,ch}$ distributions are shown in figures 4.2 and 4.3 respectively. The 18 troughs in the $\phi^{jet,ch}$ distribution correspond to the 18 sector design of the TPC (see section 3.2.1). Even though the TPC has an $-0.9 \leq \eta \leq 0.9$ range at its maximum radius, the jet axis is limited to $-0.5 \leq \eta \leq 0.5$ for jets with $R = 0.4$. This is due to the requirement that the full jet radius be contained within the confines of the TPC.

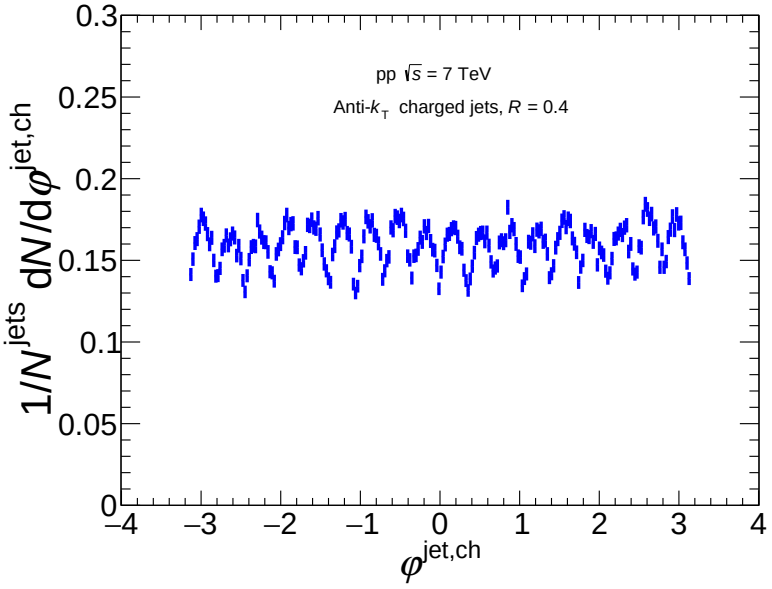

Figure 4.2: The $\phi^{jet,ch}$ distribution, obtained for the measured pp data sets, is shown.

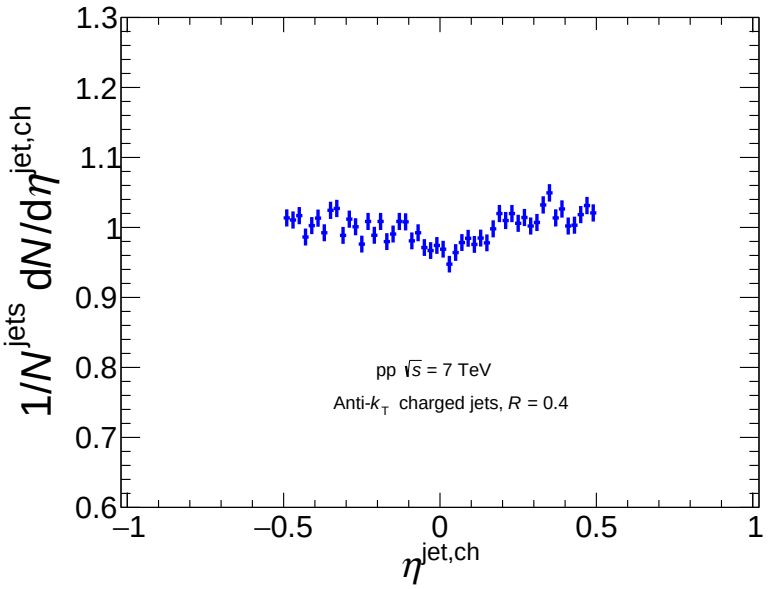

Figure 4.3: The $\eta^{jet,ch}$ distribution, obtained for measured pp data sets, is shown.

The number of charged tracks clustered per jet is shown in Fig 4.4. The distribution peaks at 5 tracks per jet with a mean of 5.61.

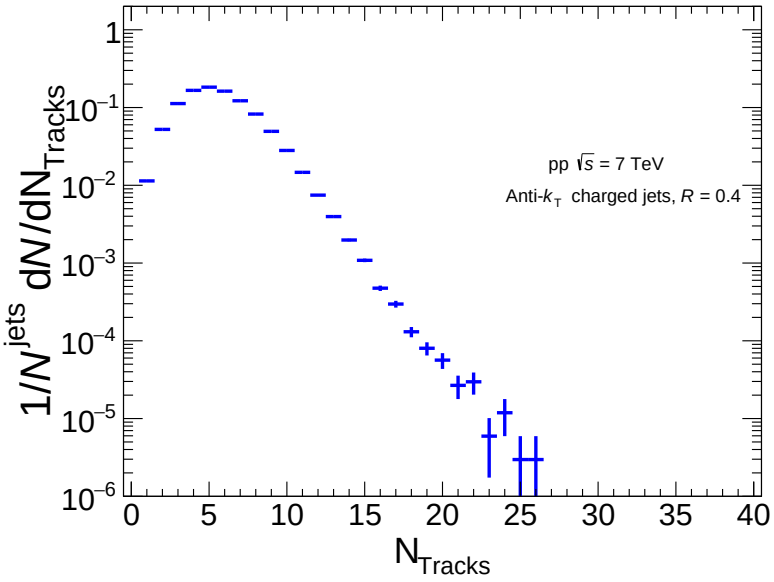

Figure 4.4: The number of charged tracks clustered per jet, obtained for the measured pp data sets, is shown.

4.2 Raw Jet Shapes

Once jet finding has been performed using the anti-k_T algorithm, the jet constituents are reclustered using four different algorithms. These are the exclusive k_T, exclusive C/A, exclusive C/A followed by a minimisation procedure and the soft drop groomer with C/A reclustering. These exclusive algorithms are employed with both $N = 1$ and $N = 2$ and the soft drop parameters are $z_{cut} = 0.1$ and $\beta = 0$. Each reclustering algorithm returns N axes in the jet, which are then used to construct the ΔR ($N = 2$), τ_1 ($N = 1$) and τ_2 ($N = 2$) jet shapes. The τ_2/τ_1 jet shape is obtained by taking the ratio of the τ_2 and τ_1 jet shapes, on a jet-by-jet basis.

4.2.1 ΔR

For the case of $N = 2$, the ΔR variable measures the $\eta - \phi$ distance between the two returned axes. The raw level results for the ΔR jet shape, measured for each

algorithm, are shown in figure 4.5.

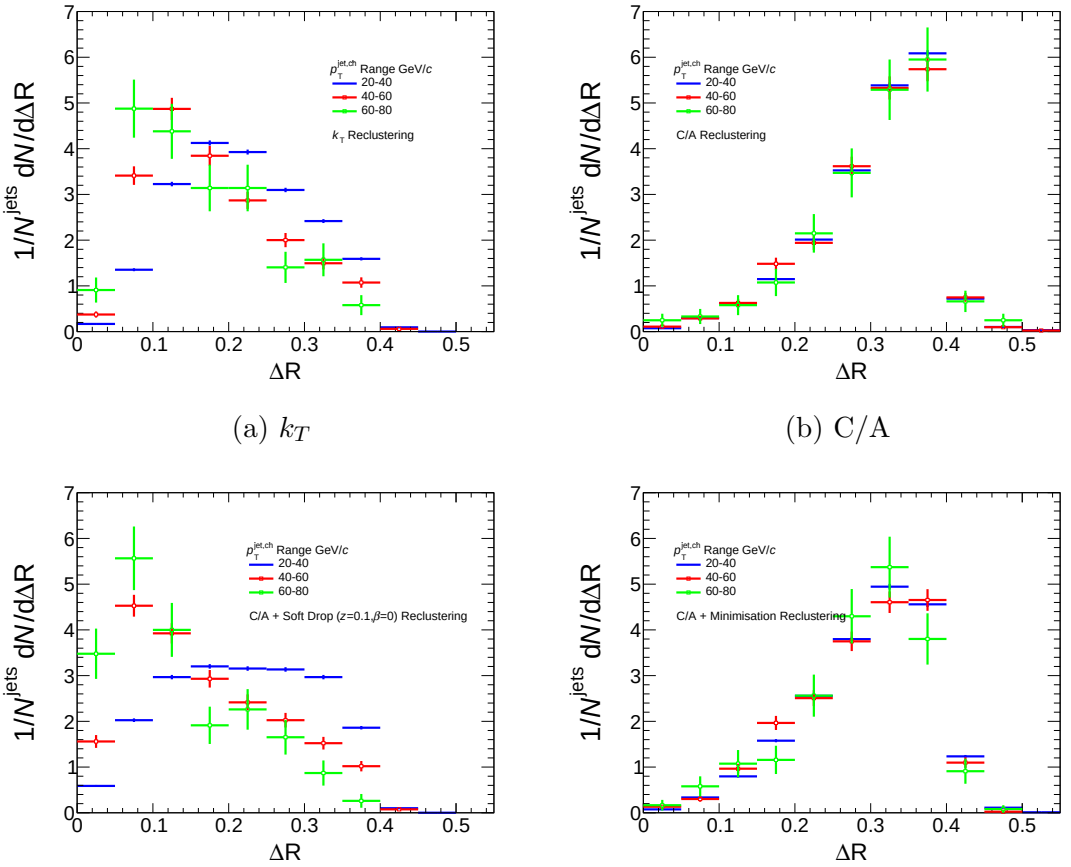

(a) k_T (b) C/A

(c) C/A + soft drop (d) C/A + minimisation

Figure 4.5: The uncorrected ΔR jet shapes are shown in three differential $p_T^{jet,ch}$ bins, for each reclustering algorithm.

The axes (ΔR) returned by the different reclustering algorithms vary significantly. The k_T algorithm returns the axes of hardest (and often first) splitting in the jet. This distribution peaks at low values ($\sim 0.1 - 0.2$), indicating that the bulk of QCD jets are predominantly contained within small cores. There is a mild $p_T^{jet,ch}$ dependence for this algorithm, since QCD jets are more collimated (jet constituents are closer to the jet axis) at higher $p_T^{jet,ch}$ [118].

The C/A reclustering algorithm clusters tracks based solely on their angular distance from each other. The final clustering step will bring together the structures that are furthest apart in the jet. As a result, one of the axes usually remains in the jet

core, whilst the second axis picks out the constituent or cluster furthest away from the core. Therefore, the ΔR distribution for this algorithm peaks at the jet radius. The one pass minimisation of τ_2 has little effect on the position of the axes, due to the small number of constituents present per jet, which limits the possibilities for minimisation. The ΔR distributions for both these axes show no $p_T^{jet,ch}$ dependence, indicating that the presence of soft radiation at large angles is invariant of the $p_T^{jet,ch}$.

The C/A algorithm, when preceded by a soft drop grooming procedure, attempts to identify the axes of hardest splitting in a jet (see section 2.1.2.4). The soft drop procedure modifies the ΔR distribution of the C/A algorithm significantly and brings it close to the distribution obtained by the k_T algorithm, which corresponds to a physical set of axes (axes of hardest splitting). This suggests that the soft drop procedure is effective at removing soft large angle radiation from the jet. The same mild $p_T^{jet,ch}$ dependence, as seen for the k_T reclustering case, is observed.

4.2.2 τ_1

This variable is constructed according to equation 1.9, for the case of $N = 1$. The raw level results for the τ_1 jet shape are shown in figure 4.6, for each reclustering algorithm.

The k_T and C/A algorithms return identical τ_1 values. Both algorithms are limited in the number of possible axes they can return, by the number of jet constituents. The jet constituents are combined using the E-scheme recombination, which is a linear sum and independent of the order of clustering for the $N = 1$ case. Therefore, both algorithms return the (same) jet axis. The one pass minimisation will attempt to minimise τ_1 by altering the jet axis returned by the C/A algorithm. This induces a small shift to lower values of τ_1. Since QCD jets have the bulk of their $p_T^{jet,ch}$ distributed in a relatively small area around the jet axis (they are predominantly

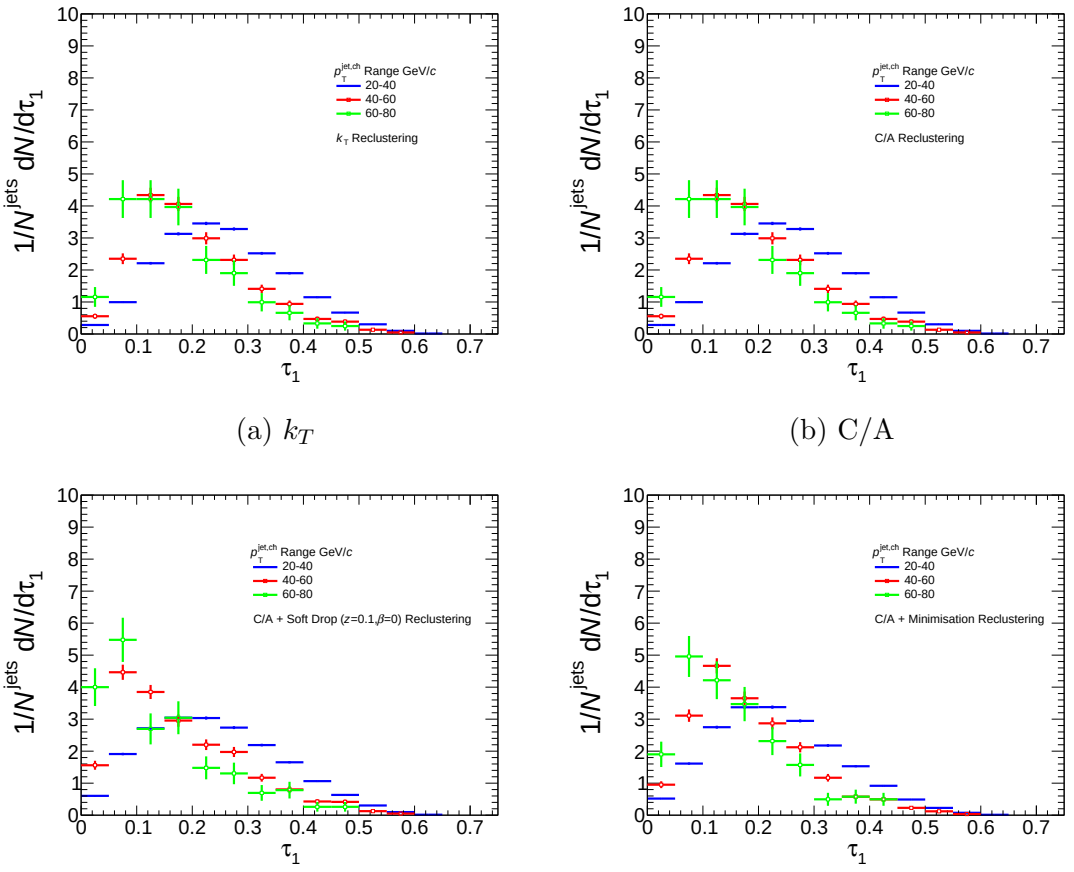

(a) k_T (b) C/A

(c) C/A + soft drop (d) C/A + minimisation

Figure 4.6: The uncorrected τ_1 jet shapes are shown in three differential $p_T^{jet,ch}$ bins, for each reclustering algorithm.

single-core [68]), this minimisation procedure has little effect on the returned axis. The soft drop procedure attempts to remove soft constituents found at large angles from the jet axis, resulting in a decreased value of τ_1. A mild $p_T^{jet,ch}$ dependence is seen across all four algorithms. This is due to the fact that higher $p_T^{jet,ch}$ jets are more collimated, resulting in lower values of τ_1.

4.2.3 τ_2

This variable is constructed according to equation 1.9, for the case of $N = 2$. The raw level results for the τ_2 jet shape are shown in figure 4.7, for each reclustering

algorithm.

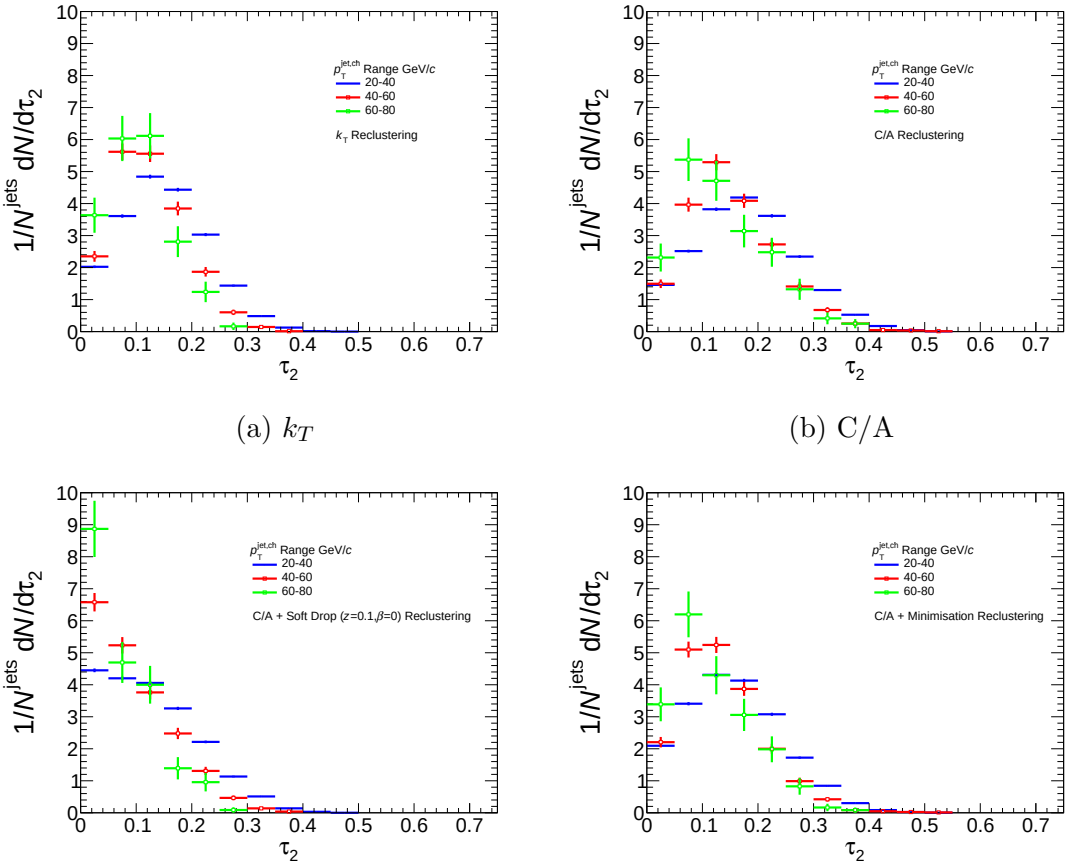

(a) k_T (b) C/A

(c) C/A + soft drop (d) C/A + minimisation

Figure 4.7: The uncorrected τ_2 jet shapes are shown in three differential $p_T^{jet,ch}$ bins, for each reclustering algorithm.

The τ_2 distributions appear at lower values compared to their τ_1 counterparts, due to two main factors. Firstly, by definition, the τ_2 jet shape is sensitive to both two-core and single-core jets, whereas τ_1 is only sensitive to the latter. Therefore, a larger sample of the jet population will contribute to low τ_2 values (strongly two-core and strongly single-core jets) than to low τ_1 values (strongly single-core jets). Secondly, all two track jets will by definition have a $\tau_2 = 0$, which increases the yield of jets in the first bin.

The τ_2 distributions are similar for both the k_T and C/A algorithms. In both cases, one of the axes are likely to remain in the jet core. In the k_T case, the second axis

will follow the next hardest track or cluster whereas in the C/A case the second axis is likely to be further out in the jet, tending towards tracks or clusters at a large radial distance (which tend to be soft). For the majority of jets, the value of τ_2 obtained from both algorithms will be heavily impacted by the axis or axes remaining in the core, since most of the $p_T^{jet,ch}$ is situated in the core of QCD jets (they tend to be single-core). Since both algorithms return a similar axis in the core, their τ_2 values will also be similar.

Although similar, the values of τ_2 obtained via the k_T algorithm will be slightly lower than those obtained via the C/A algorithm, since the second axis is picking up additional hard substructure within the jet or jet core where available. This results in a lower value of τ_2 compared to τ_1, for the k_T case. This holds true for all but a handful of particular configurations, which are not discussed due to their low likelihood of occurring. For most jets, the τ_2 values obtained via the C/A algorithm will be almost identical to their τ_1 counterparts, since the (usually soft) tracks around the second axis contribute almost nothing to the variable. Therefore, even though the τ_2 distributions are visually similar for both algorithms, this small difference makes the k_T algorithm much more sensitive to structures within the jet. This sensitivity can be extracted by taking the ratio of τ_2 and τ_1, as shown in section 4.2.4.

The minimisation procedure shifts the τ_2 distribution to slightly lower values, compared to the C/A case, inducing only a small effect. The soft drop grooming procedure also shifts the distribution to smaller values, albeit to a larger extent. Soft drop removes the large angle soft radiation and attempts to strip the jet to uncover its harder splittings. Therefore, the second axis obtained via this algorithm is more likely to follow a hard splitting, rather than a soft large angle constituent (making it similar to the k_T case). The removal of tracks by the grooming procedure also results in more two-tracked jets, which have a $\tau_2 = 0$ value.

The τ_2 distributions measured for all four algorithms exhibit a mild $p_T^{jet,ch}$ dependence due to the collimation of high $p_T^{jet,ch}$ jets, similar to the case of τ_1.

4.2.4 τ_2/τ_1

The τ_2/τ_1 variable is calculated by dividing the measured τ_2 and τ_1 values for each jet. The raw level results for the τ_2/τ_1 jet shape are shown in figure 4.8, for each reclustering algorithm

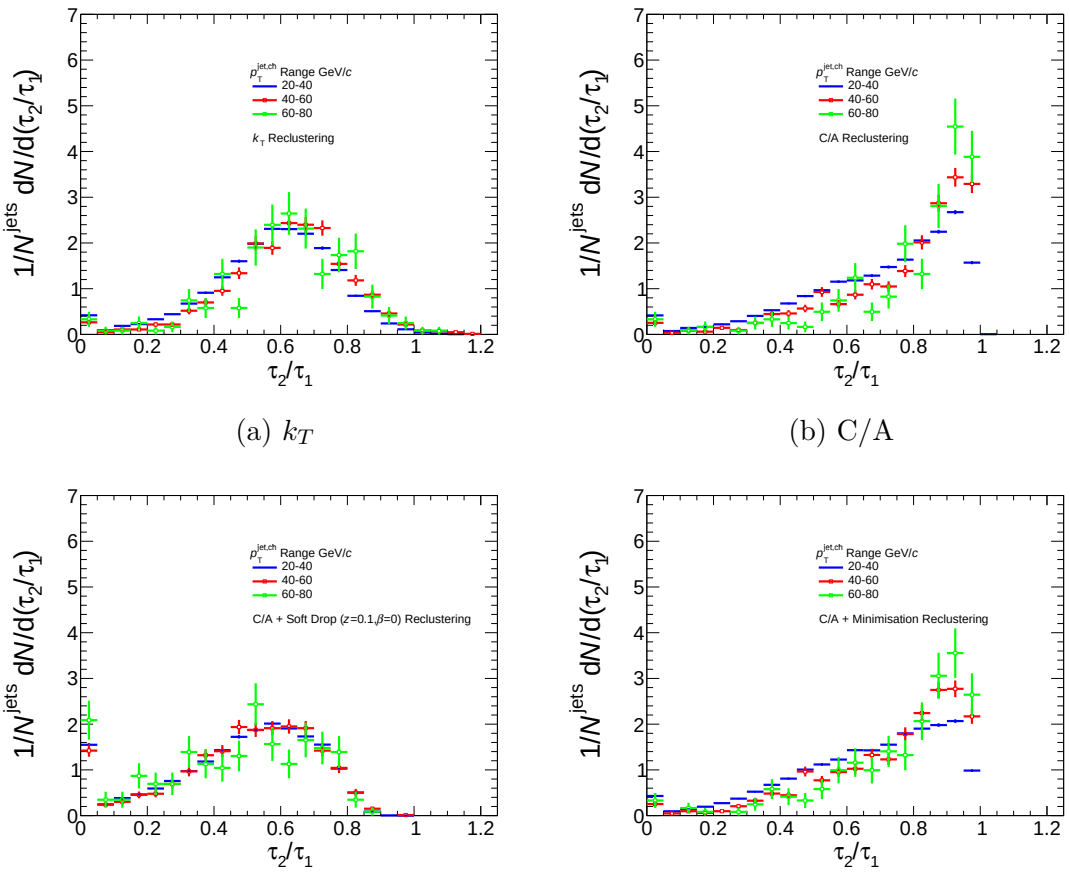

(a) k_T (b) C/A

(c) C/A + soft drop (d) C/A + minimisation

Figure 4.8: The uncorrected τ_2/τ_1 jet shapes are shown in three differential $p_T^{jet,ch}$ bins, for each reclustering algorithm.

As explained in section 4.2.3, the τ_2/τ_1 distributions for the k_T and C/A algorithms differ greatly, even though their τ_1 and τ_2 distributions look visually similar. For

the k_T case, the algorithm shows a sensitivity to two-prong substructure and peaks at ~ 0.6, since most QCD jets are single-core. The distribution peaks at a value lower than unity, due to the algorithms sensitivity to two-core jets and substructure within the core of single-core jets. For the C/A case, the distribution peaks at close to unity, since the values for τ_1 and τ_2 are very similar for the majority of single-core jets and the algorithm shows no sensitivity to the p_T scale of the substructures.

The minimisation procedure has very little impact on the distribution obtained with the C/A algorithm. For the case of C/A with soft drop, the effects of the the grooming procedure are large and the resulting τ_2/τ_1 distribution is very similar to the k_T case. This confirms that the soft drop procedure enables the C/A algorithm to pick out hard splittings in the jet and increases its sensitivity to hard substructures.

4.3 MC Response

4.3.1 Truth and Detector Level Simulations

The MC response used in the unfolding procedure (see section 2.4.2), is constructed at two levels: truth (particle level) and reconstructed (detector level). The truth level is constructed by simulating PYTHIA tune A (see section 6.1.1.2) events, at $\sqrt{s} = 7$ TeV, in ten p_T hard bins. p_T hard bins are sets of simulated events where the Q^2 of the parton interactions are controlled. Truth level events include primary particles and the daughters from strong and electromagnetic decays. However, they do not include the secondaries from interactions in the detector material or the daughters of weak decays of strange hadrons. Jet finding is performed on the events, using the anti-k_T algorithm, with a $p_T^{jet,ch} \leq 160$ GeV/c cut imposed.

The truth level events are passed through a reconstruction of the ALICE detector

using GEANT4 [119, 120] (GEANT4 simulates the passage of particles through matter), incorporating detector effects, to obtain the detector level events. These events also include secondaries from interactions in the detector material and weak decay daughters. The same experimental cuts used in data are applied at detector level as well. Jet finding is performed on these events, using the anti-k_T algorithm, with a cut of $p_T^{jet,ch} \geq 10$ GeV/c imposed. Corresponding truth and detector level jets in each event are geometrically matched. Only successfully matched jets enter the response. Jet shapes are then calculated at truth and detector levels for these matched jets, to obtain the truth and detector level distributions respectively.

The list of p_T hard bins used in this analysis is: $5-11$, $11-21$, $21-36$, $36-57$, $57-84$, $84-117$, $117-152$, $152-191$, $191-234$ and $234-1000$ GeV/c (from here on the p_T hard bins will be numbered from 1 to 10 according to this list). The final truth and detector level distributions are obtained by merging the p_T hard bins with appropriate weights (see below), to account for their differing interaction cross sections.

4.3.2 Cross Section Weights

The weight for each p_T hard bin is calculated using the following procedure. PYTHIA provides the interaction cross section, σ_{Trial}, for a $Trial$ in each p_T hard bin. A $Trial$ is defined as a PYTHIA event generated in a specific p_T hard bin. However, not all $Trials$ produce jets that appear within the detector acceptance. $Events$ are defined as $Trials$ which produce jets within the detector acceptance limits. The cross section per $Event$ can be written as,

$$\sigma_{Event} = \frac{\sigma_{Trial}}{(N_{Trials}/N_{Events})}. \tag{4.1}$$

The σ_{Event} for each p_T hard bin is normalised by the number of *Events* generated in that bin, resulting in the final weight as given by,

$$weight = \frac{1}{N_{Events}} \frac{\sigma_{Trial}}{(N_{Trials}/N_{Events})} = \frac{\sigma_{Trial}}{N_{Trials}}. \tag{4.2}$$

The weights calculated in this work, in order of increasing p_T hard bin, are shown in table A.1.

The $p_T^{jet,ch}$ distributions at particle level are shown for each p_T hard bin in figure 4.9. The effect of the weighting in adjusting the contribution of each p_T hard bin is highlighted. The weighting reduces the contribution of the higher p_T hard bins, in line with their significantly lower interaction cross sections.

4.3.3 Merged $p_T^{jet,ch}$

The final truth and detector level $p_T^{jet,ch}$ distributions, obtained by merging the weighted p_T hard bins, are shown in figure 4.10. Two main detector effects contribute to the differences observed between the two levels. The dominant effect [121] arises due to the finite tracking efficiency (see section 3.4), which means that there is a finite probability that a truth level particle is not reconstructed at detector level. This shifts the detector level distribution towards lower values. The second effect is due to the finite charged track p_T resolution [122], which means that a track can be reconstructed with an incorrect p_T^{ch}. This can shift the detector level $p_T^{jet,ch}$ distribution in either direction.

Figure 4.11 highlights these detector effects. Figure 4.11a shows the detector level $p_T^{jet,ch}$ distributions, for given bins of truth level $p_T^{jet,ch}$. The detector level distributions peak at the corresponding truth level values, with tails extending in either

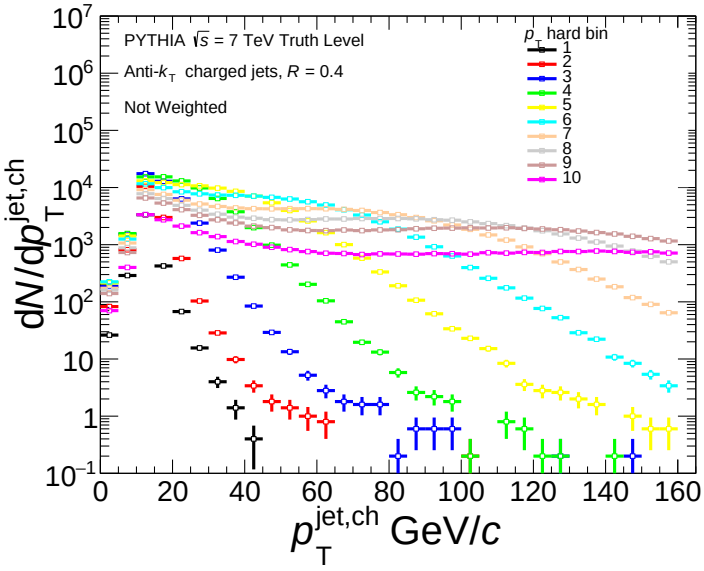

(a) Not Weighted

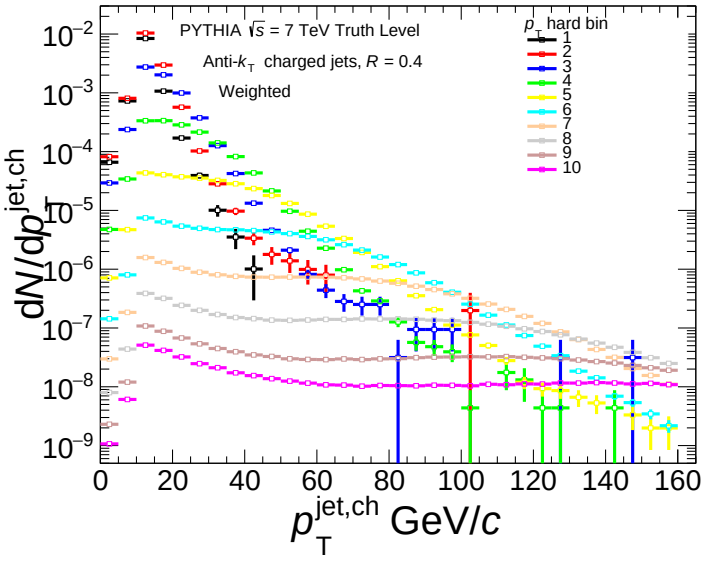

(b) Weighted

Figure 4.9: The unweighted (a) and weighted (b) $p_T^{jet,ch}$ distributions are shown for each p_T hard bin.

direction. The tails to the left of the peak fall less steeply than the tails on the right, indicating that a jet is more likely to be reconstructed with a lower $p_T^{jet,ch}$ due to detector effects, than a higher one. Since the effects of the finite charged track p_T resolution on the $p_T^{jet,ch}$ distributions are equal in either direction [121], the much larger tails to the left show that the tracking efficiency is indeed the dominant effect.

Figure 4.11b shows the fractional $p_T^{jet,ch}$ change, between particle and detector level jets. The distribution peaks at -0.030 due to the effects of tracking efficiency. The $p_T^{jet,ch}$ resolution can be extracted by calculating the standard deviation of this distribution, which is 11.6%. This is in agreement with previous studies [121].

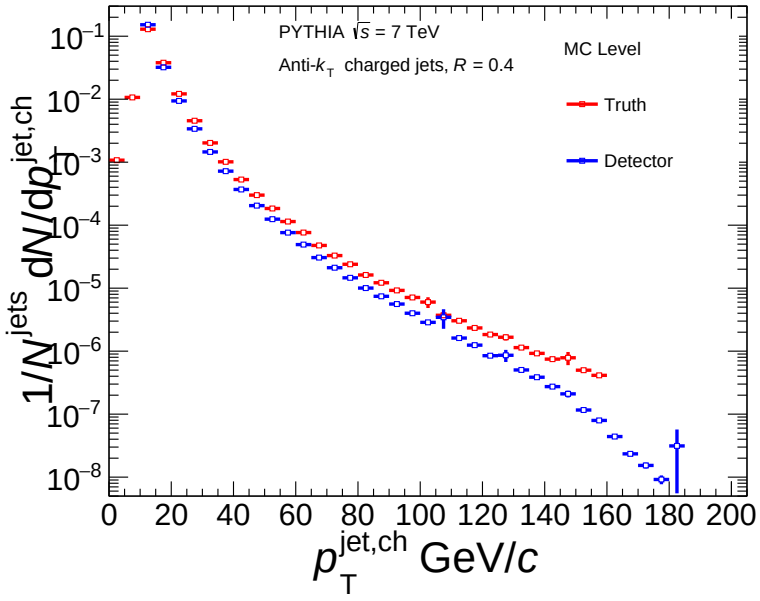

Figure 4.10: The truth and detector level $p_T^{jet,ch}$ distributions are shown.

4.3.4 ΔR

The ΔR distributions at truth and detector levels are shown in figure 4.12, for each reclustering algorithm. The corresponding truth and detector level distributions are similar across all four algorithms, suggesting that only small corrections will be needed from the unfolding procedure (see section 2.4). For the k_T algorithm, the detector effects shift the shape to slightly higher values. This is caused by the loss of tracks in the jet core, due to the finite tracking efficiency, which pushes the returned axes further apart. The likelihood of losing a track in the core, compared to tracks situated at larger angles in the jet, is higher due to the higher number of tracks in the core. Additionally, the algorithm is largely insensitive to the loss of soft large

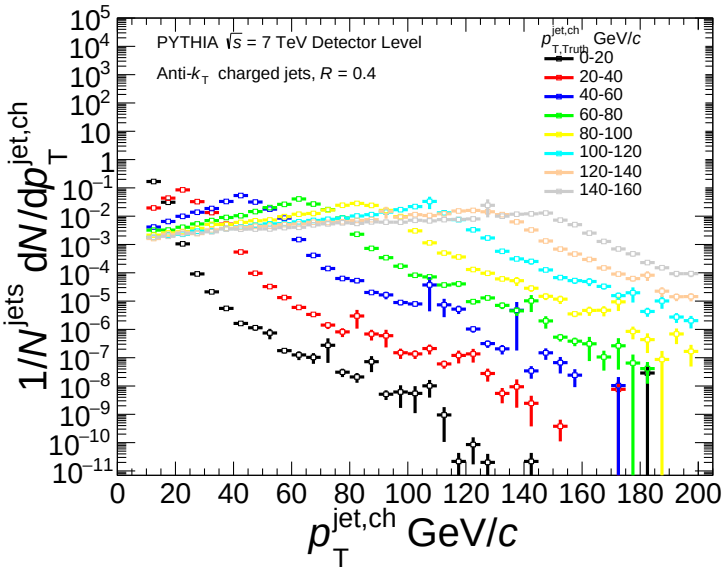

(a) The detector level $p_T^{jet,ch}$ distributions are shown for differential truth level $p_T^{jet,ch}$ bins.

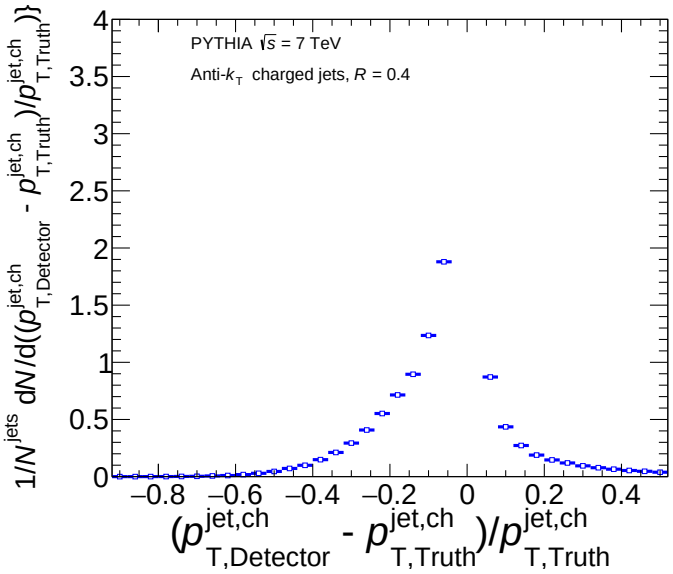

(b) The fractional difference in detector and truth level $p_T^{jet,ch}$ is shown.

Figure 4.11: Detector effects on $p_T^{jet,ch}$

angle tracks, due to the p_T dependence of its clustering.

For the C/A algorithm, the detector effects shift the ΔR shape to lower values. This can also be explained by the finite tracking efficiency. Since the C/A algorithm has

no p_T dependence in its clustering procedure, one axis will often remain in the jet core whilst the second is pulled out to the furthest track in the jet. Loss of tracks in the jet core will not alter the returned axes significantly. However, loss of the furthermost track will result in a modification of the second axis and a lowered ΔR value at detector level.

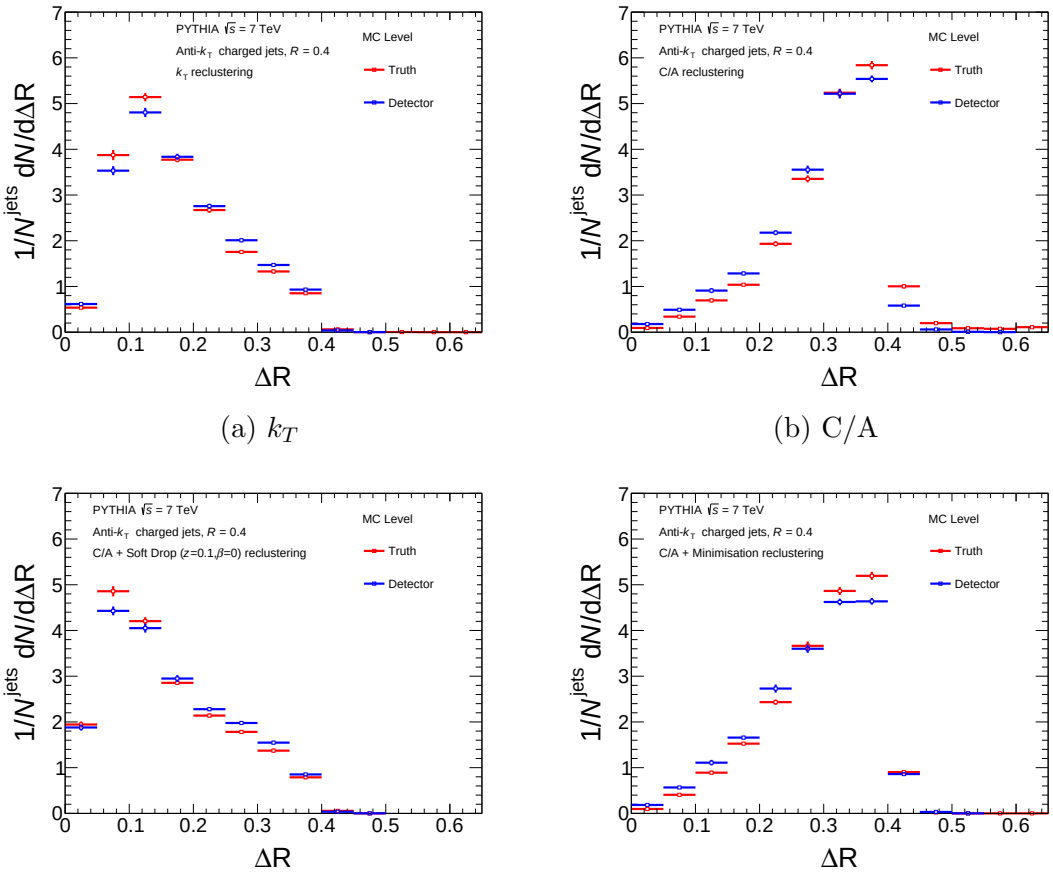

(a) k_T (b) C/A

(c) C/A + soft drop (d) C/A + minimisation

Figure 4.12: The truth and detector level ΔR distributions are shown for each reclustering algorithm, at $40 \leq p_{T,Truth}^{jet,ch} < 60$ GeV/c.

The minimisation procedure does not effect the trend seen with the C/A algorithm. However, the soft drop procedure changes this trend to a similar one as observed in the k_T case. This is also due to the finite tracking efficiency. Loss of tracks in the jet core lower the $p_T^{jet,ch}$ at detector level compared to the truth level. As a consequence, clusters at large angles from the core will carry a larger percentage of the overall

$p_T^{jet,ch}$ at detector level. Therefore, compared to their truth level counterparts, they are more likely to survive the soft drop grooming procedure. In this way, there are more tracks at large angles at detector level than at particle level for the C/A algorithm to pick out. This causes the axes (ΔR) at detector level to be separated further than at particle level.

4.3.5 τ_2/τ_1

The τ_2/τ_1 distributions at truth and detector levels are shown in figure 4.13, for each reclustering algorithm. Similar to the case for ΔR, the corresponding truth and detector level distributions for τ_2/τ_1 are similar across all four algorithms, suggesting that the unfolding procedure will only need to apply small corrections. Loss of tracks due to the finite tracking efficiency at detector level, moves the returned axes closer to the remaining tracks in the jet. This reduces the contribution of these tracks to the τ_2 variable, more than their contribution to τ_1. This translates as a shift of the detector level τ_2/τ_1 distributions to lower values, for all four algorithms. Additionally, the loss of tracks due to the finite tracking efficiency increases the number of two-tracked jets, which have a $\tau_2/\tau_1 = 0$ value.

4.3.6 Response Matrices

The response matrices used for the unfolding procedures, are four-dimensional objects constructed from the truth and detector level simulations. Their dimensions are the $p_T^{jet,ch}$ and jet shape, at both the truth and detector levels. Jets matched at truth and detector levels, form the entries into the response matrices. Due to the complexities in visualising four-dimensional objects, two-dimensional projections of the $p_T^{jet,ch}$, ΔR and τ_2/τ_1 axes (at truth and detector level) of the response matrices

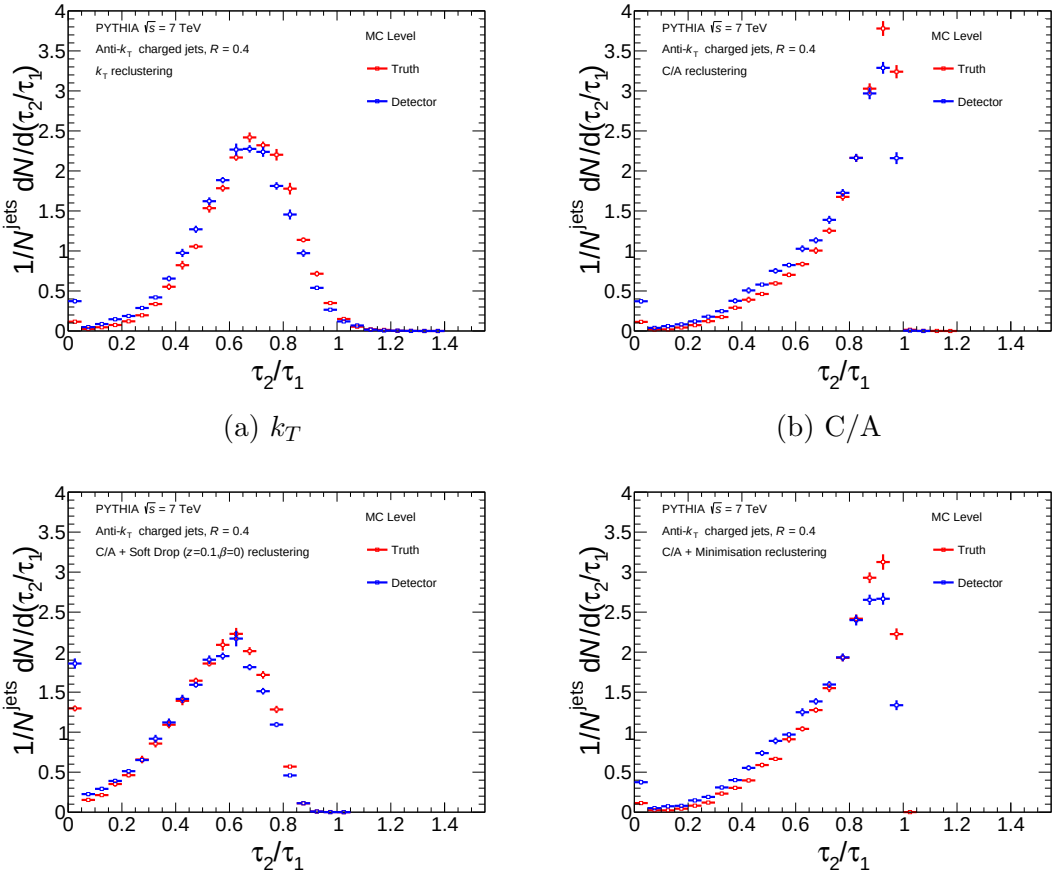

(a) k_T (b) C/A

(c) C/A + soft drop (d) C/A + minimisation

Figure 4.13: The truth and detector level τ_2/τ_1 distributions are shown for each reclustering algorithm, at $40 \leq p_{T,Truth}^{jet,ch} < 60$ GeV/c.

are shown in figures 4.14, 4.15 and 4.16 respectively. The clear diagonal correlations between truth and detector levels for all three variables, emphasise that only small corrections are expected via the unfolding procedure.

It should be noted that the exact mapping between truth and detector levels in each response matrix, is to some extent influenced by the choice of MC used to generate the truth level. A complete study should therefore reproduce the response matrices using a variety of different event generators and evaluate the differences on the unfolding procedure. However, the framework available for this analysis did not permit the use of any MC generators other than PYTHIA 6. This work has attempted to partially remedy this by reweighing the response matrices when

evaluating the prior systematic (see Appendix B.4).

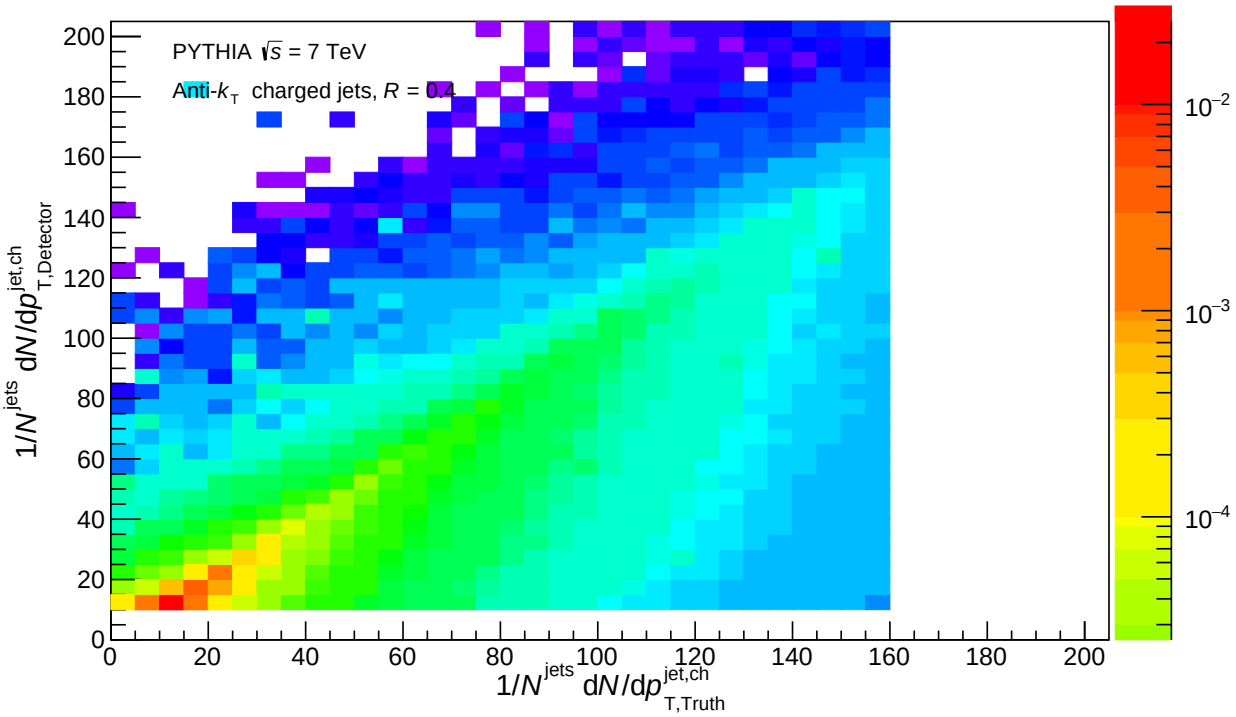

Figure 4.14: The two-dimensional projections of the truth vs detector level $p_T^{jet,ch}$ components of the response matrix are shown.

4.4 Unfolding

The unfolding procedure corrects the measured raw data for detector effects, as described in section 2.4. The ingredients used for unfolding are the raw $p_T^{jet,ch}$ and jet shapes as shown in sections 4.1 and 4.2, along with the response matrices constructed in section 4.3.6.

4.4.1 Raw Data Statistics

The raw data are inputted as 2D distributions of $p_T^{jet,ch}$ and jet shape. These input matrices are required to be rectangular, with all bins containing counts (no empty

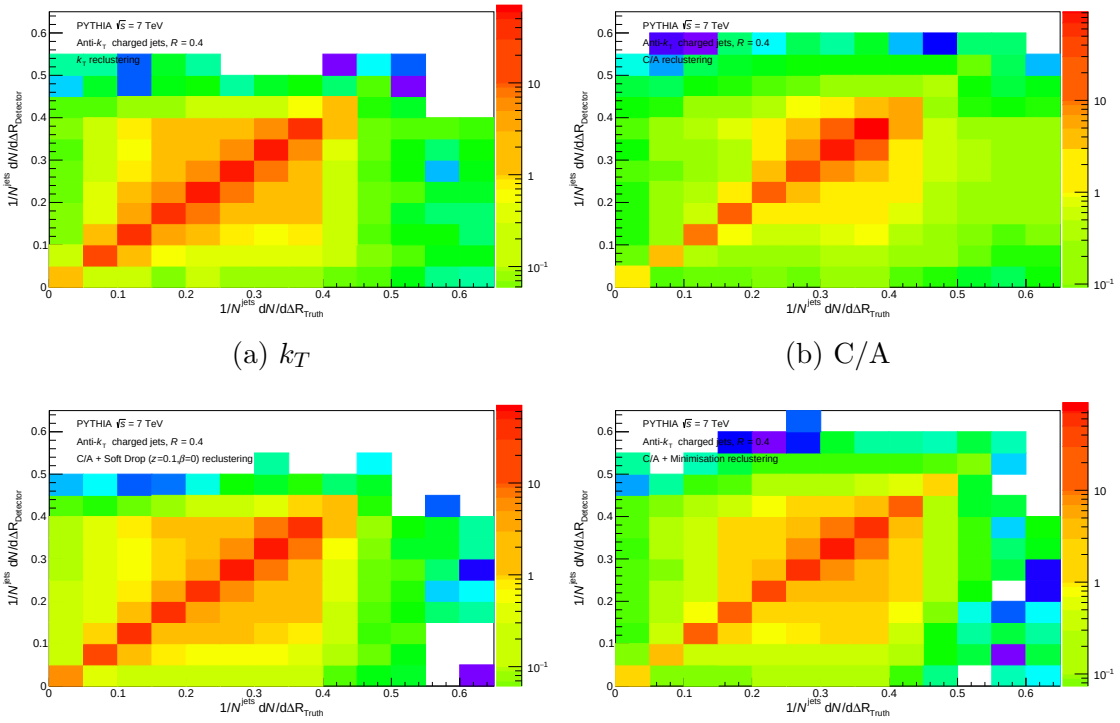

(a) k_T (b) C/A

(c) C/A + soft drop (d) C/A + minimisation

Figure 4.15: The two-dimensional projections of the truth vs detector level ΔR components of the response matrices are shown, for each reclustering algorithm.

bins). Under the rules of matrix multiplication, this binning should be mirrored by that of the detector level quantities in the response matrix.

The input ranges for the $p_T^{jet,ch}$ and ΔR shape are $20-80$ GeV/c and $0-0.5$ respectively. The input ranges for the τ_2/τ_1 jet shape vary for each reclustering algorithm, whilst the $p_T^{jet,ch}$ ranges remain at $20-80$ GeV/c. The τ_2/τ_1 ranges are $0-1.2$, $0.2-1.0$ and $0-0.9$ for the k_T, C/A and soft drop with C/A reclustering respectively. The C/A with minimisation case keeps the same binning as the default C/A. The raw input matrices are shown in statistical form in figures 4.17 and 4.18, for the unfoldings involving ΔR and τ_2/τ_1 respectively.

To ensure the counts in each bin are statistically significant, it is usual to require that at least ten counts per bin are supplied as input to the unfolding. However, this analysis is exploring and pushing the statistical reach of the data sets available

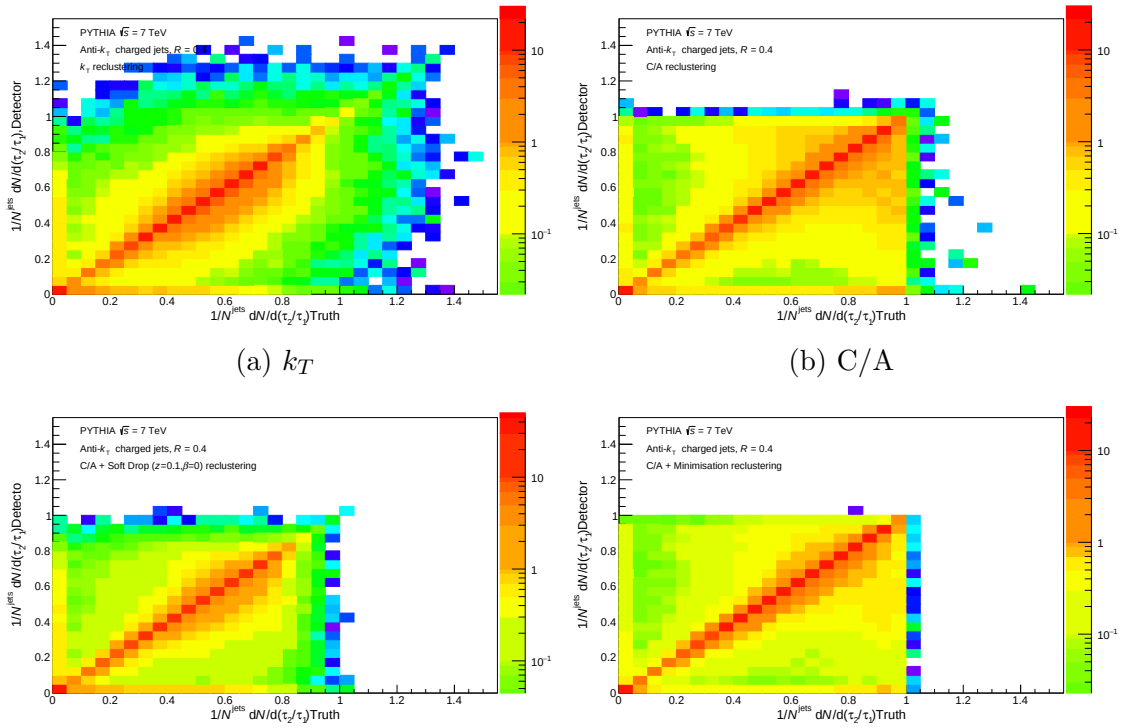

(a) k_T (b) C/A

(c) C/A + soft drop (d) C/A + minimisation

Figure 4.16: The two-dimensional projections of the truth vs detector level τ_2/τ_1 components of the response matrices are shown, for each reclustering algorithm.

at the ALICE experiment, by extending the jet resolution to $R = 0.4$ and slicing the data in two dimensions of $p_T^{jet,ch}$ and shape. Therefore, the analysis is continued to the unfolding stage, noting the lack of usual statistics in some bins. Unfolding tests will be used to determine the stability and validity of the final results.

4.4.2 Efficiency Correction

The measured data sample entered into the unfolding procedure, is limited in its $p_T^{jet,ch}$ and shape ranges due to statistical constraints. The entries into the response matrix must mirror these ranges (cuts) at detector level. In addition to migrations between truth and detector level bins within these ranges, the unfolding accounts for entries in truth level bins outside these cuts which end up within these ranges at detector level. However, unfolding cannot account for jets that have truth level

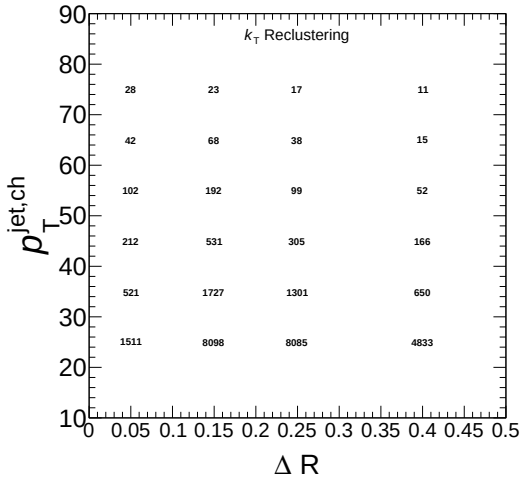

(a) k_T

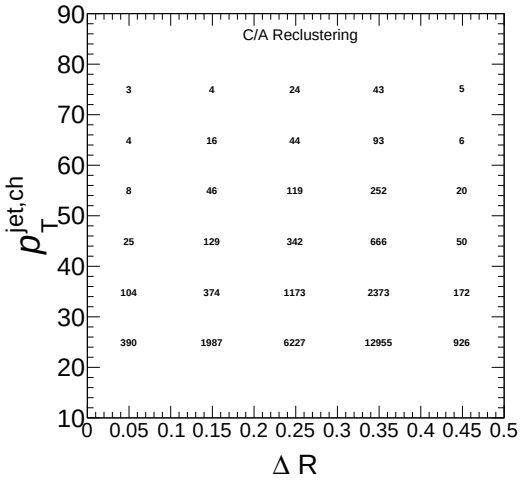

(b) C/A

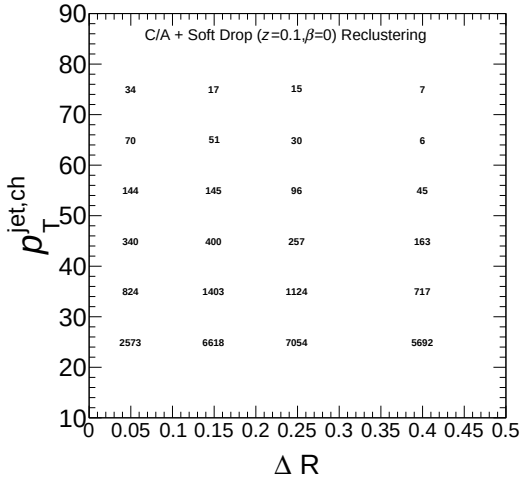

(c) C/A + soft drop

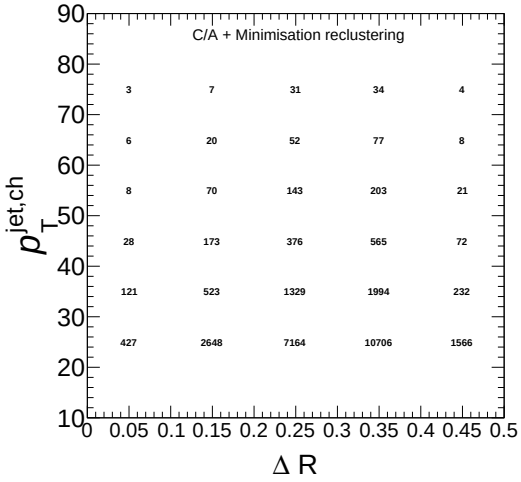

(d) C/A + minimisation

Figure 4.17: The raw data input matrices are shown in statistical form, in differential bins of $p_T^{jet,ch}$ and ΔR, for each reclustering algorithm.

values inside these cuts but are migrated out of these ranges due to detector effects, since they are not part of the response matrix. A separate efficiency correction is applied to the final unfolded solution, to account for these jets.

This efficiency correction is calculated for each bin, by taking the ratio of truth level distributions, measured for jets with and without the above cuts applied at their detector level. This produces the fraction of counts in each bin, at truth level, whose

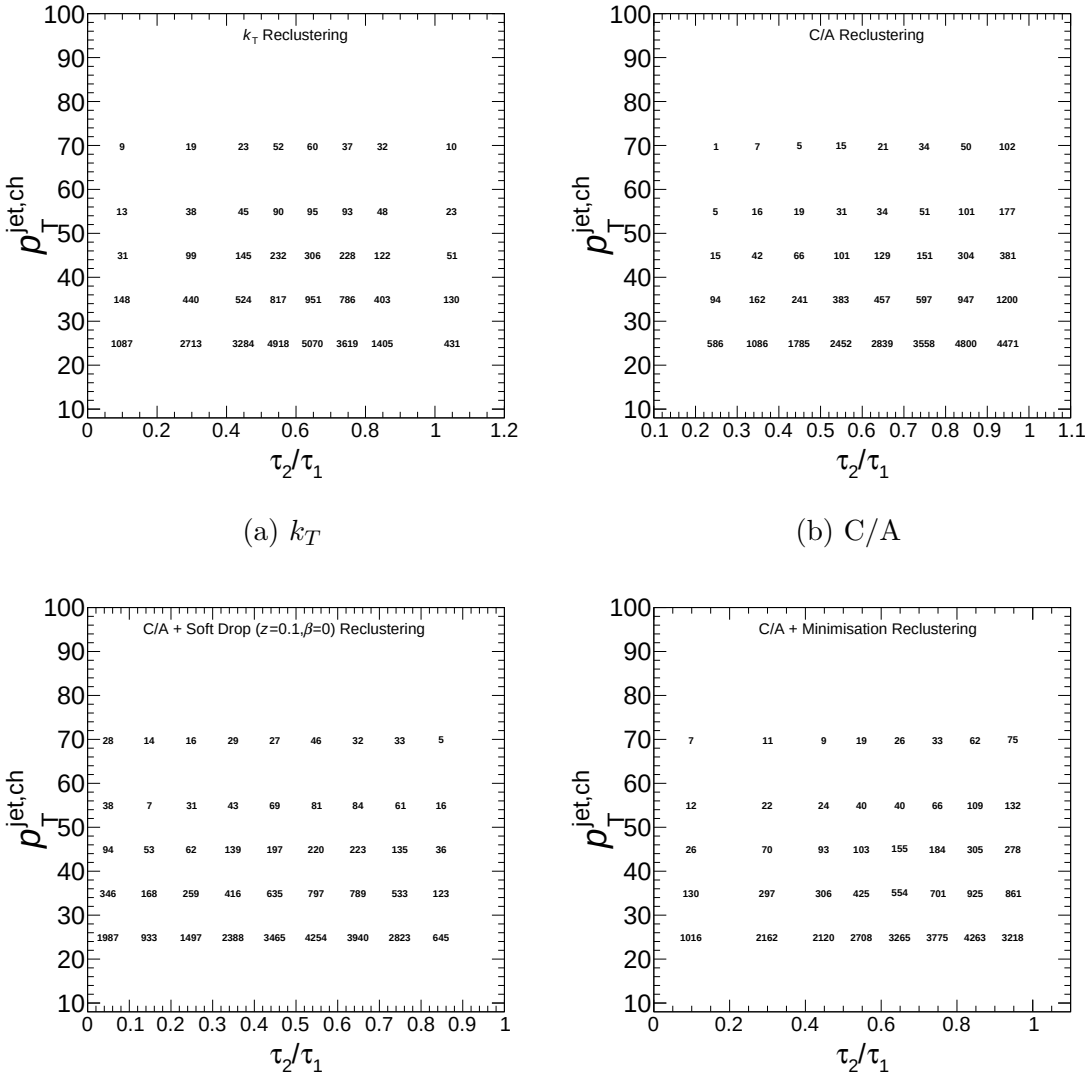

(a) k_T (b) C/A

(c) C/A + soft drop (d) C/A + minimisation

Figure 4.18: The raw data input matrices are shown in statistical form, in differential bins of $p_T^{jet,ch}$ and τ_2/τ_1, for each reclustering algorithm.

detector level values were within the detector level cuts. The unfolded result is then divided by this distribution, to obtain the final fully corrected result.

The calculated efficiency distributions are shown in figures 4.19, 4.20 and 4.21 for the $p_T^{jet,ch}$, ΔR and τ_2/τ_1 variables respectively. Since the final results of this work will be presented in bins of jet shape, only the shape efficiencies are applied. However, it is important to ascertain that the $p_T^{jet,ch}$ efficiency correction for the presented $40 \leq$

$p_T^{jet,ch} < 60$ GeV/c range, is small. The efficiency correction has a slight reliance on the underlying physics of the simulation package used. Therefore, it is preferred that the corrections are small. However, as can be seen from the figures, this is not always possible; particularly at the boundaries of the detector level cuts, where a larger fractions of the jets can be expected to have migrated out of these ranges.

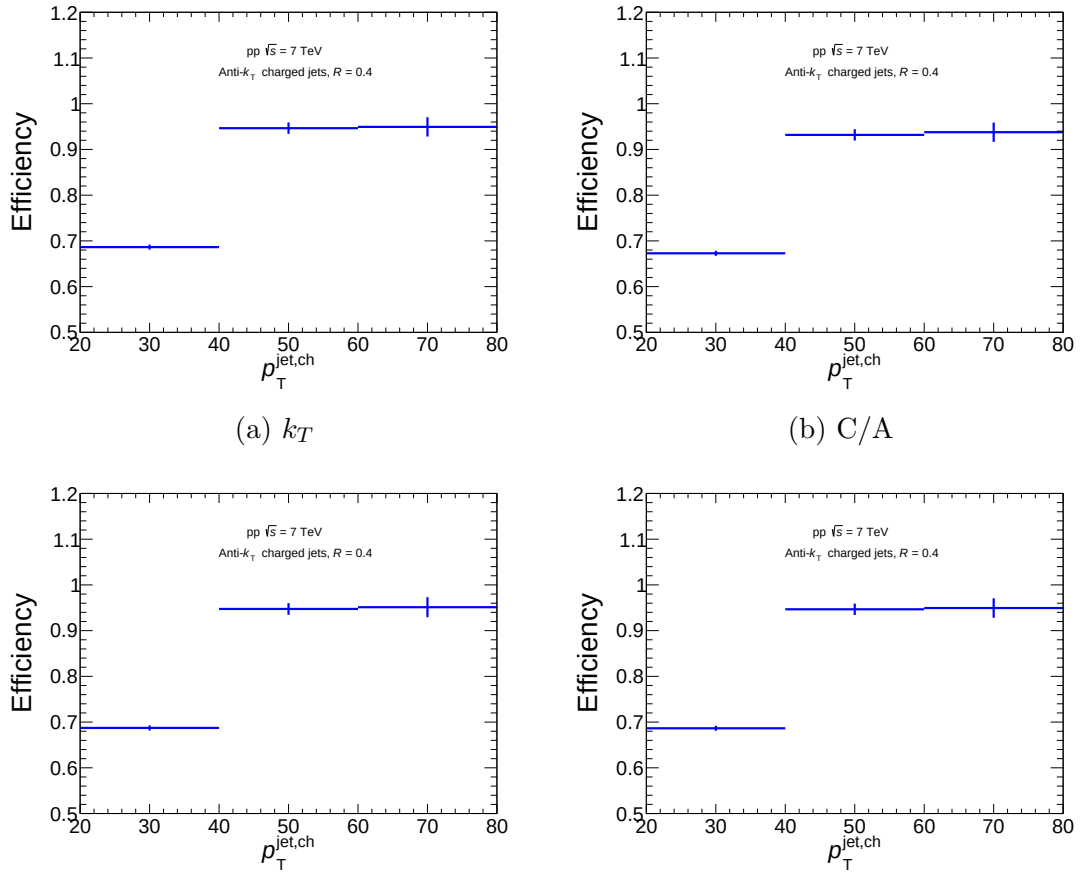

(a) k_T (b) C/A

(c) C/A + soft drop (d) C/A + minimisation

Figure 4.19: The efficiency correction is shown as a function of $p_T^{jet,ch}$, for each reclustering algorithm.

4.4.3 Unfolding Tests

The unfolding procedure requires several iterations, before converging onto a stable (the true) solution. However, each subsequent iteration results in a larger statistical error. Therefore, one of the first converging iterations must be chosen as the final

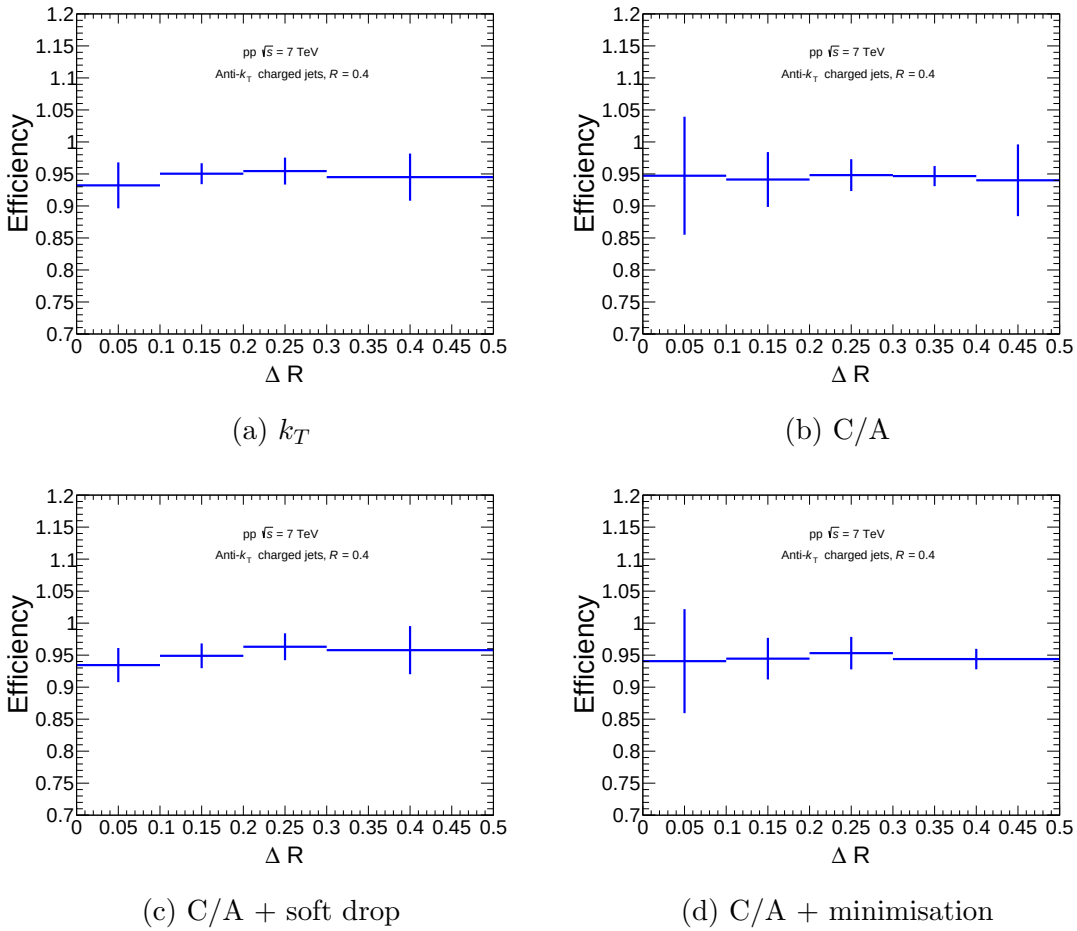

(a) k_T (b) C/A

(c) C/A + soft drop (d) C/A + minimisation

Figure 4.20: The efficiency correction is shown as a function of ΔR, for each reclustering algorithm.

result. A series of tests are devised to chose the best iteration, whilst simultaneously checking that the unfolding procedure is working correctly. Unless otherwise specified, all tests are performed within the unfolded $40 \leq p_T^{jet,ch} < 60$ GeV/c range, which is the range in which the final results are presented. For each test, only the results for the jet shapes are shown. The results for the $p_T^{jet,ch}$ were also calculated and are consistent with that of the shapes. They have therefore been omitted to avoid repetition. The unfolding tests presented in this section, point to the fourth iteration being the iteration of choice for both jet shapes, across all algorithms.

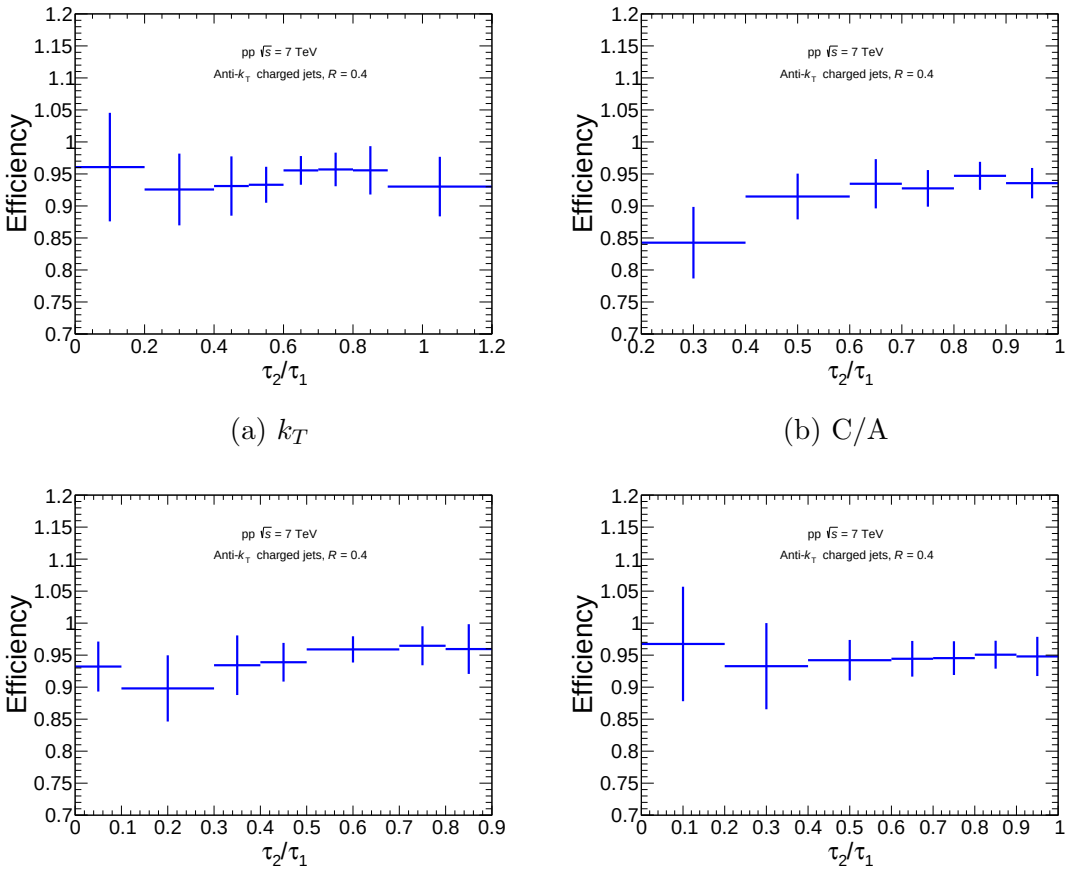

(a) k_T

(b) C/A

(c) C/A + soft drop

(d) C/A + minimisation

Figure 4.21: The efficiency correction is shown as a function of τ_2/τ_1, for each reclustering algorithm.

4.4.3.1 Convergence Test

Convergence tests the stability of the unfolding procedure, by checking if the unfolded iterations quickly converge onto a true solution. Figures 4.22 and 4.23 show the convergence of the different iterations for the ΔR and τ_2/τ_1 jet shapes respectively. All bins converge onto a solution within just a few iterations.

4.4.3.2 Refolding Test

Refolding determines the robustness of the response matrix and the subsequent stability of the unfolding procedure. A stable unfolded solution, obtained using

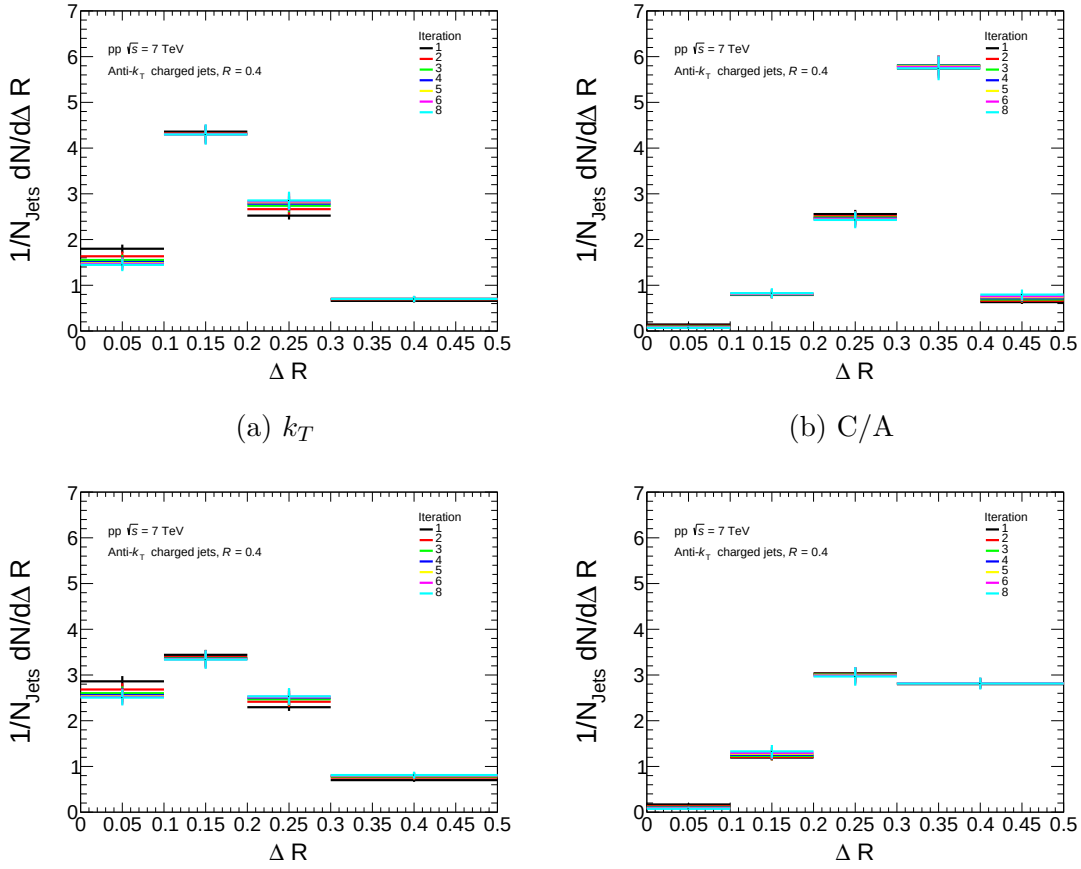

(a) k_T (b) C/A

(c) C/A + soft drop (d) C/A + minimisation

Figure 4.22: The convergence tests for the ΔR jet shape, at $40 \leq p_T^{jet,ch} < 60$ GeV/c, are shown for each reclustering algorithm.

an appropriate response matrix, should be reversible. Folding back an unfolded iteration, using the response matrix, should produce the original input. This folding is performed for each unfolded iteration and the result is compared to the raw input data. Iterations where the ratio of the two distributions are within 10% of unity across all bins, are considered stable. For the ΔR and τ_2/τ_1 jet shapes, the refolding is done for the full input range of $20 \leq p_T^{jet,ch} < 80$ GeV/c. The results are shown in figures 4.24 and 4.25 respectively. The refolding tests are satisfied by the second iteration and converge by the fourth iteration, across all bins.

For the ΔR jet shapes measured using the C/A algorithm, with and without minimisation, the refolding ratios in the last bin show a larger displacement from unity

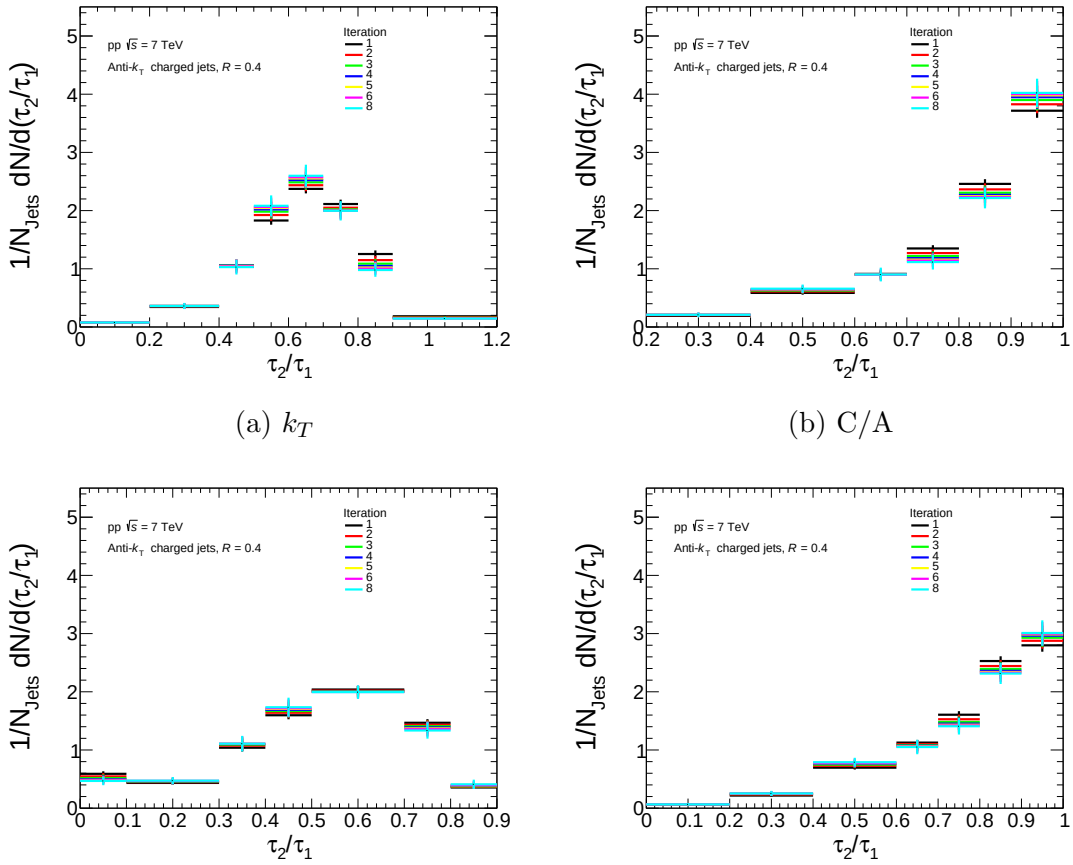

(a) k_T (b) C/A

(c) C/A + soft drop (d) C/A + minimisation

Figure 4.23: The convergence tests for the τ_2/τ_1 jet shape, at $40 \leq p_T^{jet,ch} < 60$ GeV/c, are shown for each reclustering algorithm.

compared to the rest of the bins. This is due to the shape of these ΔR distributions, which show a sudden discontinuity in this region (figure 4.12). This discontinuity, coupled with the lower statistics in these bins, causes this small deviation of the ratios from unity. Given these stipulations, the deviations are considered small enough to be deemed reasonable for a stable unfolding.

4.4.3.3 Closure Test

Closure tests the validity of the unfolding procedure with the given response matrix and statistical reach of the ingredients. MC simulations at detector level are used

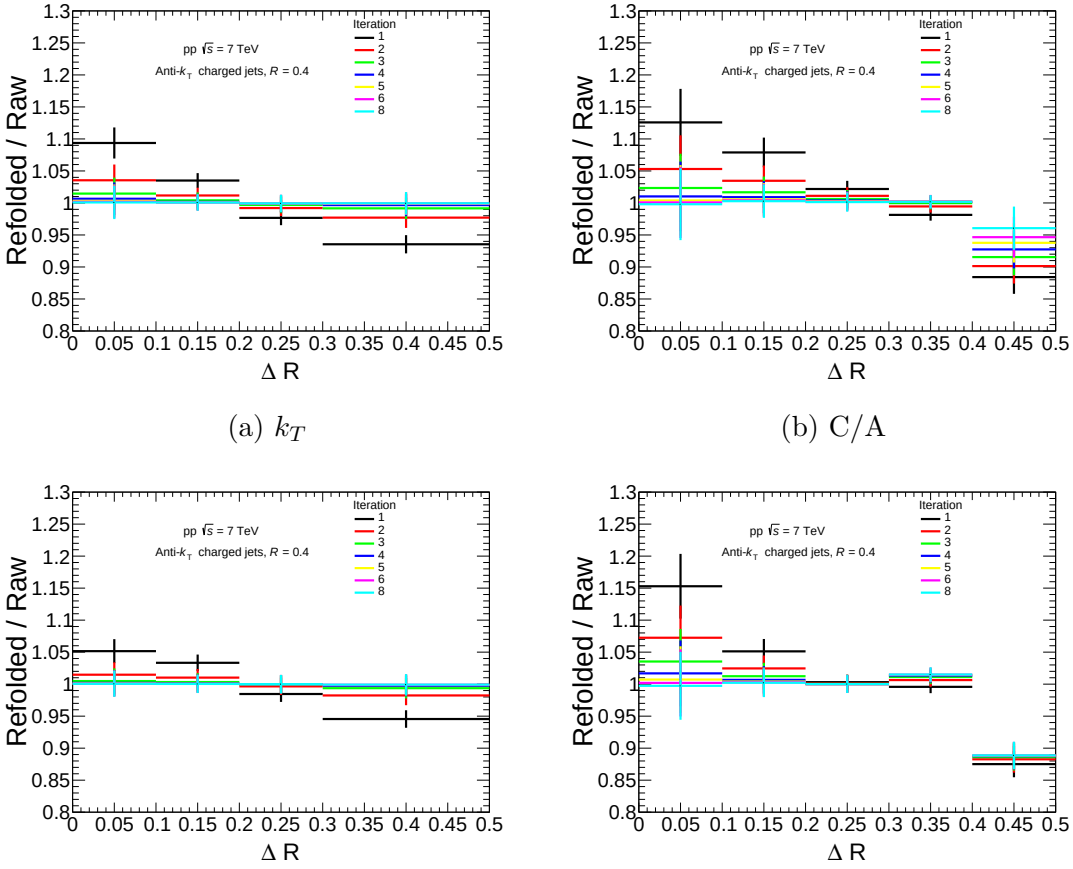

(a) k_T (b) C/A

(c) C/A + soft drop (d) C/A + Minimisation

Figure 4.24: The refolding tests for the ΔR jet shape, at $20 \leq p_T^{jet,ch} < 80$ GeV/c, are shown for each reclustering algorithm.

as the input into the unfolding procedure. Since the truth level for this input is known, it can be compared to the unfolded solution to test the performance of the unfolding.

For the purposes of this test, the MC data are split into two statistically independent sets. 6.5% of the statistics, at detector level, are used as the input into the unfolding procedure. This percentage reflects the statistics available in the raw measured data. The other 93.5% of the statistics are used to construct the response matrix. The unfolding is performed and the solution is compared to the truth level distribution (in the unfolded range) of the initial 6.5% of the statistics. Since the input and response matrix are statistically independent samples, a 10% (of unity) tolerance is

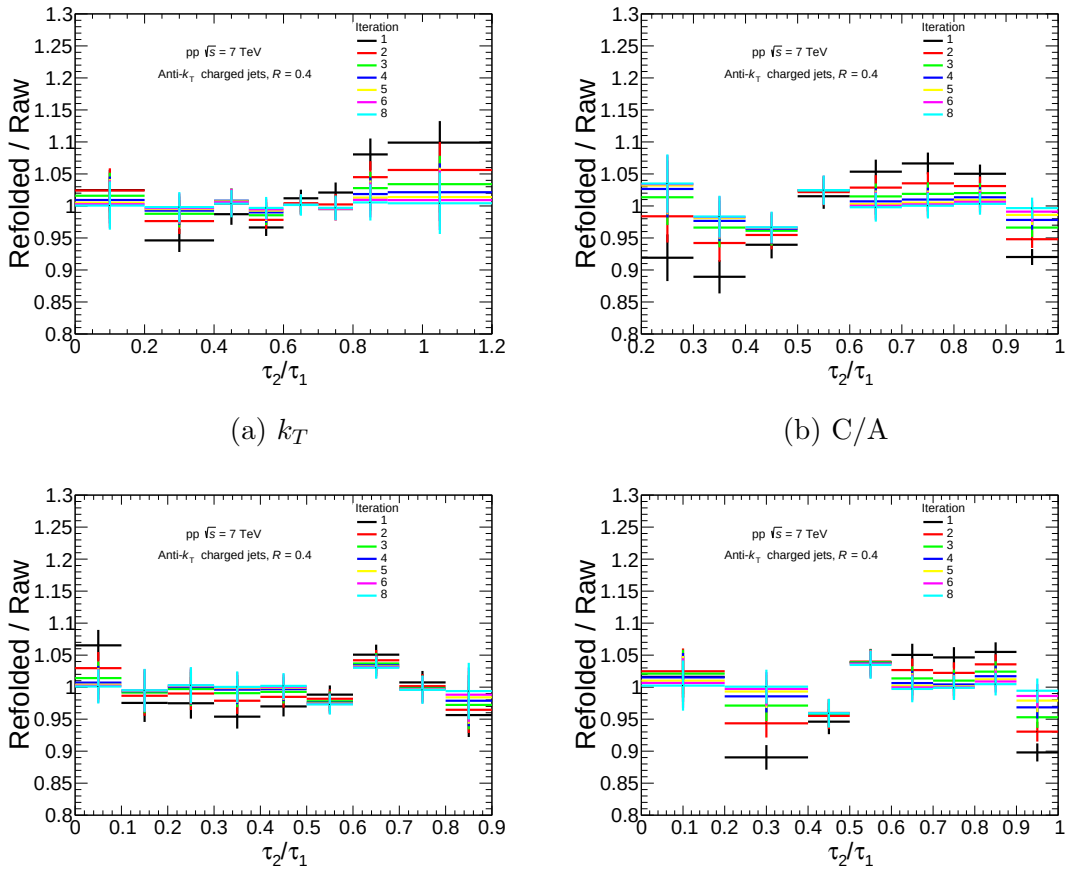

(a) k_T (b) C/A

(c) C/A + soft drop (d) C/A + Minimisation

Figure 4.25: The refolding tests for the τ_2/τ_1 jet shape, at $20 \leq p_T^{jet,ch} < 80$ GeV/c, are shown for each reclustering algorithm.

set for a successful closure, to account for statistical fluctuations. The results of the closure tests are shown in figures 4.26 and 4.27 for the ΔR and τ_2/τ_1 jet shapes respectively. By the third iteration, all bins satisfy the closure test.

4.4.3.4 Pearson's Coefficient

High (past the optimal) iterations of the unfolding can induce large statistical fluctuations, which can in turn cause (anti) correlations between bins. The unfolding procedure is most reliable (best iteration) when there is minimal correlation between different bins. This is also dependent on the diagonality of the response matrix, with

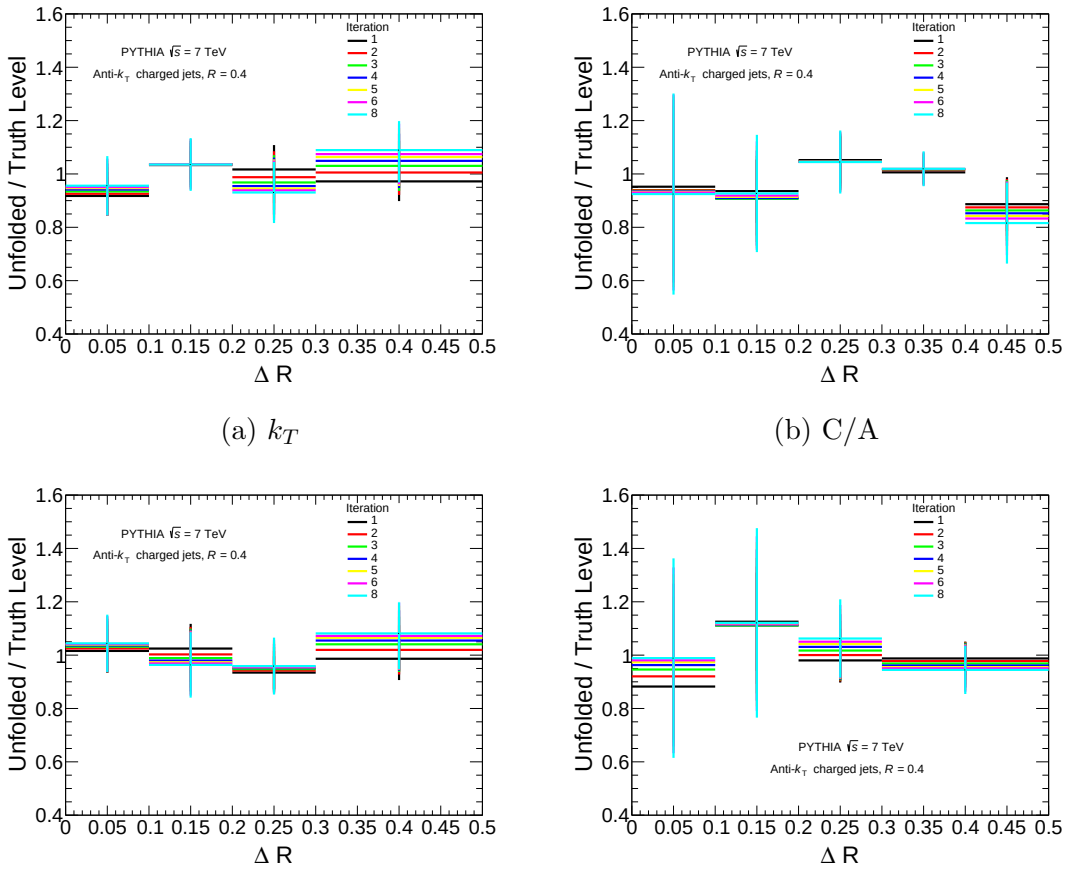

(a) k_T (b) C/A

(c) C/A + soft drop (d) C/A + Minimisation

Figure 4.26: The closure tests for the ΔR jet shape, at $40 \leq p_{T,Truth}^{jet,ch} < 60$ GeV/c, are shown for each reclustering algorithm.

a more diagonal response expected to induce less correlations between unfolded bins.

The bin-by-bin correlations of the chosen unfolding iteration must be tested. The Pearson's coefficient is a measure of the correlation between two bins. To extract this quantity, the covariance matrix from the unfolding is used. The covariance, $\sigma_{X,Y}$, between two bins, X and Y, is defined as the expected product of their deviations from their individual expected values and can be written as,

$$\sigma_{X,Y} = \overline{(X - \overline{X})(Y - \overline{Y})}, \tag{4.3}$$

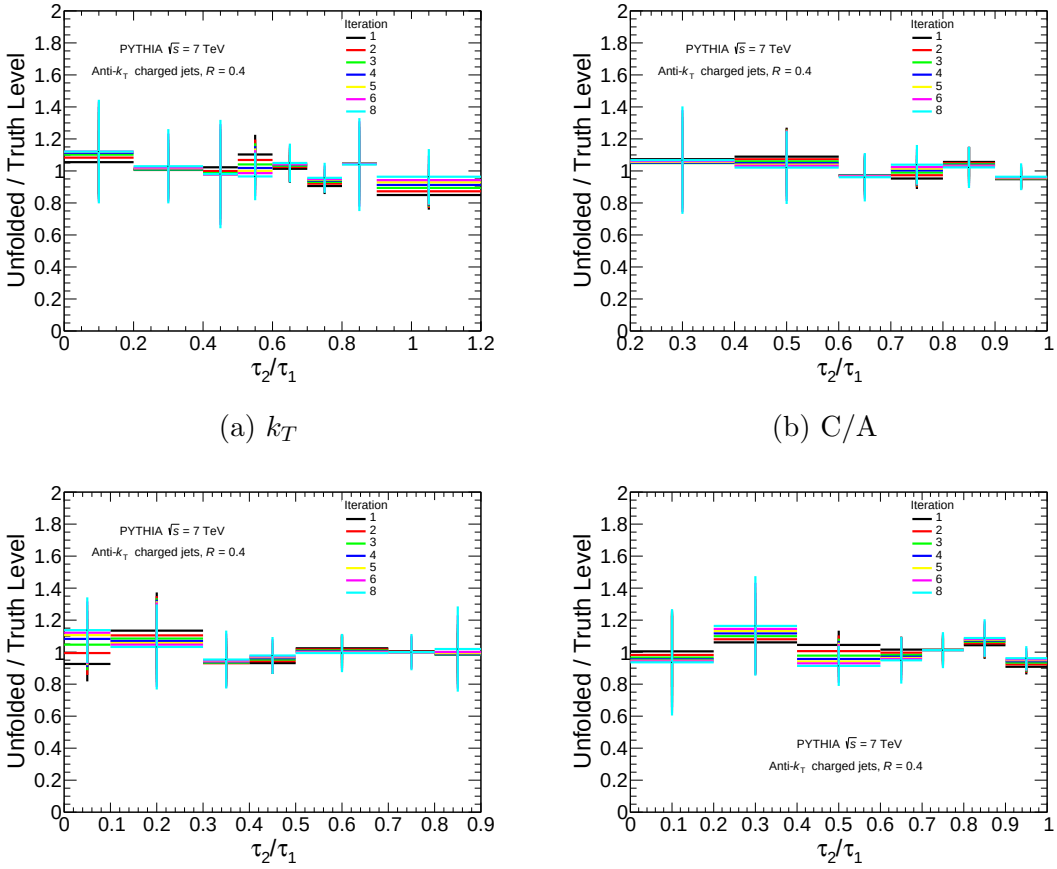

(a) k_T (b) C/A

(c) C/A + soft drop (d) C/A + Minimisation

Figure 4.27: The closure tests for the τ_2/τ_1 jet shape, at $40 \leq p_{T,Truth}^{jet,ch} < 60$ GeV/c, are shown for each reclustering algorithm.

which can can be simplified to

$$\sigma_{X,Y} = \overline{XY} - \overline{X}\,\overline{Y}. \tag{4.4}$$

The Pearson's coefficient between bins X and Y, $\rho_{X,Y}$, can be calculated using the covariance. This is given by,

$$\rho_{X,Y} = \frac{\sigma_{X,Y}}{\sqrt{\sigma_{X,X}\,\sigma_{Y,Y}}}. \tag{4.5}$$

The value of the Pearson's coefficient can be interpreted as follows: +1 shows a maximum positive correlation, −1 shows a maximum negative correlation and 0 shows no correlation. Since the response matrices in pp are diagonal, for each bin in a successful unfolding, very little correlation with other bins is expected.

The results for the calculated Pearson's coefficients, for the fourth iteration of the ΔR and τ_2/τ_1 jet shapes, are shown in figures 4.30 and 4.29 respectively. For the regions in the shapes where input data are provided, the unfolded solutions show very little correlation between off diagonal bins. Diagonal bins exhibit maximum self correlation, as expected.

4.5 Systematic Uncertainties

There are four sources of systematic uncertainty considered in this analysis. These are the tracking efficiency, truncation, prior and regularisation errors. The tracking efficiency error accounts for the event-by-event fluctuations of the tracking efficiency. The truncation systematic investigates the effect of the finite (truncated) range of the input data on the unfolding procedure. The prior error represents the dependence of the unfolding procedure on the underlying simulation package used to construct the response matrix. Regularisation takes into account the effect of the choice of unfolding iteration, selected as the final result. More detailed descriptions of each systematic uncertainty, along with the calculations required to obtain them, are presented in Appendix B. Numerical tables, listing the contribution of each systematic error, can also be found in Appendix B.

To calculate each systematic uncertainty, the unfolding procedure is repeated with a modified response matrix and an alternative unfolded solution is obtained. Each uncertainty is placed (per bin) in either a higher or lower category, depending on

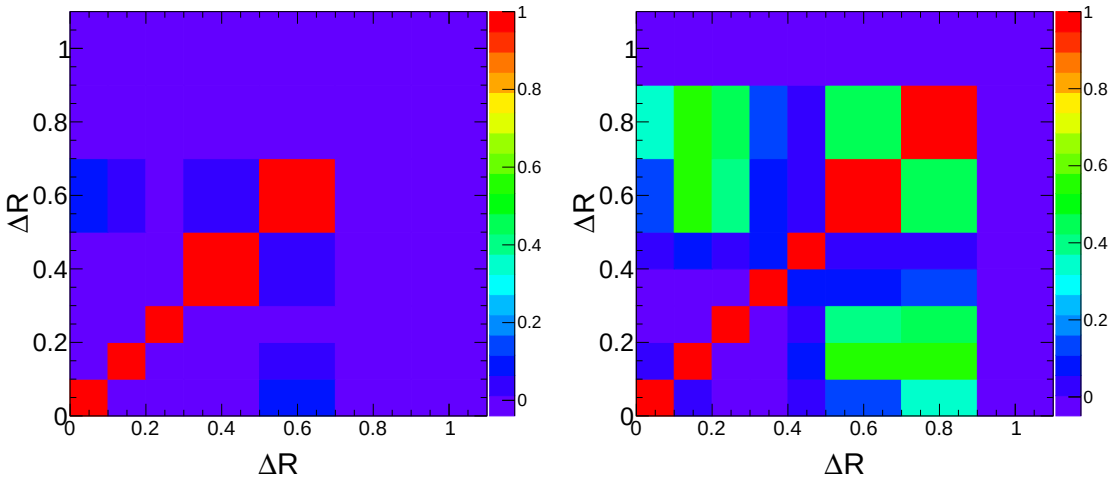

(a) k_T (b) C/A

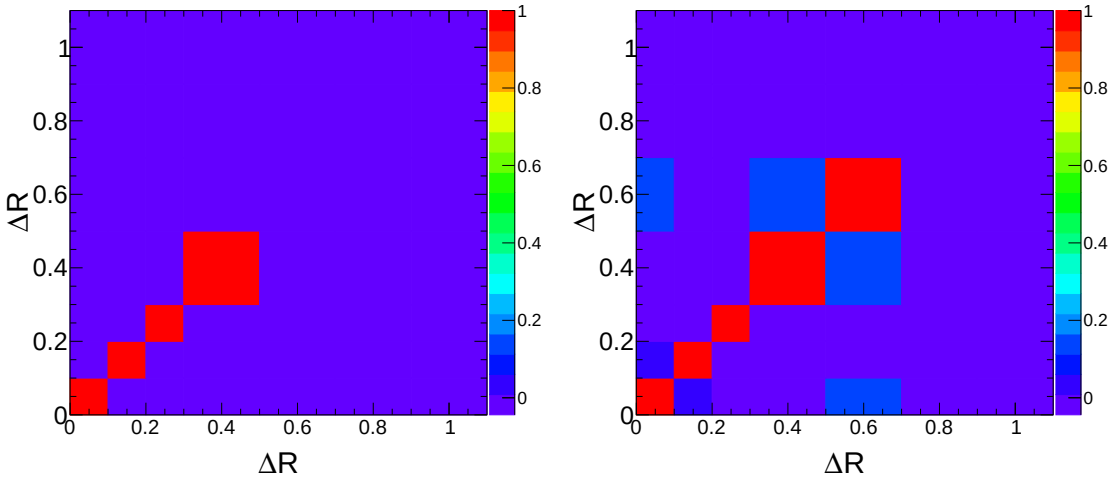

(c) C/A + soft drop (d) C/A + Minimisation

Figure 4.28: The Pearson's coefficients for the ΔR jet shape, at $40 \leq p_T^{jet,ch} < 60$ GeV/c, are shown for the fourth unfolded iteration for each reclustering algorithm.

the relative value of its unfolded solution, compared to the default result. For the systematic uncertainties where two or more separate variations of the error are considered, if the resulting solutions are on different sides of the default solution, they each contribute to the corresponding upper or lower category. However, if they are on the same side of the default solution, only the larger error is considered. The systematic errors in each category (higher or lower) are added in quadrature for each bin, to produce the overall shape (systematic) uncertainty.

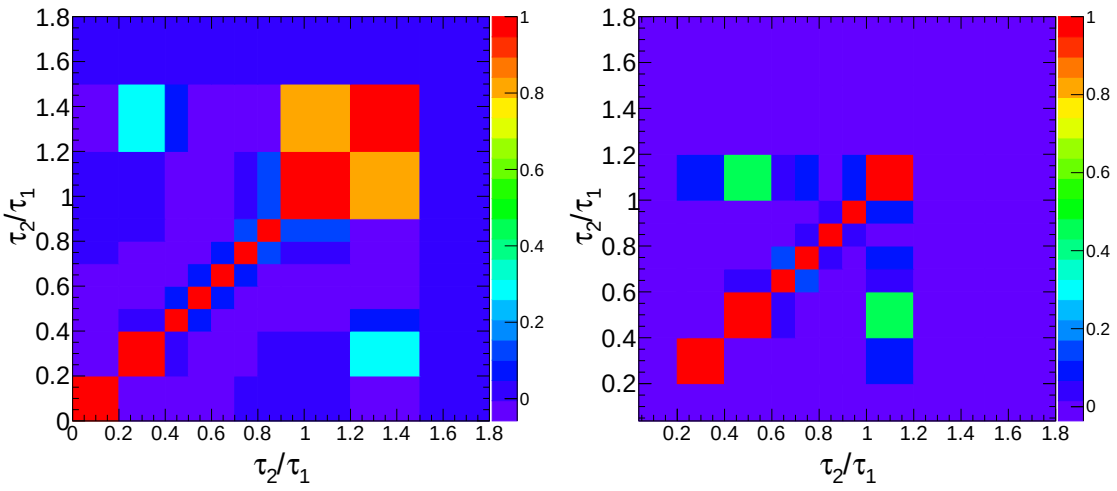

(a) k_T

(b) C/A

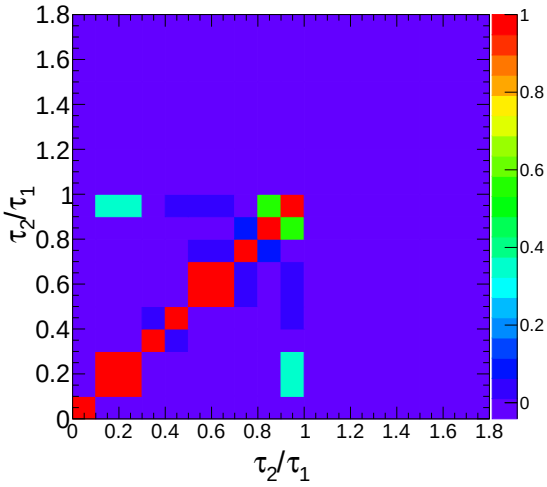

(c) C/A + soft drop

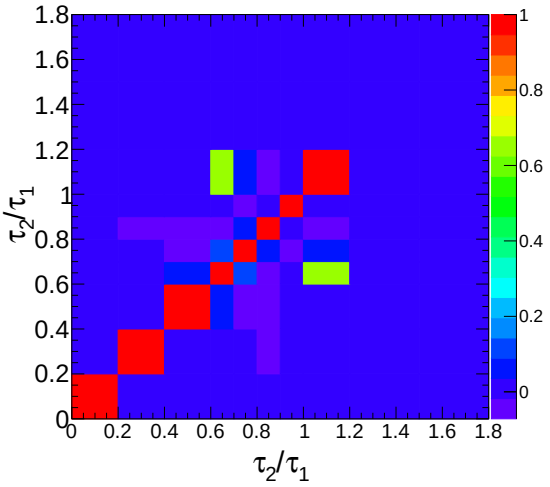

(d) C/A + minimisation

Figure 4.29: The Pearson's coefficients for the τ_2/τ_1 jet shape, at $40 \leq p_T^{jet,ch} < 60$ GeV/c, are shown for the fourth unfolded iteration for each reclustering algorithm.

The relative contributions of each systematic uncertainty, compared to the default solutions, are shown in figures 4.30 and 4.31 for the ΔR and τ_2/τ_1 jet shapes respectively. The contributions of each systematic source vary across bins and algorithms. The tracking efficiency and regularisation uncertainties tend to be the largest sources of systematic error in most bins. In particular, the large tracking efficiency uncertainties can be attributed to the low multiplicity of jets in pp collisions.

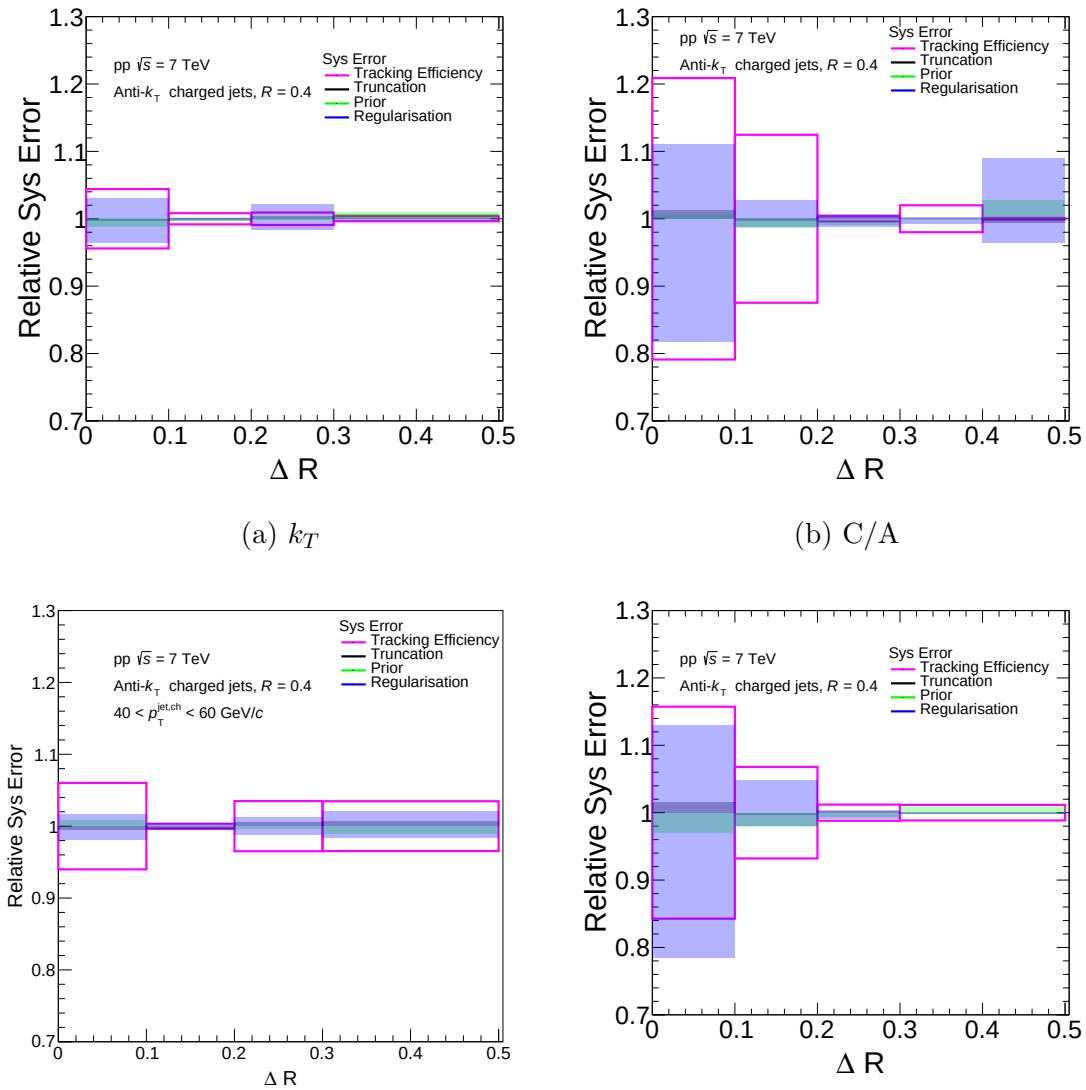

(a) k_T (b) C/A

(c) C/A + soft drop (d) C/A + minimisation

Figure 4.30: The relative contributions of each systematic uncertainty for the ΔR jet shape, at $40 \leq p_T^{jet,ch} < 60$ GeV/c, are shown for each reclustering algorithm.

4.6 pp Results

Throughout the course of this chapter, the analytical steps involved in measuring and unfolding the raw jet shapes have been presented. The final unfolded distributions, with full systematic and statistical uncertainties, are shown in figures 4.32 and 4.33 for the ΔR and τ_2/τ_1 jet shapes respectively. These results are presented at $40 \leq p_T^{jet,ch} < 60$ GeV/c for all four algorithms. These figures also include the

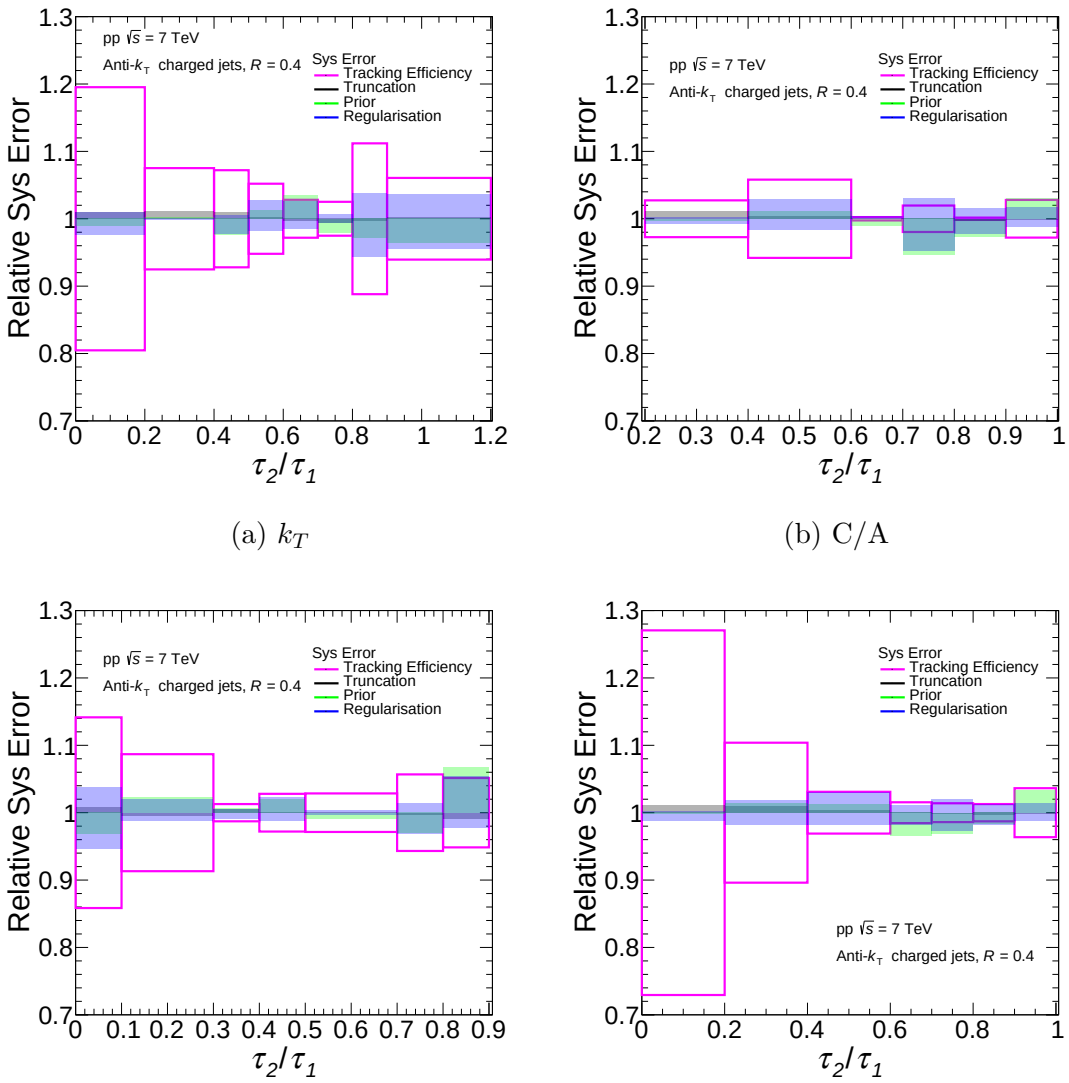

(a) k_T

(b) C/A

(c) C/A + soft drop

(d) C/A + minimisation

Figure 4.31: The relative contributions of each systematic uncertainty for the τ_2/τ_1 jet shape, at $40 \leq p_T^{jet,ch} < 60$ GeV/c, are shown for each reclustering algorithm.

measured raw jet shapes. As expected from the comparisons of truth and detector level MC simulations (see sections 4.3.4 and 4.3.5), the corrections from the unfolding procedure are small. Since the measured raw and unfolded distributions are similar, the same conclusions that were presented for the different shapes and algorithms at raw level (section 4.2), also hold for the unfolded solutions.

The ΔR distributions for the hard scale sensitive algorithms (k_T and soft drop with

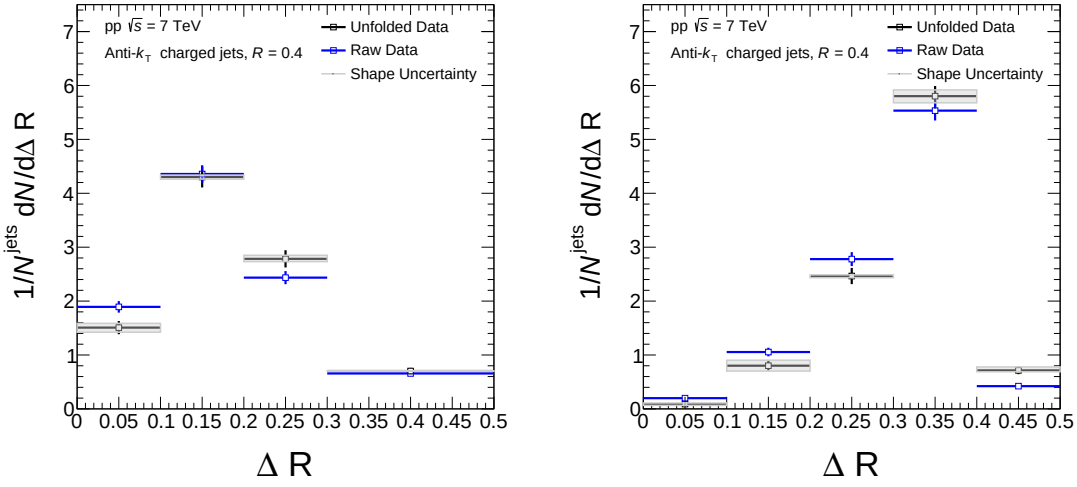

(a) k_T (b) C/A

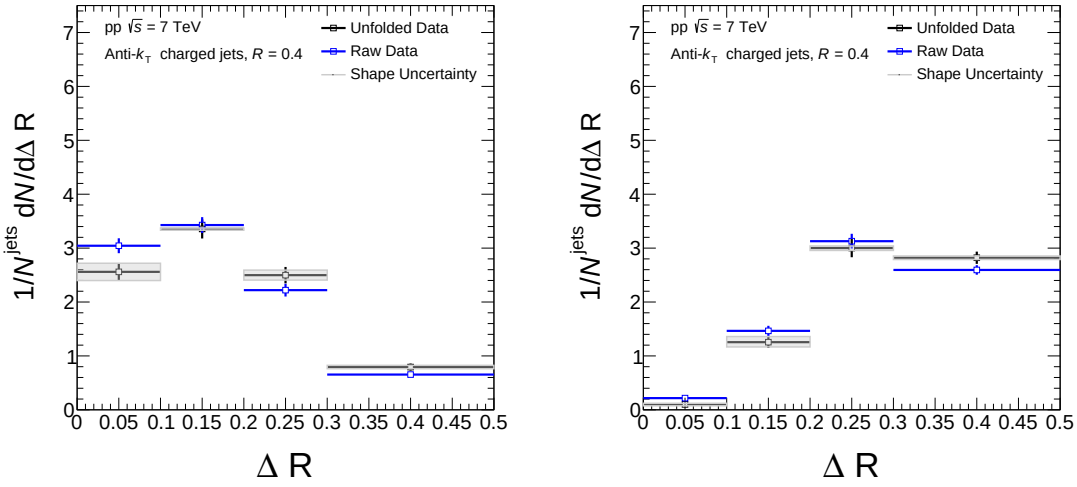

(c) C/A + soft drop (d) C/A + minimisation

Figure 4.32: The fully corrected ΔR distributions in pp collisions are shown, along with their associated statistical and systematic uncertainties, at $40 \leq p_T^{jet,ch} < 60$ GeV/c for each of the reclustering algorithms. The raw ΔR jet shapes, measured at $40 \leq p_T^{jet,ch} < 60$ GeV/c in pp collisions, are also provided for comparison.

C/A reclustering), peak at small values. This indicates that the hard splittings of the jets are primarily situated in a small core. The τ_2/τ_1 distributions peak at ~ 0.6, showing that the majority of the $p_T^{jet,ch}$ is situated within this core. This is consistent with the strongly collimated, single-core nature of QCD jets.

The ΔR distributions measured using the soft scale sensitive algorithms (C/A with

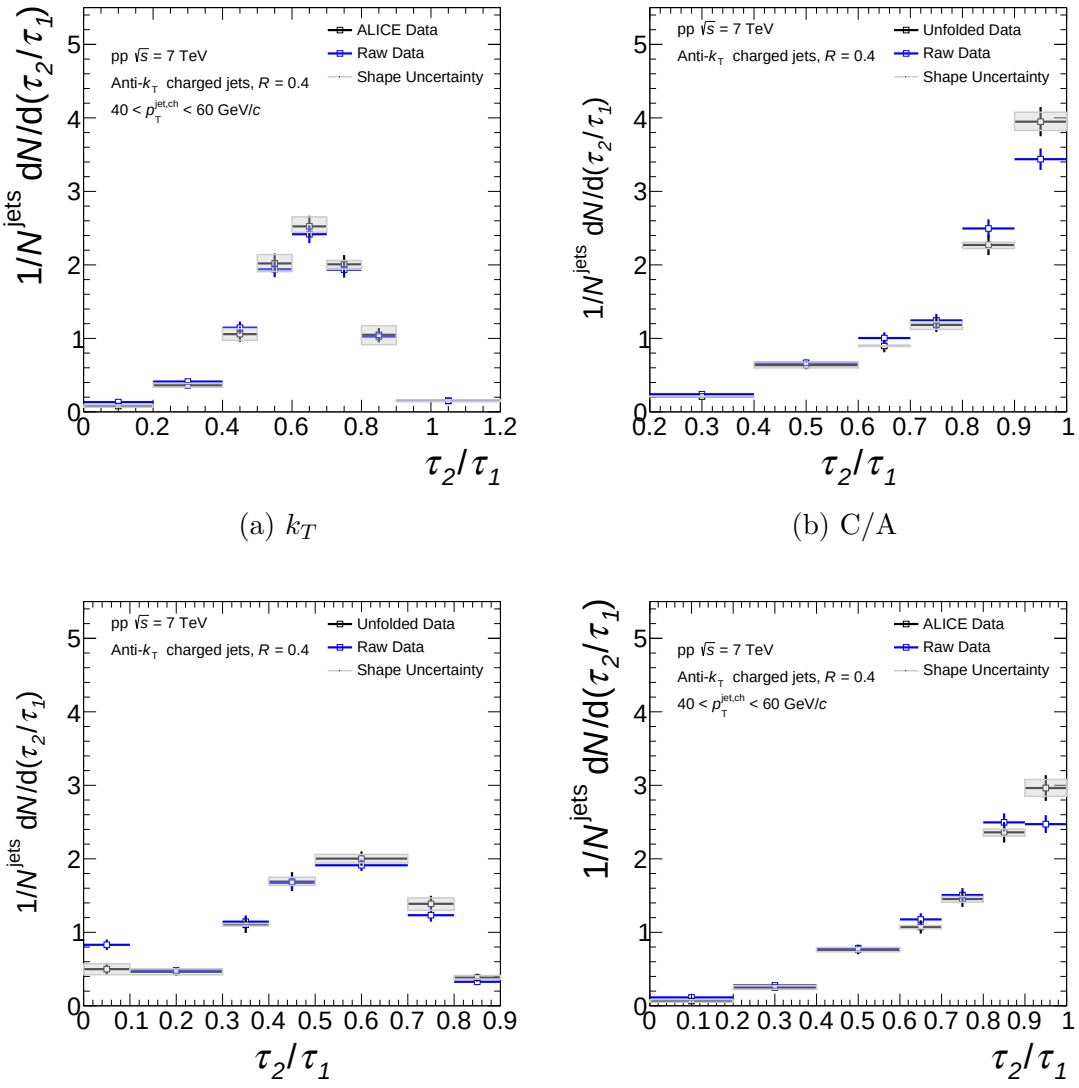

(a) k_T (b) C/A

(c) C/A + soft drop (d) C/A + minimisation

Figure 4.33: The fully corrected τ_2/τ_1 distributions in pp collisions are shown, along with their associated statistical and systematic uncertainties, at $40 \leq p_T^{jet,ch} < 60$ GeV/c for each of the reclustering algorithms. The raw τ_2/τ_1 jet shapes, measured at $40 \leq p_T^{jet,ch} < 60$ GeV/c in pp collisions, are also provided for comparison.

and without minimisation), peak at the jet radius. This indicates that some radiation appears at large angles from the jet core. The τ_2/τ_1 distributions measured with these algorithms peak at ~ 1, indicating that the bulk of the $p_T^{jet,ch}$ is only correlated to one of the returned axes (the one in the core).

The performances of the algorithms in pp collisions (vacuum), can hint to their

possible performances in the heavy ion environment of central Pb-Pb collisions. The k_T and soft drop with C/A algorithms have shown to be sensitive to the hard scale physics within the jet. As such, they will be the primary algorithms for investigating the physics of interest in Pb-Pb collisions (QGP medium). The k_T algorithm has the advantage of being p_T sensitive by construction, which could make it resilient to the soft large angle radiation of the heavy ion background. Even though the C/A algorithm has no such resilience, the inclusion of the soft drop groomer appears to remove large angle soft radiation from the jet and uncovers the hard splittings. Due to this extra grooming step, it has the potential to remove a larger amount of the heavy ion background and uncover the hard splittings more cleanly than the k_T algorithm. However, this is dependent on the extent to which the soft drop groomer, with the given parameters, is successful at removing this background in heavy ion collisions. This will be tested in the following chapter.

The C/A algorithm shows a strong sensitivity to large angle tracks within the jet cone, which are predominantly soft. As such, it is expected to be dominated by the large heavy ion-background. This limits the impact of this algorithm in probing the substructure of the fragments arising from the scattered parton. The minimisation procedure could have a larger effect in Pb-Pb collisions compared to pp, due to the higher multiplicities present in the jet cone. This will be tested in Pb-Pb collisions. Despite its projected lack of impact, the C/A algorithm will still be measured in Pb-Pb collisions, to serve as a benchmark when considering the effects of the soft drop groomer and minimisation procedures.

CHAPTER 5

Pb-Pb Analysis

In this chapter, the tools developed during the pp analysis will be applied to the much more challenging environment of central Pb-Pb collisions. The large heavy ion background necessitates the application of additional procedures, including background subtraction and the rejection of combinatorial jets. Response matrices are constructed by embedding MC generated jets into Pb-Pb data. For the τ_2/τ_1 jet shapes, a two-dimensional Bayesian unfolding procedure is applied to correct the raw distributions, for background fluctuations and detector effects, in both shape and $p_T^{jet,ch}$ simultaneously. It will be shown that the unfolding procedure is unstable for the ΔR shapes and only an uncorrected result can be presented. Four different reclustering algorithms are employed to calculate the jet shapes, as discussed in section 2.1.2. For the steps in the analysis where the process is identical to that employed in pp collisions, as described in chapter 4, the methodology will be referenced

to the appropriate section of the chapter and only the results will be shown.

5.1 Clustering Jets

The anti-k_T algorithm, with a jet resolution of $R = 0.4$, is used to cluster tracks measured by the detector into jets. Only the $0 - 10\%$ most central events (see section 1.1.3) are considered, as these contain the largest and longest lived QGPs. The average event-wise background contribution is then removed on a jet-by-jet basis, from both the $p_T^{jet,ch}$ and shape, as described in section 2.2. Constituent subtraction is the default background subtraction method used in this analysis, with derivative subtraction employed as a systematic cross-check where possible. The performance of these methods will be discussed in the next section. A $p_T^{jet,ch} \geq 20$ GeV/c cut is enforced, after background subtraction, as jets below this threshold are almost entirely combinatorial in origin. Similar to the case in pp, only jets with at least two tracks are accepted, since this is the minimum requirement for calculating the ΔR and τ_2 jet shapes.

This inclusive sample yields approximately 6.7 million jets, with the $p_T^{jet,ch}$ distribution shown in figure 5.1. A comparison to the inclusive $p_T^{jet,ch}$ spectrum measured in pp collisions (figure 4.1) is also presented. For the purposes of this comparison, the minimum $p_T^{jet,ch}$ threshold for the pp sample has been increased to 20 GeV/c (from its original cut-off at 10 GeV/c). It can be seen that for $p_T^{jet,ch} \leq 60$ GeV/c, the Pb-Pb distribution has a steeper slope than the pp case. This is due to the contribution of combinatorial jets, which originate from the heavy ion background. At larger $p_T^{jet,ch}$ values, where combinatorial jets are suppressed, the Pb-Pb distribution follows a similar power law behaviour as the one observed in pp.

The $\phi^{jet,ch}$ and $\eta^{jet,ch}$ distributions are shown in figures 5.2 and 5.3 respectively.

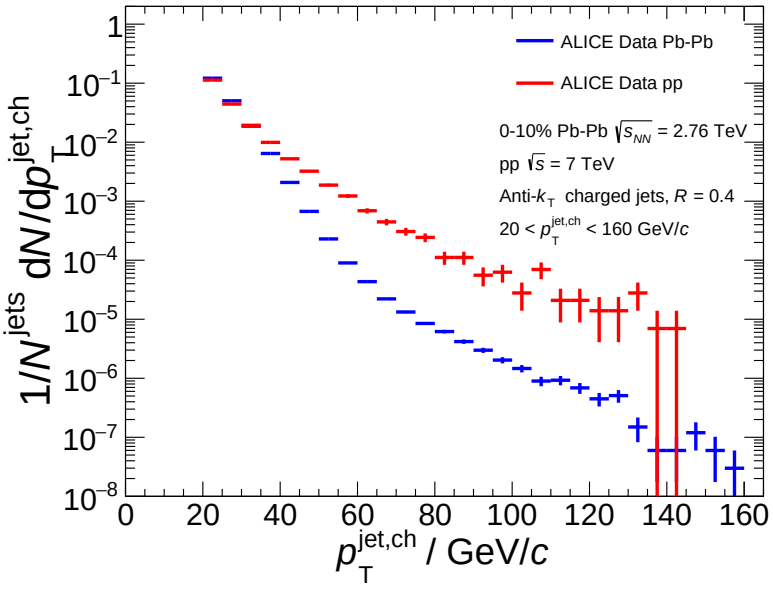

Figure 5.1: The inclusive $p_T^{jet,ch}$ distributions, measured in the pp and $0-10\%$ most central Pb-Pb collisions, are shown.

The non-flat $\phi^{jet,ch}$ distribution is due to the exclusion of one of the hybrid track classes from the data set. This class, which requires no SPD hits or ITS refits (see section 3.4.2.4), accounts for only 6% of the total track population. Despite this small percentage, its exclusion has an effect on the uniformity of the $\phi^{track,ch}$ distribution. This non-uniformity is further magnified when looking at the $\phi^{jet,ch}$ distribution of jets with a high minimum $p_T^{jet,ch}$ threshold. The reason for the larger induced azimuthal non-uniformity in the jet population, compared to the track population, arises from the power law like distribution of the $p_T^{jet,ch}$. A reduction in the population of tracks in a given region of phase space, causes a downward shift of the $p_T^{jet,ch}$ scale. Since the yield of jets is largest at low $p_T^{jet,ch}$, this downward shift causes a significant number of jets to fall below the minimum $p_T^{jet,ch}$ threshold, inducing a large loss of jets in this region of phase space. The $\eta^{jet,ch}$ distribution, follows the shape of the charged track η distribution [123]. The non-uniformity of the track η^{ch} distribution is also magnified when clustering jets. Since the jet shapes measured in this analysis have no dependence on the η and ϕ of the jet, within the

limits of the detector acceptance, the non-uniformity of these distributions has no impact on the final results. Additionally, the normalisation of the jet shapes to the number of total jets, further mitigates against any potential effects.

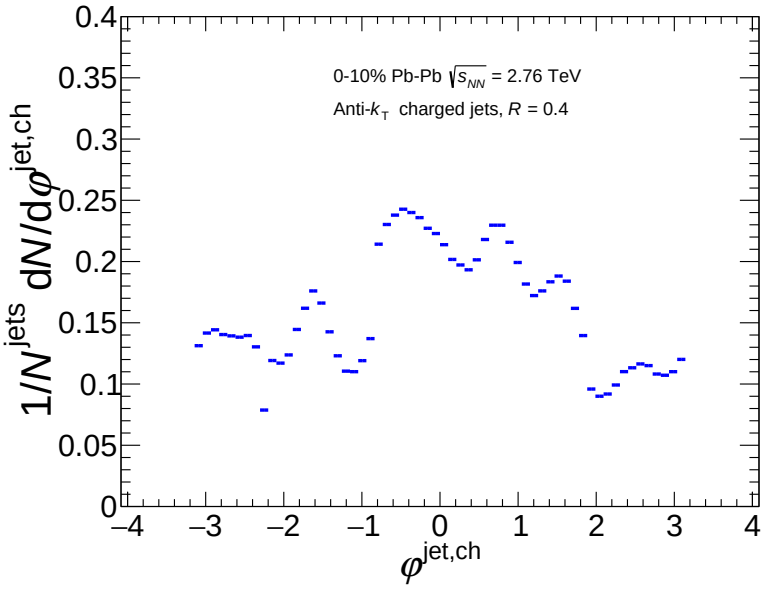

Figure 5.2: The $\phi^{jet,ch}$ distribution, obtained for the measured Pb-Pb data sets, is shown.

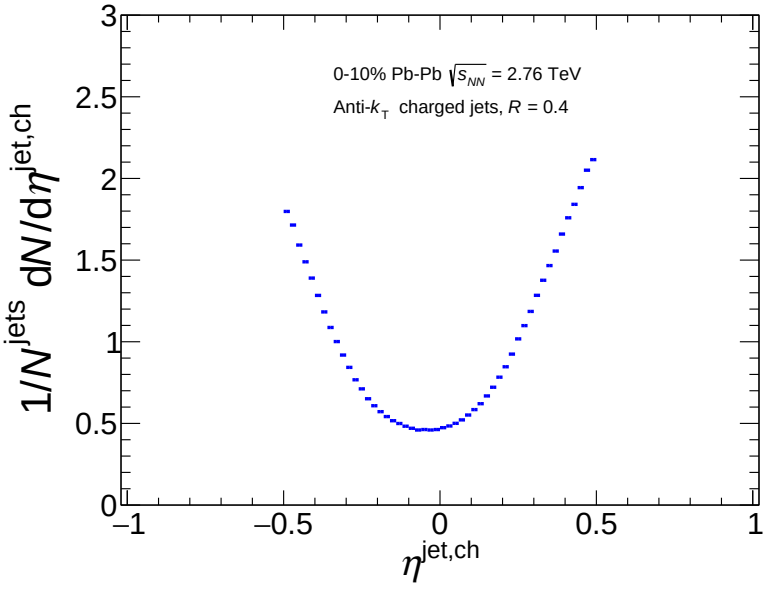

Figure 5.3: The $\eta^{jet,ch}$ distribution, obtained for the measured Pb-Pb data sets, is shown.

The number of charged tracks clustered per jet, is shown in Fig 5.4. A comparison is provided between the constituent subtraction method, where the background is subtracted at track level and the area-based subtraction method, where no subtraction is applied to the tracks and only the $p_T^{jet,ch}$ is corrected. The corresponding pp distribution, which is the same as figure 4.4 with the added requirement of $p_T^{jet,ch}$ $\geq$ 20 GeV/c, is also presented.

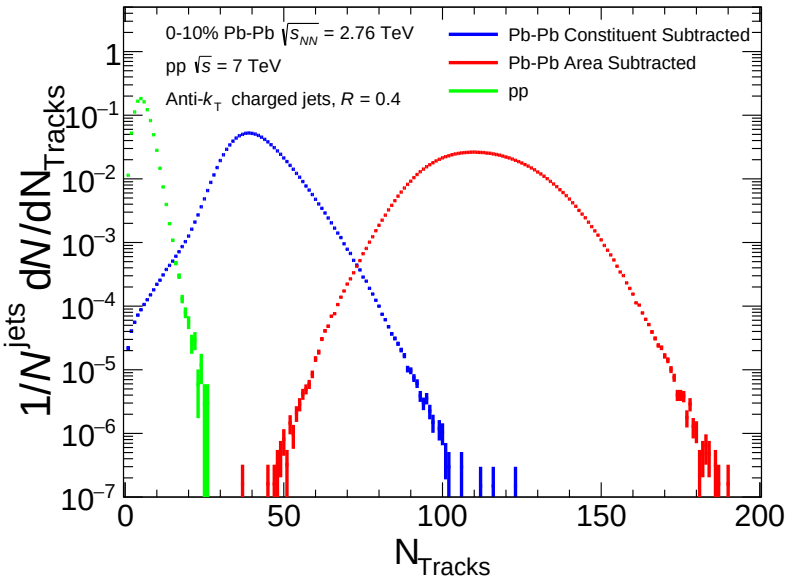

Figure 5.4: The number of charged tracks clustered per jet, obtained for the measured Pb-Pb data sets, is shown.

The presence of the heavy ion background (red), overwhelms the true jet signal in the jet cone. Even though constituent subtraction (blue) is successful at removing much of this background, the number of tracks remaining is still significantly larger than the number of jet constituents in pp collisions (green). This can be partly explained through the fragmentation differences of jets in central Pb-Pb and pp collisions, as traversing the QGP induces radiative energy losses in the jet. This radiation is partially recovered in the jet cone. However, there is also a large contribution from the remaining background, which has not been removed by the subtraction mechanism. The subtraction removes the average event-wise background from the

jets. Therefore, local fluctuations in the background can cause the subtraction mechanism to under-subtract or even over-subtract the background contribution. This highlights the importance of the unfolding procedure in fully correcting the jets of these background fluctuations.

5.2 Background Subtraction Performance

The performance of the background subtraction techniques used in this analysis are tested via an embedding procedure. MC generated jets are embedded into real $0-10\%$ central Pb-Pb data and are clustered again in the presence of the heavy ion background. Background subtraction is then performed at this embedded level and the jets are matched to the their truth level counterparts (for further details on embedding see section 5.4.1). In this way, background subtracted jets can be compared to their truth level, background free, state. This background subtraction procedure only removes the event average background from each jet. Local fluctuations in the background are removed via the unfolding procedure.

The effect of background subtraction on the measured jet shapes, is discussed below for all four reclustering algorithms. Each shape is presented in the same $p_{T,Truth}^{jet,ch}$ range as its final presented result. For the ΔR shape (uncorrected final result) this is $80 \leq p_{T,Truth}^{jet,ch} < 100$ GeV/c, whilst for the τ_2/τ_1 shape (fully corrected result) it is $40 \leq p_{T,Truth}^{jet,ch} < 60$ GeV/c. In the plots shown in this section, the truth level is displayed in blue, whilst the unsubtracted embedded level is displayed in black. The two background subtraction algorithms considered are constituent subtraction (red) and second order derivative subtraction (green), which are described in sections 2.2.2 and 2.2.3 respectively.

5.2.1 ΔR

The performances of the background subtraction algorithms on the ΔR jet shapes, are presented in figure 5.5. Due to the differing sensitivity of the reclustering algorithms to remaining soft background, the performances of the subtraction algorithms vary depending on the reclustering algorithm used. The k_T and C/A with soft drop algorithms are sensitive to hard splittings in the jet, which are picked out at truth level. The resultant distributions peak at small values of ΔR, due to the single-core nature of QCD jets. The presence of the heavy ion background shifts these distributions to significantly higher values, approaching the jet radius, by replacing one of the hard splitting axes with a "fake" soft axis. It can be noted that, at this unsubtracted level, the soft drop algorithm is unsuccessful at removing the background contribution at large angles from the jet axis. This background contribution overwhelms the "true" jet signal (see figure 5.4) and always provides a substructure with at least 10% of the $p_T^{jet,ch}$, which is the criteria for passing the soft drop condition.

Both subtraction procedures attempt to remove the average event-wise background contribution from the jet. For the case of the k_T reclustering, the subtractions have moderate success and manage to correct part of the jet sample back to the truth level. However, a large proportion of the jet sample is not fully corrected, which induces a large second peak at high ΔR. Constituent subtraction performs slightly better than derivative subtraction on the shape obtained with this reclustering algorithm. For the case of soft drop with C/A reclustering, the combination of background subtraction and soft drop grooming manages to successfully remove the large angle soft background from a larger proportion of the jet sample than in the k_T case. However, a substantial second peak at large ΔR still persists. For this particular reclustering algorithm derivative subtraction is not performed, as it is computationally incompatible with the soft drop procedure.

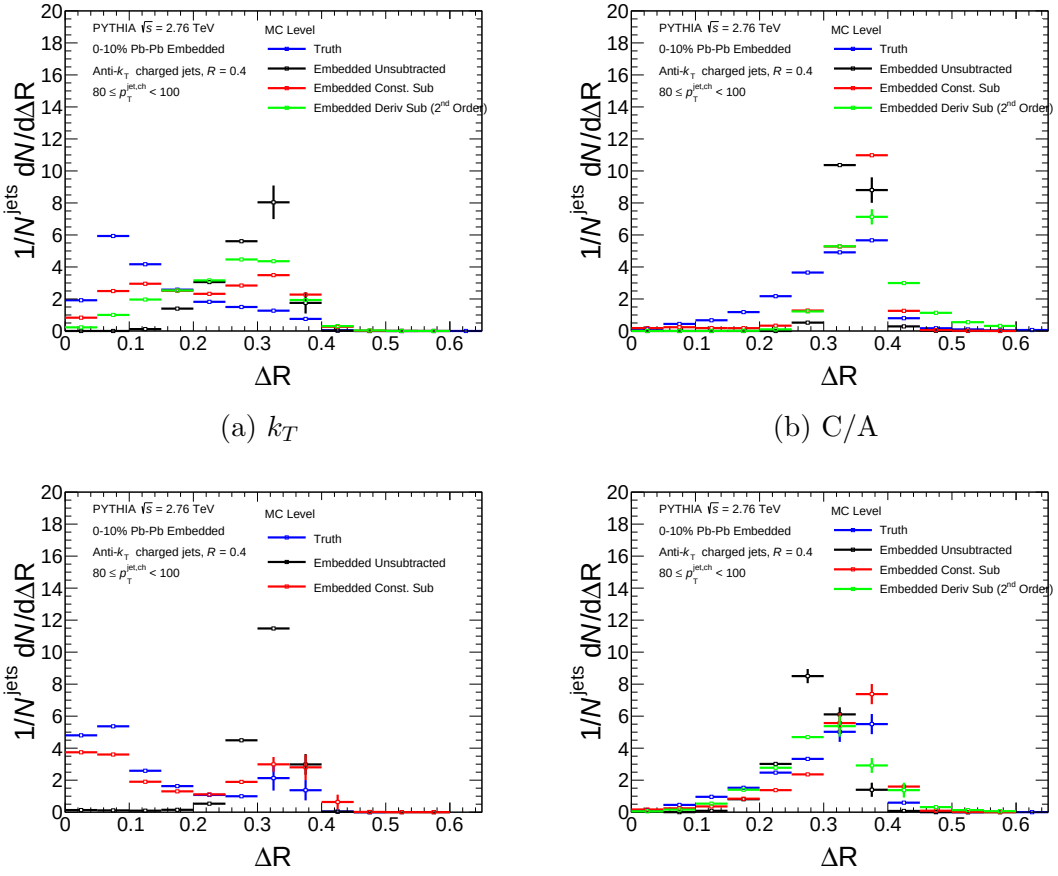

(a) k_T (b) C/A

(c) C/A + soft drop (d) C/A + minimisation

Figure 5.5: The performances of the constituent (default) and second order derivative background subtraction algorithms on the ΔR jet shape are shown, at $80 \leq p_{T,Truth}^{jet,ch} < 100$ GeV/c, for each reclustering algorithm.

For the case of the C/A algorithm, the presence of the background moves the unsubtracted distribution to larger values compared to the truth level. The heavy ion background guarantees the presence of radiation at large angles from the jet axis, which draws the second reclustering axis towards it. For the case of the C/A algorithm followed by a minimisation procedure, the minimisation has a larger effect on the ΔR distribution in the presence of the background compared to the vacuum (truth level). This is due to the larger number of tracks clustered into the jet cone, which provide more opportunities for local minimisation.

For the C/A case, the subtraction procedures are largely unsuccessful at correcting

the ΔR jet shape back to truth level, since even a single remaining track at large angles can pull the second reclustering axis towards it in this algorithm. The derivative subtraction procedure is slightly more successful than the constituent subtraction, since the latter corrects jets at track level. This can sometimes lead to tracks being modified, rather than fully removed, leaving soft tracks at large angles. For the case of C/A followed by a minimisation procedure, the combination of the subtraction and minimisation processes does a much better job of correcting the jet shape back to truth level, compared to the default C/A case.

5.2.1.1 Uncorrectable Distributions

The double peak structures of the ΔR distributions at subtracted embedded level, for the hard scale sensitive reclustering algorithms, prohibit stable unfolding. The mapping of the response matrices contain two equally probable regions at embedded level, for the same values at truth level. These correspond to both the portions of the jet sample that have been contaminated by the soft "fake" axes (large ΔR values at embedded level) and the portions which have had this contamination succesfully removed by the subtraction algorithms (low ΔR values at embedded level). Due to this structure of the response matrix, the unfolding procedure fails to converge onto an unfolded solution (this will be shown in section 5.5.3.1 for the k_T and soft drop with C/A algorithms).

For the case of the soft scale sensitive reclustering algorithms, both algorithms suffer from a lack of adequate statistics at low ΔR in the measured data sample, as shown in figure 5.6. Therefore, a rectangular input matrix, with counts in each bin, cannot be constructed. This also renders the unfolding unstable, which is particularly apparent in the refolding tests (these will be shown in section 5.5.3.2). As such, further processing of the ΔR jet shape, with the aim of obtaining a fully unfolded

solution, will be stopped at this stage. Instead, a comparison of the inclusive measured distribution, to the subtracted embedded level, is presented at the end of this chapter for the k_T algorithm. This represents an uncorrected final result, which is the best solution possible, given the stipulations above.

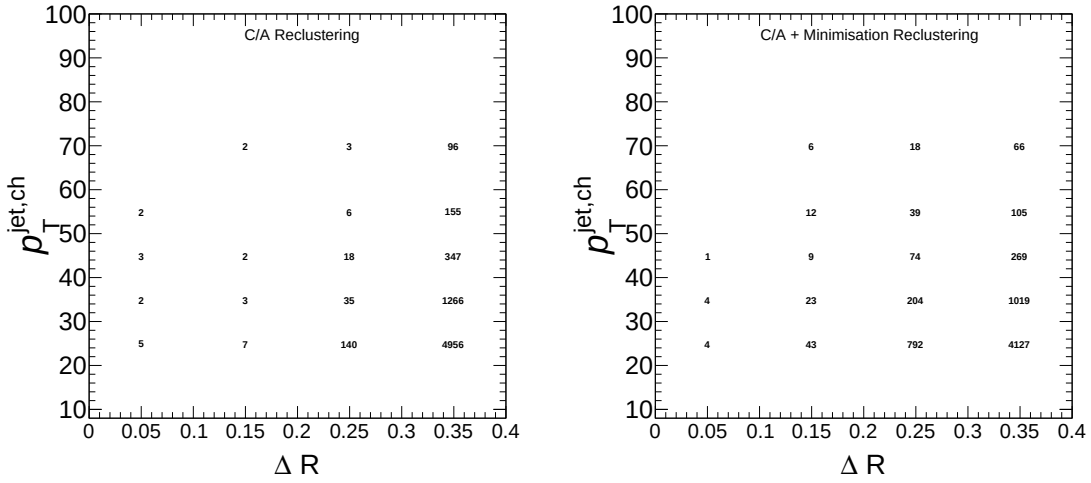

(a) C/A (b) C/A + minimisation

Figure 5.6: The raw data input matrices are shown in statistical form, in differential bins of $p_T^{jet,ch}$ and ΔR, for the soft scale sensitive reclustering algorithms.

5.2.2 τ_1

The axis returned by each reclustering algorithm for the $N = 1$ case at truth level (described in section 4.2.2), is similar across all algorithms, with only slight modifications due to soft drop and minimisation. As shown in figure 5.7, the same arguments still hold at the embedded level. The homogenous nature of the heavy ion background causes no significant modification of the returned axis, compared to truth level. However, the distribution of the tracks around this axis has changed. The heavy ion background is uncorrelated to the initial hard scatter and smears the one-prong structure of the QCD jets. In effect, the jet is broadened without any significant displacement of its axis. This results in a large shift to higher values

of τ_1. The distributions are similar between the different algorithms, due to the background overwhelming the "true" jet signal.

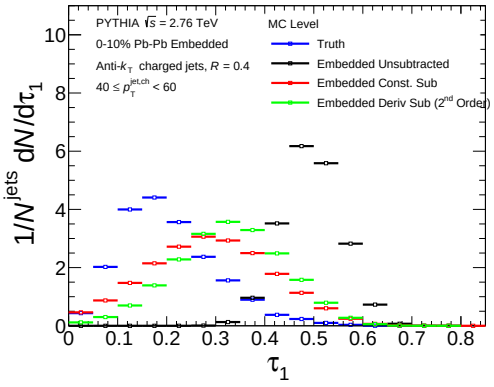

(a) k_T

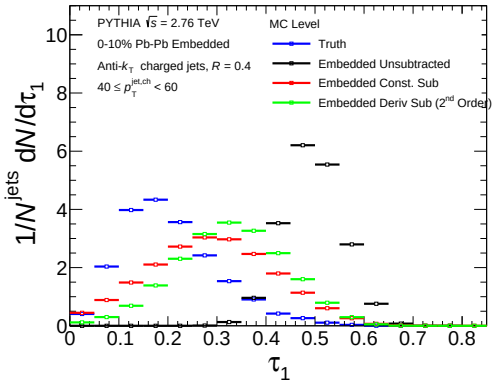

(b) C/A

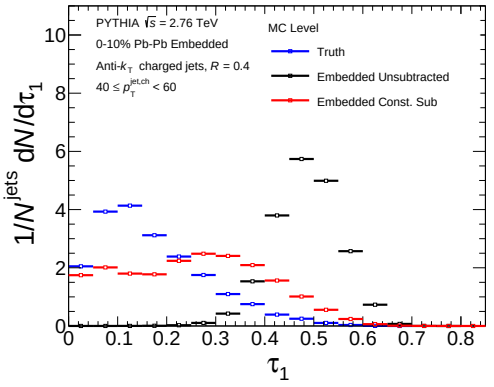

(c) C/A + soft drop

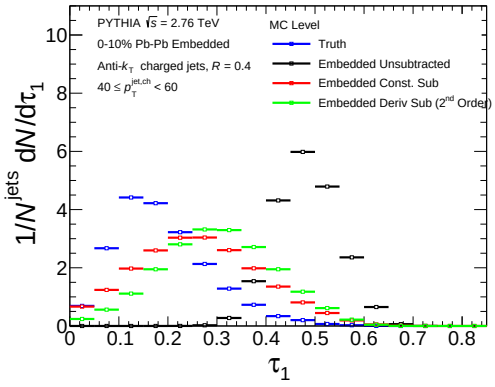

(d) C/A + minimisation

Figure 5.7: The performances of the constituent (default) and second order derivative background subtraction algorithms on the τ_1 jet shape are shown, at $40 \le p_{T,Truth}^{jet,ch} < 60$ GeV/c, for each reclustering algorithm.

For all four reclustering algorithms, the background subtraction techniques partially correct the shapes towards truth level, with constituent subtraction slightly outperforming derivative subtraction. However, since the background is not fully removed from the jet cone in the majority of cases, the subtracted distributions are larger than their truth level counterparts. Given that the axis definitions are similar for all four reclustering algorithms, the subtracted τ_1 distributions are also similar. The only exception arises from the soft drop groomer which, when combined with a background subtraction technique, has a larger impact on correcting the shape back

to truth level. This is due to the further removal of soft radiation at large angles from the jet axis, by the grooming procedure.

5.2.3 τ_2

As shown in figure 5.8, the τ_2 distributions at truth level are visually similar for both the k_T and C/A reclustering algorithms. The minimisation procedure induces only a small modification. The effect of the soft drop groomer is larger, since the removal of soft large angle radiation increases the possibility of uncovering a hard splitting.

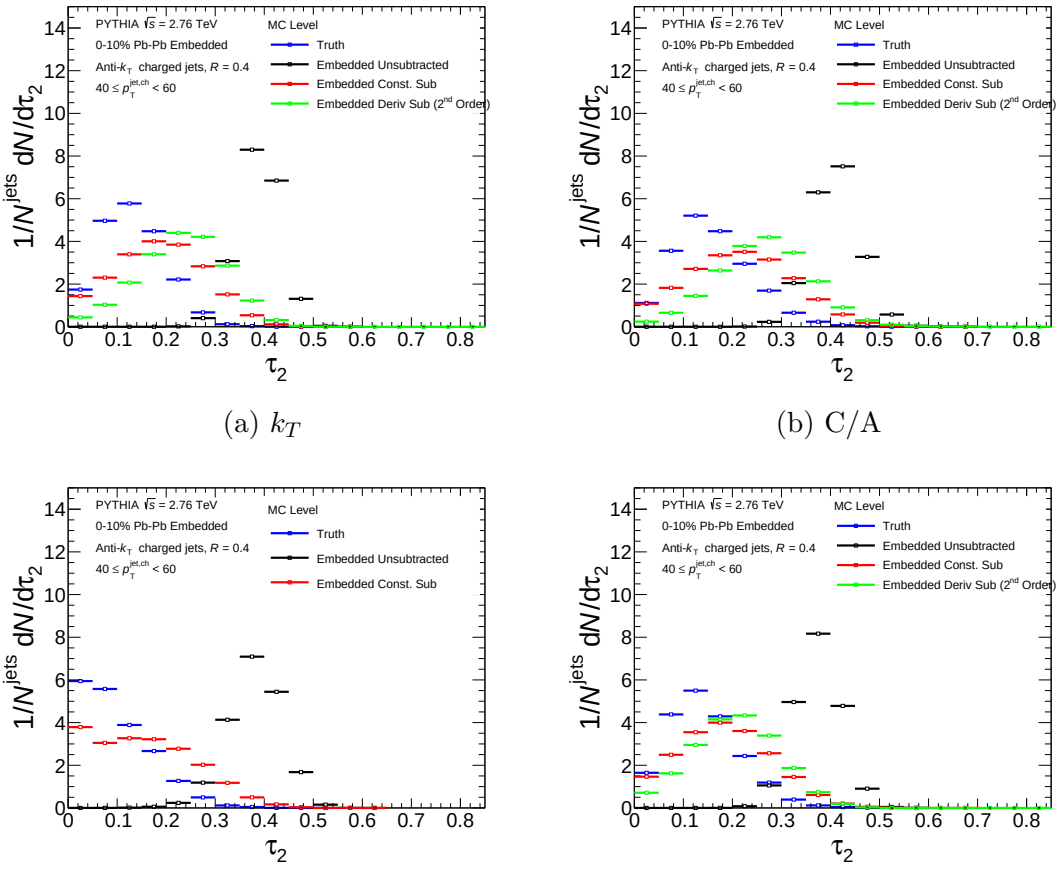

(a) k_T (b) C/A

(c) C/A + soft drop (d) C/A + minimisation

Figure 5.8: The performances of the constituent (default) and second order derivative background subtraction algorithms on the τ_2 jet shape are shown, at $40 \leq p_{T,Truth}^{jet,ch} < 60$ GeV/c, for each reclustering algorithm.

The presence of the heavy ion background shifts the τ_2 distributions to significantly larger values, compared to truth level, since it obscures any one or two-prong substructure in the jet. The subtraction techniques correct the shapes back towards truth level with moderate success, with constituent subtraction once again outperforming derivative subtraction. However, the subtracted distributions still show a displacement relative to the truth level. This is due to the remaining uncorrelated heavy ion background smearing the substructures in the jet. For the hard scale sensitive reclustering algorithms, in some cases, the heavy ion background can replace one of the returned reclustered axes with a soft large angle "fake" axis, as described in section 5.2.1.

5.2.4 τ_2/τ_1

In vacuum, the ratio of τ_2/τ_1 is sensitive to the key physics differences between the τ_1 and τ_2 distributions, which are not easily visible by eye. At truth level, the τ_2/τ_1 distributions for k_T and C/A preceded by soft drop algorithms are sensitive to both two-prong jets (low τ_2/τ_1) and hard substructure in one-prong jets (intermediate τ_2/τ_1). The τ_2/τ_1 distributions for the C/A algorithm, with and without minimisation, tend to unity due to the insensitivity of the reclustering to the p_T scale of the substructures.

As shown in figure 5.9, the heavy ion background shifts the unsubtracted τ_2/τ_1 distributions towards higher (less two-prong) values, compared to the truth level, for the hard scale sensitive reclustering algorithms (k_T and C/A with soft drop). This is due to the obscuration of substructure within the jet by this background. Even though the background subtraction techniques only had moderate success at correcting the τ_1 and τ_2 jet shapes, the ratios of the subtracted shapes exhibit an almost full correction back to truth level. The τ_N jet shapes are sensitive to the p_T

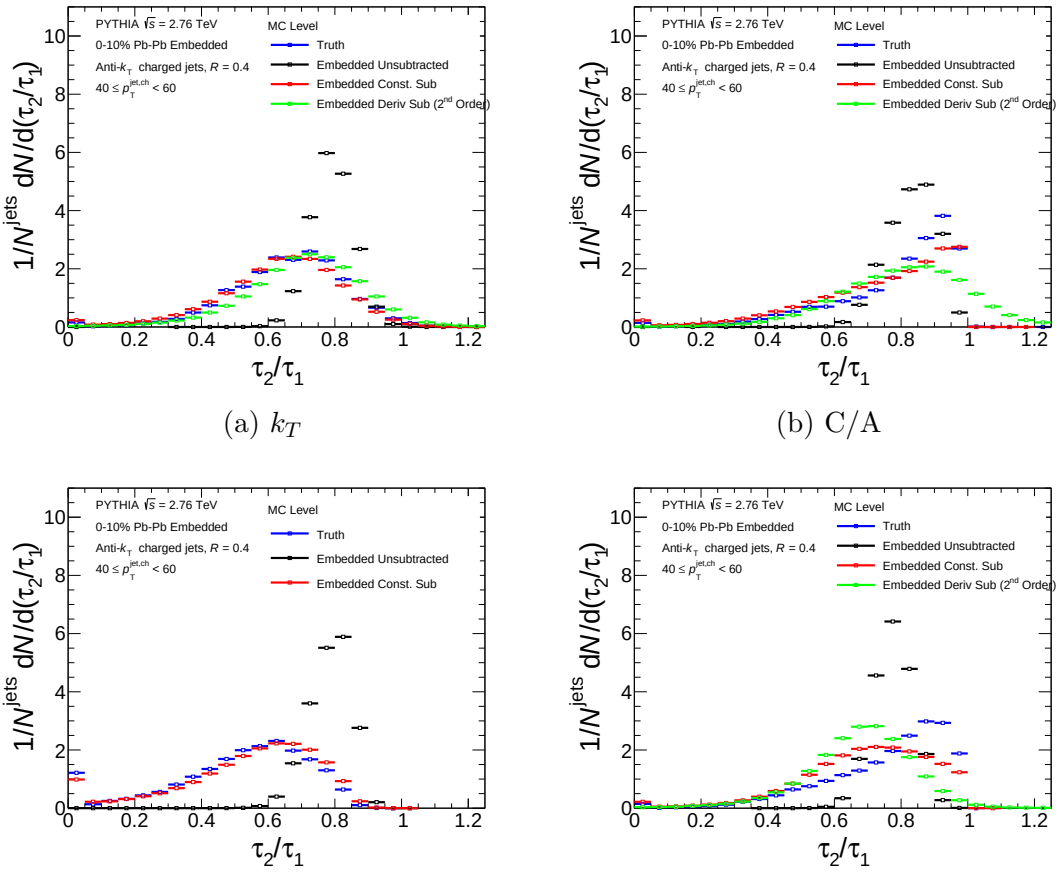

(a) k_T (b) C/A

(c) C/A + soft drop (d) C/A + minimisation

Figure 5.9: The performances of the constituent (default) and second order derivative background subtraction algorithms on the τ_2/τ_1 jet shape are shown, at $40 \leq p_{T,Truth}^{jet,ch} < 60$ GeV/c, for each reclustering algorithm.

of the jet constituents. Therefore, the shifts of the jet shapes due to the remaining uncorrelated soft background are suppressed in their ratio.

For the case of the C/A algorithm, with and without minimisation, the unsubtracted distributions undergo a shape change relative to the truth level, with their means shifting to larger values whilst their peaks move in the opposite direction. As with the other reclustering algorithms, the presence of the heavy ion background overwhelms the true jet signal and dictates the position of the second reclustered axis. The unsubtracted τ_2/τ_1 distributions for the C/A algorithm are therefore similar to the distributions obtained with the hard scale sensitive algorithms. The smearing of

single-core QCD jets, shifts the peaks of the τ_2/τ_1 distributions obtained with the C/A algorithm, to slightly lower values than unity.

An improved subtraction correction is also observed for the C/A algorithm, with and without minimisation, when taking the τ_2/τ_1 ratio (compared to the cases for τ_1 and τ_2). However, this is only true when using constituent subtraction. Derivative subtraction does not reproduce the shapes back to truth level well. For both reclustering algorithms, there is still a noticeable displacement between the constituent subtracted and truth level distributions. This displacement is larger for the case with minimisation, where the shape is over subtracted. This is due to the minimisation procedure having a larger effect on τ_2 than τ_1, as it has more opportunities to minimise when given the extra axis. The effects of minimisation also increase with increasing track multiplicity. Therefore, the minimisation procedure at the subtracted level is more successful than at the truth level and shifts the distribution to slightly lower values.

Constituent subtraction performs well for the τ_2/τ_1 jet shape, in correcting the embedded level back to the truth. Therefore, only small corrections are expected via the unfolding procedure. For the cases of C/A, with and without minimisation, a large subtraction systematic error (see section 5.6) is expected, due to the large differences between the subtraction algorithms.

5.3 Recoil Jets

The response matrices obtained via the embedding procedure, only contain entries for jets originating from a hard scatter. Combinatorial jets, which are a manifestation of fluctuations in the heavy ion background (see section 2.3.1), cannot be simulated and have no truth level (obtained in the vacuum) associated with them.

Therefore, in order to successfully unfold the data set and correct for detector effects and background fluctuations, the input sample must be free of combinatorial jets.

One method of obtaining this pure jet sample, for jets with a resolution of $R = 0.4$, is to choose a high $p_T^{jet,ch}$ range when making measurements. For the uncorrected inclusive distribution of ΔR, presented at the end of this chapter, a $p_T^{jet,ch}$ range of $80-100$ GeV/c is chosen. Up until this $p_T^{jet,ch}$, the fraction of combinatorial jets are still significant in the measured sample. However, the data set used in this analysis falls short of the required statistical reach to unfold jets at this $p_T^{jet,ch}$. Additionally, there is interest in measuring jets across a wide range of the $p_T^{jet,ch}$ phase space, including measurements of jets at low $p_T^{jet,ch}$.

An alternative approach is to select a yield of jets, from the inclusive jet distribution, which is free of combinatorial jets. This can be achieved by using the semi-inclusive hadron-jet coincidence technique, as described in section 2.3.2, to obtain a recoil jet sample.

5.3.1 Recoil $p_T^{jet,ch}$

Two exclusive high p_T^{ch} trigger hadron classes are selected. The chosen p_T^{ch} ranges are $15-45$ GeV/c and $8-9$ GeV/c, for the signal and reference classes respectively. Jet finding is performed in a window ($\Delta\phi$) of $\pi - \Delta\phi < 0.6$ with respect to the trigger hadron. The trigger hadron classes are chosen to be at a high enough p_T^{ch} so as to guarantee a hard scatter origin, but sufficiently separated to still have a large enough difference yield of true (hard scatter origin) jets. The trigger hadron classes selected in this analysis, maximise the available statistics, whilst maintaining the above requirements. Figure 5.10 shows the $p_T^{jet,ch}$ yields for the signal and reference classes, along with their difference yield obtained using the methods described in section 2.3.2. The area-based subtraction method, described in section 2.2.1, has

been applied to the distributions in this figure to correct the jet energy scale. This is in contrast to all following figures, where the subtraction algorithm used will be constituent subtraction. However, consitutent subtraction has a computational hard coded cut-off at $p_T^{jet,ch} = 0$ GeV/c, which is not optimal for the purposes of this figure. The distributions of $p_T^{jet,ch} \geq 0$ GeV/c, are independent of the choice of subtraction algorithm used. The number of trigger hadrons obtained in the signal and reference classes are 71, 687 and 69, 337 respectively.

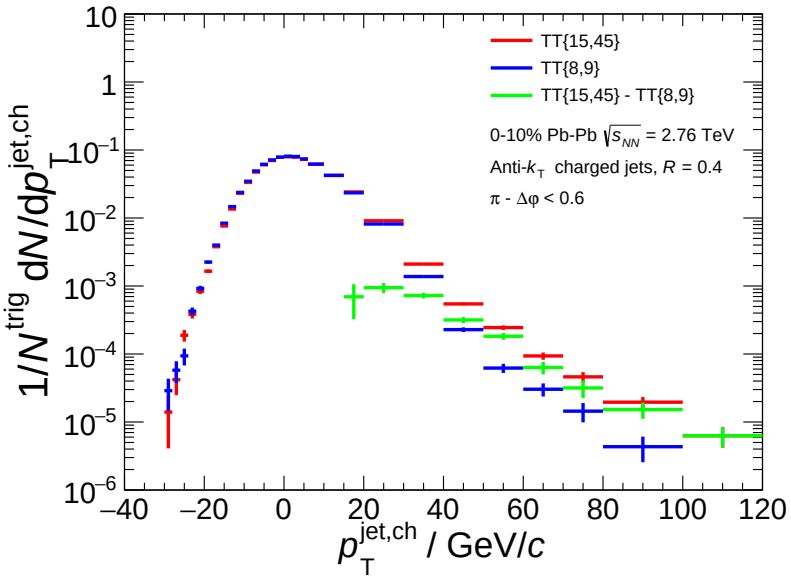

Figure 5.10: The $p_T^{jet,ch}$ yields for jets recoiling from two exclusive high p_T trigger hadron classes of $TT\{15-45\}$ GeV/c and $TT\{8-9\}$ GeV/c, are shown. The difference yield of these two classes is also plotted.

The negative $p_T^{jet,ch}$ regions are populated by jets with a $p_T^{jet,ch}$ lower than the average event-wise background p_T^{ch}, which is removed from all jets on an event-by-event basis. The low $p_T^{jet,ch}$ regions are dominated by combinatorial jets, which leads to only small differences in the yields of the signal and reference classes. This difference yield, which represents a combinatorial free jet yield, increases with increasing $p_T^{jet,ch}$ as more jets originate from a hard scatter. With increasing $p_T^{jet,ch}$, the difference yield approaches the signal yield.

5.3.2 Extension to 2D

The Recoil method has been extended to two dimensions, for the first time, in this analysis. The two-dimensional reference distribution is subtracted from the two-dimensional signal yield, as described in section 2.3.2. This results in a two-dimensional difference yield, calculated in bins of $p_T^{jet,ch}$ and shape. Figure 5.11 illustrates this subtraction pictorially. Constituent subtraction has been used to subtract the average event-wise background from the jets.

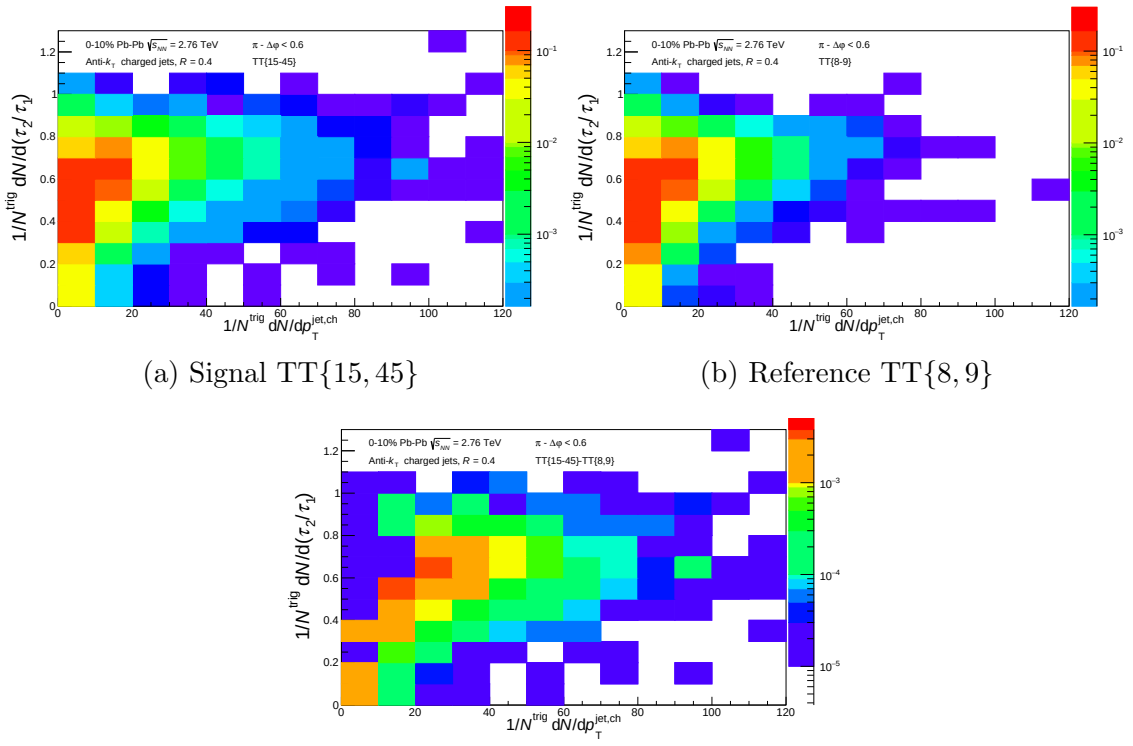

(a) Signal TT$\{15, 45\}$

(b) Reference TT$\{8, 9\}$

(c) Difference TT$\{15, 45\}$ - TT$\{8, 9\}$

Figure 5.11: The two-dimensional $p_T^{jet,ch}$ and τ_2/τ_1 yields are shown for the signal ($TT\{15-45\}$), reference ($TT\{8-9\}$) and difference ($TT\{15-45\} - TT\{8-9\}$) classes, using the k_T reclustering algorithm.

Shape distributions are projected from the two-dimensional difference yield, in given bins of $p_T^{jet,ch}$. Figure 5.12 shows the projected signal, reference and difference yields for the τ_2/τ_1 jet shape, measured using the k_T reclustering algorithm, in three increasing bins of $p_T^{jet,ch}$. As the $p_T^{jet,ch}$ is increased, the difference yield approaches the

signal yield. This is indicative of a suppression in the contribution of combinatorial jets with increasing $p_T^{jet,ch}$.

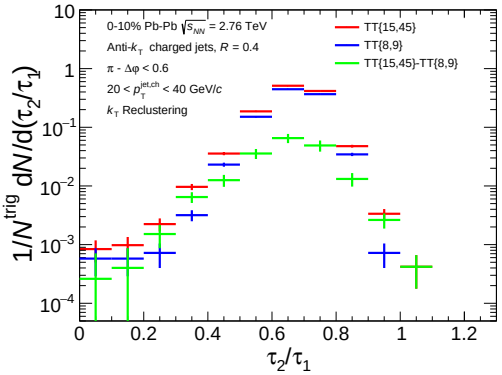

(a) $20 \leq p_T^{jet,ch} < 40$ GeV/c

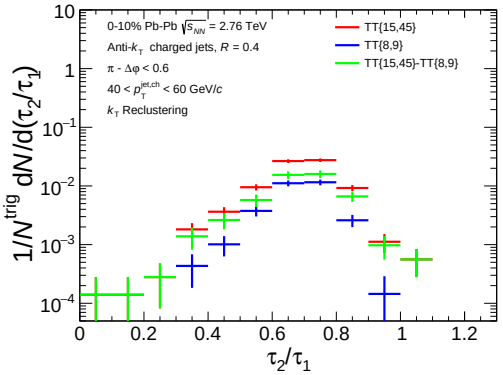

(b) $40 \leq p_T^{jet,ch} < 60$ GeV/c

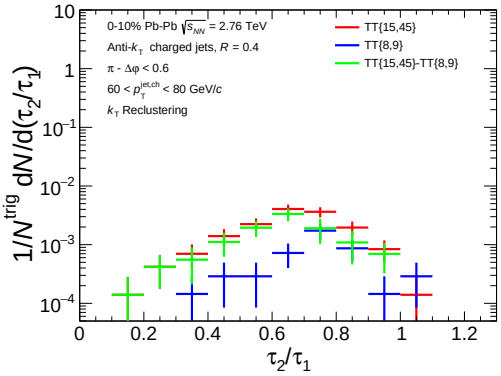

(c) $60 \leq p_T^{jet,ch} < 80$ GeV/c

Figure 5.12: The signal ($TT\{15-45\}$), reference ($TT\{8-9\}$) and difference ($TT\{15-45\} - TT\{8-9\}$) yields are shown for the τ_2/τ_1 jet shape, in three consecutive bins of $p_T^{jet,ch}$, using the k_T reclustering algorithm.

The constituent subtracted recoil shapes (projections of the difference class) will be presented below. The effects of the remaining background on the shapes have already been discussed in section 5.2. The remainder of this section will be used to investigate the $p_T^{jet,ch}$ dependence of the shapes and present the uncorrected τ_2/τ_1 recoil distributions at $40 \leq p_T^{jet,ch} < 60$ GeV/c, which will be fully corrected via the unfolding procedure.

5.3.3 τ_1

The τ_1 recoil shapes are shown in figure 5.13, for three consecutive bins of $p_T^{jet,ch}$. These are $20-40$, $40-60$ and $60-80$ GeV/c. The distributions shift to lower values with increasing $p_T^{jet,ch}$. This trend is similar to the one observed in pp collisions (figure 4.6) and is attributed to the collimation of jets with increasing $p_T^{jet,ch}$. However, for the $60 \leq p_T^{jet,ch} < 80$ GeV/c bin, the shift is more pronounced in Pb-Pb collisions than in pp. This is due to the presence of the remaining background in the jet, which competes with the collimation and shifts the distributions to higher values. For high $p_T^{jet,ch}$ jets, the background comprises a smaller percentage of the overall $p_T^{jet,ch}$. Therefore, the effect of the background on the distributions is reduced with increasing $p_T^{jet,ch}$, causing a smaller shift to higher values. When combined with the effects of the collimation, this results in a larger relative shift to lower values with increasing $p_T^{jet,ch}$, in Pb-Pb collisions compared to pp collisions. Similarly, the soft drop groomer is also more effective at removing large angle soft radiation in higher $p_T^{jet,ch}$ jets, since the background is less likely to form a structure which amounts to at least 10% of the overall $p_T^{jet,ch}$.

5.3.4 τ_2

The τ_2 recoil shapes are shown in figure 5.14, for the same three consecutive bins of $p_T^{jet,ch}$ as in the τ_1 case. As with the case for τ_1, the trend is similar to that observed in pp collisions (figure 4.7), with the distributions shifting to lower values with increasing $p_T^{jet,ch}$. However, the difference in the shift of the $60 \leq p_T^{jet,ch} < 80$ GeV/c bin, between Pb-Pb and pp, is larger for the τ_2 shape than τ_1. In addition to the reasons given in the section above for this behaviour, the smaller proportional contribution of the background at high $p_T^{jet,ch}$ reduces the contamination of "fake" soft axes. Therefore, the hard scale sensitive reclustering algorithms can pick out

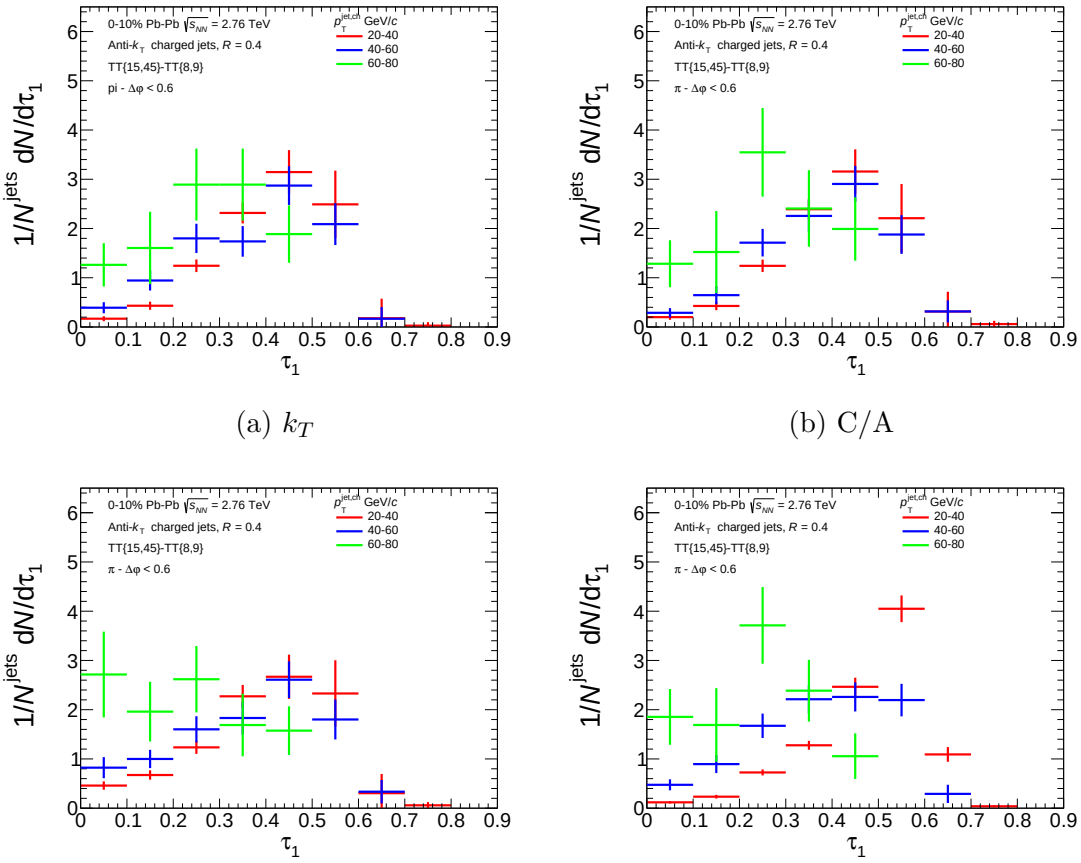

(a) k_T

(b) C/A

(c) C/A + soft drop

(d) C/A + minimisation

Figure 5.13: The difference yields ($TT\{15-45\} - TT\{8-9\}$) are shown for the τ_1 jet shape, in three consecutive bins of $p_T^{jet,ch}$, for each of the reclustering algorithms.

the hard splittings in the jets more often. This is particularly apparent when using the soft drop groomer, since it removes soft radiation at large angles from the core, which further reduces the background contribution.

5.3.5 τ_2/τ_1

The τ_2/τ_1 recoil shapes are shown in figure 5.15, for the same three consecutive bins of $p_T^{jet,ch}$ as in the τ_1 and τ_2 cases. Similar to the case in pp collisions (figure 4.8), no strong $p_T^{jet,ch}$ dependence is seen when taking the ratio of the τ_2 and τ_1 values, for any of the algorithms. The only exception is the case involving minimisation, where

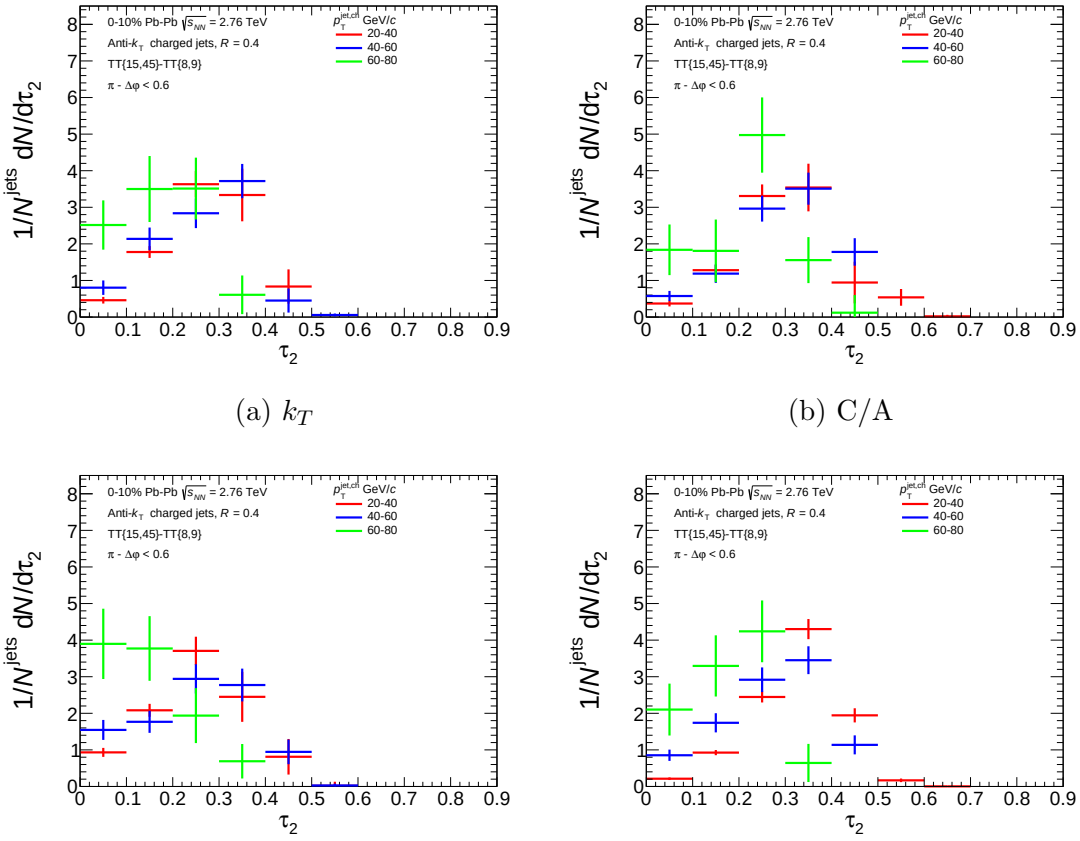

(a) k_T (b) C/A

(c) C/A + soft drop (d) C/A + minimisation

Figure 5.14: The difference yields ($TT\{15-45\} - TT\{8-9\}$) are shown for the τ_2 jet shape, in three consecutive bins of $p_T^{jet,ch}$, for each of the reclustering algorithms.

the distribution shifts to higher values for the $60 \leq p_T^{jet,ch} < 80$ GeV/c bin. However, it is important to note that the distribution contains large statistical errors at this $p_T^{jet,ch}$, which can cause fluctuations in the data points. This makes the extent of a shift (if any) less clear.

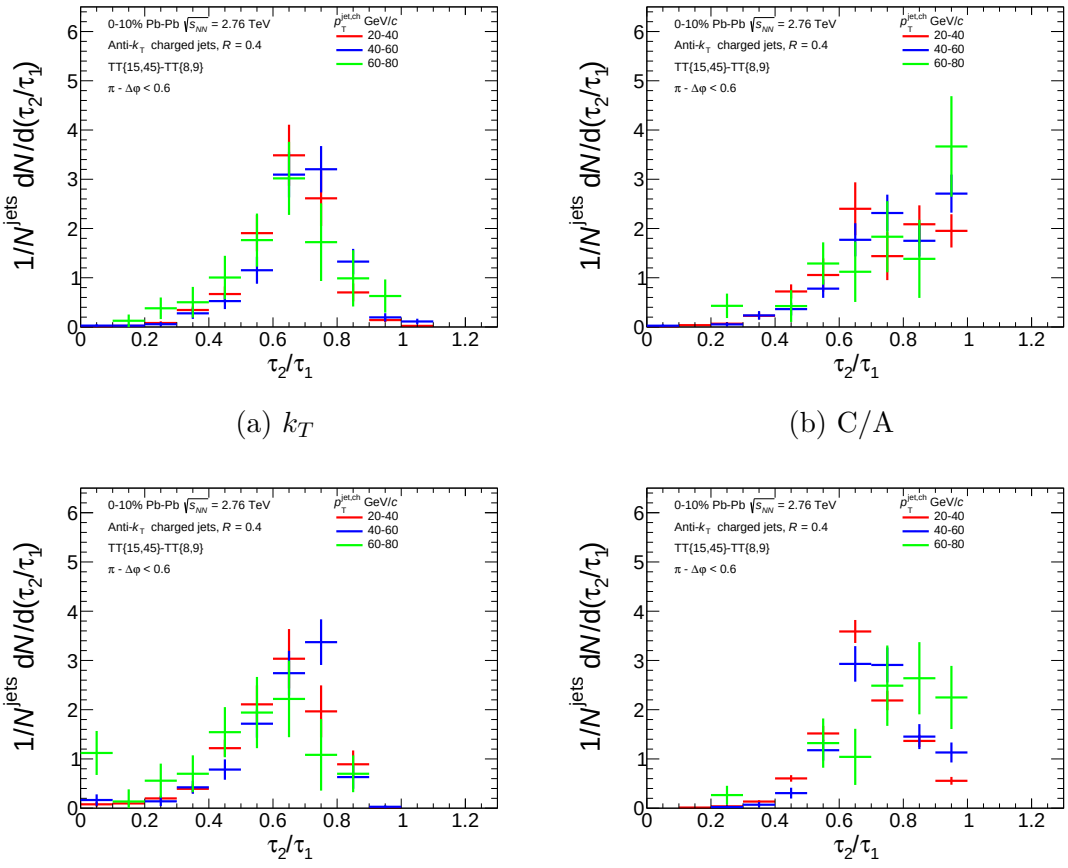

(a) k_T (b) C/A

(c) C/A + soft drop (d) C/A + minimisation

Figure 5.15: The difference yields ($TT\{15-45\} - TT\{8-9\}$) are shown for the τ_2/τ_1 jet shape, in three consecutive bins of $p_T^{jet,ch}$, for each of the reclustering algorithms.

5.4 Embedding Response

5.4.1 Embedding

The response matrices used to unfold the Pb-Pb data (see section 2.4.2), are constructed via an embedding process. Particle level MC jets are generated using PYTHIA. They are subsequently passed through a reconstruction of the ALICE detector using GEANT4 (see section 4.3.1), incorporating detector effects. This results in a set of detector level jets, which are matched to their particle level counterparts geometrically. The detector level jets are then embedded into real $0-10\%$ most

central Pb-Pb events. Jet clustering is performed in the presence of the heavy ion background. If required, background subtraction can be performed, at this stage, on these embedded level jets.

The embedded level jets are then matched geometrically to their detector level counterparts, to create a one to one matching. For this matching, there is an additional requirement that the PYTHIA tracks present in the embedded level jet, contain at least 50% of the matched detector level jet's $p_T^{jet,ch}$. In this way, through a series of matchings, embedded level jets can be compared back to their truth level counterparts. This comparison highlights both the impact of the Pb-Pb background and detector effects on the jets. The detector effects were shown to be small in section 4.3. Therefore, any large differences between the truth and embedded levels are due to the effects of the heavy ion background.

The matched truth and background subtracted embedded level jets, form the entries into the response matrices. In addition to the detector effects encoded into the response matrices in the pp analysis, the Pb-Pb response matrices also include the effects of background fluctuations across the event sample. These will be corrected from the input jet sample through the unfolding procedure.

5.4.1.1 $p_T^{jet,ch}$ Cut

The truth and detector level MC simulations used for the Pb-Pb analysis, are the same as those described for the pp analysis in section 4.3.1. However, the centre of mass energy of the collisions has been reduced to $\sqrt{s} = 2.76$ TeV, inline with that of the data. The only other difference compared to the pp analysis, is that there is no $p_T^{jet,ch}$ cut imposed on jets at the detector level. Instead, a $p_T^{jet,ch} \geq 20$ GeV/c cut is introduced at the subtracted embedded level. This is the minimum embedded level $p_T^{jet,ch}$ that will be used to construct the response matrices for the unfolding

procedure. Therefore, this cut is placed to minimise the size of the embedding data files.

5.4.2 Weighting

The same p_T hard bins and weighting technique, used to construct the response matrices in the pp analysis (see section 4.1), are used to merge the embedding responses as well. The weights obtained for each p_T hard bin, due to the interaction cross sections, can be found in table A.2. These differ to the pp case due to the different centre of mass energies of the collisions.

In addition to the above weights, there is an extra weighting factor that is also applied when constructing the Pb-Pb response matrices. Since the input data into the unfolding is a recoil sample, but the embedding is done with an inclusive sample, this weight parameter is used in order to transform the shape of the inclusive truth level distribution to that of a recoil jet distribution. This facilitates a more robust and stable unfolding. In order to calculate these weights, a recoil PYTHIA distribution is generated at $0 \leq p_{T,Truth}^{jet,ch} < 160$ GeV/c. The truth level inclusive PYTHIA distribution, used for the embedding process, is also plotted in the same $p_{T,Truth}^{jet,ch}$ range. This distribution is then scaled, such that the final bin ($155 - 160$ GeV/c) for both distributions coincide with one another, as shown in figure 5.16. The ratios of the two distributions, in each $p_T^{jet,ch}$ bin, form the additional weight components. 32 equally sized $p_T^{jet,ch}$ bins are constructed, from $0 - 160$ GeV/c. The respective weights, in increasing order of bin value, are presented in table A.3.

The final weight of each entry into the response matrix, is a product of the weight of the p_T hard bin in which it originated from and the additional inclusive to recoil transformation weight, which is dependent on its truth level $p_T^{jet,ch}$.

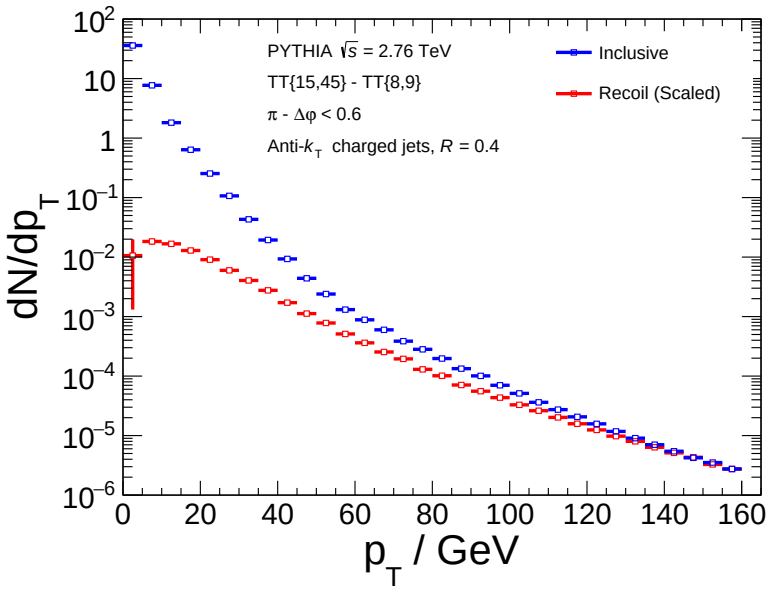

Figure 5.16: The inclusive (scaled) and recoil PYTHIA $p_{T,Truth}^{jet,ch}$ distributions, used to extract the inclusive to recoil weights, are shown.

5.4.3 Merged $p_T^{jet,ch}$

The final truth and subtracted embedded level distributions, obtained by merging the weighted (both components of the weighting) jets from all p_T hard bins, are shown in figure 5.17. In addition to the detector effects mentioned in section 4.3.3, the main differences between the subtracted embedded level and truth level distributions arise from fluctuations in the background, which make the embedded level distribution harder. It should be noted that from this point onwards, all embedded level distributions will include background subtraction, whether it is explicitly stated or not.

In addition to the final distributions, the merged p_T hard bin distributions without the inclusive to recoil aspect of the scaling (weighting), are also presented to illustrate the effect of these weights on both levels. The scaling has a larger impact at low $p_T^{jet,ch}$, where the inclusive and recoil yields exhibit the most difference in shape. This is due to the high p_T of the trigger hadron classes, which promote the likelihood of a

high $p_T^{jet,ch}$ jet recoiling from the trigger hadron. This makes the recoil distribution less steep than the inclusive one. At higher $p_T^{jet,ch}$, the corresponding scaled and not scaled distributions are almost parallel (same shape), due to the similarity of the recoil and inclusive distributions in these $p_T^{jet,ch}$ ranges.

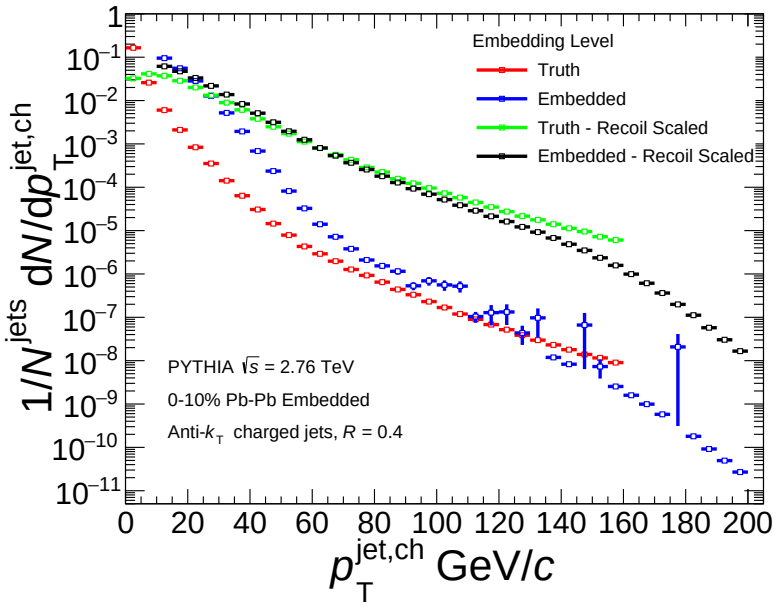

Figure 5.17: The truth and embedded level $p_T^{jet,ch}$ distributions, with and without the inclusive to recoil weighting, are shown.

5.4.4 τ_2/τ_1

The τ_2/τ_1 distributions at the truth and embedded levels, have already been discussed in section 5.2.4. Even though the final distributions will also include the inclusive to recoil weighting, which could alter the shape of both distributions, the matching between the two levels will remain the same. Therefore, the distributions will not be further examined in this section.

5.4.5 Response Matrices

Two-dimensional projections of the four-dimensional response matrices, used for the unfolding procedure, are shown in figures 5.18 and 5.19, for the axes including $p_T^{jet,ch}$ and τ_2/τ_1 respectively. The two-dimensional plots show the the truth vs subtracted embedded level distributions. The $p_T^{jet,ch}$ distribution shows a healthy diagonality between the truth and embedded levels. The smearing around this diagonal axis is larger than in the pp case (figure 4.14), due to the fluctuations of the heavy ion background.

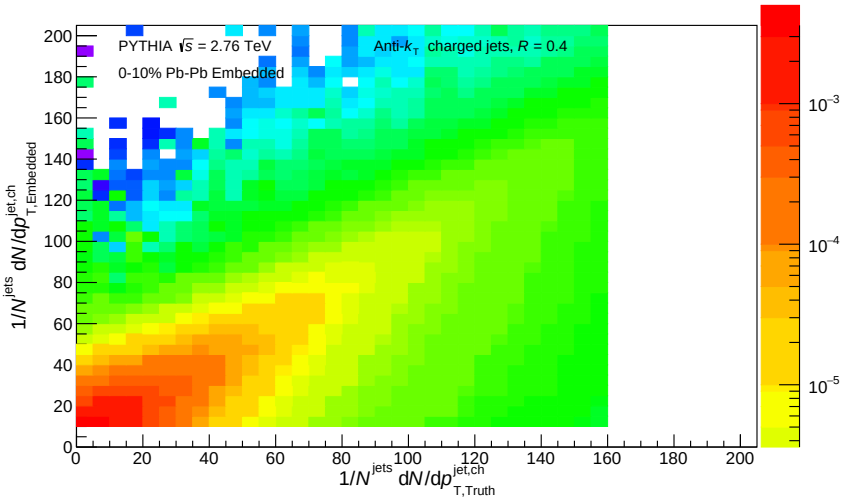

Figure 5.18: The two-dimensional projections of the truth vs embedded level $p_T^{jet,ch}$ components of the response matrix are shown.

The two-dimensional distributions for the τ_2/τ_1 jet shapes do not show a strong diagonality between the truth and embedded levels, for any of the reclustering algorithms. Instead, a large smearing is seen. In particular, low values of τ_2/τ_1 at truth level are smeared across a wide range of embedded level τ_2/τ_1 values. This is due to the low $p_{T,Truth}^{jet,ch}$ jets, which are highly affected by the background which remains in the jet cone after subtraction. These $p_{T,Truth}^{jet,ch}$ bins also contain the very low (~ 0) τ_2/τ_1 values at truth level, as they are more likely to contain two-tracked jets.

Figure 5.20 shows these two-dimensional τ_2/τ_1 plots for jets with $40 \leq p_{T,Truth}^{jet,ch} < 60$

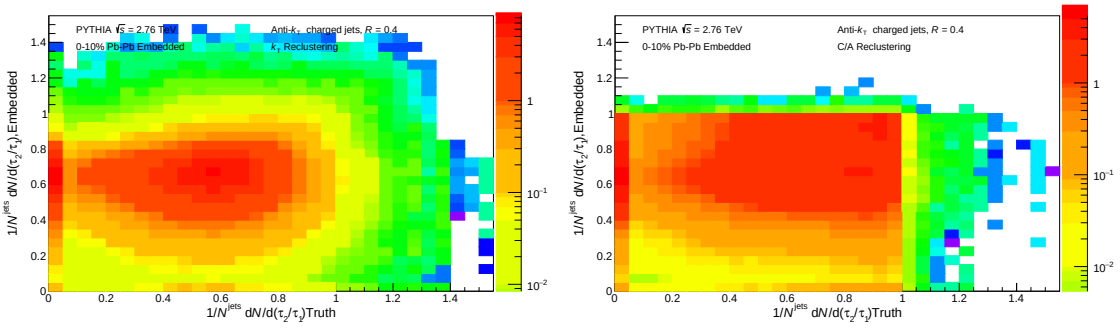

(a) k_T

(b) C/A

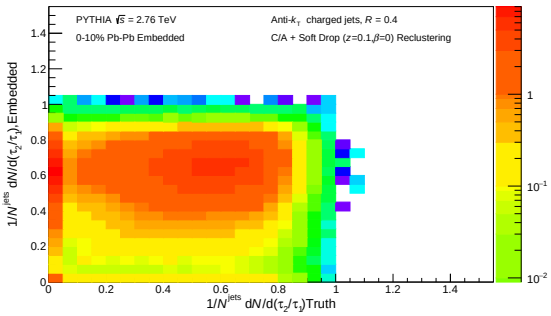

(c) C/A + soft drop

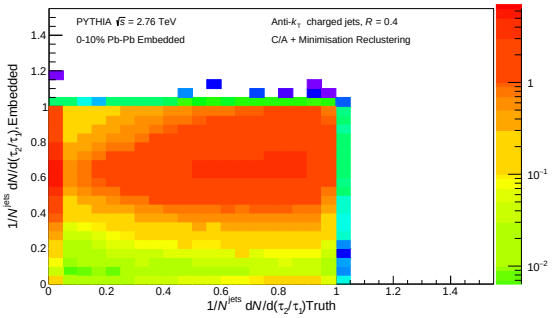

(d) C/A + minimisation

Figure 5.19: The two-dimensional projections of the truth vs embedded level τ_2/τ_1 components of the response matrices are shown, for each reclustering algorithm.

GeV/c. When the lowest $p_{T,Truth}^{jet,ch}$ $(20-40$ GeV/$c)$ bin is removed, a reduction of the smearing and an increase in the diagonality of the distributions is observed. However, the distributions are still not as strongly diagonal as in the case for pp collisions (figure 4.16). This indicates that a larger correction of the τ_2/τ_1 jet shapes, via the unfolding procedure, is expected in Pb-Pb collisions compared to pp.

5.5 Unfolding

The unfolding procedure and tests carried out for the Pb-Pb portion of this analysis, follow the same steps as those of the pp portion, described in section 4.4. Therefore, descriptions of identical procedures will not be provided, to avoid repetition. Only the relevant results will be presented, with any differences to the pp case highlighted.

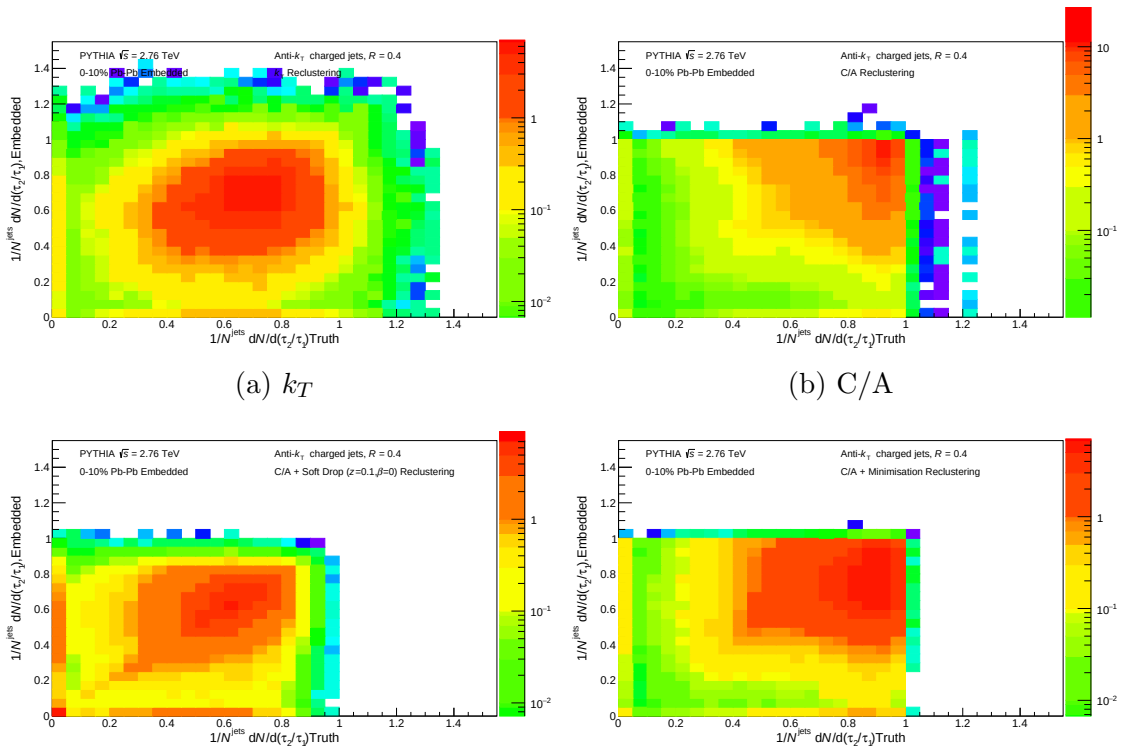

(a) k_T (b) C/A

(c) C/A + soft drop (d) C/A + minimisation

Figure 5.20: The two-dimensional projections of the truth vs embedded level τ_2/τ_1 components of the response matrices, at $40 \leq p_{T,Truth}^{jet,ch} < 60$ GeV/c, are shown for each reclustering algorithm.

5.5.1 Raw Data Statistics

The input ranges, to the unfolding, for the $p_T^{jet,ch}$ and τ_2/τ_1 jet shape are the same for each reclustering algorithm. These are $20-80$ GeV/c and $0.2-1.0$ respectively. The input matrices are shown in statistical form in figure 5.21. As with the case in pp, the lack of usual statistics in some bins is noted, with the unfolding tests used to determine the stability and validity of the final results.

5.5.2 Efficiency Correction

The procedure for determining the efficiency corrections is identical to the pp case, with the detector level cuts replaced by embedded level cuts. The calculated effi-

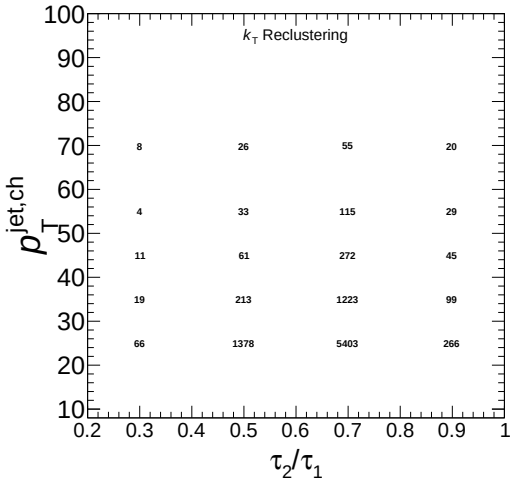

(a) k_T

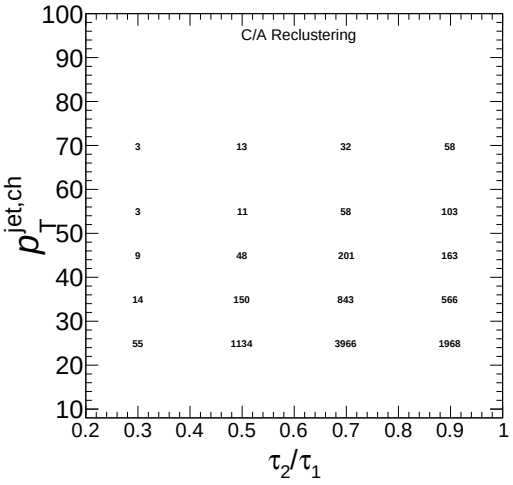

(b) C/A

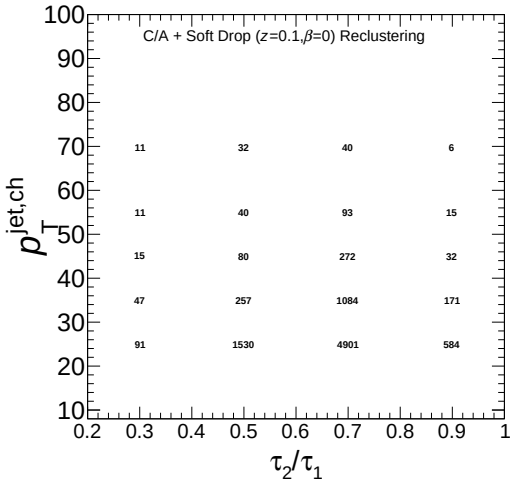

(c) C/A + soft drop

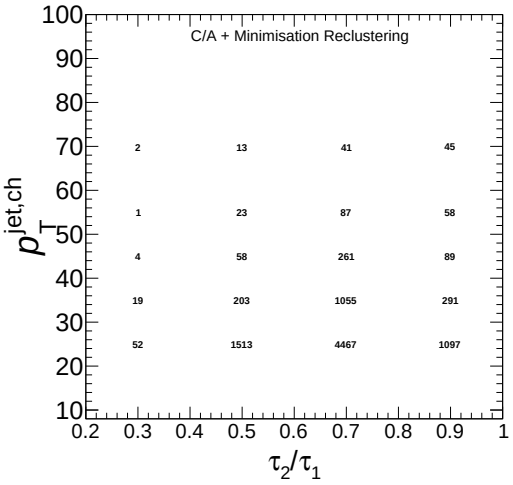

(d) C/A + minimisation

Figure 5.21: The data input matrices are shown in statistical form, in differential bins of $p_T^{jet,ch}$ and τ_2/τ_1, for each reclustering algorithm.

ciency distributions are shown in figures 5.22 and 5.23 for the $p_T^{jet,ch}$ and τ_2/τ_1 variables respectively. The unfolded distributions will be divided by the corresponding τ_2/τ_1 efficiencies, to obtain the final fully corrected results. The corrections are small across most τ_2/τ_1 bins. As expected, the bins on the borders of the embedded level cuts show a larger deviation from unity, than those further away from the edges. For the τ_2/τ_1 efficiencies, the first bin in particular is more affected. This is due to the (downward) fluctuations of the heavy ion background, which can cause

some jets to be over subtracted. This results in a significant part of the "true" jet signal being removed, leading to a possible reduction in τ_2/τ_1.

Even though the $p_T^{jet,ch}$ efficiency distributions are not applied to the unfolded τ_2/τ_1 distributions, it is important to ascertain that the corrections are small in the reported $40 \leq p_{T,Truth}^{jet,ch} < 60$ GeV/c range, where the final results are reported.

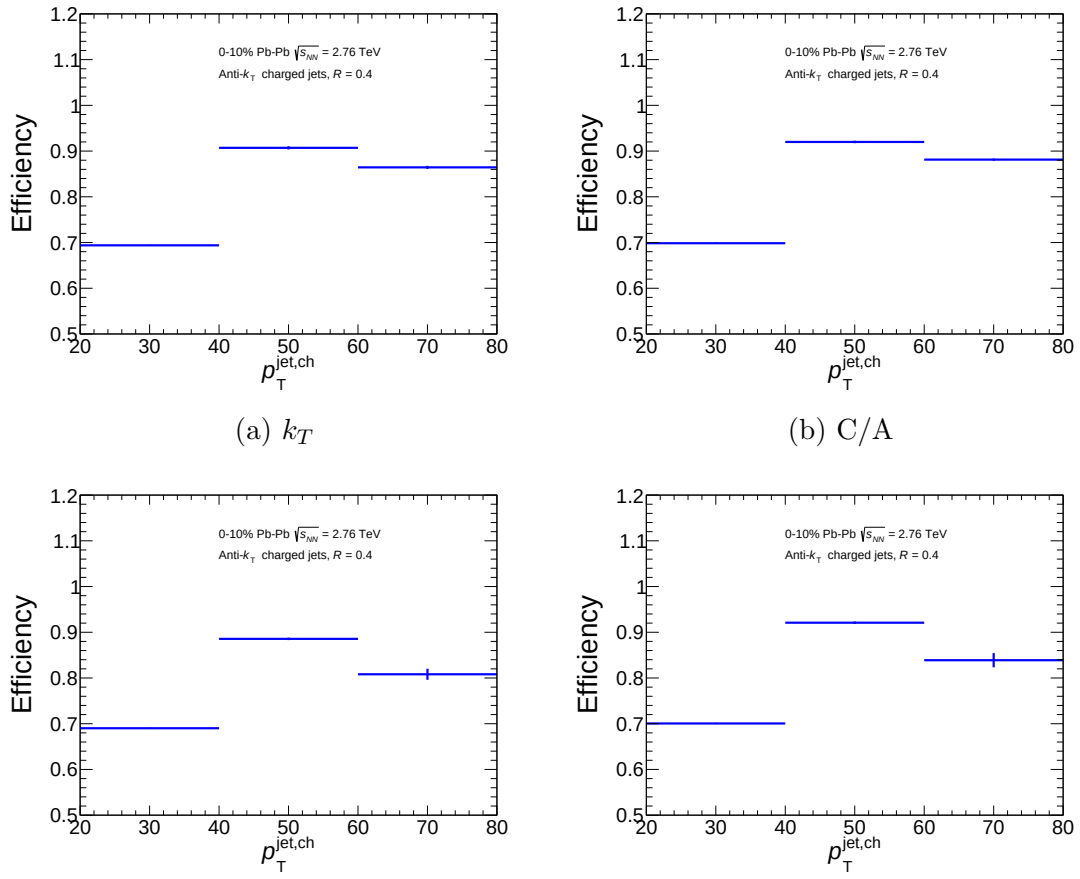

(a) k_T (b) C/A

(c) C/A + soft drop (d) C/A + minimisation

Figure 5.22: The efficiency correction is shown, as a function of $p_T^{jet,ch}$, for each reclustering algorithm.

5.5.3 Unfolding Tests

The unfolding tests presented below are identical to those performed in the pp analysis. Unless otherwise specified, all tests are performed within the unfolded

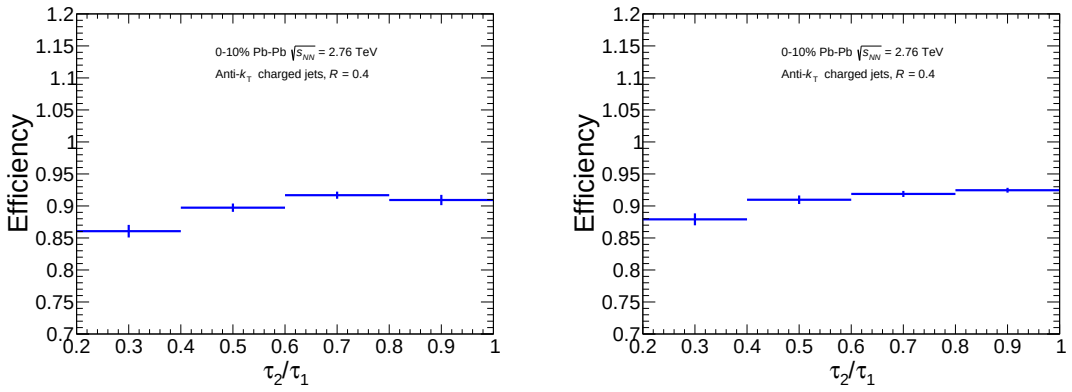

(a) k_T (b) C/A

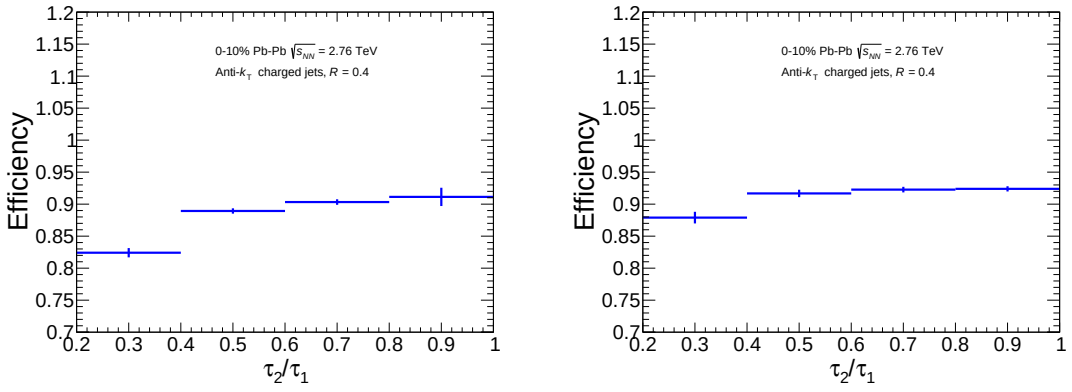

(c) C/A + soft drop (d) C/A + minimisation

Figure 5.23: The efficiency correction is shown, as a function of τ_2/τ_1, for each reclustering algorithm.

$40 \leq p_T^{jet,ch} < 60$ GeV/c range, which is the range in which the final results are presented. For each test, only the results for τ_2/τ_1 are shown. The results for $p_T^{jet,ch}$ were also calculated and are consistent with that of τ_2/τ_1. They have therefore been omitted to avoid repetition.

All the unfolding tests presented in this section are satisfied by the third iteration. However, the fourth iteration is closer to the converged solution than the third. Therefore, the fourth iteration is selected as the true solution, across all algorithms.

The unfolding tests which are not satisfied for the ΔR jet shapes, will also be shown below. These are the convergence and refolding tests, for the hard scale sensitive

and soft scale sensitive reclustering algorithms respectively.

5.5.3.1 Convergence Test

Figure 5.24 shows the convergence of the different iterations for the τ_2/τ_1 jet shapes. All bins converge onto a solution within just a few iterations.

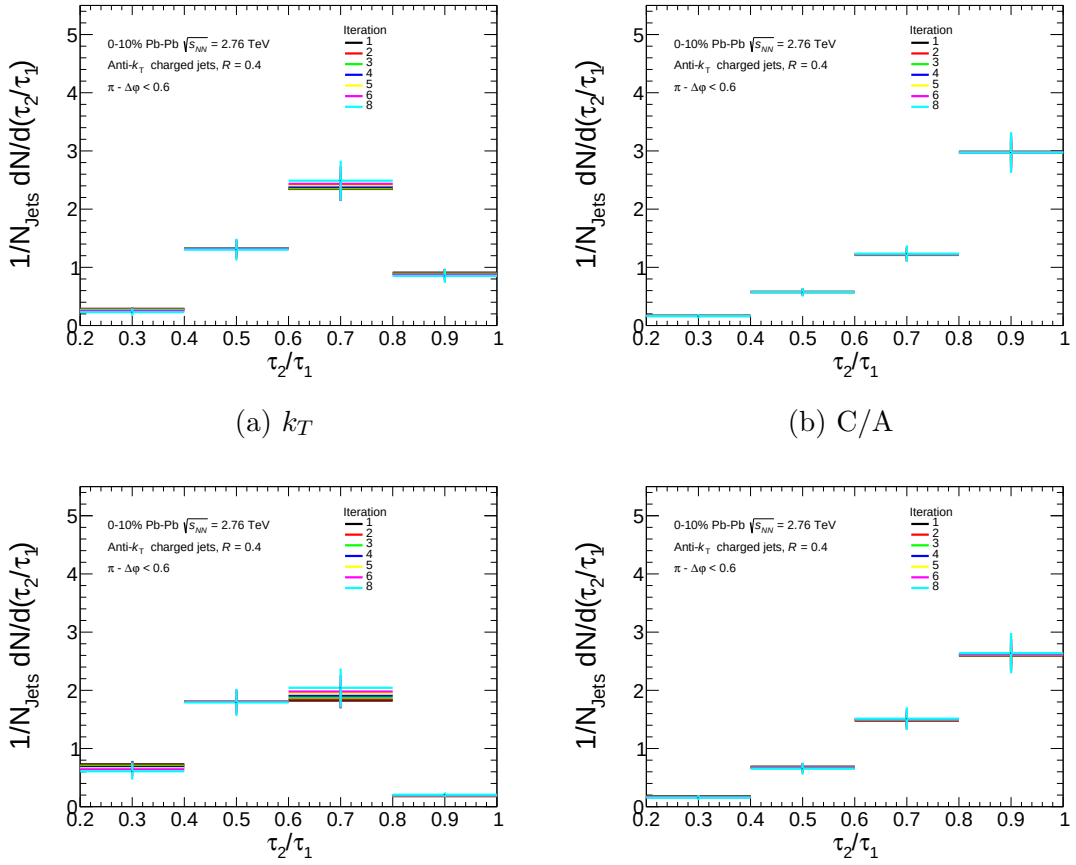

(a) k_T (b) C/A

(c) C/A + soft drop (d) C/A + minimisation

Figure 5.24: The convergence tests for the τ_2/τ_1 jet shape, at $40 \leq p_T^{jet,ch} < 60$ GeV/c, are shown for each reclustering algorithm.

The convergence tests for the ΔR jet shapes, measured using the hard scale sensitive reclustering algorithms, are shown in figure 5.25. The second and third bin for the k_T reclustering and the first and third bin for the soft drop with C/A reclustering, show a lack of convergence with increasing iterations. These bins mirror the place-

ment of the double peak structures of the corresponding subtracted embedded level distributions (figure 5.5). This points to unstable and unreliable unfolded solutions. Therefore, fully corrected results for the ΔR jet shapes, using these algorithms, cannot be presented.

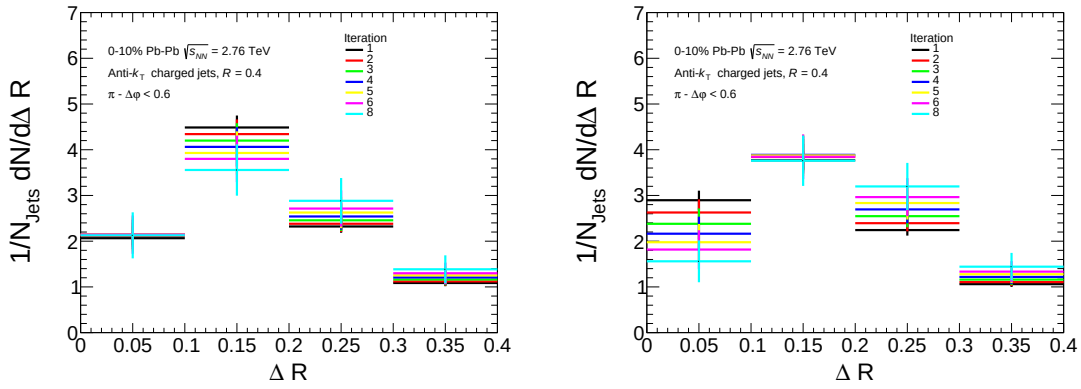

(a) k_T (b) C/A + soft drop

Figure 5.25: The convergence tests for the ΔR jet shape, at $40 \leq p_T^{jet,ch} < 60$ GeV/c, are shown for the hard scale sensitive reclustering algorithms.

5.5.3.2 Refolding Test

Refolding is done for the full input range of $20 \leq p_T^{jet,ch} < 80$ GeV/c. The results are shown in figure 5.26 for the τ_2/τ_1 jet shape. The refolding tests are satisfied by the third iteration and converge by the fourth iteration, across all bins.

The refolding tests for the ΔR jet shapes, measured using the soft scale sensitive reclustering algorithms, are shown in figure 5.27. The second bin for the C/A reclustering algorithm shows a very large deviation from unity, indicating that the unfolding is unreliable. This is due to the absence of counts in this bin, at $40 \leq p_T^{jet,ch} < 60$ GeV/c, in the input data matrix (figure 5.6). For the C/A with minimisation case, the convergence of the iterations is also outside the 10% tolerance of the refolding test, for the first two bins. This is again due to the absence of counts in some bins of the input data matrix (figure 5.6) and indicates that the unfolded

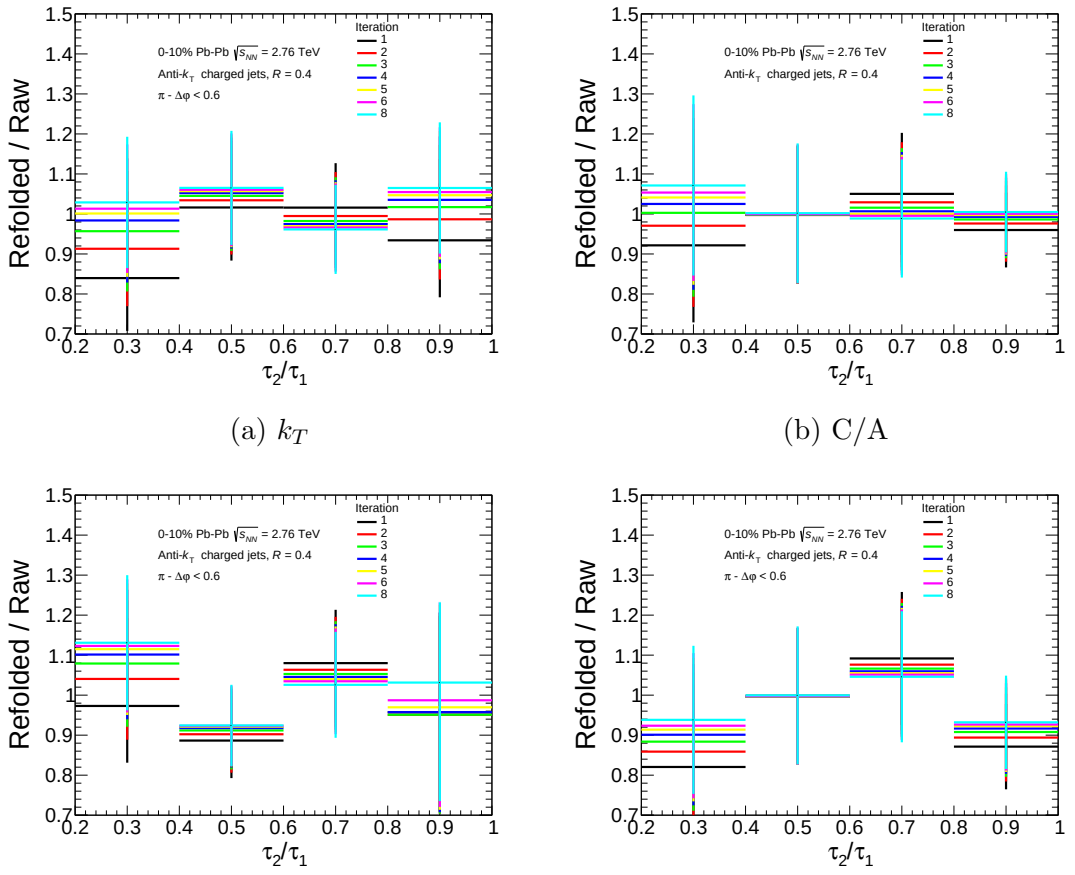

(a) k_T (b) C/A

(c) C/A + soft drop (d) C/A + minimisation

Figure 5.26: The refolding tests for the τ_2/τ_1 jet shape, at $20 \leq p_T^{jet,ch} < 80$ GeV/c, are shown for each reclustering algorithm.

solution is unreliable. However, since the convergence is not very far from the 10% tolerance of the refolding, ongoing discussions are being held as to whether this tolerance can be relaxed for such cases where the input into the unfolding has low (or no) statistics in some bins. To date, no consensus has been reached and therefore no fully corrected results for the ΔR jet shapes, using these algorithms, can be presented.

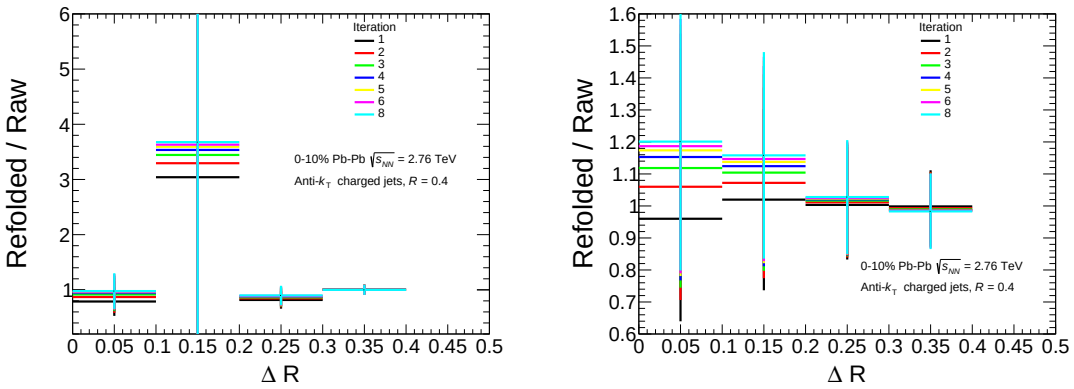

(a) C/A (b) C/A + minimisation

Figure 5.27: The refolding tests for the ΔR jet shape, at $20 \leq p_T^{jet,ch} < 80$ GeV/c, are shown for the soft scale sensitive reclustering algorithms.

5.5.3.3 Closure Test

The closure test is performed using 1.2% of the MC statistics, at embedded level, as an input to the unfolding. This represents the statistical reach of the measured data set, used as input to the default unfolding. The remainder of the MC statistics are used to construct the response matrix. Figure 5.28 shows the results for each of the four algorithms. The closure tests are satisfied within 10%, across all τ_2/τ_1 bins, from the first iteration. The bins that deviate the most from unity tend to have the largest statistical errors. This indicates that the deviations are most likely due to statistical fluctuations.

5.5.3.4 Pearson's Coefficient

The smeared response matrices used in Pb-Pb collisions for the unfolding procedure, are expected to produce more correlations between different bins in the unfolded solution (see section 4.4.3.4), compared to the case in pp. However, this is more qualitative than quantitive, since it is difficult to measure how "un-diagonal" the response matrices are. The Pearson's coefficients are shown in figure 5.29, for the

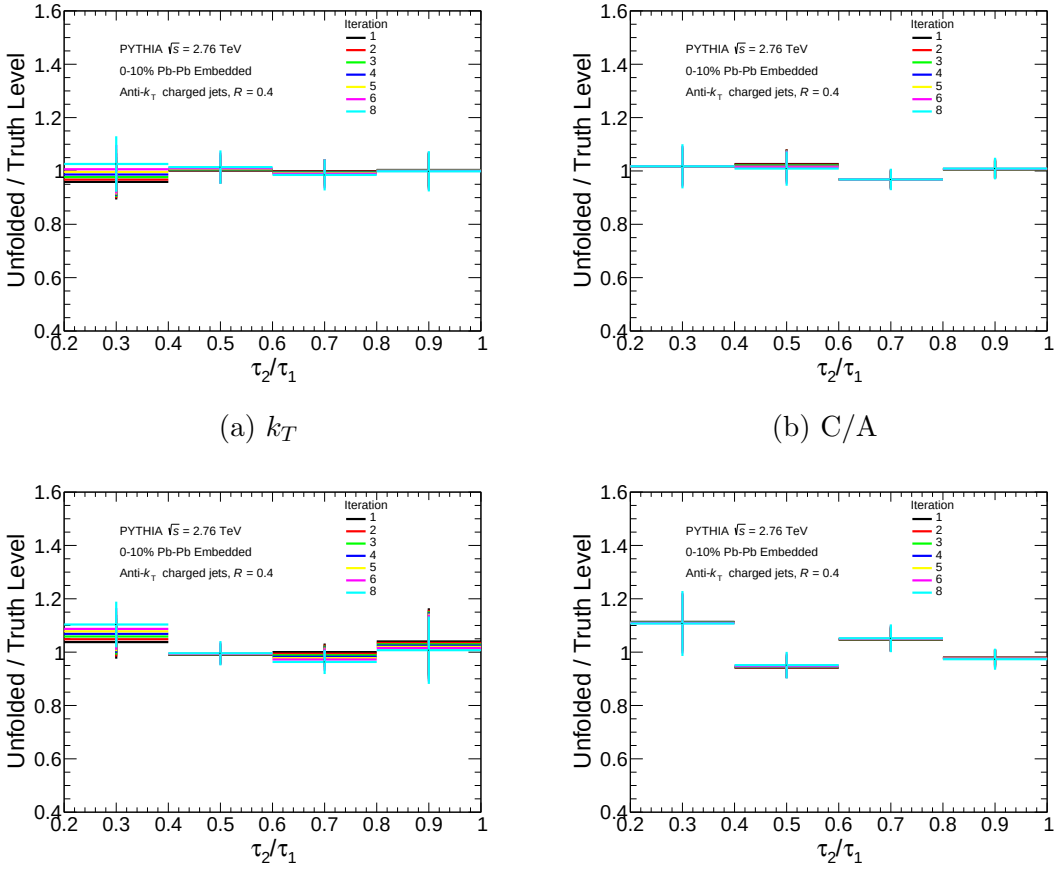

(a) k_T (b) C/A

(c) C/A + soft drop (d) C/A + minimisation

Figure 5.28: The closure tests for the τ_2/τ_1 jet shape, at $40 \leq p_{T,Truth}^{jet,ch} < 60$ GeV/c, are shown for each reclustering algorithm.

fourth unfolded iteration. The correlations mirror the smearing in the response matrices (figure 5.20). Due to this smearing, the Pearson's coefficients are a less reliable test of the correct unfolding iteration in Pb-Pb than in pp.

5.6 Systematic Uncertainties

In addition to the four systematic errors considered in section 4.5, there are two additional sources of systematic error included in the Pb-Pb analysis. These are the subtraction and event plane systematics. The subtraction error takes into account the effect of the choice of subtraction algorithm, on the unfolded result. The event

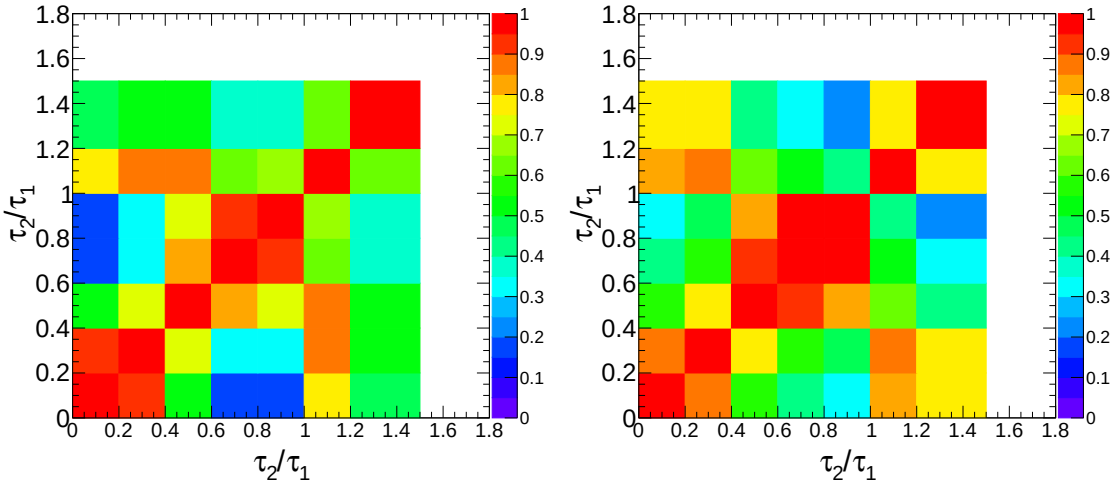

(a) k_T

(b) C/A

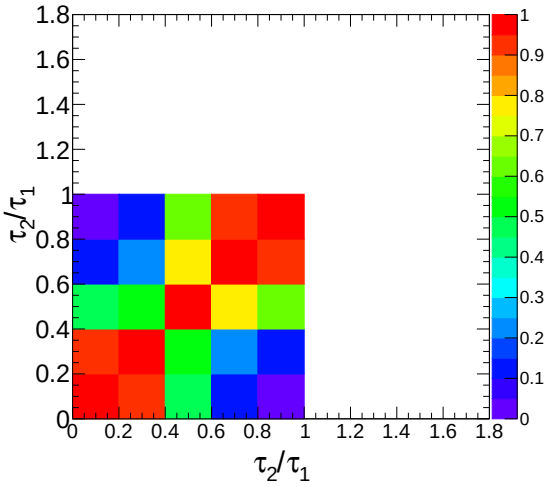

(c) C/A + soft drop

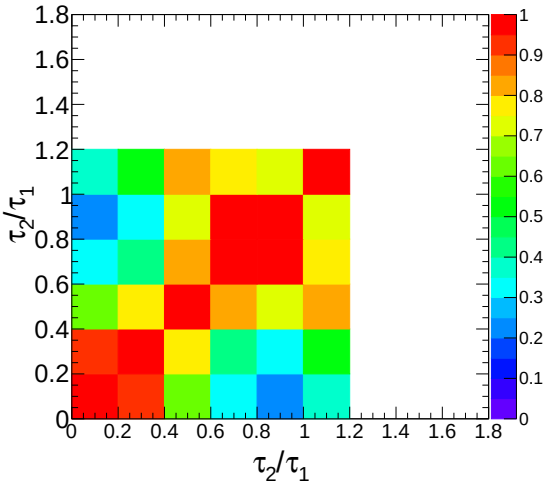

(d) C/A + minimisation

Figure 5.29: The Pearson's coefficients for the τ_2/τ_1 jet shape, at $40 \leq p_T^{jet,ch} < 60$ GeV/c, are shown for the fourth unfolded iteration for each reclustering algorithm.

plane systematic accounts for any biases in the angular selection of trigger hadrons, relative to the collision geometry. A more detailed description of these two systematic errors, along with the calculations required to obtain them, are presented in Appendix C. Numerical tables listing the contribution of each systematic, can also be found in Appendix C. Due to the incompatibility of derivative subtraction with the soft drop grooming procedure, the subtraction systematic is omitted from the τ_2/τ_1 jet shape measured using soft drop with C/A reclustering.

The relative contributions of each systematic uncertainty, compared to the default solutions, are shown in figure 5.30 for the τ_2/τ_1 jet shapes. The contributions of each systematic source vary across bins and algorithms. The choice of prior, regularisation and subtraction uncertainties tend to be the largest sources of systematic error in most bins. In particular, for the soft scale sensitive reclustering algorithms (C/A with and without minimisation), the large contribution from the subtraction systematic error was predicted in section 5.2.4. This was due to the large differences between the corresponding subtracted embedded level τ_2/τ_1 distributions, when using the constituent and second order derivative subtraction procedures.

5.7 Pb-Pb Results

5.8 Inclusive ΔR Jet Shape

Unfolding tests for the ΔR jet shapes, show a lack of stability and reliability of the unfolded results. The reasons for this have been discussed in section 5.2.1.1. Therefore, it is not currently possible to obtain a fully corrected measurement of this jet shape. Instead, a comparison of the constituent subtracted inclusive jet shape, measured in the data, to the constituent subtracted embedded level jet shape, is presented in figure 5.31 for the k_T reclustering algorithm. The $p_T^{jet,ch}$ bin chosen for this comparison, in both distributions, is $80 - 100$ GeV/c, since the contribution of combinatorial jets in this bin is suppressed for jets of $R = 0.4$ (see section 2.3.1). Even though the shape is presented at an uncorrected level, it is expected that any background and detector effects present in the data, will also be reproduced in the embedded sample. This is beacuse the embedded sample is comprised of detector level jets (incorporate detector effects) which are embedded into real Pb-Pb data (incorporate detector and background effects). Therefore, any differences

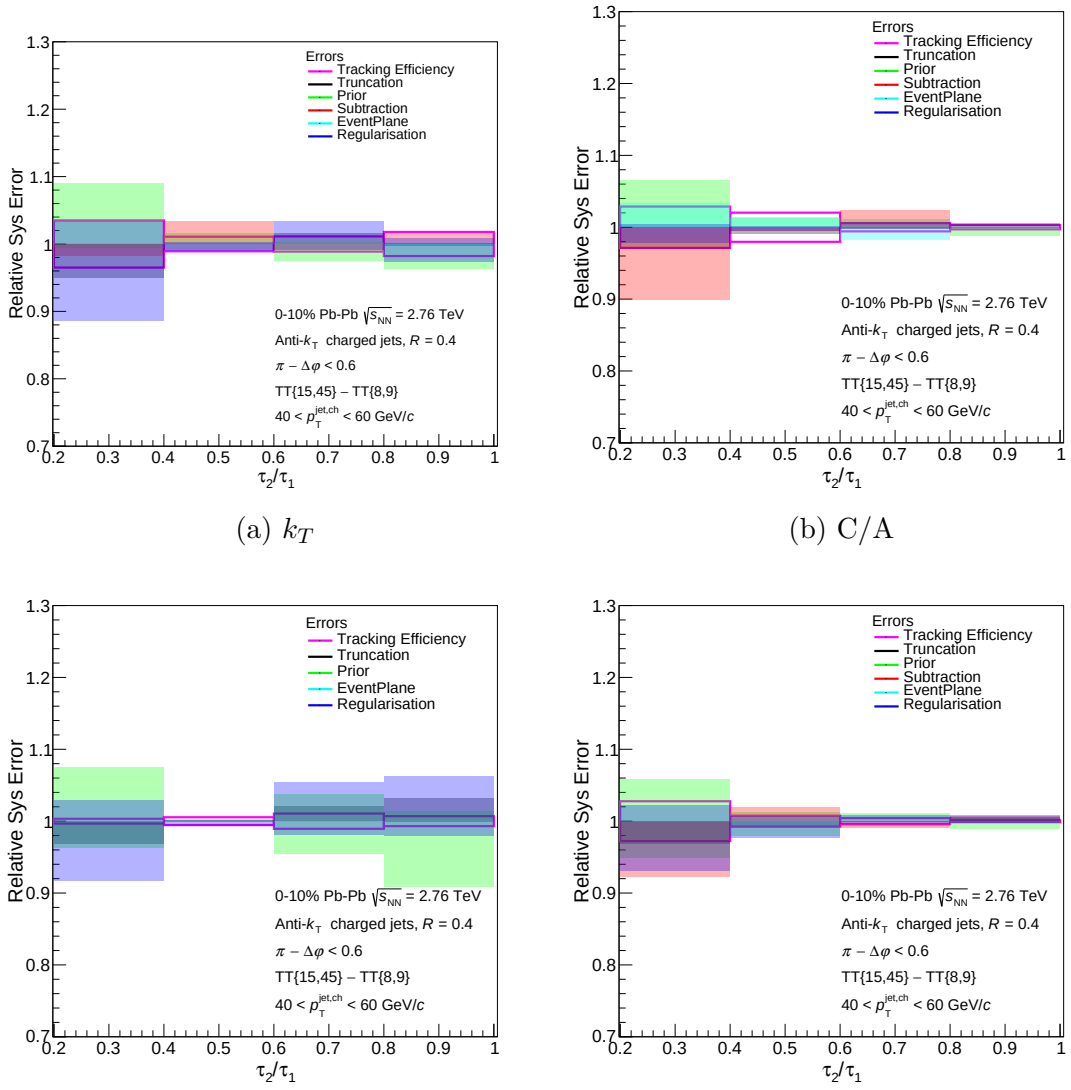

(a) k_T (b) C/A

(c) C/A + soft drop (d) C/A + minimisation

Figure 5.30: The relative contributions of each systematic uncertainty for the τ_2/τ_1 jet shape, at $40 \leq p_T^{jet,ch} < 60$ GeV/c, are shown for each reclustering algorithm.

between the two samples point to medium induced modifications of the jets in the data, as quenching effects are not present in the embedded sample. This assumes that PYTHIA is in agreement with the measured ΔR distribution in vacuum (pp collisions), which is shown to be true in the next chapter.

A good agreement between the inclusive data and embedded sample is seen in figure 5.31. The ratio of the two distributions is consistent with unity, within statistical

errors, across almost all bins. The only exception occurs in the first bin, where the statistics are low. Therefore, no quenching effects are discernible from this measurement. The presence of coherence effects would manifest as a suppression of jets at large ΔR. A possible hint of this can be seen in the very last bin (0.4-0.45), where there are no jets in the measured data sample. This could also be the source of the enhancement in the first bin, since the distributions are normalised to the number of jets (self normalised). However, as this is at the statistical limit of the data set, no conclusion can be drawn at the present stage. One way to test this further would be to make the same measurement using jets with $R > 0.4$.

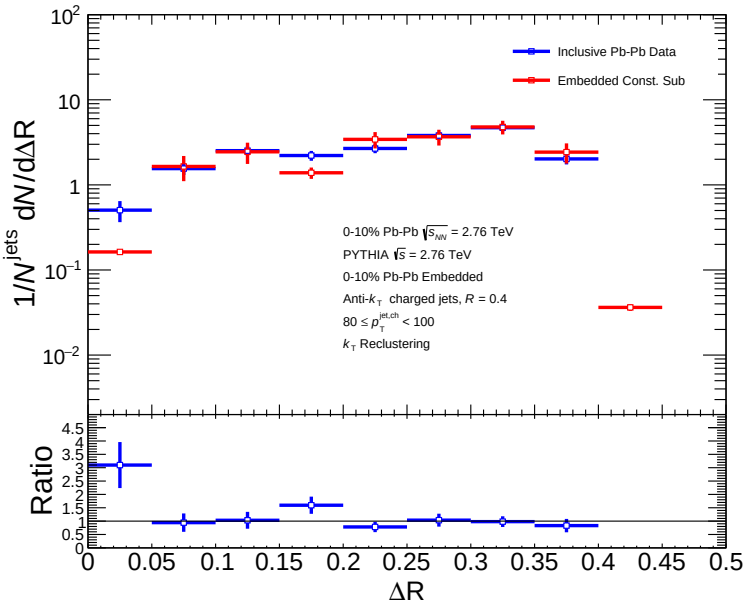

Figure 5.31: A comparison of the ΔR distributions in the inclusive subtracted measured data vs the subtracted embedded level sample, at $80 \leq p_T^{jet,ch} < 100$ GeV/c, is shown for the k_T reclustering algorithm. The ratio of the two distributions is also presented.

The subtracted embedded level sample, accounts for the detector effects and background fluctuations present in the measured subtracted data. In this way, comparisons such as the one made above can be sensitive to jet quenching effects. However, even though the background fluctuations have been fully reproduced in the embedded sample, they can mask quenching effects in the data. For example, in the case

of the ΔR jet shape measured with a hard scale sensitive reclustering algorithm, it has been shown that background fluctuations can induce soft "fake" axes. These axes hide the true hard splittings, which could have been modified in the presence of the QGP, in the measured data. Such modifications would not appear in the inclusive sample used in the above comparison. This highlights the importance of the unfolding procedure, which can remove the effects of background fluctuations and correct the measured sample back to particle level. Therefore, even though no QGP effects are discernible in the comparison presented above, a fully corrected result has the potential to alter this conclusion. To this end, the comparison has only been presented for the k_T reclustering algorithm, as an example of an uncorrected result when unfolding is not possible. However, it also serves to further highlight the importance of the unfolding procedure, when measuring jet shapes in heavy ion collisions.

5.9 Unfolded τ_2/τ_1 Jet Shapes

Throughout the course of this chapter, the analytical steps involved in measuring and correcting the raw τ_2/τ_1 jet shapes have been presented. The final unfolded distributions, with full systematic and statistical uncertainties, are shown in figure 5.32. These results are presented at $40 \leq p_T^{jet,ch} < 60$ GeV/c for all four algorithms. The measured background subtracted recoil jet shapes, without unfolding, are also included. The unfolding corrections are larger, across all algorithms, than in the pp case, due to the fluctuations in the heavy ion background. However, the extent of the corrections are exaggerated by the self normalisation properties of the distributions.

The unfolding procedure shifts the τ_2/τ_1 distributions measured with the hard scale sensitive reclustering algorithms (k_T and soft drop with C/A reclustering), to lower values, by correcting for the remaining background effects (see section 5.2.4). For the

soft scale sensitive reclustering algorithms (C/A with and without minimisation), the unfolding shifts the distributions towards unity, which is expected in the absence of background effects (see section 5.2.4). The unfolded solutions for each algorithm in Pb-Pb collisions, closely resemble the corresponding unfolded solutions in vacuum (pp collisions), which were presented in figure 4.33. Therefore, the same physics arguments that were made in section 4.6, apply to the fully corrected results in Pb-Pb collisions as well.

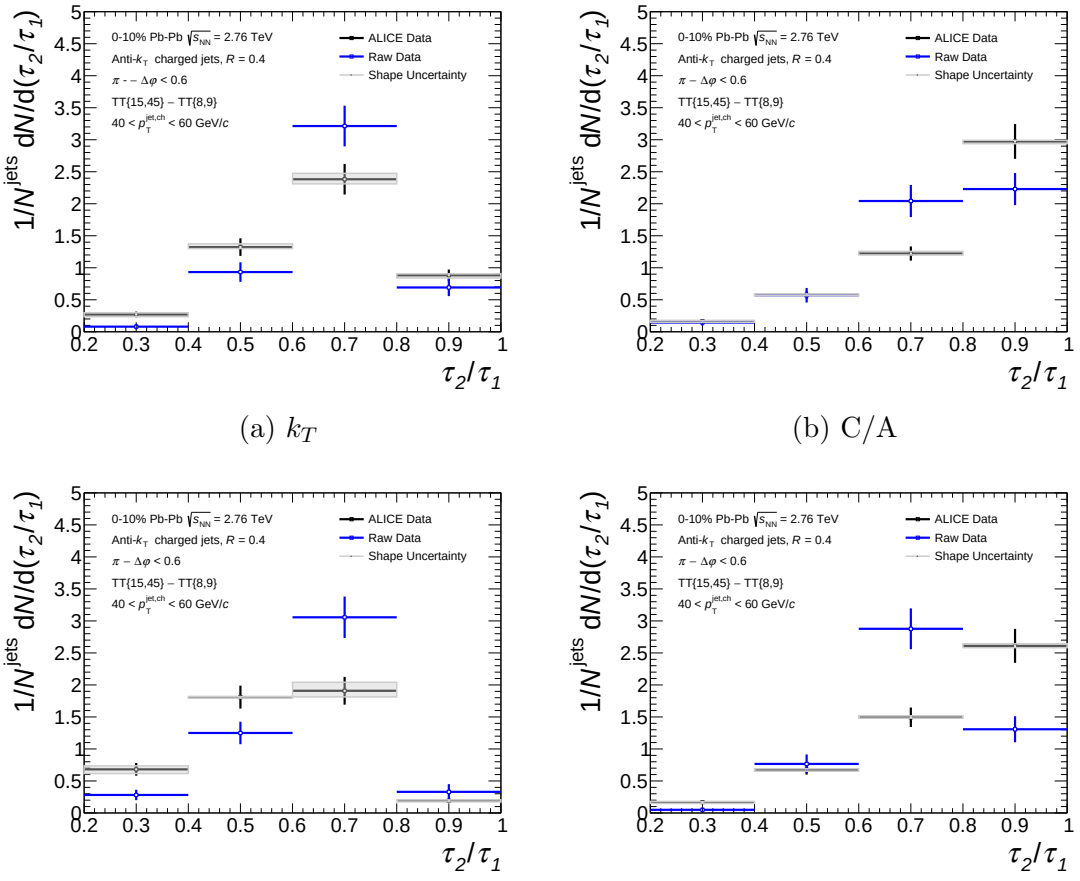

(a) k_T (b) C/A

(c) C/A + soft drop (d) C/A + minimisation

Figure 5.32: The fully corrected τ_2/τ_1 distributions in Pb-Pb collisions are shown, along with their associated statistical and systematic uncertainties, at $40 \leq p_T^{jet,ch} < 60$ GeV/c for each of the reclustering algorithms. The background subtracted recoil τ_2/τ_1 jet shapes (not unfolded), measured at $40 \leq p_T^{jet,ch} < 60$ GeV/c in Pb-Pb collisions, are also provided for comparison.

CHAPTER 6

Simulations And Results

In this chapter, MC results obtained using the PYTHIA event generator [124], which is described in section 6.1, will be presented. Section 6.2 will include simulated toy models of the τ_2/τ_1 jet shapes, probing the effect of adding a hard or semi-hard particle to the jet. Section 6.3 will compare the vacuum like simulations to the unfolded data. In pp, this will test the splitting and fragmentation properties of the event generator, using a variety of different reclustering algorithms. Since the pp and Pb-Pb data sets are at different centre of mass energies, the results are not directly comparable. Therefore, the unfolded pp results will be used to validate PYTHIA, before it is compared to the Pb-Pb results. In Pb-Pb, the comparison of vacuum like simulations to the unfolded data will be used to investigate changes to the fragmentation and splitting functions, induced by the QGP.

6.1 PYTHIA

This section will detail the properties of the PYTHIA event generator and the specific tunes used in this work.

6.1.1 PYTHIA 6

PYTHIA is one of the most complete event generators available for particle collisions. Elementary particles are collided and the event is evolved all the way to the multi-particle final states observed at real colliders. Where the physics is well described, the underlying processes are calculated. Where there is not such a clear physical description, numerical models and data driven approaches are used. The ability to control many of the underlying processes, allows for the generation of specific tunes which can be tailored to different experiments and analyses.

6.1.1.1 Perugia 2011

The PYTHIA tune used for model comparisons in this work, is the Perugia 2011 tune [125]. The Perugia family of tunes were developed to prepare for LHC era physics. Parameters were adjusted according to experimental data, to better describe the shower and underlying event. The Perugia 2011 tune in particular, uses some early lessons learnt from the first LHC data sets at $\sqrt{s} = 900$ GeV and $\sqrt{s} = 7$ TeV, to further optimise parameters. These include a faster scaling of multiplicity with energy, as motivated by ALICE [126] and ATLAS [127]. The underlying event is also slightly larger compared to the Perugia 2010 tune, motivated by measurements at ATLAS [128].

6.1.1.2 Tune A

The tune used to generate the MC component of the embedding process, is Tune A [129]. This tune provides a good description of the underlying event. The initial state radiation is increased by increasing the maximum parton virtuality for showers (in effect the Q^2 scale is increased). The radius of the hadronic hard core is also increased, which better describes multi-partonic interactions.

6.2 Simulations

This section will detail simulated results, using PYTHIA Perugia 2011 at $\sqrt{s} = 2.76$ TeV, to probe the sensitivity of the τ_2/τ_1 shape to the presence of an additional hard prong in the jet. This models the hard and semi-hard induced gluon emissions, predicted to arise due to energy loss in the QGP. In the tests outlined below, a PYTHIA jet is generated and subsequently modified by the addition of a hard particle. The resulting jet is then reclustered and its τ_2/τ_1 value is compared to that of the original jet. By comparing the modified and original jets, this test can also be used to model the suppression of two-prong jets (the suppression of one of the prongs), resulting from coherence effects in the QGP.

6.2.1 Additional Hard Prong

The effects of the additional constituent on the τ_2/τ_1 jet shapes are investigated systematically, in differential values of the constituent's p_T^{ch} and angle from the jet axis. Four track p_T^{ch} classes are chosen, each relative to the original $p_T^{jet,ch}$. These are 15%, 30%, 45% and 60%. Three angular classes are chosen at $\delta R = 0.1$, 0.2 and 0.3, where δR is the $\eta - \phi$ distance of the additional track to the jet axis. In all

cases, the p_T^{ch} of the additional track is not considered when calculating the $p_T^{jet,ch}$. This ensures that the modified jet is compared in the same $p_T^{jet,ch}$ bin as the original jet ($40 \leq p_{T,Truth}^{jet,ch} < 60$ GeV/c).

6.2.1.1 p_T^{ch}

The effect of the additional particles's p_T^{ch} is investigated by keeping the angular distance of the particle to the jet axis constant, while the p_T^{ch} of the particle is varied. The results for all four reclustering algorithms are shown in figures 6.1, 6.2 and 6.3 for $\delta R = 0.1$, 0.2 and 0.3 respectively.

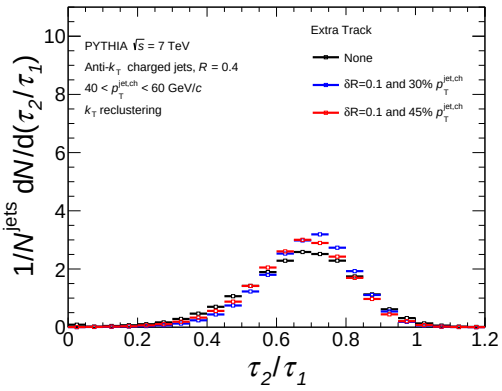

(a) k_T

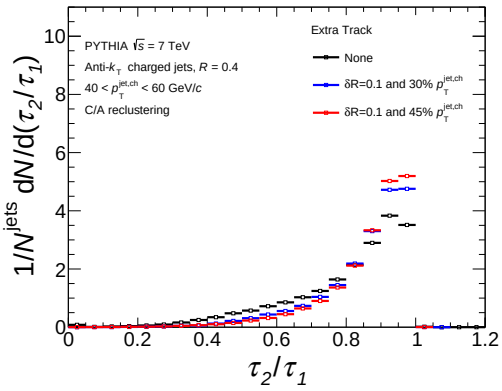

(b) C/A

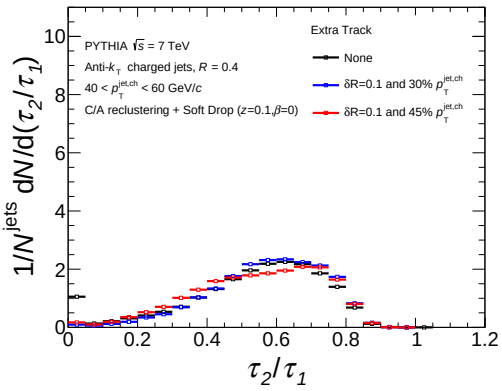

(c) C/A + soft drop

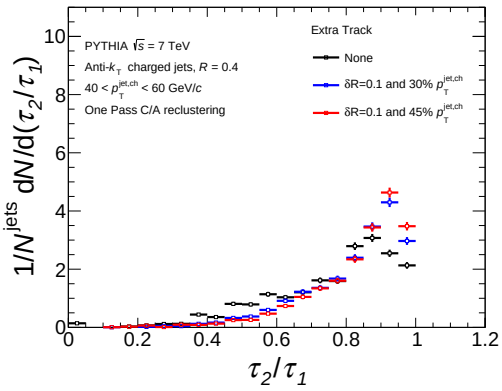

(d) C/A + minimisation

Figure 6.1: The τ_2/τ_1 distributions, for jets with an additional constituent at δR =0.1, are shown in differential p_T^{ch} classes.

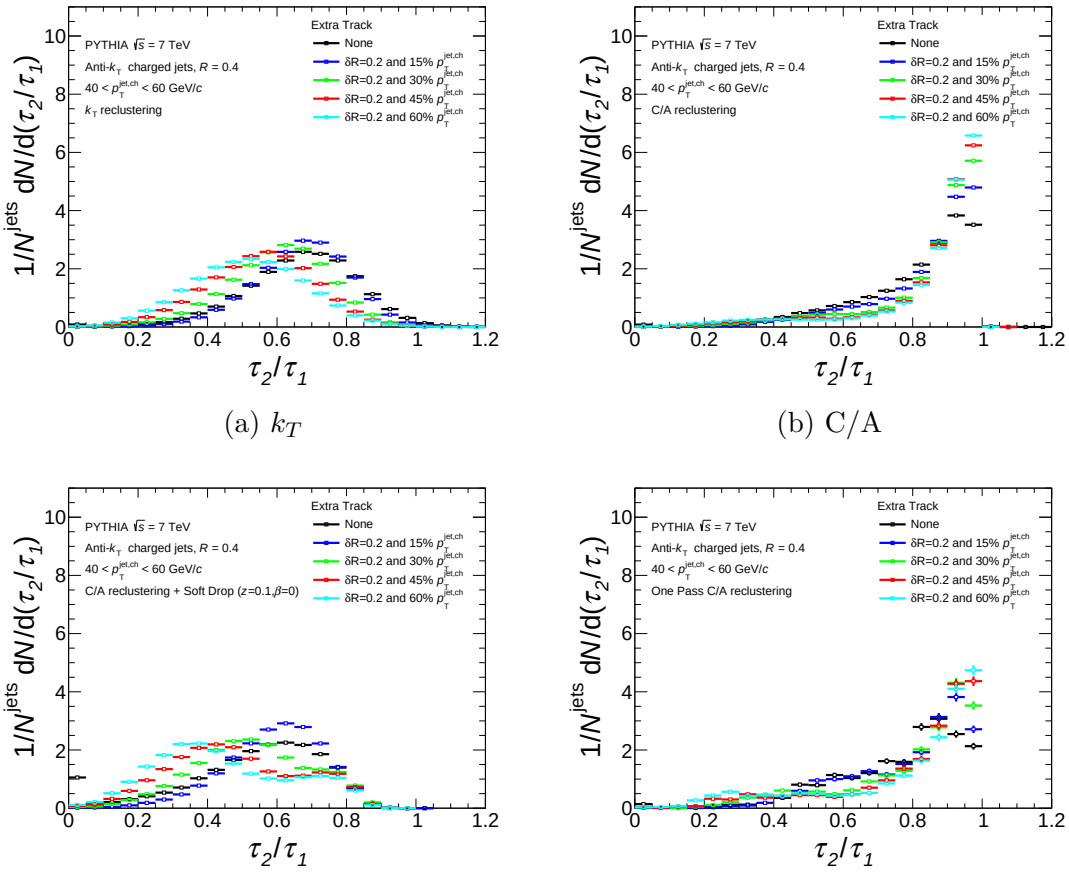

(a) k_T (b) C/A

(c) C/A + soft drop (d) C/A + minimisation

Figure 6.2: The τ_2/τ_1 distributions, for jets with an additional constituent at δR =0.2, are shown in differential p_T^{ch} classes.

For the cases where the additional constituent is close to the jet axis (figure 6.1), the effect of the constituent on the τ_2/τ_1 distributions is small across all algorithms and shows very little p_T^{ch} dependence. For both τ_1 and τ_2, the reclustering axes will remain in the jet core (no significant shift), leading to only small changes in the τ_2/τ_1 distributions.

The impact on the τ_2/τ_1 jet shape is larger, when the additional particle is displaced significantly from the jet axis (figures 6.2 and 6.3). In this case, a strong p_T^{ch} dependence is observed. For the reclustering algorithms sensitive to the hard scales (k_T and C/A preceded by soft drop), the value of τ_2/τ_1 becomes smaller with increasing p_T^{ch}. This reflects the increasing two-prongness of the jet's substructure.

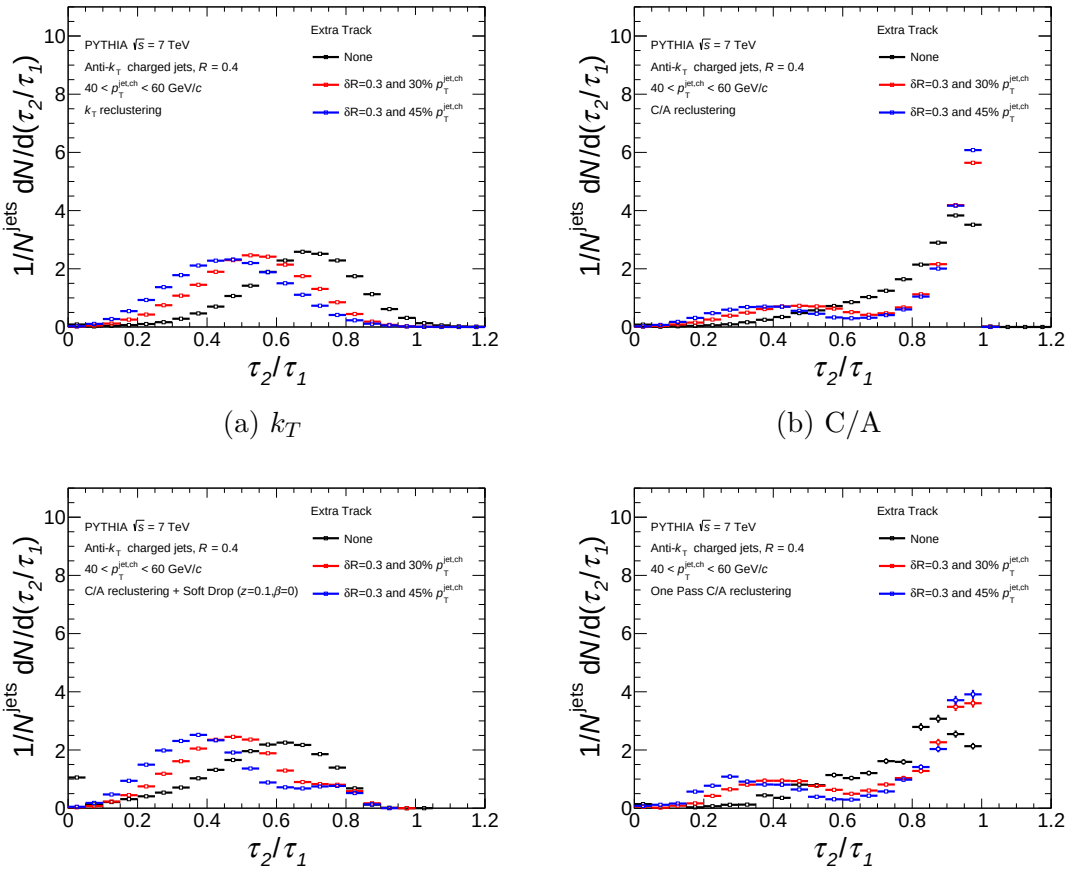

(a) k_T (b) C/A

(c) C/A + soft drop (d) C/A + minimisation

Figure 6.3: The τ_2/τ_1 distributions, for jets with an additional constituent at δR =0.3, are shown in differential p_T^{ch} classes.

An exception is observed for the case where the additional constituent at $\delta R = 0.2$, carries only 15% of the original jet's $p_T^{jet,ch}$. Here, the value of τ_2/τ_1 undergoes a very small increase. This is because the additional particle's p_T^{ch} is not significant enough to shift the reclustering axes by a large amount (they stay mostly in the jet core). As a result, the additional particle's p_T^{ch} is uncorrelated to the returned axes which increases the τ_2/τ_1 value. This shows that the p_T^{ch} dependence of the additional particle is only significant once the particle carries a large enough fraction of the $p_T^{jet,ch}$. In essence, the sensitivity of the reclustering algorithms to the hard scale, requires that the additional radiation be of a hard enough nature before it is considered as a second prong.

For the C/A and C/A with minimisation algorithms, the additional constituent's p_T^{ch} has very little impact on the τ_2/τ_1 distributions. This is expected as neither algorithm is p_T dependent. However, the mere presence of an additional constituent, irrespective of its p_T^{ch}, changes the τ_2/τ_1 distribution. This will be discussed in the section below.

6.2.1.2 δR

The effect of the angular separation of the additional constituent from the jet axis (δR) is measured, by varying this angle whilst keeping the particle's p_T^{ch} fixed. The results are shown in figures 6.4 and 6.5, for the 30% and 45% p_T^{ch} classes respectively. For the k_T and C/A with soft drop algorithms (hard scale sensitive), the increase in angular separation causes the τ_2/τ_1 distributions to shift towards lower values. This is representative of the two hard substructures in the jet (the core and the additional particle) becoming more separated and well defined. The shift in the τ_2/τ_1 value is largely due to the change in the value of τ_1, which increases with increasing δR. The value of τ_2 is less sensitive to this angular change, as it does not distinguish between one-cored and two-prong jets.

For the soft scale sensitive reclustering algorithms (C/A with and without minimisation), the τ_2/τ_1 distributions undergoe a slight shape change with increasing δR. A small increase in the yield of jets with low values of τ_2/τ_1 is observed, which induces a slight suppression at larger values, due to the self normalising nature of the distributions. The increase in the yield at low values of τ_2/τ_1, is due to configurations where the additional particle becomes the furthest constituent from the jet core. In the $N = 2$ case, one axis remains in the core whilst the other is pulled towards the additional constituent, keeping the value of τ_2 low. However, the value of τ_1 is large, due to the additional (hard) particle's large separation from the jet axis. The

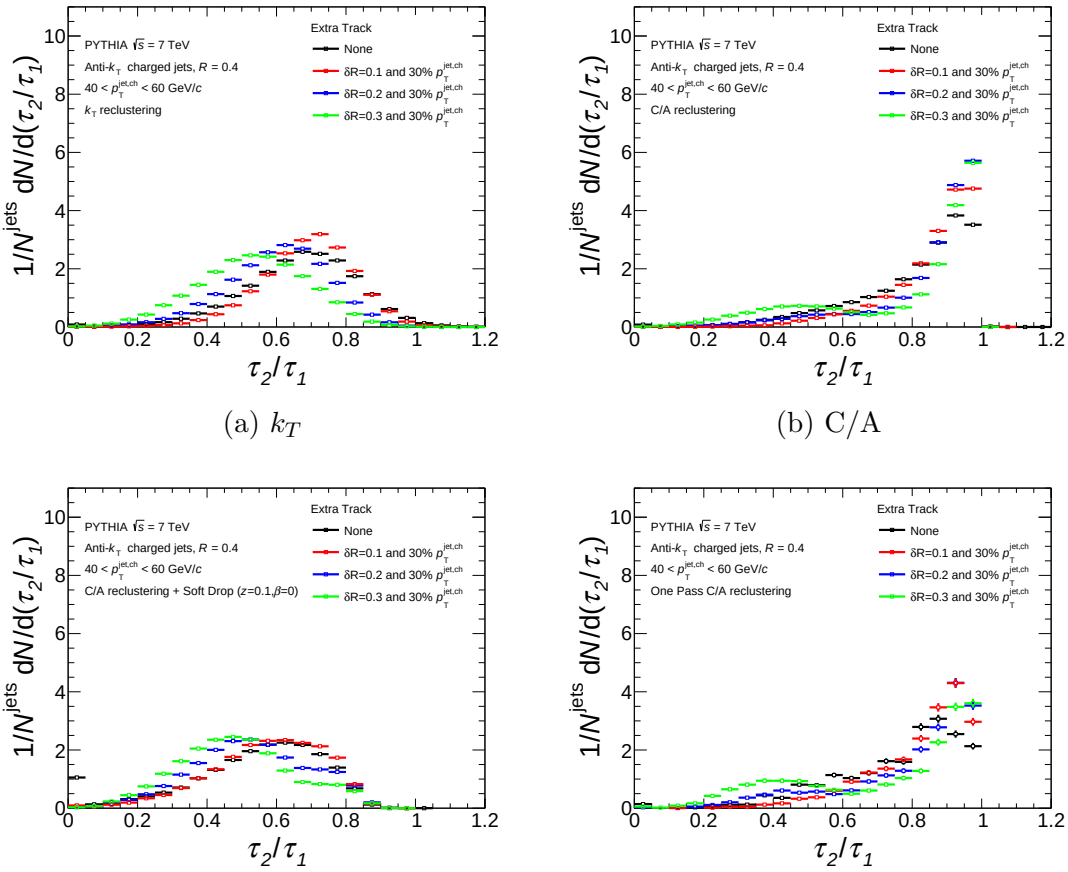

(a) k_T (b) C/A

(c) C/A + soft drop (d) C/A + minimisation

Figure 6.4: The τ_2/τ_1 distributions for jets with an additional constituent are shown for all four reclustering algorithms, in differential δR classes. The additional track has a p_T^{ch} equal to 30% of the original $p_T^{jet,ch}$.

probability of such configurations increases with increasing δR, as observed in the τ_2/τ_1 distributions.

The mean values of the τ_2/τ_1 distributions measured for jets with an additional constituent, are shown in table 6.1.

6.3 Final Results

In this section, the unfolded jet shapes measured in pp and Pb-Pb collisions will be compared to vacuum like PYTHIA Perugia 11 simulations. The unfolding procedure

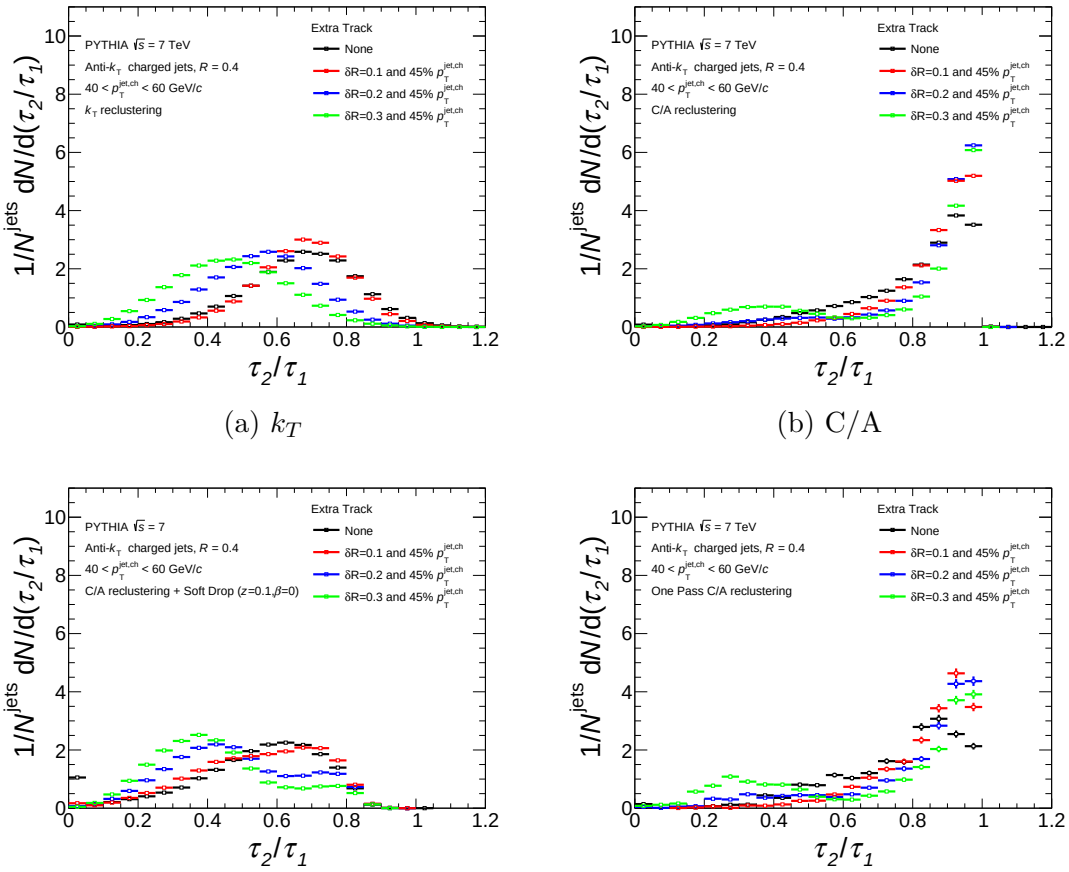

(a) k_T (b) C/A

(c) C/A + soft drop (d) C/A + minimisation

Figure 6.5: The τ_2/τ_1 distributions for jets with an additional constituent are shown for all four reclustering algorithms, in differential δR classes. The additional track has a p_T^{ch} equal to 45% of the original $p_T^{jet,ch}$.

τ_2/τ_1				
Extra Prong δR / % $p_T^{jet,ch}$	Algorithm			
	k_T	C/A	Soft Drop + C/A	C/A + Minimisation
None	0.6654 ± 0.0006	0.8255 ± 0.0006	0.5245 ± 0.0009	0.7882 ± 0.0028
0.1 / 30	0.6866 ± 0.0005	0.8521 ± 0.0005	0.5716 ± 0.0007	0.8201 ± 0.0025
0.1 / 45	0.6706 ± 0.0006	0.8636± 0.0005	0.5458 ± 0.0007	0.8328 ± 0.0024
0.2 / 15	0.6678 ± 0.0006	0.8340 ± 0.0006	0.5901 ± 0.0006	0.7862 ± 0.0029
0.2 / 30	0.6017 ± 0.0006	0.8441 ± 0.0007	0.5278 ± 0.0007	0.7905 ± 0.0034
0.2 / 45	0.5512 ± 0.0006	0.8489 ± 0.0007	0.4806 ± 0.0008	0.7958 ± 0.0036
0.2 / 60	0.5169 ± 0.0007	0.8482 ± 0.0008	0.4452 ± 0.0008	0.7784 ± 0.0040
0.3 / 30	0.5297 ± 0.0006	0.7817 ± 0.0009	0.4829 ± 0.0007	0.7213 ± 0.0043
0.3 / 45	0.4652 ± 0.0007	0.7697 ± 0.0011	0.4262 ± 0.0007	0.7037 ± 0.0049

Table 6.1: The mean values of the PYTHIA Perugia 11 τ_2/τ_1 distributions for jets with an additional constituent, obtained for each reclustering algorithm, are shown.

has removed detector and background effects, with the constituent p_T^{ch} corrected down to zero. The MC results have the same geometric cuts as the data and are

generated in two different centre of mass energies, corresponding to each of the collision systems. In Pb-Pb collisions, the recoil jet technique has been applied to the MC results, to limit method induced differences and facilitate more accurate comparisons. This section is the culmination of this thesis and will present the main physics observations obtained by this analysis.

6.3.1 pp

The unfolded ΔR and τ_2/τ_1 distributions, measured in pp collisions, are compared to inclusive PYTHIA Perugia 11 results at $\sqrt{s} = 7$ TeV, in figures 6.6 and 6.7 respectively. The ΔR measurements show that the reclustered axes found in data, are reproduced very well by PYTHIA for all four algorithms. The fragmentation of particles around these axes (τ_2/τ_1) is less well described by PYTHIA, although the description is still good. The observed discrepancies are visually enhanced by the self normalising property of the distributions. A small shift in the distribution's mean, can produce a visually larger disparity in the bin by bin comparisons. The mean values of each distribution are shown in tables 6.2 and 6.3 and show very good agreement between the data and PYTHIA. Next-to-leading-order (NLO) simulations, such as those using the POWHEG-Box [130], could be used to test the effects of higher order processes on the fragmentation. It would be of interest to test if such event generators would show better agreement with the data. Unfortunately, these generators were not readily available in the time frame of this analysis.

The results obtained in pp collisions not only measure and quantify the ΔR and τ_2/τ_1 jet shapes for a variety of reclustering algorithms, but also validate the PYTHIA Perugia 11 distributions in the vacuum. In this way, the PYTHIA distributions can be compared to the Pb-Pb results with an increased confidence.

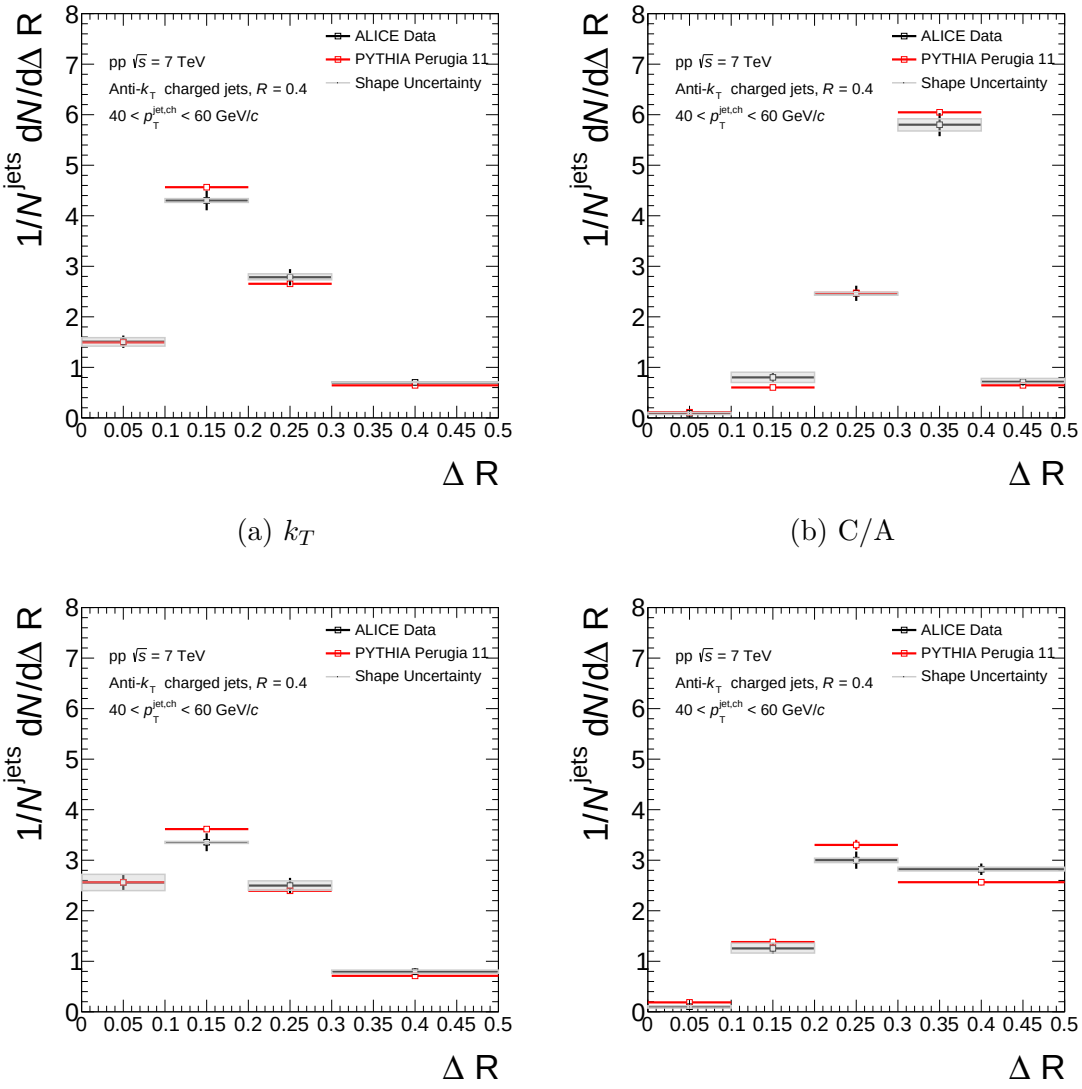

(a) k_T (b) C/A

(c) C/A + soft drop (d) C/A + minimisation

Figure 6.6: The fully corrected ΔR jet shapes, with their associated statistical and systematic uncertainties, measured in pp collisions at $40 \leq p_T^{jet,ch} < 60$ GeV/c, are shown for four reclustering algorithms. The PYTHIA Perugia 11 ΔR jet shapes at the corresponding energy, are also provided for comparisons.

6.3.2 Pb-Pb

The fully corrected τ_2/τ_1 distributions, measured in Pb-Pb collisions, are compared to PYTHIA Perugia 11 results simulated at $\sqrt{s} = 2.76$ TeV, in figure 6.8. A very good agreement is seen between the data and PYTHIA results, across all four algorithms. Table 6.4 shows the mean values of the data and PYTHIA distributions,

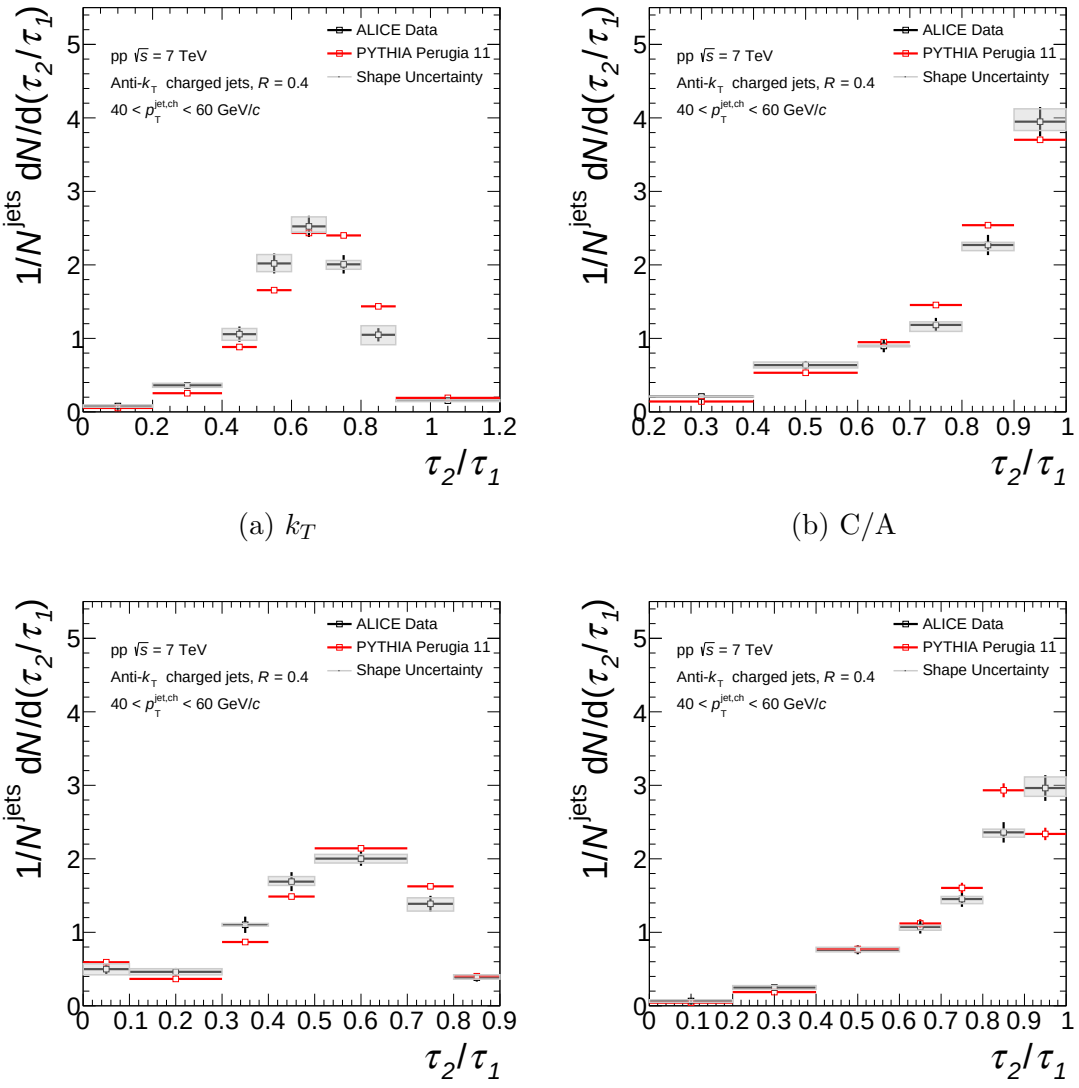

(a) k_T (b) C/A

(c) C/A + soft drop (d) C/A + minimisation

Figure 6.7: The fully corrected τ_2/τ_1 jet shapes, with their associated statistical and systematic uncertainties, measured in pp collisions at $40 \leq p_T^{jet,ch} < 60$ GeV/c, are shown for four reclustering algorithms. The PYTHIA Perugia 11 τ_2/τ_1 jet shapes at the corresponding energy, are also provided for comparisons.

which further illustrate this agreement. No discernible QGP effects can be seen in the measured τ_2/τ_1 distributions, which appear vacuum like in $0-10\%$ most central Pb-Pb collisions.

Hard and semi-hard induced gluon radiation due to quenching effects, as predicted by some energy loss models, is expected to shift (to lower values) the τ_2/τ_1 distributions

ΔR		
	Data	PYTHIA
Algorithm	Mean	Mean
k_T	0.1826 ± 0.0028	0.1796 ± 0.0004
C/A	0.3133 ± 0.0023	0.3177 ± 0.0003
Soft Drop + C/A	0.1709 ± 0.0032	0.1673 ± 0.0004
C/A + Minimisation	0.2887 ± 0.0032	0.2782 ± 0.0018

Table 6.2: The mean values of the fully corrected pp and PYTHIA Perugia 11 ΔR distributions, obtained for each reclustering algorithm, are shown.

τ_2/τ_1		
	Data	PYTHIA
Algorithm	Mean	Mean
k_T	0.6425 ± 0.0044	0.6654 ± 0.0006
C/A	0.8236 ± 0.0048	0.8255 ± 0.0006
Soft Drop + C/A	0.5091 ± 0.0068	0.5245 ± 0.0009
C/A + Minimisation	0.7973 ± 0.0050	0.7882 ± 0.0028

Table 6.3: The mean values of the fully corrected pp and PYTHIA Perugia 11 τ_2/τ_1 distributions, obtained for each reclustering algorithm, are shown.

τ_2/τ_1		
	Data	PYTHIA
Algorithm	Mean	Mean
k_T	0.6596 ± 0.0096	0.6662 ± 0.0016
C/A	0.7836 ± 0.0100	0.7948 ± 0.0019
Soft Drop + C/A	0.5701 ± 0.0102	0.5542 ± 0.0019
C/A + Minimisation	0.7646 ± 0.0106	0.7634 ± 0.0096

Table 6.4: The mean values of the fully corrected Pb-Pb and PYTHIA Perugia 11 τ_2/τ_1 distributions, obtained for each reclustering algorithm, are shown.

measured with the hard scale sensitive reclustering algorithms (k_T and C/A with soft drop). According to the toy models presented in the previous section, this shift would be strongest if the radiation was emitted at large angles from the jet axis. However, no such effect is observed.

Colour coherence energy loss models predict a suppression of two-prong jets in the medium, leading to a positive shift in the τ_2/τ_1 distributions measured with hard scale sensitive reclustering algorithms. However, the population of two-prong QCD jets in the vacuum is limited (this can be ascertained from the small yield of jets

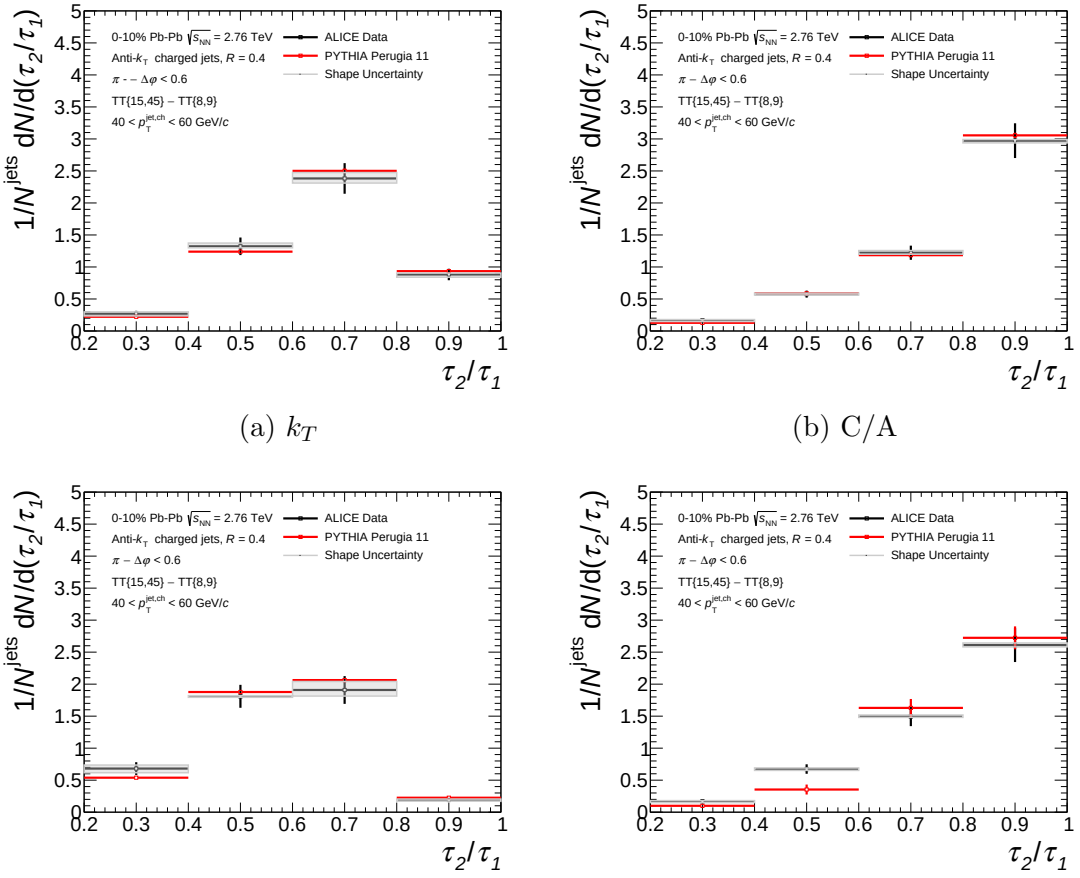

(a) k_T (b) C/A

(c) C/A + soft drop (d) C/A + minimisation

Figure 6.8: The fully corrected τ_2/τ_1 recoil jet shapes, with their associated statistical and systematic uncertainties, measured in Pb-Pb collisions at $40 \leq p_T^{jet,ch} < 60$ GeV/c, are shown for four reclustering algorithms. The PYTHIA Perugia 11 τ_2/τ_1 jet shapes at the corresponding energy, are also provided for comparisons.

at low τ_2/τ_1 values in pp collisions). Therefore, even a significant suppression of this population might not induce a noticeable shift in the overall distribution. An increase in statistics during upcoming LHC runs, would open the possibility for a more differential binning of the unfolded τ_2/τ_1 jet shape. This would increase the sensitivity of the measurement to such an effect, by making bin-to-bin comparisons at low τ_2/τ_1 values possible.

For jet shapes that exhibit a $p_T^{jet,ch}$ dependence, comparisons of the unfolded results in Pb-Pb collisions to MC results in higher $p_T^{jet,ch}$ bins, can test against the case of full coherence. In this scenario, where no substructure is resolved, the jet shapes in

Pb-Pb collisions are expected to remain vacuum like, with only a reduction in the jet energy scale observed. However, since the τ_2/τ_1 jet shapes have been shown to have no significant $p_T^{jet,ch}$ dependence (see figures 4.8 and 5.15), comparisons of the unfolded results to PYTHIA Perugia 11 simulations in higher $p_T^{jet,ch}$ bins are not presented.

The tools used in this analysis (background subtraction, hadron-jet coincidence technique, unfolding, etc), some of which have been applied for the first time, to correct the jet shapes measured in the large heavy ion background, are well developed and under control. The magnitude of these required corrections are large, with the methods attempting to correct the jet shapes back to particle level. The lessons learnt during the course of this analysis, in order to overcome these experimental challenges, were one of the main objectives of this work and lay the foundation for further jet substructure studies (for jets with low $p_T^{jet,ch}$ and large radius) in the heavy ion community.

CHAPTER 7

Conclusion

In this chapter, a summary of the main results and objectives of this work will be presented, followed by a discussion on the future work pertaining to this analysis.

7.1 pp

Measurements of the ΔR and τ_2/τ_1 jet shapes are presented in pp collisions, at $40 \leq p_T^{jet,ch} < 60$ GeV/c, for jets with a resolution of $R = 0.4$ (section 6.3.1). The results are corrected for detector effects, in $p_T^{jet,ch}$ and shape simultaneously, using two-dimensional Bayesian unfolding. The results are obtained for four different reclustering algorithms. The k_T and soft drop with C/A algorithms are sensitive to the hard scale splittings in the jet, providing access to the largest hard splitting.

This is often the hardest and earliest splitting in the jet. The C/A algorithm, with and without minimisation, is sensitive to the soft scale splittings and provides access to splittings occurring later in the evolution of the jet.

The ΔR shapes, measured with the hard scale sensitive algorithms, show that the hard splittings in the jet occur mostly at small angles. This is evidence for the primarily single-core nature of QCD jets. The ΔR shapes measured using the soft scale algorithms, show that soft splittings frequently occur at larger angles from the jet core, peaking at the radius of the jet. This is due to the larger concentric area at large radii, which increases the probability of finding a soft particle with increasing distance from the jet axis. The measured τ_2/τ_1 distributions confirm these observations, with peaks at large values. This is representative of a primarily single-core jet sample. The shape of the τ_2/τ_1 distributions are different for the soft and hard scale sensitive algorithms. The k_T and soft drop with C/A algorithms have a gaussian like distribution, peaking at ~ 0.6.

The C/A algorithm, with and without minimisation, is sensitive to the largest splitting in the jet, since the reclustering procedure is independent of p_T and only clusters particles based on their distance from one another. The τ_2/τ_1 values measured with these algorithms peak at ~ 1 This means that the majority of the $p_T^{jet,ch}$ remains in the core and that these algorithms are probing the soft scales of the jet. The minimisation procedure has little effect on the overall shape of the distributions obtained with the C/A algorithm, due to the low multiplicity of the jet constituents. However, the soft drop groomer has a large effect by successfully removing the large angle soft radiation and uncovering the hard splittings in the jet. This procedure transforms the C/A algorithm to a hard scale sensitive algorithm which can pick out the hardest splittings.

Comparisons of theoretical models with these results, can give access to the un-

derlying QCD processes [67]. These measurements provide theorists with a set of shapes which have been differentially measured for a variety of different reclustering algorithms, probing different scales in the evolution and fragmentation of the jet. The results have also been used to validate PYTHIA Perugia 11 simulations, for later comparisons to results measured in Pb-Pb collisions (at a different centre of mass energy). PYTHIA Perugia 11 describes the reclustered axes (ΔR) with a high precision. The fragmentation of constituents around these axes (τ_2/τ_1) are also well described, albeit to a lesser extent than the axes themselves.

7.2 Pb-Pb

Measurements of the τ_2/τ_1 jet shapes, in the $0-10\%$ most central Pb-Pb collisions at $40 \leq p_T^{jet,ch} < 60$ GeV/c, are presented for jets with a resolution of $R = 0.4$ (section 6.3.2). The large heavy ion background, clustered in to the jet, smears the "true" jet signal: hadrons arising from the fragmentation of the hard scattered parton. This is further compounded by the large jet radius and low $p_T^{jet,ch}$ used in this analysis, which lead to both a larger background in the jet cone and a lower ratio of signal to background. In addition to the smearing of "true" jets, the measured jet sample is also populated by combinatorial jets which are derived solely from fluctuations in the background. Prior to this work, measurements of fully corrected jet shapes for these low $p_T^{jet,ch}$ and large radius jets, were experimentally unattainable in Pb-Pb collisions. The use of constituent subtraction to remove the event average background at a constituent level from the jets, coupled with the first extension of the semi-inclusive hadron-jet coincidence technique to two dimensions in order to reject combinatorial jets from the measured sample, have made such measurements possible for the first time. The data are corrected for background fluctuations and detector effects, in $p_T^{jet,ch}$ and shape, using two-dimensional Bayesian unfolding.

The τ_2/τ_1 distributions measured in Pb-Pb collisions, are similar to the corresponding τ_2/τ_1 distributions measured in pp collisions. Therefore, the same qualitative conclusions drawn for each algorithm in the pp case, apply to Pb-Pb collisions as well. The minimisation procedure continues to have only a small effect on the overall shape of the τ_2/τ_1 distribution obtained with the C/A algorithm, despite the higher multiplicity of jet constituents. The effect of the soft drop groomer remains large, as it successfully manages to uncover the hard splitting in a large number of jets (section 5.2). The additional removal of soft large angle tracks, which have survived the background subtraction procedure, results in a slightly more two-prong distribution of jets compared to the k_T case. This suggests that the soft drop with C/A algorithm is more sensitive to the hard splittings of the jet in heavy ion collisions, compared to the k_T algorithm.

The fully corrected τ_2/τ_1 distributions are in close agreement with PYTHIA Perugia 11 simulations, for all algorithms. This suggests that the two-prong substructure of jets traversing the QGP medium is vacuum like. An enhancement in the two-prongness of jets would be expected in energy loss models involving hard and semi-hard gluon radiation at large angles from the jet core. The presence of colour coherence effects is expected to result in a suppression of two-prong jets. No shift is observed in the hard scale sensitive τ_2/τ_1 distributions.

The background correcting procedures applied in this work, attempt to correct the measured raw data samples down to particle level, despite the large degree of corrections required. This showcases the most recent developments in the field which, when applied together, can deal with the large background of central heavy ion collisions to uncover the physical signals of interest.

7.3 Future Work

The measurement of jet shapes using reclustering techniques, is at the forefront of current advances in the study of jet quenching in relativistic heavy ion collisions. The soft drop algorithm in particular, has prompted a large amount of recent theoretical and experimental work. The lessons learnt during the course of this analysis, in order to fully correct jet shapes at low $p_T^{jet,ch}$ for large radius jets, have laid the foundation for new analyses that are currently ongoing at ALICE. The author plans to continue contributing to the jet substructure program at ALICE, through further jet shape measurements, using the techniques developed through this work. In particular, measuring jet shapes originating from the fragmentation of a scattered heavy quark, can probe interesting physics regarding the role of heavy flavour in QCD and the differences in the fragmentation of quark and gluon jets [131].

APPENDIX A

Response Matrix Weights

The numerical values of the weights calculated when constructing the response matrices, in pp and Pb-Pb collisions, are presented below. These weights are applied to each entry in the response matrices, according to their p_T hard bin (pp and Pb-Pb) or $p_{T,Truth}^{jet,ch}$ (Pb-Pb) value.

A.1 pp

The weights applied to the entires from each p_T hard bin in the pp analysis, as described in section 4.3.2, are given in table A.1.

p_T hard bin dependent weights in the pp analysis					
p_T hard bin GeV/c	$5-11$	$11-21$	$21-36$	$36-57$	$57-84$
weight	2.52×10^{-6}	9.91×10^{-7}	1.57×10^{-7}	2.19×10^{-8}	3.32×10^{-9}
p_T hard bin GeV/c	$84-117$	$117-152$	$152-191$	$191-234$	$234-1000$
weight	6.40×10^{-10}	1.72×10^{-10}	4.97×10^{-11}	1.65×10^{-11}	1.52×10^{-11}

Table A.1: The weights calculated for each p_T hard bin, when building the response matrices in the pp analysis, are shown.

A.2 Pb-Pb

The p_T hard bin dependent factor of the weights applied to the entries of the response matrices in the Pb-Pb analysis, as described in section 5.4.2, are given in table A.2.

p_T hard bin dependent weights in the Pb-Pb analysis					
p_T hard bin GeV/c	$5-11$	$11-21$	$21-36$	$36-57$	$57-84$
weight	1.81×10^{-5}	6.22×10^{-6}	1.05×10^{-6}	9.32×10^{-8}	1.11×10^{-8}
p_T hard bin GeV/c	$84-117$	$117-152$	$152-191$	$191-234$	$234-1000$
weight	1.92×10^{-9}	2.70×10^{-10}	5.26×10^{-11}	1.73×10^{-11}	6.65×10^{-12}

Table A.2: The weights calculated for each p_T hard bin, when building the response matrices in the Pb-Pb analysis, are shown.

The $p_{T,Truth}^{jet,ch}$ dependent factor of the weights applied to the entries of the response matrices in the Pb-Pb analysis, as described in section 5.4.2, are given in table A.2.

$p_{T,Truth}^{jet,ch}$ dependent weights in the Pb-Pb analysis					
$p_{T,Truth}^{jet,ch}$ GeV/c	$0-5$	$5-10$	$10-15$	$15-20$	$20-25$
weight	2.94×10^{-4}	2.37×10^{-3}	9.20×10^{-3}	2.03×10^{-2}	3.58×10^{-2}
$p_{T,Truth}^{jet,ch}$ GeV/c	$25-30$	$30-35$	$35-40$	$40-45$	$45-50$
weight	5.60×10^{-2}	9.39×10^{-2}	1.42×10^{-1}	1.84×10^{-1}	2.55×10^{-1}
$p_{T,Truth}^{jet,ch}$ GeV/c	$50-55$	$55-60$	$60-65$	$65-70$	$70-75$
weight	3.26×10^{-1}	3.90×10^{-1}	4.10×10^{-1}	4.24×10^{-1}	5.04×10^{-1}
$p_{T,Truth}^{jet,ch}$ GeV/c	$75-80$	$80-85$	$85-90$	$90-95$	$95-100$
weight	4.61×10^{-1}	5.14×10^{-1}	5.31×10^{-11}	5.53×10^{-1}	6.20×10^{-1}
$p_{T,Truth}^{jet,ch}$ GeV/c	$100-105$	$105-110$	$110-115$	$115-120$	$120-125$
weight	6.42×10^{-1}	7.22×10^{-1}	7.40×10^{-1}	7.65×10^{-1}	7.91×10^{-1}
$p_{T,Truth}^{jet,ch}$ GeV/c	$125-130$	$130-135$	$135-140$	$140-145$	$145-150$
weight	8.32×10^{-1}	8.85×10^{-1}	9.05×10^{-1}	9.40×10^{-1}	1.02
$p_{T,Truth}^{jet,ch}$ GeV/c	$150-155$	$155-160$			
weight	9.30×10^{-1}	1.00			

Table A.3: The weights calculated for each $p_{T,Truth}^{jet,ch}$ bin, when building the response matrices in the Pb-Pb analysis, are shown.

APPENDIX B

Systematic Uncertainties in pp

A full description of the calculations undertaken to obtain the systematic errors, in pp collisions, is presented below. Unless explicitly stated, each error is calculated by performing the unfolding procedure with a modified response matrix. The unfolded result is compared to the default unfolded solution, to obtain the systematic error for each bin.

B.1 Tracking Efficiency

The ALICE detector has a finite tracking efficiency, as detailed in section 3.4. The associated error on this tracking efficiency is $\pm 4\%$, which can fluctuate on an event-by-event basis. To account for this variation, a response matrix is constructed with a

reduced (4% less than the default value) tracking efficiency at detector level (we will refer to the default tracking efficiency as 100%, even though this does not correspond to an actual value of 100% for the tracking efficiency). Since tracks cannot be reliably added to an event, the systematic errors for when the tracking efficiency is 4% higher than the default value are obtained by symmetrising the errors from the 4% lower case. The tracking efficiency uncertainty is the dominant systematic uncertainty in this analysis for pp collisions.

Figure B.1 shows the effect of the reduced tracking efficiency on the $p_T^{jet,ch}$ distribution, at detector level. The reduced tracking efficiency has negligible effect on the distribution. The low average number of tracks per jet (figure 4.4), coupled with the higher probability of losing low p_T^{ch} constituents (they are more numerous than their high p_T^{ch} counterparts), account for this lack of impact.

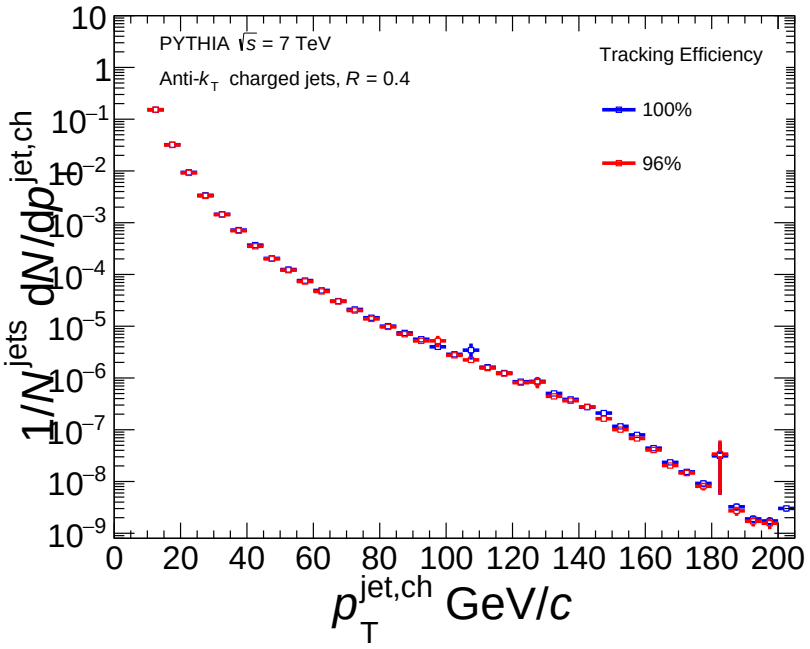

(a) Detector Level

Figure B.1: The detector level $p_T^{jet,ch}$ distribution is shown, measured with the default and reduced tracking efficiencies.

Figure B.2 shows the effects of the reduced tracking efficiency on the ΔR jet shapes,

at detector level. These effects are negligible for the hard scale sensitive algorithms (k_T and soft drop with C/A), which are not affected due to the higher probability of losing a low p_T^{ch} track. For the soft scale sensitive algorithms (C/A and C/A with minimisation), the ΔR shape is only affected when the furthermost track from the core is lost. This is reflected in a very slight shift, to lower values, of the reduced tracking efficiency distributions.

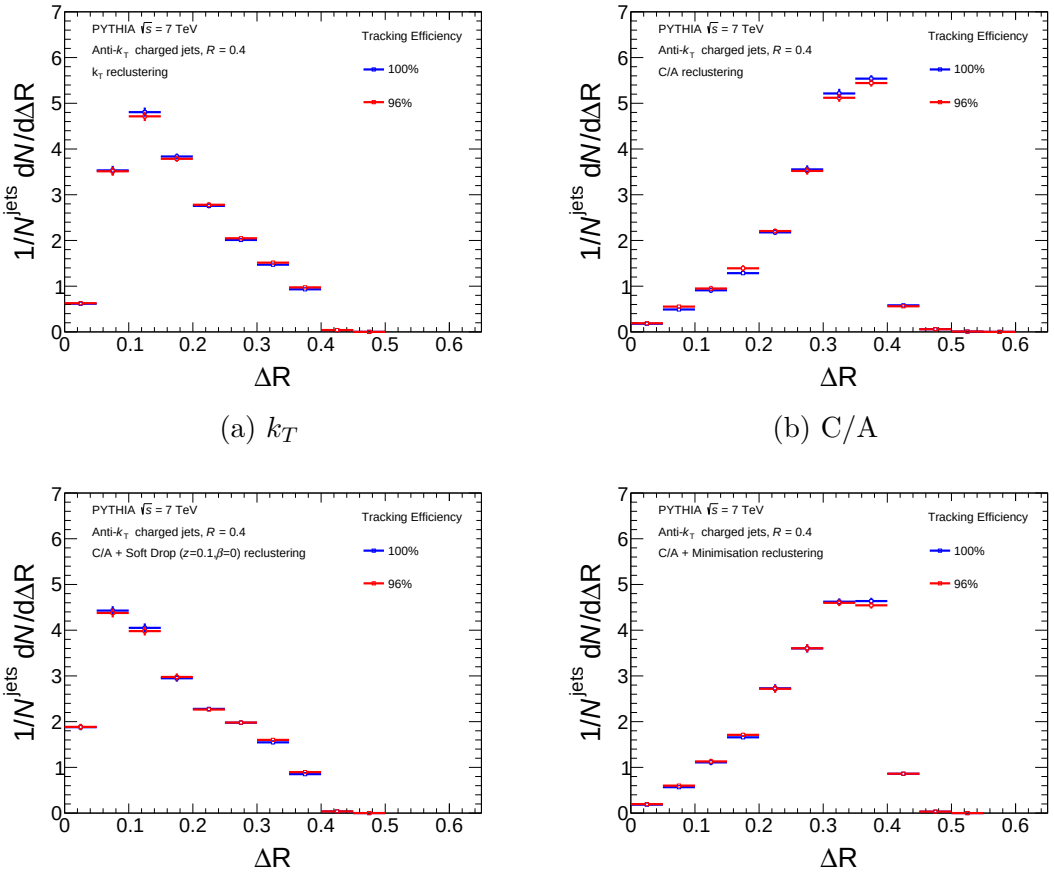

(a) k_T (b) C/A

(c) C/A + soft drop (d) C/A + minimisation

Figure B.2: The detector level ΔR distributions are shown for each reclustering algorithm, measured with the default and reduced tracking efficiencies. The results are shown for $40 \leq p_{T,Truth}^{jet,ch} < 60$ GeV/c.

Figure B.3 shows the effects of the reduced tracking efficiency on the τ_2/τ_1 jet shapes, at detector level. The effects are negligible and the distributions are consistent with one another within statistical errors. Minor differences in the first bin are attributed to the increased number of two track jets, induced by the reduced tracking efficiency.

For the C/A and C/A with minimisation algorithms, the yields at values of τ_2/τ_1 ~ 1, exhibit a slight suppression when the tracking efficiency is reduced. These bins are populated by strongly single-core jets, where the second axis in the $N = 2$ case is pulled to large angles by a soft track. If these soft tracks are not reconstructed due to the reduced tracking efficiency, the second axis can remain in the core. This slightly reduces the τ_2 value of the jet, without any significant change occurring to the value of τ_1.

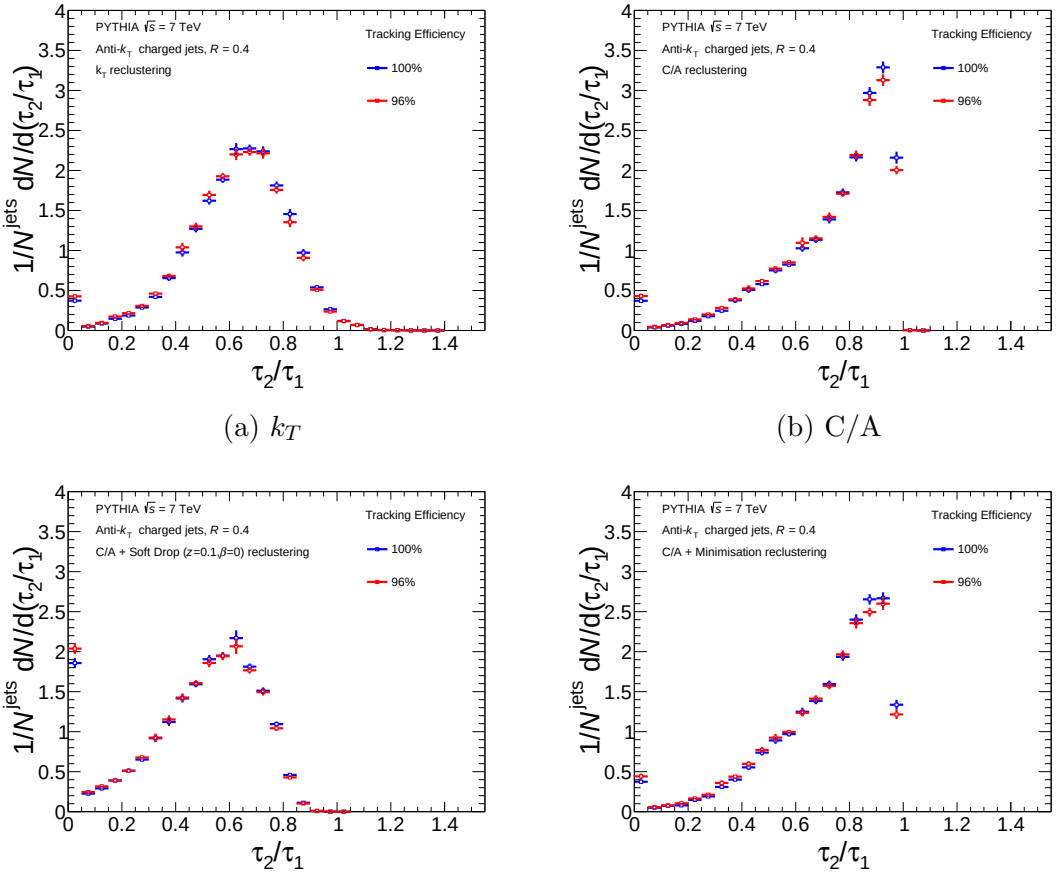

(a) k_T (b) C/A

(c) C/A + soft drop (d) C/A + minimisation

Figure B.3: The detector level τ_2/τ_1 distributions are shown for each reclustering algorithm, measured with the default and reduced tracking efficiencies. The results are shown for $40 \leq p_{T,Truth}^{jet,ch} < 60$ GeV/c.

B.2 Truncation

A statistically rich response matrix will include contributions from all reconstructed level bins into a single truth level bin (and vice versa), due to detector effects. When producing a fully corrected result in a given range, the unfolding procedure will consider the contribution from all bins in the data (in accordance with the response matrix's truth to detector level mapping). Due to the statistical limits of the measured data sets, only a truncated input range can be supplied to the unfolding procedure. The rules of matrix multiplication dictate that this range must also be mirrored in the reconstructed level of the response matrix. In practice, this range ($20 \leq p_T^{jet,ch} < 80$ GeV/c in this work) is chosen so as to be sufficiently separated on either side from the reported unfolded range ($40 \leq p_T^{jet,ch} < 60$ GeV/c in this work), since the amount of entires in a truth level bin, from any given reconstructed level bin, is inversely proportional to the difference in value of the truth and reconstructed bins.

The truncation uncertainty tests the adequacy of this separation. The lower bounds of the input data and hence the response matrix at reconstructed level, are extended to 10 GeV/c. Only an extension in the lower bound is considered, as the power law behaviour of the $p_T^{jet,ch}$ distribution dictates that the effect of extending the lower bound is much more significant than that of the upper bound (assuming the $p_T^{jet,ch}$ dependence of the detector effects is insignificant in comparison). In pp collisions, only an extension in $p_T^{jet,ch}$ is considered, as the full range of available data in shape bins is already supplied to the default unfolding. The truncation uncertainty is the least significant of the systematic uncertainties considered here.

B.3 Regularisation

This uncertainty reflects the choice of iteration chosen as the default unfolded solution. Iterations above (iteration 7) and below (iteration 3) the chosen iteration (iteration 4) are selected and compared to the default solution. Figures 4.22 and 4.23 show the magnitude of this effect, for the ΔR and τ_2/τ_1 shapes respectively. This error is small, due to the fast convergence of iterations onto the true solution.

B.4 Prior

This uncertainty reflects the choice of MC generator, used to construct the response matrix, on the unfolded solution. This is ascertained (in the absence of having access to an independent event generator) by smearing the $p_T^{jet,ch}$ and shape correlations at truth level. Each entry (jet) in the response matrix is weighted according to its τ_2/τ_1 value at truth level. The weights are calculated in bins of τ_2/τ_1, by comparing (taking the ratio of) the unfolded and truth level τ_2/τ_1 distributions, as shown in figure B.4. This translates into a moderate change in the response matrix, whilst still keeping the values physical. The truth and unfolded distributions exhibit a slight displacement relative to each other, whilst maintaining the same overall shape. The same weights are used to evaluate the uncertainty for both the ΔR and τ_2/τ_1 jet shapes, since the aim of smearing the $p_T^{jet,ch}$ and shape correlations is achieved, regardless of the variable used in the weighting procedure.

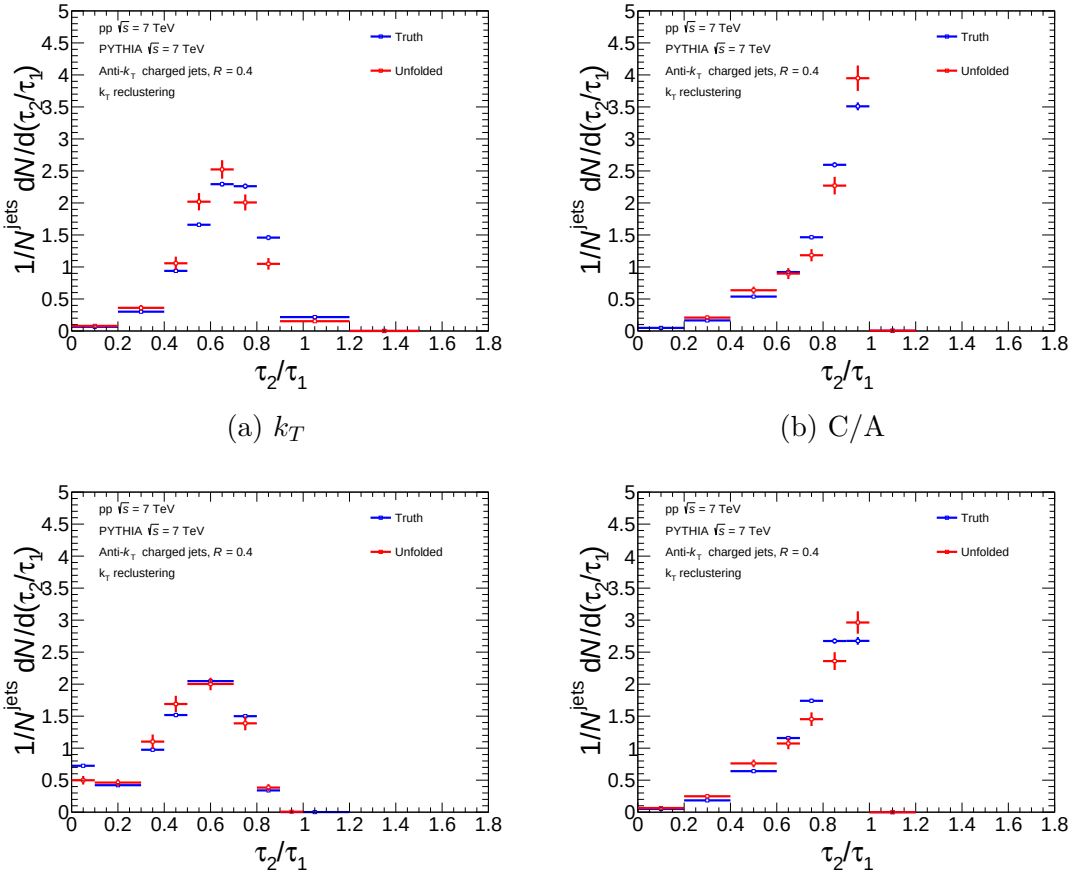

(a) k_T (b) C/A

(c) C/A + soft drop (d) C/A + minimisation

Figure B.4: The truth level and unfolded τ_2/τ_1 distributions, used to obtain the weights for the prior systematic, are shown for each reclustering algorithm.

B.5 Numerical Values

The contributions of each source of systematic error, in terms of a percentage deviation from the default solutions, are shown below. Tables B.1, B.2, B.3 and B.4 show the systematic errors for the ΔR jet shape for each of the reclustering algorithms, whilst tables B.5, B.6, B.7 and B.8 show this for the τ_2/τ_1 jet shapes.

Systematic Uncertainties				
Shape	ΔR using k_T reclustering			
Shape interval	0.0-0.1	0.1-0.2	0.2-0.3	0.3-0.5
Tracking Efficiency	4.4%	0.8%	0.9%	0.4%
Truncation	$^{+0.0}_{-0.2}$%	$^{+0.0}_{-0.3}$%	$^{+0.3}_{-0.0}$%	$^{+0.6}_{-0.0}$%
Regularisation	$^{+3.0}_{-3.6}$%	$^{+0.1}_{-0.1}$%	$^{+2.2}_{-1.6}$%	$^{+0.0}_{-0.3}$%
Prior	$^{+0.0}_{-1.2}$%	$^{+0.2}_{-0.0}$%	$^{+0.0}_{-0.2}$%	$^{+1.0}_{-0.0}$%

Table B.1: The percentage deviation of each systematic error, in comparison to the final unfolded solution, is shown for the ΔR jet shape measured using the k_T reclustering algorithm.

Systematic Uncertainties					
Shape	ΔR using C/A reclustering				
Shape interval	0.0-0.1	0.1-0.2	0.2-0.3	0.3-0.4	0.4-0.5
Tracking Efficiency	20.9%	12.5%	0.4%	2.0%	0.1%
Truncation	$^{+1.2}_{-0.0}$%	$^{+0.0}_{-0.3}$%	$^{+0.3}_{-0.0}$%	$^{+0.0}_{>-0.1}$%	$^{+0.0}_{-0.6}$%
Regularisation	$^{+11.1}_{-18.2}$%	$^{+2.8}_{-1.1}$%	$^{+0.7}_{-1.2}$%	$^{+0.1}_{-0.8}$%	$^{+9.0}_{-3.6}$%
Prior	$^{+0.5}_{-0.0}$%	$^{+0.0}_{-1.3}$%	$^{+0.0}_{-0.8}$%	$^{+0.0}_{>-0.1}$%	$^{+2.8}_{-0.0}$%

Table B.2: The percentage deviation of each systematic error, in comparison to the final unfolded solution, is shown for the ΔR jet shape measured using the C/A reclustering algorithm.

Systematic Uncertainties				
Shape	ΔR using C/A with minimisation reclustering			
Shape interval	0.0-0.1	0.1-0.2	0.2-0.3	0.3-0.5
Tracking Efficiency	15.7%	6.8%	1.2%	1.2%
Truncation	$^{+1.6}_{-0.0}$%	$^{+0.0}_{-0.3}$%	$^{+0.3}_{-0.0}$%	$^{+0.0}_{-0.1}$%
Regularisation	$^{+13.0}_{-21.6}$%	$^{+4.8}_{-1.9}$%	$^{+0.4}_{-0.9}$%	$^{<+0.1}_{-0.2}$%
Prior	$^{+0.0}_{-3.0}$%	$^{+0.0}_{-2.0}$%	$^{+0.0}_{-0.6}$%	$^{+0.8}_{-0.0}$%

Table B.3: The percentage deviation of each systematic error, in comparison to the final unfolded solution, is shown for the ΔR jet shape measured using the C/A with minimisation reclustering algorithm.

Systematic Uncertainties				
Shape	ΔR using soft drop with C/A reclustering			
Shape interval	0.0-0.1	0.1-0.2	0.2-0.3	0.3-0.5
Tracking Efficiency	6.0%	0.3%	3.5%	3.5%
Truncation	$^{+0.0}_{-0.4}$%	$^{+0.0}_{-0.4}$%	$^{+0.5}_{-0.0}$%	$^{+0.7}_{-0.0}$%
Regularisation	$^{+1.7}_{-1.9}$%	$^{+0.4}_{-0.5}$%	$^{+1.3}_{-1.1}$%	$^{+2.1}_{-1.6}$%
Prior	$^{+0.8}_{-0.0}$%	$^{<+0.1}_{-0.0}$%	$^{+0.0}_{-0.3}$%	$^{+0.0}_{-1.0}$%

Table B.4: The percentage deviation of each systematic error, in comparison to the final unfolded solution, is shown for the ΔR jet shape measured using the soft drop with C/A reclustering algorithm.

Systematic Uncertainties								
Shape	τ_2/τ_1 using k_T reclustering							
Shape interval	0.0-0.2	0.2-0.4	0.4-0.5	0.5-0.6	0.6-0.7	0.7-0.8	0.8-0.9	0.9-1.2
Tracking Efficiency	19.5%	7.5%	7.2%	5.2%	2.8%	2.5%	11.2%	6.1%
Truncation	$^{+0.9}_{-0.0}$%	$^{+1.1}_{-0.0}$%	$^{+1.0}_{-0.0}$%	$^{+0.2}_{-0.0}$%	$^{+0.0}_{-0.3}$%	$^{+0.0}_{-0.6}$%	$^{+0.0}_{-0.4}$%	$^{+0.2}_{-0.0}$%
Regularisation	$^{+0.9}_{-2.4}$%	$^{+0.0}_{-0.2}$%	$^{+0.6}_{-2.1}$%	$^{+2.7}_{-1.9}$%	$^{+2.5}_{-1.5}$%	$^{+0.7}_{-0.5}$%	$^{+3.7}_{-5.7}$%	$^{+2.0}_{-1.5}$%
Prior	$^{+0.0}_{-1.1}$%	$^{+0.3}_{-0.0}$%	$^{+0.0}_{-2.4}$%	$^{+1.2}_{-0.0}$%	$^{+3.5}_{-0.0}$%	$^{+0.0}_{-2.0}$%	$^{+0.0}_{-2.8}$%	$^{+0.0}_{-3.6}$%

Table B.5: The percentage deviation of each systematic error, in comparison to the final unfolded solution, is shown for the τ_2/τ_1 jet shape measured using the k_T reclustering algorithm.

Systematic Uncertainties						
Shape	τ_2/τ_1 using C/A reclustering					
Shape interval	0.2-0.4	0.4-0.6	0.6-0.7	0.7-0.8	0.8-0.9	0.9-1.0
Tracking Efficiency	2.7%	5.8%	0.3%	2.0%	0.2%	2.8%
Truncation	$^{+1.2}_{-0.0}$%	$^{+0.4}_{-0.0}$%	$^{<+0.1}_{-0.0}$%	$^{<+0.1}_{-0.0}$%	$^{+0.0}_{-0.3}$%	$^{+0.0}_{-0.1}$%
Regularisation	$^{+0.2}_{-0.8}$%	$^{+2.8}_{-1.7}$%	$^{+0.3}_{-0.0}$%	$^{+3.0}_{-4.8}$%	$^{+1.6}_{-2.1}$%	$^{+1.7}_{-1.2}$%
Prior	$^{+0.0}_{-0.2}$%	$^{+1.1}_{-0.0}$%	$^{+0.0}_{-1.0}$%	$^{+0.0}_{-5.4}$%	$^{+0.0}_{-2.6}$%	$^{+3.0}_{-0.0}$%

Table B.6: The percentage deviation of each systematic error, in comparison to the final unfolded solution, is shown for the τ_2/τ_1 jet shape measured using the C/A reclustering algorithm.

Systematic Uncertainties							
Shape	τ_2/τ_1 using C/A with minimisation reclustering						
Shape interval	0.0-0.2	0.2-0.4	0.4-0.6	0.6-0.7	0.7-0.8	0.8-0.9	0.9-1.0
Tracking Efficiency	27.1%	10.4%	3.1%	1.5%	1.4%	1.3%	3.6%
Truncation	$^{+1.1}_{-0.0}$%	$^{+0.9}_{-0.0}$%	$^{+0.4}_{-0.0}$%	$^{+0.1}_{-0.0}$%	$^{+0.0}_{-0.1}$%	$^{+0.0}_{-0.4}$%	$^{+0.0}_{-0.1}$%
Regularisation	$^{+0.2}_{-1.1}$%	$^{+1.8}_{-1.8}$%	$^{+3.1}_{-1.8}$%	$^{+1.1}_{-1.8}$%	$^{+2.0}_{-2.7}$%	$^{+1.3}_{-1.7}$%	$^{+1.4}_{-1.2}$%
Prior	$^{+0.0}_{-0.2}$%	$^{+1.3}_{-0.0}$%	$^{+1.2}_{-0.0}$%	$^{+0.0}_{-3.5}$%	$^{+0.0}_{-3.1}$%	$^{+0.0}_{-1.7}$%	$^{+3.3}_{-0.0}$%

Table B.7: The percentage deviation of each systematic error, in comparison to the final unfolded solution, is shown for the τ_2/τ_1 jet shape measured using the C/A with minimisation reclustering algorithm.

Systematic Uncertainties							
Shape	τ_2/τ_1 using soft drop with C/A reclustering						
Shape interval	0.0-0.1	0.1-0.3	0.3-0.4	0.4-0.5	0.5-0.7	0.7-0.8	0.8-0.9
Tracking Efficiency	14.2%	8.7%	1.3%	2.8%	2.9%	5.7%	5.1%
Truncation	$^{+0.8}_{-0.0}$%	$^{+0.0}_{-0.4}$%	$^{+0.5}_{-0.0}$%	$^{+0.1}_{-0.0}$%	$^{+0.0}_{>-0.1}$%	$^{+0.0}_{-0.3}$%	$^{+0.0}_{-0.8}$%
Regularisation	$^{+3.7}_{-5.4}$%	$^{+2.0}_{-1.3}$%	$^{+0.6}_{-0.9}$%	$^{+2.2}_{-1.2}$%	$^{+0.3}_{-0.4}$%	$^{+1.4}_{-3.0}$%	$^{+5.4}_{-2.3}$%
Prior	$^{+0.0}_{-3.2}$%	$^{+2.4}_{-0.0}$%	$^{+0.7}_{-0.0}$%	$^{+2.0}_{-0.0}$%	$^{+0.0}_{-0.8}$%	$^{+0.0}_{-3.0}$%	$^{+6.8}_{-0.0}$%

Table B.8: The percentage deviation of each systematic error, in comparison to the final unfolded solution, is shown for the τ_2/τ_1 jet shape measured using the soft drop with C/A reclustering algorithm.

APPENDIX C

Systematic Uncertainties in Pb-Pb

A full description of the calculations undertaken to obtain the systematic errors, in Pb-Pb collisions, is presented below. Unless explicitly stated, each error is calculated by performing the unfolding procedure with a modified response matrix. The unfolded result is compared to the default unfolded solution, to obtain the systematic error for each bin. The first four systematic errors have already been described in Appendix B and only the differences compared to the pp case will be discussed below.

C.1 Tracking Efficiency

The default tracking efficiency during the Pb-Pb data taking runs was 2% lower than in pp, due to a reduced performance of the detector in the high multiplicity environment of heavy ion collisions. The simulations are performed with tracking efficiencies at 98% and 94% of the default used in pp collisions, for the corresponding default and reduced cases in Pb-Pb collisions respectively. The effect of the reduced tracking efficiency on the embedded level $p_T^{jet,ch}$ distribution, shown in figure C.1, is negligible.

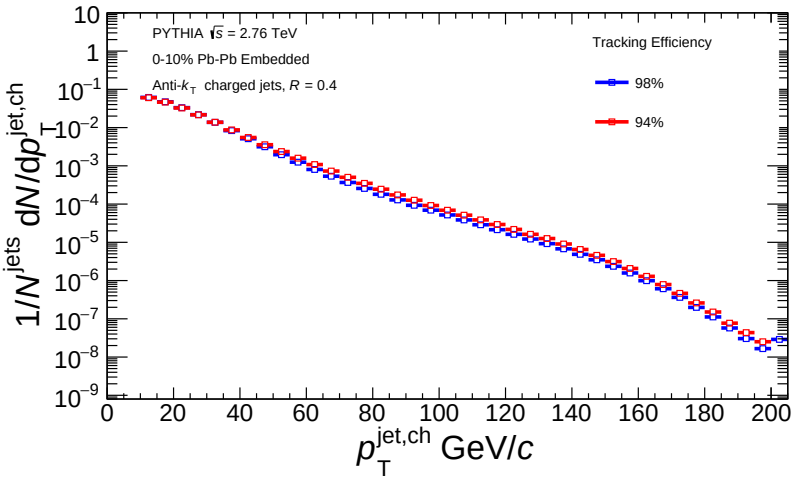

(a) Embedded Level

Figure C.1: The embedded level $p_T^{jet,ch}$ distribution is shown, measured with the default and reduced tracking efficiencies.

The effects of the reduced tracking efficiency, on the embedded level τ_2/τ_1 distributions, are shown in figure C.2. These effects are negligible across all algorithms, due to the large number of low p_T^{ch} background tracks (which are more likely to be removed). The enhancement in the yield of two track jets ($\tau_2/\tau_1 = 0$) at reduced tracking efficiency, as observed in pp, is not present here. This is also due to the large number of background tracks remaining in the jet, after background subtraction.

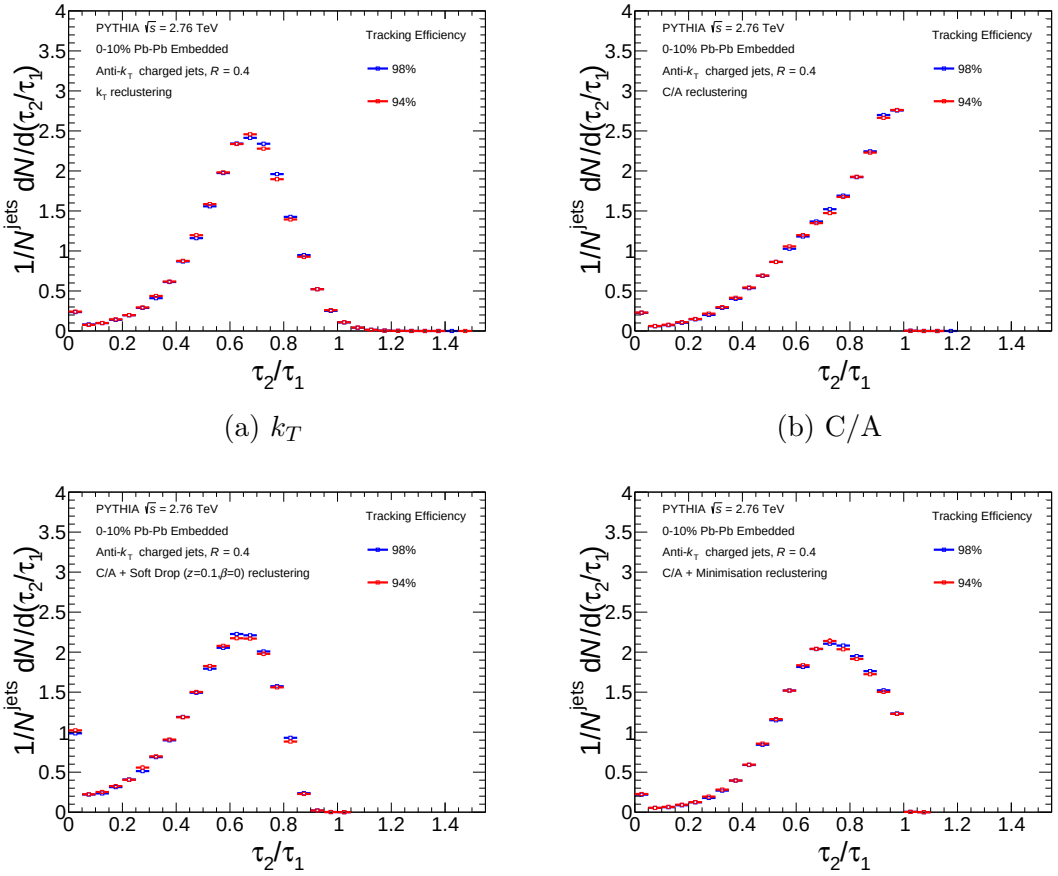

(a) k_T (b) C/A

(c) C/A + soft drop (d) C/A + minimisation

Figure C.2: The embedded level τ_2/τ_1 distributions are shown for each reclustering algorithm, measured with the default and reduced tracking efficiencies. The results are shown for $40 \leq p_{T,Truth}^{jet,ch} < 60$ GeV/c.

C.2 Truncation

In addition to extending the lower bound of the input $p_T^{jet,ch}$ acceptance by 10 GeV/c, the upper bound of the input shape acceptance is also separately extended to 1.2, for all four reclustering algorithms. The default unfolding did not incorporate this full range due to statistical limitations.

C.3 Regularisation

The treatment of this systematic is identical to the pp case, with the same iterations above and below (3 and 7) the default iteration (4) chosen. These iterations are shown in figure 5.24. The contribution from this systematic is small, due to the strong convergence already present by the third iteration

C.4 Prior

The same technique used to calculate the prior systematic in pp collisions, is repeated here. The unfolded Pb-Pb and truth level distributions are shown in figure C.3. The distributions exhibit strong similarities and their ratios do not induce a large systematic contribution.

In addition to the method described above, a separate variation of the prior systematic is also considered in Pb-Pb collisions. The response matrix is weighted according to each entry's $p_T^{jet,ch}$ value at truth level. These weights reflect the energy shift of the jets due to quenching effects, which is estimated to be $\sim 20\%$ in central Pb-Pb collisions [132]. The weights are extracted from the ratio of the the two distributions shown in figure C.4. These are the $p_T^{jet,ch}$ distribution at truth level and the same distribution but with a 20% downward shift applied to the $p_T^{jet,ch}$ of each entry in to the distribution.

C.5 Background Subtraction

Constituent subtraction is the default subtraction method used in this analysis. As a systematic cross-check, we repeat the unfolding procedure using second or-

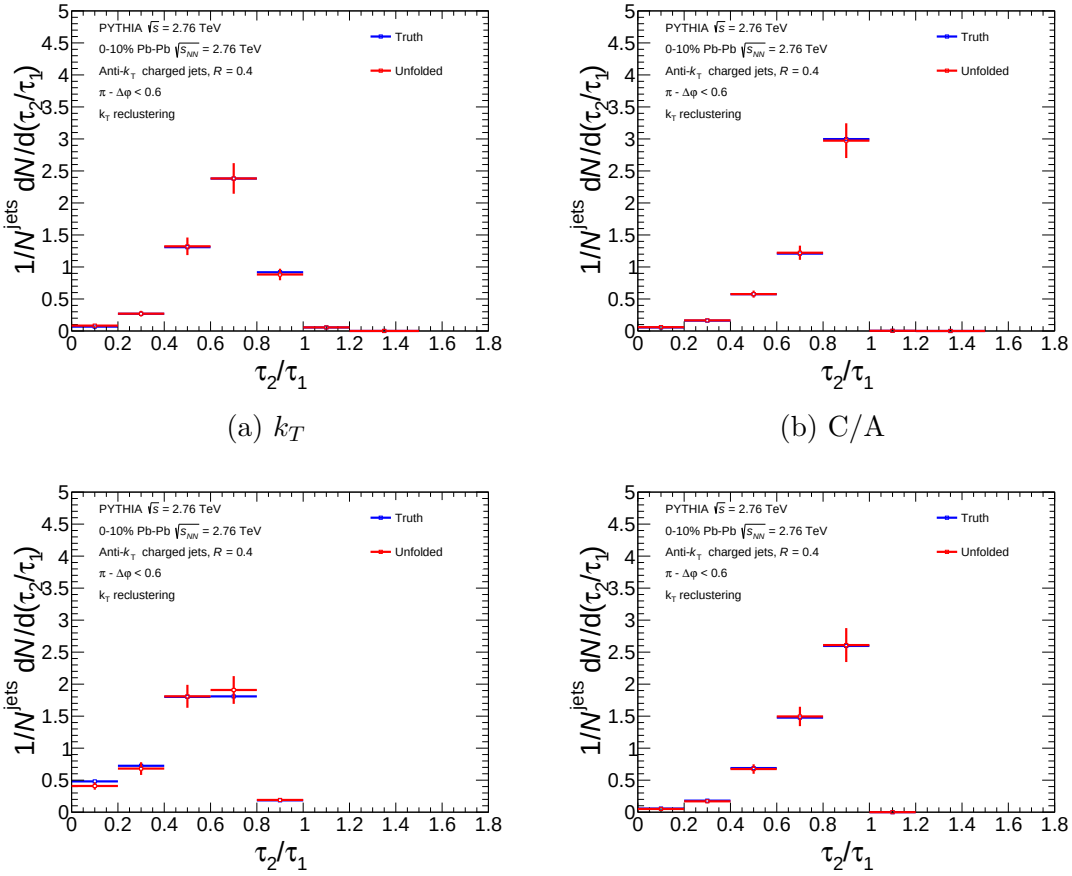

(a) k_T (b) C/A

(c) C/A + soft drop (d) C/A + minimisation

Figure C.3: The unfolded Pb-Pb and truth level τ_2/τ_1 distributions, used to obtain the weights for the prior systematic, are shown for each reclustering algorithm.

der derivative subtraction on the data and response matrix (at embedded level). The differences in these subtraction techniques have been explored in section 5.2. This systematic error is not considered for the soft drop with C/A algorithm, since derivative subtraction is not computationally compatible with soft drop.

C.6 Event Plane

The asymmetry in the collision geometry of the nuclei (particularly in non-central collisions), gives rise to a larger pressure gradient in one direction, compared to its perpendicular orientation. An axis of symmetry, of the emitted final state particles,

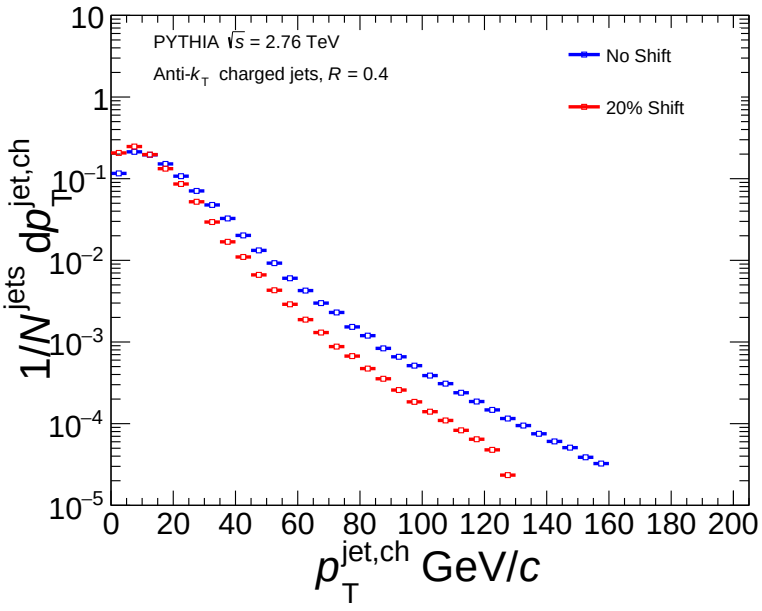

Figure C.4: The default and 20% downward shifted truth level $p_T^{jet,ch}$ distributions, used to obtain the weights for the prior systematic, are shown.

can be defined. This is known as the event plane [133]. Hadrons oriented in the direction of the event plane (in-plane) acquire a positive p_T shift, compared to their out of plane counterparts. Therefore, the probability of finding a high p_T trigger hadron in the in-plane direction, is increased. This induces a slight geometrical bias in the measured data. However, when embedding jets, this bias is not accounted for since the generated PYTHIA jets are embedded randomly within the Pb-Pb event.

The event plane systematic measures the effect of this bias on the unfolded solution. Entries in the response matrix are weighted, according to their orientation with respect to the event plane. Three orientations of in-plane, mid-plane and out of plane are defined, each covering $\pi/3$ in azimuth. The weights are extracted from data, by measuring the orientation of the trigger hadrons in the signal class, with respect to the event plane. This is shown in figure C.5. The ratio of the integrals of the in-pane, mid-plane and out of plane sections of this distribution, with respect to the integral of the in-plane section, form the weights. The obtained weights are as follows: 1. In-plane : 1.0 2. Mid-plane : 0.987 3. Out of plane : 0.966

The contribution of this systematic error is small, since the weights are close to unity. This is due to the largely symmetric collision geometries of central collisions.

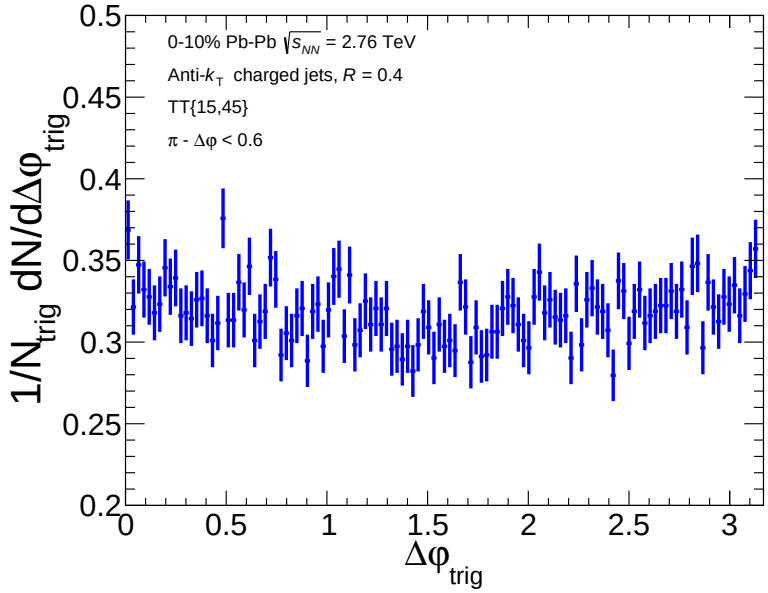

Figure C.5: The orientation of the trigger hadrons in the signal class (TT$\{15, 45\}$), with respect to the event plane, is shown. The distribution is split in to three sections of in-plane ($0-\frac{\pi}{3}$), mid-plane($\frac{\pi}{3}-\frac{2\pi}{3}$) and out of plane ($\frac{2\pi}{3}-\pi$).

C.7 Numerical Contributions

The contributions of each source of systematic error, in terms of a percentage deviation from the default solutions, are shown below. Tables C.1, C.2, C.3 and C.4 show the systematic errors for the τ_2/τ_1 jet shapes, for each of the reclustering algorithms.

Systematic Uncertainties				
Shape	τ_2/τ_1 using k_T reclustering			
Shape interval	0.2-0.4	0.4-0.6	0.6-0.8	0.8-1.0
Tracking Efficiency	3.5%	1.1%	1.1%	1.8%
Truncation	$^{+0.0}_{-4.9}$%	$^{+0.1}_{-0.9}$%	$^{+1.6}_{-0.0}$%	$^{<+0.1}_{-0.3}$%
Regularisation	$^{+3.4}_{-11.4}$%	$^{+0.2}_{-1.0}$%	$^{+3.3}_{-0.9}$%	$^{+0.9}_{-2.6}$%
Prior	$^{+9.0}_{-0.6}$%	$^{+1.6}_{-0.0}$%	$^{+0.2}_{-2.5}$%	$^{+0.0}_{-3.6}$%
Subtraction	$^{+0.0}_{-1.7}$%	$^{+3.3}_{-0.0}$%	$^{+0.0}_{-0.8}$%	$^{+1.6}_{-0.0}$%
Event Plane	$^{+0.1}_{-0.0}$%	$^{<+0.1}_{-0.0}$%	$^{<+0.1}_{-0.0}$%	$^{+0.0}_{>-0.1}$%

Table C.1: The percentage deviation of each systematic error, in comparison to the final unfolded solution, is shown for the τ_2/τ_1 jet shape measured using the k_T reclustering algorithm.

Systematic Uncertainties				
Shape	τ_2/τ_1 using C/A reclustering			
Shape interval	0.2-0.4	0.4-0.6	0.6-0.8	0.8-1.0
Tracking Efficiency	2.9%	2.0%	0.6%	0.3%
Truncation	$^{+0.0}_{-0.3}$%	$^{<+0.1}_{-0.8}$%	$^{<+0.1}_{-0.2}$%	$^{+0.5}_{-0.0}$%
Regularisation	$^{+0.4}_{-2.2}$%	$^{+0.1}_{-0.5}$%	$^{+0.7}_{-0.2}$%	$^{+0.1}_{>-0.1}$%
Prior	$^{+6.5}_{-0.0}$%	$^{+1.4}_{-0.0}$%	$^{+1.1}_{-0.0}$%	$^{+0.0}_{-1.1}$%
Subtraction	$^{+0.0}_{-10.1}$%	$^{+0.0}_{-0.5}$%	$^{+2.4}_{-0.0}$%	$^{+0.0}_{>-0.1}$%
Event Plane	$^{+3.3}_{-0.0}$%	$^{+1.2}_{-0.0}$%	$^{+0.0}_{-1.8}$%	$^{+0.1}_{-0.0}$%

Table C.2: The percentage deviation of each systematic error, in comparison to the final unfolded solution, is shown for the τ_2/τ_1 jet shape measured using the C/A reclustering algorithm.

Systematic Uncertainties				
Shape	τ_2/τ_1 using C/A with minimisation reclustering			
Shape interval	0.2-0.4	0.4-0.6	0.6-0.8	0.8-1.0
Tracking Efficiency	2.8%	0.8%	0.4%	0.1%
Truncation	$^{<+0.1}_{-3.1}\%$	$^{<+0.1}_{-0.6}\%$	$^{<+0.1}_{-0.0}\%$	$^{+0.5}_{>-0.1}\%$
Regularisation	$^{+2.2}_{-6.9}\%$	$^{+0.7}_{-2.3}\%$	$^{+0.9}_{-0.3}\%$	$^{+0.8}_{-0.2}\%$
Prior	$^{+5.8}_{-5.1}\%$	$^{+1.2}_{-1.9}\%$	$^{+1.1}_{-0.0}\%$	$^{+0.4}_{-1.1}\%$
Subtraction	$^{+0.0}_{-7.7}\%$	$^{+1.9}_{-0.0}\%$	$^{+0.0}_{-0.8}\%$	$^{+0.7}_{-0.0}\%$
Event Plane	$^{+0.0}_{>-0.1}\%$	$^{<+0.1}_{-0.0}\%$	$^{+0.0}_{>-0.1}\%$	$^{<+0.1}_{-0.0}\%$

Table C.3: The percentage deviation of each systematic error, in comparison to the final unfolded solution, is shown for the τ_2/τ_1 jet shape measured using the C/A with minimisation reclustering algorithm.

Systematic Uncertainties				
Shape	τ_2/τ_1 using soft drop with C/A reclustering			
Shape interval	0.2-0.4	0.4-0.6	0.6-0.8	0.8-1.0
Tracking Efficiency	0.3%	0.5%	1.1%	0.7%
Truncation	$^{<+0.1}_{-3.1}\%$	$^{+0.2}_{-0.0}\%$	$^{+2.0}_{-0.0}\%$	$^{+3.2}_{-0.0}\%$
Regularisation	$^{+2.9}_{-8.3}\%$	$^{<+0.1}_{-0.7}\%$	$^{+5.4}_{-1.8}\%$	$^{+6.2}_{>-2.1}\%$
Prior	$^{+7.6}_{-3.6}\%$	$^{+0.2}_{-0.0}\%$	$^{+3.8}_{-4.5}\%$	$^{+1.4}_{-9.1}\%$
Event Plane	$^{<+0.1}_{-0.0}\%$	$^{<+0.1}_{-0.0}\%$	$^{+0.0}_{>-0.1}\%$	$^{<+0.1}_{-0.0}\%$

Table C.4: The percentage deviation of each systematic error, in comparison to the final unfolded solution, is shown for the τ_2/τ_1 jet shape measured using the soft drop with C/A reclustering algorithm.

REFERENCES

[1] S.L. Glashow, "Partial-symmetries of Weak Interactions", Nucl.Phys. 22 (1961) 579-588

[2] S. Weinberg, "A Model of Leptons", Phys.Rev.Lett. 19 (1967) 1264-1266

[3] A. Salam, "Weak and Electromagnetic Interactions", proceedings 8th Nobel Symp ed N Svartholm (1968)

[4] D.J. Gross, F. Wilczek, "Asymptotically Free Gauge Theories. I", Phys.Rev. D8 (1973) 3633-3652

[5] S. Weinberg, "Non-Abelian Gauge Theories of the Strong Interactions", Phys.Rev.Lett. 31 (1973) 494-497

[6] H. Fritzsch, M. Gell-Mann, H. Leutwyler, "Advantages of the Color Octet Gluon Picture", Phys.Lett. 47B (1973) 365-368

[7] N. Brambilla, A. Pineda, J. Soto, A. Vairo, "Potential NRQCD: An Effective Theory for Heavy Quarkonium", Nucl.Phys. B566 (2000) 275

[8] E. Eichten, K. Gottfried, T. Kinoshita, John B. Kogut, K.D. Lane, Tung-Mow Ya, "The Spectrum of Charmonium", Phys.Rev.Lett. 36 (1976) 1276

[9] G.S. Bali, K. Schilling, A. Wachter, "Complete O(v^2) Corrections to the static Interquark Potential from SU(3) Gauge Theory", Phys.Rev. D56 (1997) 2566-2589

[10] K.G. Wilson, "Confinement of Quarks", Phys.Rev. D10 (1974) 2445-2459

[11] A. Deur, S.J. Brodsky, G.F. de Teramond, "The QCD Running Coupling", Prog.Part.Nucl.Phys. 90 (2016) 1-74

[12] G.S. Bali, N. Brambilla, A. Vairo, "A Lattice Determination of QCD Field Strength Correlators", Phys.Lett. B421 (1998) 265-272

[13] CMS Collaboration, "Determination of the Strong Coupling Constant from the Measurement of Inclusive Multijet Event Cross Sections in pp Collisions at $\sqrt{s} = 8$ TeV", CMS-PAS-SMP-16-008

[14] D.J. Gross, F. Wilczek, "Ultraviolet Behavior of Nonabelian Gauge Theories", Phys.Rev.Lett. 30 (1973) 1343-1346

[15] M. Gao, "Debye Screening in the QCD Gluonic Plasma", Phys.Rev. D41 (1990) 626

[16] N.F. Mott, "Metal-Insulator Transition", Rev.Mod.Phys. 40 (1968) 677-683

[17] F. Karsch, "Lattice Results on QCD Thermodynamics", Nucl.Phys. A698 (2002) 199-208

[18] U. Heinz, M. Jacob, "Evidence for a New State of Matter: An Assessment of the Results from the CERN Lead Beam Programme", arXiv:nucl-th/0002042

[19] STAR Collaboration, "Centrality Dependence of High-pT Hadron Suppression in Au+Au Collisions at $\sqrt{s_{NN}} = 130$ GeV", Phys.Rev.Lett. 89 (2002) 202301

[20] PHENIX Collaboration, "Formation of Dense Partonic Matter in Relativistic Nucleus-Nucleus Collisions at RHIC: Experimental Evaluation by the PHENIX Collaboration", Nucl.Phys. A757 (2005) 184-283

[21] C. Loizides, "PhD Thesis : Jet Physics in ALICE", arXiv:nucl-ex/0501017

[22] R. Stock, "Relativistic Nucleus-Nucleus Collisions and the QCD Matter Phase Diagram", arXiv:0807.1610 [nucl-ex]

[23] Experimental Quark Physics Lab Hiroshima Uni, Retrieved July 2018: *http ://www.hepl.hiroshima-u.ac.jp/pwo/hot_dense_matter.html*

[24] ALICE Collaboration, "Measurement of Transverse Energy at Midrapidity in Pb-Pb Collisions at $\sqrt{s_{NN}} = 2.76$ TeV", Phys.Rev. C94 (2016) no.3, 034903

[25] W. Broniowski, W. Florkowski, "Geometric Relation Between Centrality and the Impact Parameter in Relativistic Heavy-Ion Collisions", Phys.Rev. C65 (2002) 024905

[26] R. Baier, Yu.L. Dokshitzer, A.H. Mueller, S. Peigné, D. Schiff, "Radiative energy loss of high energy quarks and gluons in a finite volume quark-gluon plasma", Nucl.Phys. B483 (1997) 291-320

[27] M. Gyulassy, P. Levai, I. Vitev, "Reaction Operator Approach to Non-Abelian Energy Loss", Nucl.Phys. B594 (2001) 371-419

[28] L.D. Landau, I. Pomeranchuk, "The Limits of Applicability of the Theory of Bremsstrahlung by Electrons and of the Creation of Pairs at Large Energies", Dokl. Akad, Nauk SSSR, 92, 535, (1953)

[29] L.D. Landau, I. Pomeranchuk, "Electron-Cascade Processes at Ultra-High Energies", Dokl. Akad. Nauk SSSR, 92, 735, (1953)

[30] A.B. Migdal, "Bremsstrahlung and Pair Production in Condensed Media at High Energies", Phys.Rev. 103 (1956) 1811-1820

[31] STAR Collaboration, "Transverse Momentum and Collision Energy Dependence of High p_T Hadron Suppression in Au+Au Collisions at Ultrarelativistic Energies", Phys.Rev.Lett. 91 (2003) 172302

[32] PHENIX Collaboration, "High-p_T Charged Hadron Suppression in Au+Au Collisions at $sqrt(s_N N) = 200$ GeV", Phys.Rev. C69 (2004) 034910

[33] ALICE Collaboration, "Charged Particle Production at Large Transverse Momentum in Pb-Pb Collisions at $\sqrt{s_{NN}} = 2.76$ TeV Measured with ALICE at the LHC", J.Phys. G38 (2011) 124112

[34] CMS Collaboration, "Nuclear Modification Factors from the CMS Experiment", J.Phys. G38 (2011) 124015

[35] ALICE Collaboration, "Transverse Momentum Spectra and Nuclear Modification Factors of Charged Particles in pp, p-Pb and Pb-Pb Collisions at the LHC", arXiv:1802.09145

[36] S.B. Libby, G. Sterman, "Jet and lepton-pair production in high-energy lepton-hadron and hadron-hadron scattering", Phys.Rev. D18 (1978) 3252

[37] D. Amati, R. Petronzio, G. Veneziano, "Relating Hard QCD Processes Through Universality of Mass Singularities (II)", Nucl.Phys. B146 (1978) 29-49

[38] R.K. Ellis, H. Georgi, M. Machacek, H.D. Politzer, G.G. Ross, "Perturbation Theory and the Parton Model in QCD", Nucl.Phys. B152 (1979) 285-329

[39] V.N. Gribov, L.N. Lipatov, "Deep Inelastic Electron Scattering in Perturbation Theory", Sov.J.Nucl.Phys. 15 (1972) 438-450

[40] G. Altarelli, G. Parisi, "Asymptotic Freedom in Parton Language", Nucl.Phys. B126 (1977) 298-318

[41] Y.L. Dokshitzer, "Calculation of the Structure Functions for Deep Inelastic Scattering and e^+ e^- Annihilation by Perturbation Theory in Quantum Chromodynamic", Sov.Phys.JETP 46 (1977) 641-653

[42] L.N. Lipatov, "Reggeization of the Vector Meson and the Vacuum Singularity in Nonabelian Gauge Theories", Sov.J.Nucl.Phys. 23 (1976) 338-345

[43] E.A. Kuraev, L.N. Lipatov, V.S. Fadin, "Multi-Reggeon Processes in the Yang-Mills Theory", Sov.Phys.JETP 44 (1976) 443-450

[44] E.A. Kuraev, L.N. Lipatov, V.S. Fadin, "The Pomeranchuk Singularity in Non-abelian Gauge Theories", Sov.Phys.JETP 45 (1977) 199-204

[45] I.I. Balitsky, L.N. Lipatov, "The Pomeranchuk Singularity in Quantum Chromodynamics", Sov.J.Nucl.Phys. 28 (1978) 822-829

[46] A.D. Martin, W.J. Stirling, R.S. Thorne, G. Watt, "Parton Distributions for the LHC", Eur.Phys.J. C63 (2009) 189-285

[47] E. Eichten, I. Hinchliffe, K. Lane, C. Quigg, "Super Collider Physics", Rev.Mod.Phys. 58 (1986) 1065-1073

[48] G. Altarelli, R.K. Ellis, G. Martinelli, "Lepton Pair Production at ISR Energies and QCD", Phys.Lett. 151B (1985) 457

[49] S.D. Drell, T.M. Yan, "Massive Lepton-Pair Production in Hadron-Hadron Collisions at High-Energies", Phys.Rev.Lett. 25 (1970) 902

[50] G. Altarelli, R.K. Ellis, G. Martinelli, "Leptoproduction and Drell-Yan Processes Beyond the Leading Approximation in Chromodynamics", Nucl.Phys. B146 (1978) 544

[51] S.M. Berman, J.D. Bjorken, J.B. Kogut, "Inclusive Processes at High Transverse Momentum", Phys.Rev. D4 (1971) 3388

[52] J.C. Collins, D.E. Soper, "Parton Distribution and Decay Functions", Nucl.Phys. B194 (1982) 445-492

[53] P.J. Mulders, R.D. Tangerman, "The Complete tree level result up to order 1/Q for polarized deep inelastic leptoproduction ", Nucl.Phys. B484 (1997) 538-540

[54] A. Bianconi, S. Boffi, R. Jakob, M. Radici, "Two-Hadron Interference Fragmentation Functions Part I: General Framework", Phys.Rev. D62 (2000) 034008

[55] JADE Collaboration, "Particle Distribution in Three Jet Events Produced by e^+ e^- Annihilation", Z.Phys. C21 (1983) 37

[56] OPAL Collaboration, "A Direct Observation of Quark - Gluon Jet Differences at LEP", Phys.Lett. B265 (1991) 462-474

[57] DELPHI Collaboration, "Charged Particle Multiplicity Distributions for Fixed Number of Jets in Z0 Hadronic Decays", Z.Phys. C56 (1992) 63-76

[58] ATLAS Collaboration, "Measurement of the Jet Fragmentation Function and Transverse Profile in Proton-Proton Collisions at a Center-of-Mass Energy of 7 TeV with the ATLAS Detector", Eur.Phys.J. C71 (2011) 1795

[59] CMS Collaboration, "Measurements of Differential Jet Cross Sections in Proton-Proton Collisions at $\sqrt{s} = 7$ TeV with the CMS Detector", Phys.Rev. D87 (2013) no.11, 119902

[60] Y. Lee, "Jet Quenching at RHIC and the LHC", J.Phys.Conf.Ser. 446 (2013) 012001

[61] Y. Mehtar-Tani, C.A. Salgado, K. Tywoniuk, "Anti-Angular Ordering of Gluon Radiation in QCD Media", Phys.Rev.Lett. 106 (2011) 122002

[62] Y. Mehtar-Tani, K. Tywoniuk, "Jet (De)Coherence in Pb-Pb Collisions at the LHC", Phys.Lett. B744 (2015) 284-287

[63] J. Casalderrey-Solana, Y. Mehtar-Tani, C.A. Salgado, K. Tywoniuk, "New Picture of Jet Quenching Dictated by Color Coherence", Phys.Lett. B725 (2013) 357-360

[64] Y. Mehtar-Tani, K. Tywoniuk, "Groomed Jets in Heavy-Ion Collisions: Sensitivity to Medium-Induced Bremsstrahlung", JHEP 1704 (2017) 125

[65] ALICE Collaboration, "Medium Modification of the Shape of Small-Radius Jets in Central Pb-Pb Collisions at $\sqrt{s_{NN}} = 2.76$ TeV", arXiv:1807.06854 [nucl-ex]

[66] J. Thaler, K.V. Tilburg, "Identifying Boosted Objects with N-subjettiness", JHEP 1103 (2011) 015

[67] A.J. Larkoski, I. Moult, "The Singular Behavior of Jet Substructure Observables", Phys.Rev. D93 (2016) 014017

[68] J. Shelton, "TASI Lectures on Jet Substructure", arXiv:1302.0260

[69] ALICE Collaboration, "Measurement of Jet Quenching with Semi-Inclusive Hadron-Jet Distributions in Central Pb-Pb Collisions at $\sqrt{s_{NN}} = 2.76$ TeV", JHEP 1509 (2015) 170

[70] M. Cacciari, G.P. Salam, G. Soyez, "FastJet User Manual", Eur.Phys.J. C72 (2012) 1896

[71] S. Moretti, L. Lonnblad, T. Sjostrand, "New and Old Jet Clustering Algorithms for Electron Positron Events", JHEP 9808 (1998) 001

[72] J.B. Babcock, R.E. Cutkosky, "Identification of Jets", Nucl.Phys. B176 (1980) 113-134

[73] S.D.Ellis, J. Huston, M. Toennesmann"On Building Better Cone Jet Algorithms", eConf C010630 (2001) 513

[74] R. Atkin"Review of Jet Reconstruction Algorithms", J.Phys.Conf.Ser. 645 (2015) no.1, 012008

[75] M. Cacciari, G.P. Salam, G. Soyez, "The anti-k_t jet clustering algorithm", JHEP 0804 (2008) 063

[76] S.D. Ellis, D.E. Soper, "Successive Combination Jet Algorithm For Hadron Collisions", Phys.Rev. D48 (1993) 3160-3166

[77] M. Wobisch, T. Wengler, "Hadronization Corrections to Jet Cross Sections in Deep-Inelastic Scattering", arXiv:hep-ph/9907280

[78] G. Soyez, "Pileup Mitigation at the LHC: a Theorist's View", arXiv:1801.09721 [hep-ph]

[79] Z. Kang, F. Ringer, I. Vitev, "Inclusive Production of Small Radius Jets in Heavy-Ion Collisions", Phys.Lett. B769 (2017) 242-248

[80] I.W. Stewart, F.J. Tackmann, J. Thaler, C.K. Vermilion, T.F. Wilkason, "XCone: N-jettiness as an Exclusive Cone Jet Algorithm", JHEP 1511 (2015) 072

[81] A.J. Larkoski, S. Marzani, G. Soyez, J. Thaler, "Soft Drop", JHEP 1405 (2014) 146

[82] C. Frye, A.J. Larkoski, M.D. Schwartz, K. Yan, "Factorization for Groomed Jet Substructure Beyond the Next-to-Leading Logarithm", JHEP 1607 (2016) 064

[83] ALICE Collaboration, "Centrality Determination of Pb-Pb Collisions at $\sqrt{s_{NN}} = 2.76$ TeV with ALICE", Phys.Rev. C88 (2013) no.4, 044909

[84] ALICE Collaboration, "Charged-Particle Multiplicity Density at Mid-Rapidity in Central Pb-Pb Collisions at $\sqrt{s_{NN}} = 2.76$ TeV", Phys.Rev.Lett. 105 (2010) 252301

[85] ALICE Collaboration, "Charged-Particle Multiplicity Measurement in Proton-Proton Collisions at $\sqrt{s_{NN}} = 0.9$ and $\sqrt{s_{NN}} = 2.36$ TeV with ALICE at LHC", Eur.Phys.J. C68 (2010) 89-108

[86] ALICE Collaboration, "Centrality Dependence of the Pseudorapidity Density Distribution for Charged Particles in Pb-Pb Collisions at $\sqrt{s_{NN}} = 2.76$ TeV", Phys.Lett. B726 (2013) 610-622

[87] ALICE Collaboration, "Measurement of Event Background Fluctuations for Charged Particle Jet Reconstruction in Pb-Pb Collisions at $\sqrt{s_{NN}} = 2.76$ TeV", JHEP 1203 (2012) 053

[88] M. Cacciari, G.P. Salam, "Pileup Subtraction Using Jet Areas", Phys.Lett. B659 (2008) 119-126

[89] P. Berta, M. Spousta, D.W. Miller, R. Leitner, "Particle-Level Pileup Subtraction for Jets and Jet Shapes", JHEP 1406 (2014) 092

[90] G. Soyez, G.P. Salam, J. Kim, S. Dutta, M. Cacciari, "Pileup Subtraction for Jet Shapes", Phys.Rev.Lett. 110 (2013) no.16, 162001

[91] ALICE Collaboration, "Measurement of Charged Jet Suppression in Pb-Pb Collisions at $\sqrt{s_{NN}} = 2.76$ TeV", JHEP 1403 (2014) 013

[92] ATLAS Collaboration, "Measurement of Jet Fragmentation in Pb+Pb and pp Collisions at $\sqrt{s_{NN}} = 2.76$ TeV with the ATLAS Detector", Eur.Phys.J. C77 (2017) no.6, 379

[93] T. Renk, H. Holopainen, R. Paatelainen, K.J. Eskola, "Systematics of the Charged-Hadron P_T Spectrum and the Nuclear Suppression Factor in Heavy-Ion Collisions from $\sqrt{s_{NN}} = 200$ GeV to $\sqrt{s_{NN}} = 2.76$ TeV", Phys.Rev. C84 (2011) 014906

[94] D. de Florian, "Next-to-leading order QCD corrections to hadron+jet production in pp collisions at RHIC", Phys.Rev. D79 (2009) 114014

[95] G. D'Agostini, "A Multidimensional Unfolding Method Based on Bayes' Theorem", Nucl.Instrum.Meth. A362 (1995) 487-498

[96] T. Adye, "Unfolding Algorithms and Tests Using RooUnfold", C11-01-17.2, p.313-318 Proceedings

[97] L. Evans , P. Bryant, "LHC Machine", JINST 3 (2008) S08001

[98] CERN, Retrieved July 2018: *https ://lhc-machine-outreach.web.cern.ch/lhc-machine-outreach/images/lhc-schematic.jpg*

[99] K. Schindl, "The Injector Chain for the LHC", C99-01-26, p.47-52 Proceedings

[100] CERN, Retrieved July 2018: *http ://atlas.kek.jp/sub/photos/Accelerator/*010 7024_01.*jpg*

[101] E. Ciapala, L. Arnaudon, P. Baudrenghien, O. Brunner, A. Butterworth, T. Linnecar, P. Maesen, J. Molendijk, E. Montesinos, D. Valuch, F. Weierud, "Commissioning of the 400 MHz LHC RF System", CERN-LHC-PROJECT-REPORT-1147

[102] L.Evans, P.Bryant, "Performance of the ALICE Experiment at the CERN LHC", Int.J.Mod.Phys. A29 (2014) 1430044

[103] ALICE Collaboration, "Measurement of Inelastic, Single- and Double-Diffraction Cross Sections in Proton-Proton Collisions at the LHC with ALICE", Eur.Phys.J. C73 (2013) no.6, 2456

[104] K. Oyama for the ALICE Collaboration, "Reference Cross Section Measurements with ALICE in pp and Pb-Pb Collisions at LHC", arXiv:1305.7044 [nucl-ex]

[105] ALICE Collaboration, "The ALICE Experiment at the CERN LHC", JINST 3 (2008) S08002

[106] ALICE Collaboration, "Centrality Dependence of the Charged-Particle Multiplicity Density at Midrapidity in Pb-Pb Collisions at $\sqrt{s_{NN}} = 2.76$ TeV", Phys.Rev.Lett. 106 (2011) 032301

[107] ALICE Collaboration, "ALICE technical design report of the inner tracking system (ITS)", CERN-LHCC-99-12

[108] P. Kuijer for the ALICE Collaboration, "The Inner Tracking System of the Alice Experiment", Nucl.Instrum.Meth. A530 (2004) 28-32

[109] F. Meddi for the ALICE Collaboration, "The ALICE Silicon Pixel Detector (SPD)", Nucl.Instrum.Meth. A465 (2000) 40-45

[110] A. Morsch, B. Pastircak, "Radiation in ALICE detectors and electronics racks", ALICE Internal Note ALICE-INT-2002-028

[111] LHC ALICE J-Group, Retrieved June 2018: *http ://alice-j.org/alice*

[112] ALICE Collaboration, "Performance of the ALICE VZERO System", JINST 8 (2013) P10016

[113] P. Antonioli for the ALICE Collaboration, "Soft QCD, Minimum Bias and Diffraction: Results from ALICE", EPJ Web Conf. 28 (2012) 02004

[114] ALICE Collaboration, "Jet-Like Correlations with Neutral Pion Triggers in pp and Central Pb-Pb Collisions at 2.76 TeV", Phys.Lett. B763 (2016) 238-250

[115] M.L. Miller, K. Reygers, S.J. Sanders, P. Steinberg, "Glauber Modeling in High Energy Nuclear Collisions", Ann.Rev.Nucl.Part.Sci. 57 (2007) 205-243

[116] R. Fruhwirth, "Application of Kalman Filtering to Track and Vertex Fitting", Nucl.Instrum.Meth. A262 (1987) 444-450

[117] ALICE CERN Twiki, Retrieved June 2018: *https ://twiki.cern.ch/twiki-/bin/viewauth/ALICE/HybridTracks*

[118] ATLAS Collaboration, "Performance of $b-$Jet Identification in the ATLAS Experiment", JINST 11 (2016) no.04, P04008

[119] GEANT4 Collaboration, "Geant4 A Simulation Toolkit", Nucl.Instrum.Meth. A506 (2003) 250-303

[120] GEANT4 Collaboration, "Recent Developments in Geant4", Annals Nucl.Energy 82 (2015) 19-28

[121] ALICE Collaboration, "Charged Jet Cross Sections and Properties in Proton-Proton Collisions at $\sqrt{s} = 7$ TeV", Phys.Rev. D91 (2015) no.11, 112012

[122] G. Contin, "Performance of the Present ALICE Inner Tracking System and Studies for the Upgrade", JINST 7 (2012) C06007

[123] ALICE Collaboration, "Centrality Dependence of the Pseudorapidity Density Distribution for Charged Particles in Pb-Pb Collisions at $\sqrt{s_{NN}} = 2.76$ TeV", Phys.Lett. B726 (2013) 610-622

[124] T. Sjostrand, S. Mrenna, P. Skands,, "PYTHIA 6.4 Physics and Manual", JHEP 0605 (2006) 026

[125] P.Z. Skands, "Tuning Monte Carlo Generators: The Perugia Tunes", Phys.Rev. D82 (2010) 074018

[126] ALICE Collaboration, "Charged-Particle Multiplicity Measurement in Proton-Proton Collisions at $\sqrt{s} = 2.76$ TeV with ALICE at LHC", Eur.Phys.J. C68 (2010) 345-354

[127] ATLAS Collaboration, "Charged-Particle Multiplicities in pp Interactions Measured with the ATLAS Detector at the LHC", New J.Phys. 13 (2011) 053033

[128] ATLAS Collaboration, "Measurement of Underlying Event Characteristics Using Charged Particles in pp Collisions at $\sqrt{s} = 900$GeV and 7 TeV with the ATLAS Detector", Phys.Rev. D83 (2011) 112001

[129] R. Field for the CDF Collaboration, "DF Run II Monte-Carlo tunes", C06-10-20.2 Proceedings

[130] C. Oleari, "The POWHEG-BOX", Nucl.Phys.Proc.Suppl. 205-206 (2010) 36-41

[131] P. Ilten, N.L. Rodd, J. Thaler, M. Williams, "Disentangling Heavy Flavor at Colliders", Phys.Rev. D96 (2017) no.5, 054019

[132] T. Sakaguchi for the PHENIX collaboration, "PHENIX Highlights", Nucl.Phys. A904-905 (2013) 11c-18c

[133] T. Drozhzhova for the ALICE collaboration, "Centrality and Collision Event-Plane Determination in ALICE at the LHC", J.Phys.Conf.Ser. 798 (2017) 012061